Nuclear Charge Radii of Light Isotopes Based on Frequency Comb Measurements

Monika Žáková geboren in Trstená, Slowakei

Mainz, den 11. Februar 2010

Zusammenfassung

In dieser Arbeit wurde die optische Frequenzkamm-Technologie erstmals für Kernstrukturuntersuchungen von leichten radioaktiven Isotopen genutzt. Dafür wurden ingesamt drei Lasersysteme mit verschiedenen Methoden auf genau bekannte Frequenzen stabilisiert und diese dann bei zwei verschiedenen Experimenten eingesetzt. Messungen der absoluten Übergangsfrequenz in Lithium- und Berylliumisotopen wurden mit relative Genauigkeiten in der Größenordnung von 10^{-10} durchgeführt. Eine solche hohe Genauigkeit ist bei den leichten Elementen notwendig, weil der Kernvolumeneffekt nur einen Anteil von 10^{-9} zur gesamten Übergangsfrequenz beiträgt. Für die Berylliumisotope wurde daraus die Isotopieverschiebung mit einer Genauigkeit bestimmt, die ausreicht, um den Kernladungsradius aller gemessenen Isotope zu extrahieren.

An den stabilen Li-Isotopen ^{6,7}Li wurde eine Doppler-freie Zweiphotonen-Spektroskopie durchgeführt und die absolute Frequenz des $2S \rightarrow 3S$ Übergangs bestimmt. Die erreichte relative Genauigkeit von 2×10^{-10} übertrifft die früherer Messungen um etwa eine Größenordnung. Dies stellt die Grundlage für eine rein optische Bestimmung der absoluten Kernladungsradien der stabilen und kurzlebigen Isotope dar. Allerdings gilt es dazu von theoretischer Seite noch die Berechnungen um etwa zwei Größeordnung zu verbessern.

Das zweite im Rahmen dieses Arbeit durchgeführte Experiment fand bei ISOLDE/CERN statt. Eine eigens entwickelte Methode der kollinearen Spektroskopie bei der zwei gegeneinander propagierende Laserstrahlen genau bekannter Frequenz verwendet werden, erlaubte es die Übergangsfrequenzen der D_1- und D_2-Linien in Beryllium-Ionen der Isotope ^{7,9,10,11}Be mit deiner Genauigkeit von etwa 1 MHz zu messen. Durch die Kombination der daraus bestimmten Isotopieverschiebung mit kürzlich durchgeführten, sehr genauen Berechnungen des spezifischen Masseneffektes der untersuchten Übergänge wurden die Kernladungsradien von ^{7,10}Be und des Ein-Neutronen-Halokerns ^{11}Be bestimmt. Die Ladungsradien nehmen von ^{7}Be bis ^{10}Be monoton ab, um danach bei ^{11}Be wieder anzusteigen. Während die Abnahme auf die kompakter werdende Clusterstruktur der Berylliumkerne zurückgeführt wird, kann die markante Zunahme zwischen ^{10}Be und ^{11}Be durch eine Kombination aus einer Schwerpunktsbewegung des ^{10}Be Rumpfkerns von ^{11}Be und einer Änderung der inneren Struktur des erklärt werden. Um die Beiträge der beiden Effekte zu quantifizieren, wurden experimentale Resultate aus Kernreaktionsexperimenten herangezogen. Es zeigt sich, dass die Schwerpunktsbewegung der dominante Beitrag ist.

Darüberhinaus wurde der Unterschied in der Isotopieverschiebung zwischen den D_1 und D_2 Feinstruktur-Übergängen ermittelt. Das Resultat ist in guter Übereinstimmung mit den theoretischen Berechnungen und stellt einen unabhängigen Test der Berechnungen und des Experiments dar.

Abstract

Optical frequency comb technology has been used in this work for the first time to investigate the nuclear structure of light radioactive isotopes. Therefore, three laser systems were stabilized with different techniques to accurately known optical frequencies and used in two specialized experiments. Absolute transition frequency measurements of lithium and beryllium isotopes were performed with accuracy on the order of 10^{-10}. Such a high accuracy is required for the light elements since the nuclear volume effect has only a 10^{-9} contribution to the total transition frequency. For beryllium, the isotope shift was determined with an accuracy that is sufficient to extract information about the proton distribution inside the nucleus.

A Doppler-free two-photon spectroscopy on the stable lithium isotopes ^{6,7}Li was performed in order to determine the absolute frequency of the $2S \rightarrow 3S$ transition. The achieved relative accuracy of 2×10^{-10} is improved by one order of magnitude compared to previous measurements. The results provide an opportunity to determine the nuclear charge radius of the stable and short-lived isotopes in a pure optical way but this requires an improvement of the theoretical calculations by two orders of magnitude.

The second experiment presented here was performed at ISOLDE/CERN, where the absolute transition frequencies of the D_1 and D_2 lines in beryllium ions for the isotopes ^{7,9,10,11}Be were measured with an accuracy of about 1 MHz. Therefore, an advanced collinear laser spectroscopy technique involving two counter-propagating frequency-stabilized laser beams with a known absolute frequency was developed. The extracted isotope shifts were combined with recent accurate mass shift calculations and the root-mean square nuclear charge radii of ^{7,10}Be and the one-neutron halo nucleus ^{11}Be were determined. Obtained charge radii are decreasing from ^{7}Be to ^{10}Be and increasing again for ^{11}Be. While the monotone decrease can be explained by a nucleon clustering inside the nucleus, the pronounced increase between ^{10}Be and ^{11}Be can be interpreted as a combination of two contributions: the center-of-mass motion of the ^{10}Be core and a change of intrinsic structure of the core. To disentangle these two contributions, the results from nuclear reaction measurements were used and indicate that the center-of-mass motion is the dominant effect.

Additionally, the splitting isotope shift, i.e. the difference in the isotope shifts between the D_1 and D_2 fine structure transitions, was determined. This shows a good consistency with the theoretical calculations and provides a valuable check of the beryllium experiment.

Contents

List of Figures

List of Tables

1 Introduction

The shapes and radial sizes of nuclei are among the most basic properties for the verification of nuclear models. Exceptionally large nuclei, which did not follow the normal $A^{1/3}$ distribution from the liquid drop model, were observed for the first time in 1985 in the measurements of interaction cross section by Tanihata *et al.* [Tan85, Tan88]. They performed nuclear scattering experiments with light elements and observed significant changes in the interaction cross sections between neighboring isotopes. It was soon proposed that the observed large nuclei consist of a compact nuclear core and one or more nucleons (mostly neutrons) which are weakly bound, extend the nucleus and form a so-called 'halo' nucleus [Han87]. This discovery inspired a variety of experiments [Tan96, Jon04] and theoretical models [Alk04] in which properties of halo nuclei were studied. The halo systems are mostly in their ground states or low-lying excited states. Nearly all observed halos are in the mass region $A = 6 - 19$ mainly located close to the neutron drip-line, which is a border of particle stability. A number of light neutron-rich nuclei are now known to have a pronounced halo ground state, such as ^{6}He, ^{11}Li, ^{11}Be, ^{12}Be, ^{14}Be, ^{15}C and ^{19}C and others in excited states, like ^{17}B, ^{19}B and ^{22}C. There are fewer proton halos (^{8}B, ^{13}N, ^{17}Ne), which are spatially less extended compared to neutron halos because of the confining Coulomb barrier.

The binding energy of the halo nucleon (nucleons) is typically 1 MeV or less, and thereby much weaker than typical binding energies of nucleons observed in stable nuclei. The valence neutron (neutrons) for one- and two-neutron halos is (are) known to be on orbitals composed of s- and p-waves [Rii06]. The combination of a weak binding energy with low angular momentum ($l = 0, 1$) allows the halo nucleon (nucleons) to explore regions well beyond the nuclear core.

Laser spectroscopy provides a model-independent way to access nuclear ground state properties, like nuclear spin, electromagnetic moments and nuclear charge radii also in light isotopes. ^{11}Li was the first halo nucleus that was studied in this way. The collinear laser spectroscopy collaboration (COLLAPS) at ISOLDE determined the spin, the nuclear magnetic dipole moment and the electric quadrupole moment using the β-NMR technique in a series of measurements [Arn87, Arn92, Arn94]. Concerning the two-neutron halo structure of ^{11}Li, the most remarkable result is the small difference in the moments of ^{9}Li and ^{11}Li which excludes large deformations of this nucleus.

More recently, the magnetic dipole moment of ^{11}Be (one-neutron halo) has been measured [Gei99] by the same technique and the measurements of ^{9,11}Li were improved [Bor05, Neu08].

The proton distribution inside the nucleus (nuclear charge radius) is one of the properties which can indicate the influence of the valence nucleon (nucleons) on the compact nuclear core since all protons are part of the core in a neutron halo nucleus. The large matter radius of ^{11}Li was explained by the weak binding between the compact ^{9}Li core and two loosely bound neutrons. A possible difference in charge radii between these two neighboring isotopes can answer an interesting question, whether the compact core of ^{11}Li, with the same number of nucleons as ^{9}Li, is modified by the additional neutrons and has different structure than the free ^{9}Li.

The charge radii can be determined in a model-independent way from optical isotope shift measurements. The isotope shift is the difference in the transition frequencies between two isotopes of the same element, described in detail in section 2.2. The technique is widely used for stable and unstable nuclei with medium and high Z, but is rather challenging for very light species [Ott89]. The standard collinear laser spectroscopy approach is not suitable for the very light species because of a limited knowledge of the acceleration voltage, at ISOLDE typically 60 000(6) eV. The voltage uncertainty is too large to perform the isotope shift measurements at a precision that is sufficient to extract nuclear charge radii. The lightest isotope that was measured at COLLAPS was ^{17}Ne. To access lighter elements new methods were developed during the last years.

Based on new and very specialized techniques, two groups have succeeded in measuring optical isotope shifts of very light radioactive nuclei ($Z < 10$) with sufficient accuracy. At the Argonne National Laboratory and at GANIL, the charge radii of ^{6,8}He were obtained from laser spectroscopy on helium atoms confined in a magneto-optical trap [Wan04, Mue07], while an international collaboration, lead by GSI Darmstadt and the University of Tübingen, developed a method for high-resolution resonance ionization spectroscopy and measured the charge radii of ^{8,9}Li at GSI [Ewa04], [Ewa05] and of ^{11}Li [San06] at the ISAC mass separator at TRIUMF. ^{6}He and ^{11}Li are two-neutron halo nuclei and ^{8}He is considered to be a four-neutron halo nucleus.

In this work two experiments are presented that deal with the nuclear charge radius determination of light elements, namely lithium and beryllium.

Lithium   We have performed further Doppler-free two-photon spectroscopy measurements on the stable lithium isotopes ^{6,7}Li at GSI, Darmstadt in order to determine the absolute frequency of the $2S \rightarrow 3S$ transition with a spectroscopy laser stabilized to a fem-

tosecond laser frequency comb. The experiment and results are presented in this thesis. The accuracy was improved by one order of magnitude compared to previous measurements [Bus03]. The achieved accuracy provides an additional test of the atomic theory calculations that are the basis for the charge radius determination. On a long-term perspective, this measurement might also provide an all-optical value for the nuclear charge radii of the lithium isotopes, once the accuracy in theory can be further improved and QED terms of order α^4 can be calculated. Then, the absolute field effect in the transition and, therefore, the absolute charge radius could be extracted – similarly to measurements in hydrogen [Ude97] and deuterium [Hub98]. More details about the direct charge radius determination are given in section 2.3 and in the introduction of the recently published article[1] [San09] about the absolute frequency measurements in stable lithium isotopes.

Beryllium An advanced technique for spectroscopy on fast beryllium ions was described recently in [Noe09, Tie09], where we have performed combined collinear and anti-collinear spectroscopy. The absolute frequencies of the $2s_{1/2} \rightarrow 2p_{1/2}$ transition for ^{7,9,10,11}Be were measured with an accuracy of 1.5 MHz with a frequency comb. In combination with accurate mass-dependent isotope shift calculations [Yan08, Puch08] these frequencies were used to determine the changes in the mean-square nuclear charge radii along this chain of isotopes [Noe09].

In this work, the laser system for these measurements was developed and the results presented here are from the isotope shifts on the $2s_{1/2} \rightarrow 2p_{3/2}$ transitions with an accuracy of 2 MHz, which is more than one order of magnitude better than that in [Nak06]. The nuclear charge radii, extracted from the isotope shift measurements and mass-shift calculations [Yan08, Puch09b], are in very good agreement with the charge radii obtained from the $2s_{1/2} \rightarrow 2p_{1/2}$ transition. Additionally, the splitting isotope shift, i.e. the difference in the isotope shift between the two fine structure levels, which is nearly independent of QED and nuclear volume effects was determined and compared to the theoretical predictions [Yan08, Puch09].

In the following theory section different techniques for the matter and charge radii determinations are described. The description of the atomic isotope shift technique and how to extract the charge radius from theoretical calculations and measured isotope shifts is given in detail. The Doppler-free two-photon spectroscopy and resonance ionization used in the lithium experiment and the modified collinear laser spectroscopy applied in the beryllium experiment are discussed in detail in chapter 3. The lasers used in this

---

[1]The article is attached at the end of the thesis.

experiment and the frequency comb as a frequency reference and a tool to measure laser frequencies with high accuracy are described in chapter 4. The setup for the lithium experiment is reported in the first part of chapter 5. This includes the complete setup for the laser stabilization to the frequency comb. The results of the absolute transition frequencies and a discussion about observed systematic uncertainties are given in the second part of the chapter. The laser system for the beryllium experiment was developed and tested at the Institute of Nuclear Chemistry at the University of Mainz and partly at the GSI facility in Darmstadt before it was transported to the ISOLDE facility at CERN. The measurements on stable and radioactive beryllium isotopes and the results are discussed in chapter 6.

2 Theory

2.1 Nuclear Matter and Charge Distribution

Various methods have been developed to study the proton and neutron distribution in the nucleus. In this chapter several of them are briefly introduced. The nucleon distribution (p+n) defines the matter radius $\bar{r}_m = \sqrt{\int_N |(r)|^2 r^2 d^3 r}$, whereas the proton distribution (p) defines the charge radius $\bar{r}_c = \sqrt{\int [\Psi_p(r)]^2 r^2 d^3 r}$.

Electron Scattering   Electron scattering provides a rich database of charge radii but the technique is so far limited to stable or long-lived isotopes. The electron is a structureless, point-like particle and interacts electromagnetically with the protons inside the nucleus. This kind of interaction is theoretically well described and the charge radius can be extracted in a model-independent way from the experimental elastic cross section measurements as shown in Fig. 2.1. The differential scattering cross section σ_E obtained from an experiment can be written as

$$\sigma_E = F^2(q)\sigma_M, \tag{2.1}$$

where $F(q)$ is the form factor and σ_M is the Mott scattering cross section. The form factor for the charge distribution is given by

$$F(q) = \frac{1}{Ze} \int e^{i\vec{q}\cdot\vec{r}} \rho(r) d^3 r, \tag{2.2}$$

$\vec{q}$ is the momentum transfer vector, $\rho(r)$ is the nuclear charge density and e is the proton charge. Hence, the form factor and the charge distribution are connected by a Fourier transformation and for the spherically symmetric charge distribution one obtains

$$F(q) = \frac{4\pi}{Zeq} \int\limits_0^\infty sin(qr)\rho(r)r dr. \tag{2.3}$$

For very low momentum transfer, the form factor can be written in a Taylor series expansion

$$F(q) = 1 - \frac{1}{6}\left\langle r_c^2 \right\rangle q^2 + \dots, \tag{2.4}$$

where $\langle r^2 \rangle$ is the mean square charge radius [Bum72]. Low momentum elastic electron
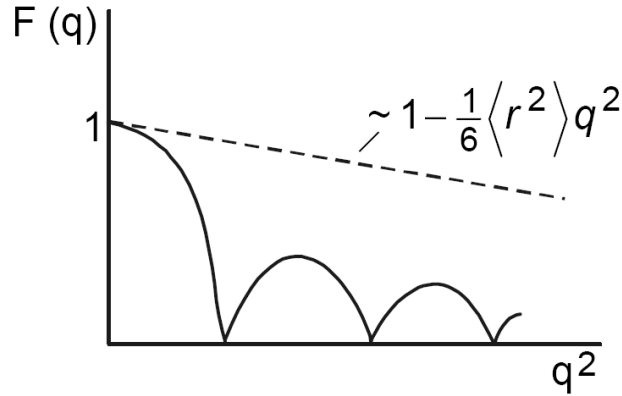
Figure 2.1. Elastic electron scattering at low momentum transfer q. The mean-square nuclear charge radius $\langle r^2 \rangle$ can be obtained from the slope of the curve near $q^2 = 0$ [Elze].

scattering experiments have been performed in the case of ^{6,7}Li and ^{9}Be and resulting charge radii are given in [Bum72] and [Jan72], respectively.

Experiments performed at higher momentum transfer values are able to extract more details of the charge distribution but become model-dependent since a nuclear model must be used to describe the experimental data. Very often the shell model is used, as described e.g. in [Sue67] for ^{6,7}Li and in [Sic75] for ^{58}Ni measurements.

The planned electron-nucleus collider ELISe (ELectron-Ion Scattering in a Storage Ring) at FAIR[1] and future experiments at RIKEN will give an access to electron scattering studies also for radioactive species including halo nuclei [Sim05, Rii06].

Interaction Cross Section A new technique to access the matter and charge distribution of short-lived species was developed with the production of the radioactive nuclear beams in the middle 1980's. Total interaction cross section measurements were performed by Tanihata *et al.* [Tan85, Tan88] in 1985, where the halo structure of some light isotopes was discovered. The information about the charge radius extracted from these measurements is typically strongly model-dependent. The obtained matter radii were later reexamined and the correlation of the projectile constituents were included in the calculations. At the projectile incident energies of the order of 800 MeV/nucleon it is important to consider the motion of the valence nucleons inside the projectile when passing the target interaction region [Alk96]. The extracted matter radii for lithium and beryllium isotopes from the interaction cross section measurements [Tan88] as well as corresponding reevaluated matter radii [Alk96] are listed in table 2.1.

---

[1]FAIR - Facility for Antiproton and Ion Research planned at GSI, Darmstadt

Table 2.1. Nuclear properties of Li and Be isotopes: nuclear spins (I), half lives ($T_{1/2}$), nuclear masses (M), magnetic-dipole (μ_I) and electric-quadrupole moments (Q) and nuclear matter radii ($\bar{r}_m$) for lithium and beryllium isotopes. The quadrupole moment of ^{7}Be was not measured yet. The value listed in the table is a theoretical prediction [Ara01].

	I	$T_{1/2}$	M [u]	$\mu_I[\mu_N]$	Q [e fm^2]	$\bar{r}_m$[fm]
^{6}Li	1	∞	6.01512280(2)[Aud97]	0.8220473(6)[Sto05]	-0.083(8)[Sto05]	2.32(3)*[Tan88]
						2.45(7)$^\diamond$[Ege02]
^{7}Li	3/2	∞	7.01600455(9)[Aud97]	3.2564625(4)[Sto05]	-4.06(8)[Sto05]	2.33(2)*[Tan85]
^{8}Li	2	838 ms	8.02248736(10)[Aud97]	1.65340(2)[Sto05]	3.14(2)[Sto05]	2.37(2)*[Tan88]
						2.45(6)$^\diamond$[Ege02]
^{9}Li	3/2	178.3 ms	9.026790(2)[Aud97]	3.43678(6)[Bor05]	-3.06(2)[Bor05]	2.32(2)*[Tan88]
						2.43(7)$^\diamond$[Ege02]
^{11}Li	3/2	8.6 ms	11.043716(6)[Aud97]	3.6712(3)[Neu08]	-3.33(5)[Neu08]	3.12(16)*[Tan88]
						3.55(10)$^\nabla$[Alk96]
						3.62(19)$^\diamond$[Ege02]
^{7}Be	3/2	53 d	7.01692983(11)[Aud97]	-1.39928(2)[Oka08]	-6.11[Ara01]	2.33(2)*[Tan88]
^{9}Be	3/2	∞	9.01218220(43)[Aud97]	-1.177432(3)	-5.288(38)[Sun91]	2.38(1)*[Tan88]
				[Win83, Bol85]		
^{10}Be	0	1.6×10^6 a	10.01353382(43)[Aud97]	-	-	2.28(2)*[Tan88]
^{11}Be	1/2	13.8 s	11.02166155(62)[Rin09]	-1.6813(5)[Noe09]	-	2.71(5)*[Tan88]
^{12}Be	0	23.8 ms	12.026921(16)[Aud97]	-	-	2.57(5)*[Tan88]
						2.82(12)$^\diamond$[Ili08]
^{14}Be	0	4.35 ms	14.042890(140)[Aud97]	-	-	3.11(38)*[Tan88]
						3.11(14)$^\diamond$[Ili08]

* interaction cross section measurements, static density calculations

$^\nabla$ interaction cross section measurements, including the valence neutrons correlation

$^\diamond$ elastic proton scattering in inverse kinematics
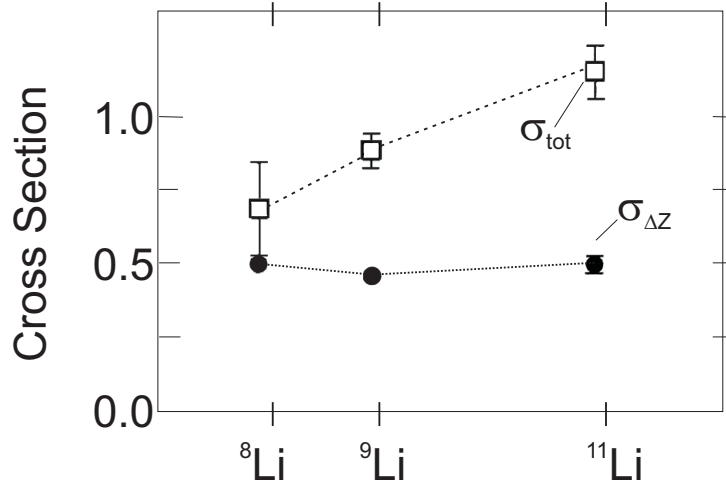
Figure 2.2. Charge-changing cross sections (full circles) and total reaction cross sections (open squares) from the interaction of the different lithium isotopes with different targets (C, Pb, Al, Sn) [Bla92]. The total reaction cross section increases due to the larger matter radius, whereas the charge-changing cross section stay constant for all measured lithium isotopes.

Charge Changing Cross Section Measurements of the inelastic charge-changing cross sections of the lithium isotopes were performed with the lithium projectiles ^{8,9,11}Li on different targets [Bla92]. In this case only reactions which lead to a change of the projectile charge, like the removal of a proton, are considered. In order to obtained the respective cross section, only the proton density distribution of the lithium projectile is used, whereas for the target the proton as well as the neutron distribution is taken into account. The charge changing cross sections extracted with a Glauber model are shown in Fig. 2.2. It is obvious that the proton distribution stays nearly constant along the lithium isotopes, although the total interaction crass section is increasing. This is a clear indication for an extended neutron distribution.

Elastic Proton Scattering An alternative method to the total cross section measurements was proposed by G. Alkhazov in 1992 [Alk06, Dob06]. Measurements are based on a differential cross-section $d\sigma/dt$ for intermediate-energy proton-nucleus elastic scattering. The reactions are typically studied in inverse kinematics, where the incident particle is the nucleus of interest. The matter and charge radii of the lithium isotopes obtained from these measurements are reported in [Dob06, Ege02]. The example of ^{11}Li nuclear core and total matter distribution obtained from the elastic proton scattering in inverse kinematics is shown in Fig. 2.3. Recent measurements of the beryllium halo isotopes ^{12,14}Be are discussed in the PhD thesis of Stoyanka Ilieva [Ili08]. Contrary to the electron scatter-
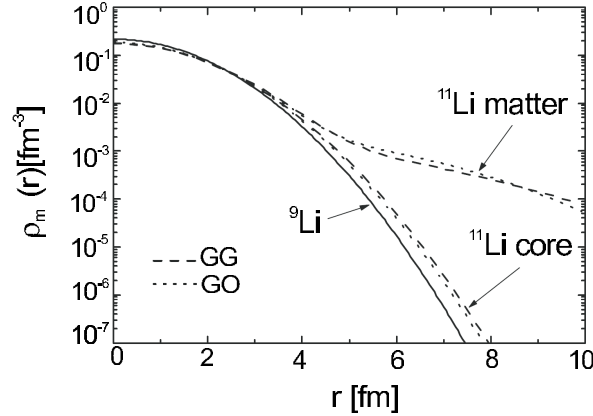
Figure 2.3. Nuclear core and total density distribution in ^{11}Li, using Gaussian-Gaussian (GG) and Gaussian-oscillator (GO) density distribution parametrizations. The distributions are obtained from elastic proton scattering in inverse kinematics [Dob06].

ing, the nucleon scattering analysis cannot be performed in a strictly model-independent way. A nuclear model has to be used to separate the contribution from protons and neutrons. Glauber theory is used to connect the cross section and the density distribution [Wan04b, Tan96].

Isotope Shift   Another approach to determine the nuclear charge radius is to measure the shift in the atomic energy levels caused by the finite mass and finite size of the nucleus. This results in a change of the transition frequency between two isotopes of the same element. Muonic atoms, inner-shell x-ray transition and optical transition can be used for such measurements. Muonic atoms and x-ray transitions can be used to extract absolute nuclear charge radii, however they are not free from some model-dependence since they are also sensitive to higher radial moments . The spectroscopy on the muonic atom is used to determine the charge radius of stable isotopes from isotope shift measurements, e.g. the charge radius measurements of ^{4}He [Car76] or ^{9}Be [Scha80]. When the muon is captured by the atom it is bound very close to the nucleus, because it is 207 times heavier than an electron. The probability density for finding the muon inside the nucleus is much greater than for electronic atoms, the muonic atoms are therefore sensitive probes for studying the charge distribution [Yan96].

Optical isotope shift measurements provide a nuclear model-independent way to extract mean square nuclear charge radii as it will be discussed in the next section. This technique became very important because laser spectroscopic measurements are very sensitive and fast and can therefore be applied to short-lived isotopes. A multitude of laser

spectroscopic techniques were developed during the last decades. Collinear laser spectroscopy is one of the most productive methods and will be described in chapter 3.

2.2 Atomic Isotope Shift

The isotope shift is the difference of the transition frequency between two isotopes A and A' of the same element $\delta\nu_{IS}^{A,A'} = \nu^{A'} - \nu^A$. If the transition exhibits hyperfine structure the frequency ν^A is taken as the center-of-gravity of all hyperfine components. The isotope shift has its origin in the finite mass and volume of the nucleus. The finite mass of the nucleus causes a center-of-mass motion of the nucleus. In lowest order, this can be taken into account by replacing the electron mass with the reduced mass of the system. This contribution is called the normal mass shift (NMS). However, when more than one electron is present, the correlation of the motion between the electrons, the so called specific mass shift (SMS) has to be taken into account as well. When the nuclear mass is known, the NMS can be easily calculated, whereas the SMS is in general very difficult to calculate. Nowadays, calculations with spectroscopic accuracy can be performed for up to three-electron systems [Yan08, Puch09].

The volume or field shift (FS) is present due to the finite volume of the nucleus. The total isotope shift is the sum of the mass shift $\delta\nu_{MS}^{A,A'}$ and the field shift $\delta\nu_{FS}^{A,A'}$

$$\delta\nu_{IS}^{A,A'} = \delta\nu_{MS}^{A,A'} + \delta\nu_{FS}^{A,A'}. \tag{2.5}$$

The total mass shift of a system with more than one electron is given by

$$\delta\nu_{MS}^{A,A'} = \delta\nu_{NMS}^{A,A'} + \delta\nu_{SMS}^{A,A'} = (N+S)\frac{M_A - M_{A'}}{M_A M_{A'}}, \tag{2.6}$$

where N and S are the coefficients of the NMS and the SMS, respectively and both contributions have the same mass dependence. Theoretical mass shift calculations for lithium and beryllium isotopes are listen in table 2.2.

The second part of the isotope shift, is calculated from the electron binding energy in the finite nuclear charge distribution of the nucleus. The electrostatic energy of the s-electron with the spherically symmetric wave function and the nucleus can be written as

$$E = \int\limits_{r<R_1} \rho_r(\mathbf{r}) V(\mathbf{r}) d^3\mathbf{r}. \tag{2.7}$$

$V(\mathbf{r})$ is the potential caused by the electron distribution and $\rho_r(\mathbf{r})$ is the nuclear charge distribution, for $|r| > R_1$ $\rho_r(\mathbf{r}) = 0$. Assuming electron density distribution with a

Table 2.2. Summary of the mass shift calculations and C coefficients for the lithium and beryllium isotopes. The reference isotopes for lithium and beryllium are ^{7}Li and ^{9}Be$^+$, respectively. Theoretical mass shifts are given in MHz. The first uncertainty comes from the calculation itself, the second uncertainty is due to the atomic mass used in the calculations.

	$(2s_{1/2} \rightarrow 3s_{1/2})$		C [MHz/fm^2]	Reference
^{6}Li	-11 452.820 5(23)(2)		-1.571 9(16)	[Puch08]
	-11 452.821(2)		-1.5661	[Dra02]
^{8}Li	8 634.981 2(17)(9)		-1.572 0(16)	[Puch08]
	8 634.989(2)		-1.5661	[Dra02]
^{9}Li	15 331.799 5(31)(12)		-1.572 1(16)	[Puch08]
	15 331.799(13)		-1.5661	[Dra02]
^{11}Li	25 101.502 8(64)(27)		-1.576 8(17)	[Puch08]
	25 101.470(22)		-1.5661	[Dra02]
	$(2s_{1/2} \rightarrow 2p_{1/2})$	$(2s_{1/2} \rightarrow 2p_{3/2})$		
^{7}Be$^+$	-49 225.744(35)(9)	-49 231.779(35)(9)	-17.021(31)	[Puch09b]
	-49 225.765(19)	-49 231.814(19)	-16.912	[Dra02]
^{10}Be$^+$	17 310.459(13)(11)	17 312.553(13)(11)	-17.027(31)	[Puch09b]
	17 310.44(6)	17 312.57(6)	-16.912	[Dra02]
^{11}Be$^+$	31 560.245(31)(12)	31 564.207(31)(12)	-17.020(31)	[Puch09b]
	31 560.01(6)	31 563.89(6)	-16.912	[Dra02]

constant electron wave function $\Psi(0)$ within the nuclear volume, the electron potential $V(r)$ inside the nucleus can be written as

$$V(\mathbf{r}) = -2\pi e \left|\Psi(0)\right|^2 (R_1^2 - r^2/3), \ \ |r| < R_1, \tag{2.8}$$

For the light isotopes this is a very good approximation [Ott89].

The total charge of the nucleus is given by definition as

$$\int_{r<R_1} \rho_r(\mathbf{r})d^3\mathbf{r} \ \ = \ \ Ze, \tag{2.9}$$

$$\int_{r<R_1} r^2 \rho_r(\mathbf{r})d^3\mathbf{r} \ \ = \ \ Ze \left\langle r_c^2 \right\rangle, \tag{2.10}$$

where $Ze \left\langle r_c^2 \right\rangle$ is the total charge multiplied by the mean-square charge radius. The electrostatic energy 2.7 can then be written as

$$E = Ze \ V(0) + \frac{2\pi}{3} Ze^2 \left|\Psi(0)\right|^2 \left\langle r_c^2 \right\rangle, \tag{2.11}$$

where the first term describes the interaction between the electron and a point-like nucleus and the second term is the finite size correction. In principle, the mean square charge radius is encoded in the level energy and therefore in the total transition energy. However, the field shift is too small to determine the nuclear charge radius directly. The problematic part is the calculation of the QED contribution, which is, so far, only possible for hydrogen as it will be discussed below. But, the difference in the transition energies between two isotopes A, A' is used to extract the difference in the nuclear charge radii $\delta \left\langle r^2 \right\rangle^{A,A'}$, where most of the theoretical contributions cancel out

$$\delta\nu_{FS}^{A,A'} = -\frac{2\pi}{3} Ze^2 \Delta \left|\Psi(0)\right|^2 \delta \left\langle r_c^2 \right\rangle^{A,A'}. \tag{2.12}$$

Here, $\Delta \left|\Psi(0)\right|^2$ is the change of the electron's wave function at the nucleus between the upper and lower state of the optical transition. To obtain absolute charge radius information, one needs to know the charge radius r_c^A of one of the isotopes from another measurement. Then all charge radii $r_c^{A'}$ can be calculated according to

$$r_c^{A'} = r_c^A + \delta \left\langle r^2 \right\rangle^{A,A'}. \tag{2.13}$$

In the light nuclei the mass shift strongly dominates the field shift. For lithium and beryllium, the mass shift is some 10 GHz, whereas the field shift is only few MHz. To separate the field shift from the dominating mass shift and, hence, extract nuclear charge radius information, a precise calculation of the SMS and electron wave function is required. So far, many-body calculations reach the precision of the experiment only up to three-electron systems [Yan08, Puch09] as will be discussed in the next section.

2.3   Atomic Theory

Exact theoretical calculation of the energy level requires, besides several other contributions, also a specific treatment of the electron correlations (SMS) and quantum electrodynamic (QED) corrections. A short summary of the way how these calculations are performed will now be given. For more details it is referred to [Dra02, Dra05, Puch08].

The nonrelativistic Schrödinger equation for the three-electron atomic system can be written as

$$\left(-\frac{1}{2} \sum_{i=1}^{3} \nabla_{\rho_i}^2 - Z \sum_{i=1}^{3} \frac{1}{\rho_i} + \sum_{i>j}^{3} \frac{1}{|\boldsymbol{\rho}_i - \boldsymbol{\rho}_j|} - \frac{\mu}{M} \sum_{i>j}^{3} \boldsymbol{\nabla}_{\rho_i} \cdot \boldsymbol{\nabla}_{\rho_j} \right) \Psi = \mathcal{E}\Psi, \qquad (2.14)$$

where $\boldsymbol{\rho}_i = \mathbf{r}_i(\mu e^2/\hbar^2)$ is the scaled electron distance and $\mu = m_e M/(m_e + M)$ is the reduced mass of the system. Variational solutions are obtained by expanding the nonrelativistic wave function in Hylleraas coordinates with large basis sets which were found to be advantageous for the treatment of electron correlations [Hyl28]. This is a specialized approach which has been used so far only for two and three-electron systems [Yan08, Puch09, Puch06]. Energies and wavefunctions of these calculations serve then as starting points for the perturbative treatment of relativistic corrections, QED corrections and the corrections for the finite nuclear volume.

The total energy of the atomic state in terms of the fine structure constant $\alpha = e^2/\hbar c$ is given as a sum of the nonrelativistic energy E_{nr} and the corrections in higher orders of α

$$E_{tot} = E_{nr} + \alpha^2 E_{rel} + \alpha^3 E_{QED} + ... + \Delta E_{nuc}, \qquad (2.15)$$

where E_{rel} is the leading term of the relativistic corrections and E_{QED} the leading term of the QED corrections. ΔE_{nuc} is the shift in energy produced by the finite nuclear volume, which is in leading order given by

$$\Delta E_{nuc} = \frac{2\pi Z e^2 \langle r_c^2 \rangle}{3} \left\langle \sum_{i=1}^{3} \delta(\mathbf{r}_i) \right\rangle, \qquad (2.16)$$

where $\delta(\mathbf{r}_i)$ is the expectation value of the electron density at the nucleus and the term is summed over all three electrons.

The expansion of the other terms in the reduced mass factor $\frac{\mu}{M}$ are of the form

Table 2.3. Values of total energy contributions from two different theoretical groups. The calculations are for the stable isotopes ^{7}Li in the $2s_{1/2} \rightarrow 3s_{1/2}$ transition and for ^{9}Be$^+$ in the $2s_{1/2} \rightarrow 2p_{1/2}$ transition. All values are given in MHz.

Contribution to E_{tot}	^{7}Li	^{9}Be$^+$	Reference
Nonrelativistic energy E_{nr}	815 561 313.44(3)		[Yan08b]
	815 561 313.5(1)	956 709 540.2(3)	[Puch08]
Relativistic corrections E_{rel}	62 629.4(6)		[Yan08b]
	62 628.0(7)	548 061.3(1.1)	[Puch08]
QED corrections (Lamb shift) E_{QED}	-5 768(30)		[Yan08b]
	-5 763(19)	-58 126(252)	[Puch08]
Finite nuclear size ΔE_{nuc}	-8.95(24)		[Yan08b]
	-8.9(2)	-107(1)	[Puch08]
Total	815 618 166(30)		[Yan08b]
	815 618 170(19)	957 199 368(252)	[Puch08]

$$E_{nr} = E_{nr}^{(0)} + \frac{\mu}{M}E_{nr}^{(1)} + \left(\frac{\mu}{M}\right)^2 E_{nr}^{(2)} + \cdots \tag{2.17}$$

$$E_{rel} = E_{rel}^{(0)} + \frac{\mu}{M}E_{rel}^{(1)} + \cdots \tag{2.18}$$

$$E_{QED} = E_{QED}^{(0)} + \frac{\mu}{M}E_{QED}^{(1)} + \cdots . \tag{2.19}$$

The contributions to the absolute transition energy in the $2s_{1/2} \rightarrow 3s_{1/2}$ transition of ^{7}Li and in the $2s_{1/2} \rightarrow 2p_{1/2}$ transition of ^{9}Be$^+$ are listed as an example in table 2.3.

The transition energy difference between two isotopes A, A' of the same element is

$$\Delta E^{A,A'} = \left[\left(\frac{\mu}{M}\right)_A - \left(\frac{\mu}{M}\right)_{A'}\right]\left(E_{nr}^{(1)} + \alpha^2 E_{rel}^{(1)} + \alpha^3 E_{QED}^{(1)}\right)$$
$$+ \left[\left(\frac{\mu}{M}\right)_A^2 - \left(\frac{\mu}{M}\right)_{A'}^2\right] E_{nr}^{(2)} + \cdots + \Delta E_{nuc}^A - \Delta E_{nuc}^{A'}. \tag{2.20}$$

For the required level of accuracy higher orders of α and μ/M can be neglected.

Although the SMS calculations are available for the three-electron system, one can see directly from table 2.3 that the accuracy is not sufficient to extract the absolute charge radius. This can be achieved, by now, only for the hydrogen atom or hydrogen-like systems [Ude97]. The largest source of uncertainty is the QED correction caused by the vacuum polarization arising from the emission and re-absorption of virtual photons [Dra06, Yan08]. It is important to note that the mass-independent term E_{QED}^0 vanishes in the isotope shift,

see equation 2.20. This term has a relatively large uncertainty and would prohibit the extraction of $\delta \langle r_c^2 \rangle$. In fact, it is the limiting term if one tries to extract an absolute charge radius from the optical measurements by comparing the transition frequency with the calculated one, in which all but the field shift contribution has been considered as it will be discussed later. The equation (2.5) can be written as

$$\delta \nu_{IS}^{A,A'} = \delta \nu_{MS}^{A,A'} + C \delta \left\langle r_c^2 \right\rangle^{A,A'}, \qquad (2.21)$$

which is equivalent to (2.20) and the field shift can be determined from $C \delta \left\langle r_c^2 \right\rangle^{A,A'} = \Delta E_{nuc}^A - \Delta E_{nuc}^{A'}$. The important point is that the QED correction term $\alpha^3 E_{QED}^{(0)}$ completely cancels from the isotope shift, leaving only much smaller terms $\alpha^3 E_{QED}^{(1)}$, which can be calculated to sufficient accuracy [Dra05]. The factor C is almost isotope independent. The results for the calculated C factor for the lithium and beryllium isotopes are listed in table 2.2 on page 11. From the isotope shift measurements and the theoretical calculations one can obtain the difference in the nuclear charge radii $\delta \left\langle r_c^2 \right\rangle^{A,A'}$. If for one reference isotope (A) the radius is known, the root-mean-square charge radius for the other isotopes $\sqrt{\left\langle r_c^2 \right\rangle^{A'}}$ can be extracted from

$$\left\langle r_c^2 \right\rangle^{A'} = \left\langle r_c^2 \right\rangle^A + \frac{\delta \nu_{IS,\text{exp}}^{A,A'} - \delta \nu_{MS,\text{theory}}^{A,A'}}{C}, \qquad (2.22)$$

where $\sqrt{\left\langle r_c^2 \right\rangle^A}$ is the reference charge radius. In the lithium case, the isotopes ^{6}Li and ^{7}Li were measured with the elastic-electron scattering method [Sue67]. The nuclear charge radius of ^{7}Li was measured to be 2.39(3) fm and for ^{6}Li it was 2.54(6) fm [Sue67]. The charge radius of ^{9}Be was also measured with the electron-scattering method and a value of 2.519(12) fm has been reported [Jan72].

2.4   Hyperfine Structure

Properties of the nucleus such as angular momentum, spin, magnetic moments, charge distribution (quadrupole moments) and the finite size of the nucleus have an effect on the motion of the electrons in the atom and cause shifts or splittings of the atomic spectral lines. This splitting called the hyperfine structure is about three orders of magnitudes smaller than the fine structure splitting arising due to the spin of the electron.

2.4.1   Magnetic Dipole Hyperfine Interaction

The interaction of the magnetic dipole moment of the nucleus $\boldsymbol{\mu_I}$ with the magnetic field of the electrons $\boldsymbol{B}_0$ gives rise to the magnetic hyperfine splitting of the fine structure

energy levels. The Hamiltonian which describes this interaction is given by

$$H \;\; = \;\; -\boldsymbol{\mu_I} \cdot \boldsymbol{B}_0 \tag{2.23}$$

$$\boldsymbol{\mu_I} \;\; = \;\; g_I \mu_N \boldsymbol{I} \tag{2.24}$$

g_I is the effective g-factor of the nucleus and μ_N is the nuclear magneton. For an atomic level with the angular momentum quantum number J, the coupling with the nuclear spin I results in the total angular momentum

$$\boldsymbol{F} = \boldsymbol{J} + \boldsymbol{I}, \tag{2.25}$$

and the J-energy level splits into several sublevels $|I - J| \leq F \leq I + J$ and there are $(2J + 1)\,((2I + 1))$ possibilities for $J < I$ $(I < J)$, respectively.

The Hamiltonian of the F levels of the hyperfine structure in relation with the atomic fine structure is given as

$$H = A\boldsymbol{I} \cdot \boldsymbol{J} \tag{2.26}$$

and the expectation value gives

$$E_M = A\left\langle \boldsymbol{I} \cdot \boldsymbol{J} \right\rangle = \frac{A}{2}\left\{ F(F + 1) - I(I + 1) - J(J + 1) \right\} = \frac{A}{2}K. \tag{2.27}$$

A is the magnetic dipole interaction constant given by $A = \mu_I B_0/I$ and K is the Casimir factor [Yan96]. The scheme of the fine and hyperfine atomic structure of the stable lithium and ionic structure for four beryllium isotopes is shown in Fig. 2.4.

2.4.2   Electric Quadrupole Hyperfine Interaction

In some cases the charge distribution in the nucleus is not spherically symmetric and possess an electric quadrupole moment. The interaction between this quadrupole moment and the electric field gradient at the nucleus created by the electron distribution cause an additional shift of the hyperfine levels. This energy shift is given by

$$E_Q = \frac{B}{4}\frac{\frac{3}{2}K(K + 1) - 2I(I + 1)J(J + 1)}{I(2I - 1)J(2J - 1)}, \tag{2.28}$$

where $K = F(F + 1) - I(I + 1) - J(J + 1)$. B is the electric quadrupole interaction constant

$$B = eQ\left\langle \frac{\partial^2 V_e}{\partial z^2} \right\rangle \tag{2.29}$$

with the mean value of the gradient of the electric field $\langle \partial^2 V_e/\partial Z^2 \rangle$ [Yan96]. Only nuclei with a spin of 1 or larger can posses a spectroscopic nuclear quadrupole moment. It
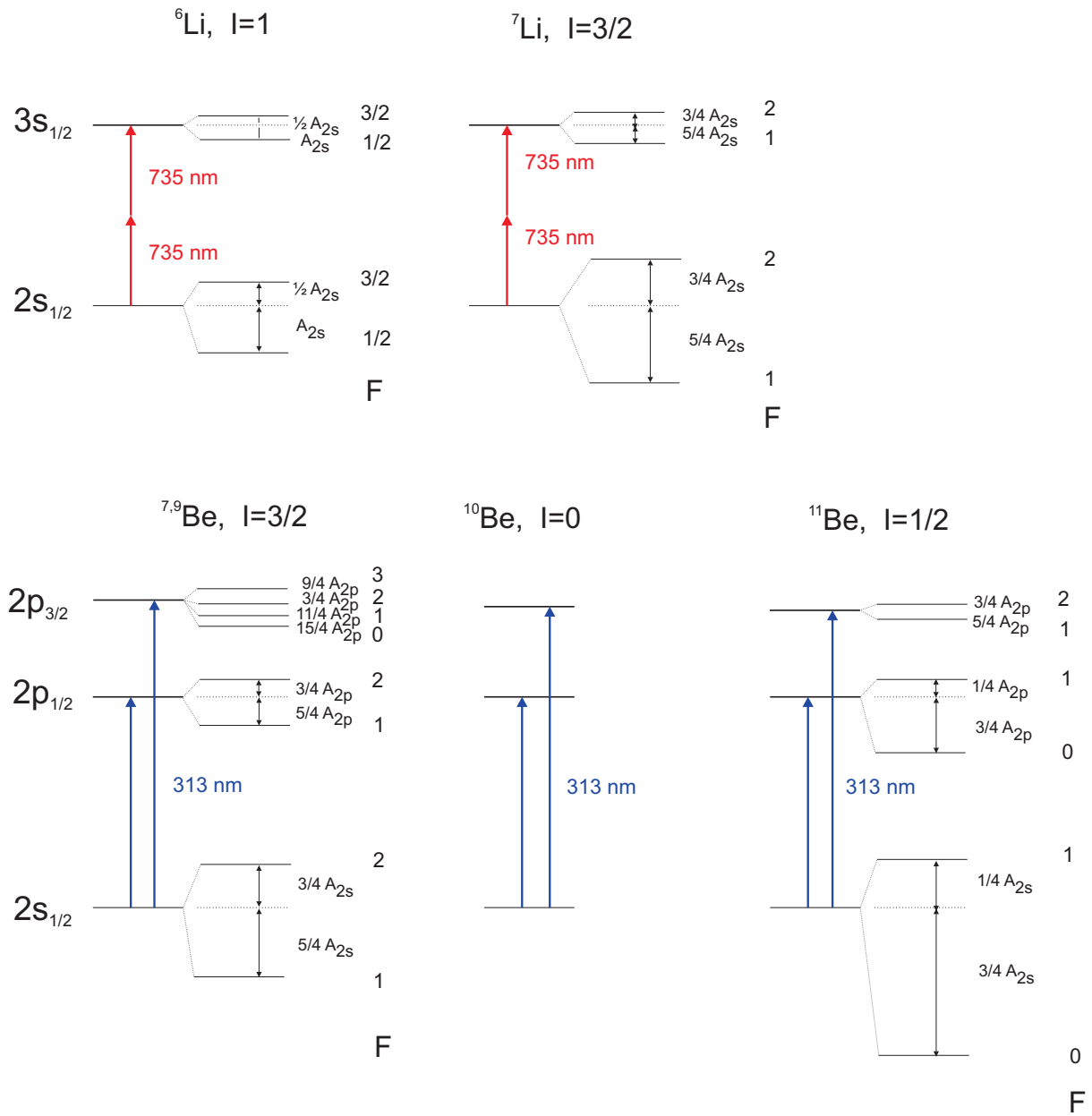
Figure 2.4. Energy level schemes for the stable lithium isotopes [6,7]Li and beryllium isotopes up to the [11]Be isotope.

should also be mentioned that a quadrupole splitting can only occur in electronic states with $J \geq 1$.

The expression for the total hyperfine energy shift is given as a sum of the magnetic dipole 2.27 and electric quadrupole 2.28 interactions

$$E = A\frac{K}{2} + \frac{B}{4}\frac{\frac{3}{2}K(K+1) - 2I(I+1)J(J+1)}{I(2I-1)J(2J-1)}. \tag{2.30}$$

2.5   Lithium and Beryllium Isotope Properties

Nuclear spins, half lives, nuclear masses, magnetic-dipole and electric-quadrupole moments and nuclear matter radii of the lithium and beryllium isotopes are listed in table 2.1. The nuclear matter radius of the radioactive isotopes was determined first with the interaction cross-section technique [Tan85, Tan88] and later also with the elastic proton scattering in inverse kinematics [Ege02, Ili08]. Both values are listed in table 2.1.

As it was mentioned in section 2.3, only the change in the nuclear charge radius between two isotopes $\delta \langle r_c^2 \rangle^{A,A'}$ can be determined from the isotope shift measurements. For the lithium isotopes [Ewa04, San06, Dra06], the reference charge radius was previously taken as the weighted average of elastic electron scattering data [Sue67, Bum72]. Recently a new analysis of the *world* scattering data [Sue67, Bum72, Li71] for ^{6}Li and ^{7}Li was performed [Sic09]. This analysis indicated that ^{6}Li provides the more reliable reference radius because here the elastic scattering could be clearly separated from inelastic scattering, whereas for ^{7}Li the first excited state at 0.478 MeV could not be resolved. Moreover, an additional substantial uncertainty for ^{7}Li comes from the quadrupole distribution, which cannot be separated. This contribution is for ^{6}Li negligible. The resulting reference charge radius for ^{6}Li from this analysis is 2.589(39) fm [Sic09], where the error bar covers both the statistical and systematic uncertainties. Additionally, the analysis indicated that the previously reported uncertainty of the ^{7}Li charge radius of 0.03 fm was underestimated. In table 2.4 the IS data from [San05, San06] has been used to calculate the charge radii of all Li isotopes according to equation 2.22 using the calculated mass shift and C factors listed in table 2.2 based on the old and new reference radii. Results are depicted in Fig. 2.5. The new calculated charge radii have slightly larger uncertainty and all values are larger by about 0.04 fm compared to those previously reported.

For the determination of the beryllium nuclear charge radii up to ^{11}Be [Noe09, Tie09], the reference radius of stable ^{9}Be extracted from an elastic electron scattering measurement, $r_c^9 = 2.519(12)$ fm [Jan72] was used. Another measurement was performed by muonic atom spectroscopy [Scha80], where a charge radius of $r_c^9 = 2.39(17)$ fm was obtained. The reference charge radii differ by 0.13 fm but agree within the uncertainties.
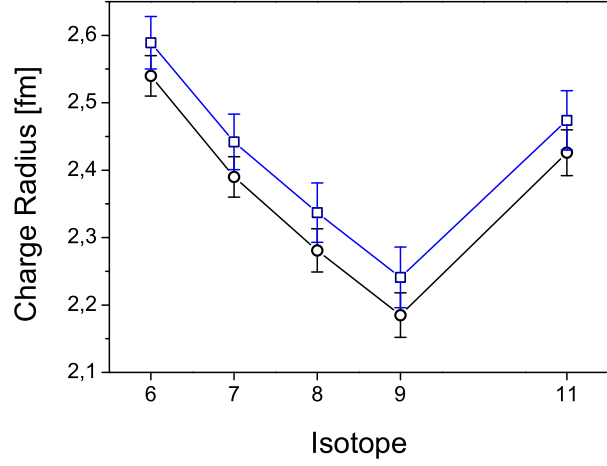
Figure 2.5. Root-mean-square nuclear charge radii of the lithium isotopes. The circles are the radii calculated with the reference charge radius of ^{7}Li, $r_c(^7\text{Li})$=2.39(3) fm, the squares are new values calculated with ^{6}Li, $r_c(^6\text{Li})$=2.589(39) fm. (details see text)

Table 2.4. Nuclear charge radii for the lithium isotopes determined from isotope shift measurements [San05, San06]. The reference charge radius was in one case the charge radius of ^{7}Li ($r_c^{7,A'}$) determined with elastic electron scattering method by Suelzle *et al.* [Sue67]. The second reference is from a new analysis of the data [Sue67, Bum72, Li71] for ^{6}Li ($r_c^{6,A'}$) made by I. Sick [Sic09].

Isotope	$r_c^{7,A'}$ [fm]	$r_c^{6,A'}$ [fm]
^{6}Li	2.540(30)	2.589(39) [Sic09]
^{7}Li	2.39(3) [Sue67]	2.442(41)
^{8}Li	2.281(32)	2.337(44)
^{9}Li	2.185(33)	2.241(45)
^{11}Li	2.426(34)	2.474(44)

Table 2.5. Measured isotope shifts [Noe09, Tie09] and nuclear charge radii of the beryllium isotopes up to ^{11}Be. The reference charge radius of ^{9}Be was measured with electron scattering by Jansen *et al.* [Jan72]. The values given for ^{12,14}Be are derived from elastic proton scattering data using Glauber theory analysis [Ili08].

	$\delta\nu^{9,A'}$[MHz]	r_c[fm]	Ref.
^{7}Be	-49 236.9(9)	2.647(17)	[Noe09]
^{9}Be	0	2.519(12)	[Jan72]
^{10}Be	17 323.8(13)	2.357(18)	[Noe09]
^{11}Be	31 565.0(9)	2.463(16)	[Noe09]
^{12}Be		2.18(10)	[Ili08]
^{14}Be		2.65(12)	[Ili08]

Although the reported uncertainty from the electron scattering is probably underestimated, a slight change in the reference radius would change all evaluated charge radii in the same direction and the trend of the charge radii would not change considerably; similar to the case of Li isotopes shown in Fig. 2.5. The isotope shift measurements and charge radii of beryllium isotopes up to ^{11}Be are listed in the table 2.5. The limitation for the isotope shift measurements of ^{12}Be and ^{14}Be were low production rates. Existing values for charge radii of ^{12,14}Be were recently determined with elastic proton scattering in inverse kinematics [Ili08] and are also listed in table 2.5.

3 Laser Spectroscopy

3.1 Collinear Laser Spectroscopy

Collinear laser spectroscopy is a technique suited for measurements of isotope shifts and hyperfine structure of isotopes far from stability provided by on-line mass separators. Compared to laser spectroscopy at collimated beams where the laser beam crosses the ion beam perpendicularly, an advantage of the co-propagating arrangement is the appreciably long interaction time between the ion and the laser beam [Dem03]. In Fig. 3.1 a set-up used for measurements with collinear laser spectroscopy is shown. Ions produced in the target ion source are accelerated to typically 60 keV. After mass separation the accelerated ions are guided to the beam-line and overlapped with a laser beam. The ions interact with the laser only at the observation region which is achieved by applying an additional scanning voltage close to the observation region. A resonance fluorescence signal is detected with a photomultiplier.

An important property of fast ion beams is a strong reduction of the velocity spread. The ions emitted from the source are accelerated to several keV. The fast ions are accelerated for shorter, the slower ones for longer time intervals. Hence, the velocity distribution along the beam direction is narrowed by a factor

$$R = 1/2\sqrt{E(0)/eU}, \tag{3.1}$$
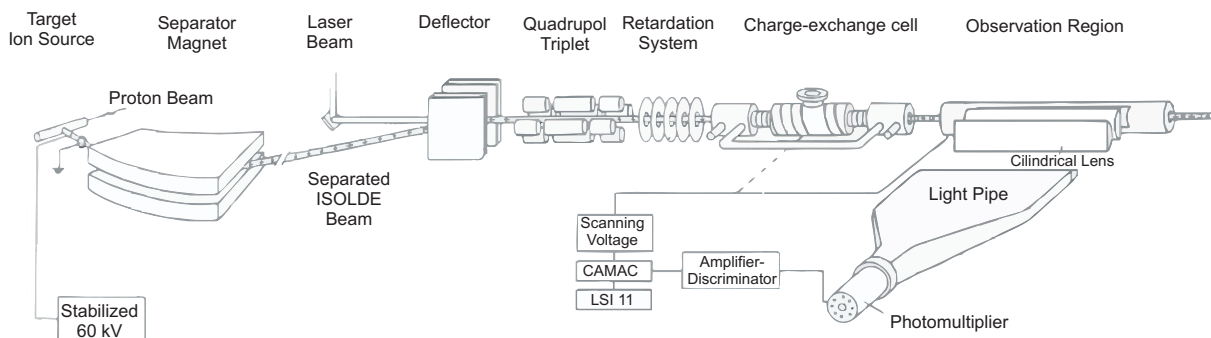
Figure 3.1. Schematic diagram of a standard collinear laser spectroscopy set-up [Ott89]. An ion beam is deflected to the beamline, overlapped with a laser beam and a scanning the resonances is performed with a variable acceleration voltage applied to the retardation system (Doppler tuning). A resonance signal is detected at the observation region with the photomultiplier.

where $E(0)$ is the thermal energy of the ions before the acceleration and U is the acceleration voltage [Kau76]. Two ions with different initial energies $E_1(0), E_2(0)$ are accelerated in the electric field eU

$$E_1 = \frac{1}{2}mv_1^2 = \frac{1}{2}mv_1^2(0) + eU \tag{3.2}$$

$$E_2 = \frac{1}{2}mv_2^2 = \frac{1}{2}mv_2^2(0) + eU. \tag{3.3}$$

If the two energies are subtracted

$$(v_1^2 - v_2^2) = [v_1^2(0) - v_2^2(0)] \tag{3.4}$$

and $v = \frac{1}{2}(v_1 + v_2)$, $v(0) = \frac{1}{2}[v_1(0) + v_2(0)]$ as well as $\Delta v = v_1 - v_2$, $\Delta v(0) = v_1(0) - v_2(0)$ are defined. The final velocity spread is given as

$$\Delta v = \frac{\bar{v}(0)}{v}\Delta v(0). \tag{3.5}$$

From the initial energy $E(0)$ we obtain $v(0) = [2E(0)/m]^{1/2}$ and if the ion velocity is after the acceleration much higher compared to the initial one, then $v = (2eU/m)^{1/2}$. The final velocity spread can be written as

$$\Delta v = \sqrt{\frac{E(0)}{eU}}\Delta v(0). \tag{3.6}$$

For high acceleration voltages $E(0) \ll eU \Rightarrow \Delta v \ll \Delta v(0)$, the velocity change is mainly determined by the acceleration voltage U [Dem03].

With the decrease in velocity spread, sensitivity increases because produced ions are addressed at the resonance to a greater extent. This increase in sensitivity is a very important point especially for ions with low production rates. Since most of the transition energies for ions are in the uv region, it is often more convenient to neutralize the accelerated ions and access a transition in atom. Such a neutralization can be performed by a charge transfer collision in a charge exchange cell. The energy loss due to such a peripheral collision is negligible for the beam energies in the range of a few 10 keV. Thus the fast atom beam does not have, after the charge transfer, any significant line broadening in comparison with the accelerated ion beam and the beam properties are preserved [Kau76]. However, slight asymmetries in the lineshape are often observed if a charge exchange cell is used.

The effect of the acceleration onto the lineshape and the resonance position of the atomic resonance is depicted in Fig. 3.2. The linewidth is reduced by about three orders of magnitude and the resonance position is shifted by 1.5 THz in the case of Be^+ ions. The shift is into higher or lower frequency for collinear or anti-collinear geometry, respectively, according to the Doppler formula $\nu_{c,a} = \nu_0\gamma(1 \pm \beta)$.
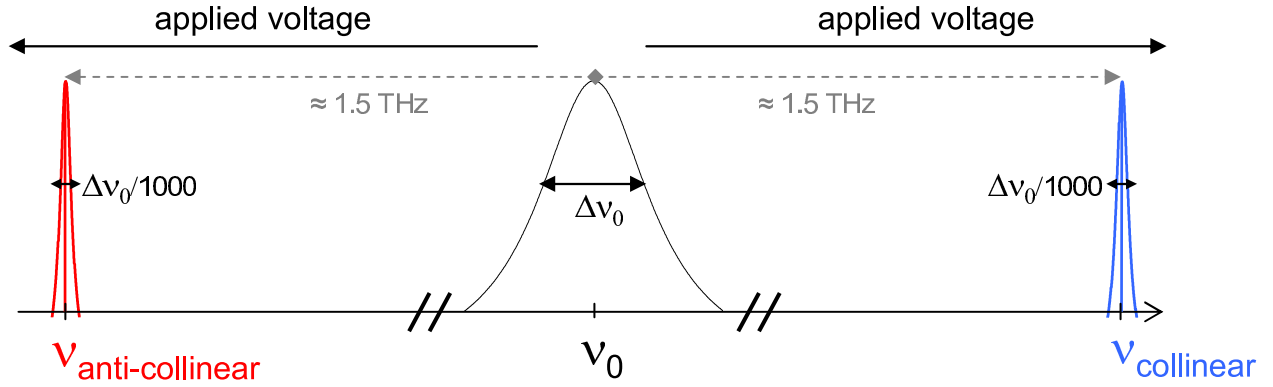
Figure 3.2. Decrease of Doppler broadened linewidth in fast ion beam spectroscopy. ν_0 is the resonance frequency of the ions at rest. Laser beams propagating in collinear ($\nu_{\text{collinear}}$) and anti-collinear ($\nu_{\text{anti-collinear}}$) geometry appear in the rest frame of the accelerated ion to be shifted in this frequency by about 1.5 THz to lower and higher frequencies, respectively. Longitudinal velocity spread of the accelerated ions in the electrostatic field is suppressed at 60 keV (available voltage at ISOLDE) by a factor of about 1000.

Scanning the laser frequency across the resonances can be performed with a tunable laser source or with a variable acceleration voltage. The latter is particularly useful when non-tunable lasers are applied. While the laser is fixed to one frequency ν_0, the scanning is accomplished with the so-called Doppler tuning where the applied variable voltage is changing in small equidistant steps. Approaching ions undergo a slight velocity change with each step and since the laser frequency is being fixed, this velocity change causes the tuning of the laser frequency in the rest frame of the ion. This variable voltage is usually additional to the acceleration voltage and it is applied shortly before the detection region. Lighter isotopes are stronger accelerated and for example for ^{9}Be with a total acceleration voltage of 50 keV, the tuning interval of 1 V corresponds to the frequency change of about 32 MHz. Due to this sensitivity, the application of the collinear laser spectroscopy for the isotope shift measurements of light elements is limited by imprecise knowledge of the acceleration voltage. Commercial power supplies providing voltages up to 60 kV have assigned accuracies of 10^{-4} which is in the order of few volts. Such an uncertainty would correspond to about 18 MHz uncertainty in the isotope shift of beryllium isotopes, yet the expected value for the field shift between the isotopes ^{9}Be and ^{11}Be is only about 10 MHz which means that the conventional collinear spectroscopy for isotope shift measurements is not adequate for the extraction of nuclear charge radii of the lightest elements.

To overcome the problem with the precise knowledge of the acceleration voltage we applied, in order to measure beryllium isotopes discussed in this theses, the second laser beam propagating opposite to the ion beam direction (anti-collinearly). Combination of the collinear laser, the anti-collinear laser and a frequency-comb metrology allowed us the interesting measurements also for light beryllium isotopes. The transition frequency

ν_0 can then be deduced from the laser frequency in the collinear ν_c and anti-collinear ν_a direction without knowing the absolute ion beam velocity β.

$$\nu_c = \nu_0 \cdot \gamma \cdot (1 + \beta) \tag{3.7}$$

$$\nu_a = \nu_0 \cdot \gamma \cdot (1 - \beta) \tag{3.8}$$

$$\nu_0^2 = \nu_c \cdot \nu_a \tag{3.9}$$

This is valid only if both frequencies are measured simultaneously, for a given ion velocity β. To our knowledge this approach was used in the measurements of short-lived isotopes for the first time. However, it was suggested for high voltage measurements previously [Kna00] and used for a precision test of time dilation with relativistic ion beams at the TSR (Test Storage Ring) [Rei07c] in Heidelberg and the ESR (Experimental Storage Ring) [Nov09] in Darmstadt.

3.2   Doppler Free Two-Photon Spectroscopy

The Doppler-free two-photon spectroscopy was used for high resolution spectroscopy of lithium. An atom at rest is irradiated by two laser beams propagating in opposite directions. The atom can absorb two photons with the electric field $E_1 = A_1 e^{(\omega_1 t - \mathbf{k}_1 \cdot \mathbf{r})}$ and $E_2 = A_2 e^{(\omega_2 t - \mathbf{k}_2 \cdot \mathbf{r})}$ only if the resonance condition

$$E_f - E_i = \hbar(\omega_1 + \omega_2) \tag{3.10}$$

is fulfilled as shown in Fig. 3.3a. If the atom is moving with the velocity $\mathbf{v}$, the laser frequencies ω_1 and ω_2 are Doppler shifted in the rest frame of the atom according to

$$\omega_{1,2}' = \frac{\omega_{1,2} - \mathbf{k}_{1,2} \cdot \mathbf{v}}{\sqrt{1 - v^2/c^2}} = \omega_{1,2} - \mathbf{k}_{1,2} \cdot \mathbf{v} + \frac{\omega_{1,2}}{2}\frac{v^2}{c^2} - \cdots, \tag{3.11}$$

and the resonance condition will change to

$$(E_f - E_i)/\hbar = (\omega_1' + \omega_2') = (\omega_1 + \omega_2) - \mathbf{v} \cdot (\mathbf{k}_1 + \mathbf{k}_2) + \frac{(\omega_1 + \omega_2)}{2}\frac{v^2}{c^2} + \cdots. \tag{3.12}$$

The first order Doppler shift is eliminated if $\mathbf{k}_1 = \text{-}\mathbf{k}_2$, i.e, the two beams propagate in opposite direction and have equal frequencies $\omega_1 = \omega_2 = \omega = (E_f - E_i)/2\hbar$. The two-photon absorption provides a spectroscopic resolution that is close to the natural linewidth and addresses all atoms independent of their velocity. Thus, if the transition can be saturated, high efficiency can be achieved, which indicates that the technique is
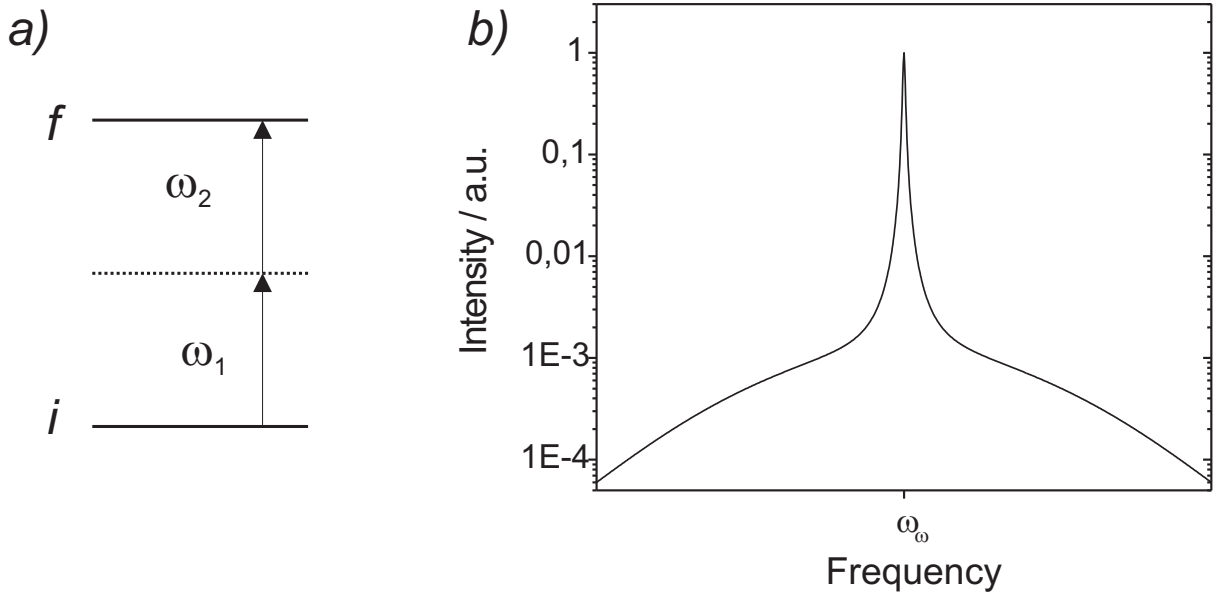
Figure 3.3. a)Two-photon transition with a 'virtual intermediate level'(dot line). b) Lineshape of the two-photon transition [San05].

suitable also for radioactive isotopes with low production rates. For two-photon absorption, selection rules are different from those of ordinary dipole transitions. The change in orbital angular momentum must be $\Delta l = 0, \pm 2; \Delta J = 0, \pm 1, \pm 2; \Delta F = 0, \pm 1, \pm 2$. In the case of an $s_{1/2} \rightarrow s_{1/2}$ transition , like the one used in lithium, only $\Delta F = 0$ transitions are allowed. Figure 3.3b shows the typical lineshape of a two-photon transition: A narrow, Doppler-free Lorentzian profile is observed above a Doppler-broadened background that is described by a Doppler or a Voigt profile. The narrow lineshape is due to the previously described process of two-photon absorption of counter-propagating photons $(k_1 = -k_2)$ while the broad background stems from the absorption of two co-propagating photons $(k_1 = k_2)$ when only a specific velocity class can contribute. In special cases, the latter process can be suppressed by a proper choice of the polarization states of the counter-propagating photons [Hae80]. However, this has not been the case in the measurements performed in the work discussed in this thesis.

3.3   Resonance Ionization Spectroscopy

For efficient detection of the two-photon excitation in lithium atoms, the technique of resonance ionization spectroscopy (RIS) was used [Hur79]. It is usually realized as a multiple-photon absorption process, where the atoms are stepwise excited by different laser beams. After the excitation, an ionization process takes place, which can be realized by many different means, e.g. field ionization, non-resonant photo-ionization or the excitation
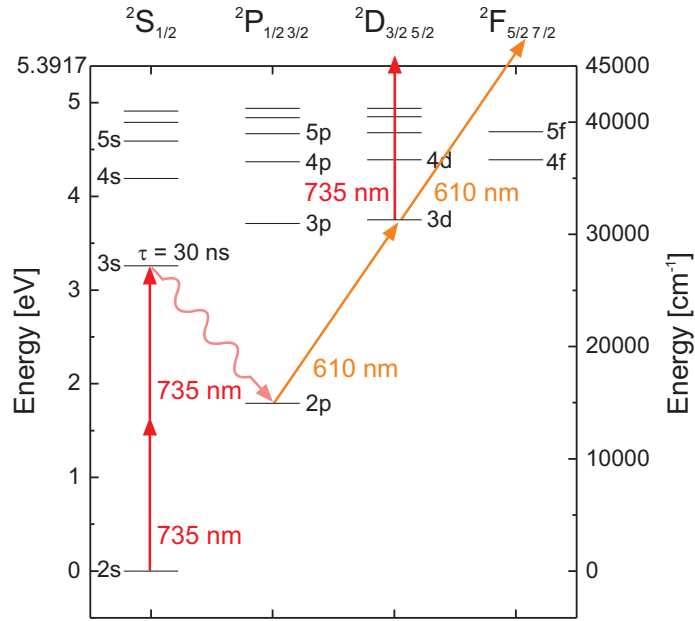
Figure 3.4. Resonance ionization scheme for lithium [San05].

to an auto-ionizing state. The advantage of this technique lies on the relative large cross section for resonant excitation and in the efficient detection of the resulting charged particles, either the electron or the ion. For this, channeltron-type detectors are often used. It is one of the most sensitive detection methods and provides very low background. In the case of lithium, non-resonant ionization after resonant excitation along the $2s_{1/2} \rightarrow 3s_{1/2} \rightarrow 2p_{1/2,3/2} \rightarrow 3d_{3/2,5/2}$ path, as shown in Fig. 3.4, was applied. A peculiarity of this scheme is the spontaneous decay from the $3s$ into $2p$ state, which was included into the scheme to decouple the efficient ionization process $2p \rightarrow 3d \rightarrow \mathrm{Li}^+$ from the two-photon excitation where the highest accuracy is required. Promoting the electron from the $3s$ to the $5p$ state would lead to a resonant coupling of the $3s$ state and therefore to strong AC Stark shifts and AC Stark broadening, which would prohibit the accurate resonance frequency determination.

4 Tools for Precise Frequency Stabilization

4.1 Tunable Lasers

Lasers with a broad homogeneous gain medium can sustain light amplification over a wide range of frequencies. Such lasers are advantageous for spectroscopic investigations because many atomic and ionic transitions can be reached. However, a precision spectroscopy usually requires single-mode operation where the laser oscillation is suppressed to a narrow spectral interval, i.e. for applications as they are discussed here, a typical laser linewidth below 1 MHz is required. The center frequency (averaged over 1 s) should have a stability on the order of a few 10 kHz at least. This can be obtained with a set of frequency selective elements inside the laser resonator and active control of the resonator length relative to a external frequency reference. Moreover, for spectroscopic applications continuous tuning over the atomic or ionic resonance structure is also desirable. Lasers can be tuned within the gain width varying the resonator length and the transmission maxima of the frequency selective elements synchronously [Dem03].

For the experiments described in this thesis, two types of single-mode, tunable, ring lasers were applied. Spectroscopy on lithium atoms was performed with a Titanium:Sapphire in the first and a dye laser in the second resonant step, whereas for the investigation of beryllium ions two frequency-doubled dye lasers were used. The principle scheme of such a tunable, single-mode ring laser from Coherent is shown in Fig. 4.1. The active medium is either a dye solution which is sustainable circulating in the laser system or a Titanium:Sapphire (Ti:Sa) crystal. The medium is optically pumped with cw pump lasers, either an Ar^+ laser or a solid-state frequency-doubled $Nd:YVO_4$ laser. The dye solution consists of organic dye molecules solved in a liquid. It is circulating in the laser system at a high pressure (7-10 bars) and a thin free jet is formed with a flat nozzle that is 5 mm wide and 0.2 mm thick. This thickness is sufficient to absorb $\approx 90\%$ of the pump power and to provide the gain required to establish and maintain laser oscillation. The solution is additionally cooled down to 16 °C to avoid thermal fluctuations. Depending on the organic dye, the tunability can be tens of nanometers (tens of THz) and using different dyes the whole frequency range from 300 nm to 1.2 μm is accessible in cw or pulsed laser operation [Dem03]. The wavelength of the pump laser must be typically at least 60 nm shorter than the operating wavelength of the dye laser. For cw operation Ar^+
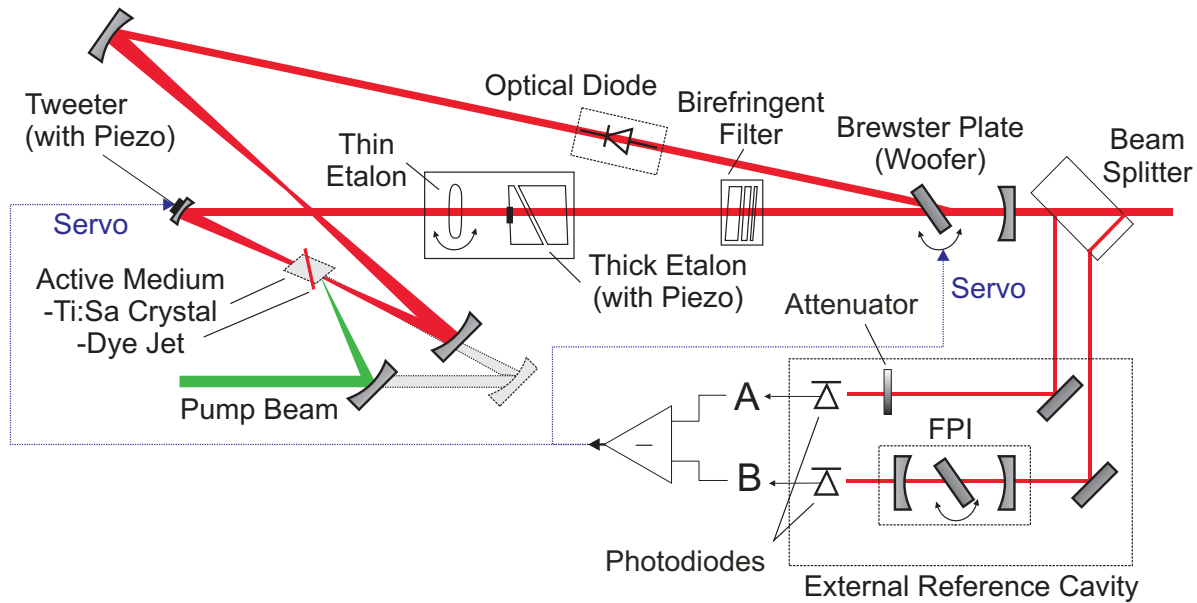
Figure 4.1. Scheme of a ring, single-mode, tunable laser (Coherent 699 and 899) as it was used for the measuremnts discussed in this thesis. Either a dye solution or a Titanium:Sapphire crystal can be used as an active medium. The laser is equipped with a temperature-stabilized external reference cavity for corrections of short-term fluctuations. The servo signal is generated by the difference between the signals transmitted through the Fabry-Perot Interferometer (FPI) and a freely propagating, slightly attenuated laser beam. Single-mode operation is obtain with three frequency-selective elements (birefringent filter, thin etalon, thick etalon).

in the uv (363 nm) or in the visible range (488, 514 nm) and the frequency doubled solid state lasers at about 532 nm are most commonly used.

The active medium of the second laser is a Ti:Sa crystal. It supports laser operation in the spectral range from 650 to 1000 nm (160 THz) and is can be pumped with the Ar^+ laser at 514 nm or nowadays with the more compact frequency-doubled Nd:YVO$_4$laser at 532 nm. The Ti:Sa crystal provides much less gain density than a dye solution and a slightly altered pump geometry is required in this case. The crystal must be pumped longitudinally, i.e., parallel to the circulating cavity mode and is therefore coupled through the curved lower fold mirror of the ring cavity, shown in Fig. 4.1.

It is important that the spot of the pump beam and the spot of the cavity mode have about the same size in the active medium. To reach sufficient gain densities both beams are focused to the same spot in the medium.

In a resonator that supports lasing in both directions, standing waves will form and at its nodes in the active medium, the inversion is not depleted. To avoid losses due

to the unused medium, and even more important to suppress competing oscillation at a different mode using the remaining inversion, an unidirectional device, the optical diode, consisting of a Faraday rotator and a phase shifter is added to the ring laser system.

To establish single-mode operation of the ring laser, three frequency-selective elements are required. For coarse frequency selection a birefringent filter (Lyot filter) is used. It consists of three birefringent crystal plates at Brewster's angle with a thickness ratio of $d : 2d : 4d$, where d is the thickness of the thinest plate. The thinest plate determines the free spectral range $\Delta\nu$ and the thickest one the width of a transmission peak $\delta\nu$. The modes of the birefringent filter have a large spacing $\Delta\nu = c/d$ of a few THz compared to the resonator modes $\Delta\nu = c/l_r$ (200 MHz) and oscillation occurs for those longitudinal resonator modes which coincide with the birefringent modes. Further frequency selection is done with a combination of a thin ($\Delta\nu = 200$ GHz) and a thick etalon ($\Delta\nu = 10$ GHz). Maximum light transmission through the frequency-selective elements is adjusted for a single chosen frequency within the whole gain bandwidth by a slight rotation (birefringent filter, thin etalon) or a change of the etalon width d (thick etalon), respectively.

The laser is also equipped with a temperature-stabilized external reference cavity for corrections of short-term fluctuations. Therefore, a thick beam-splitter after the output coupler creates two reference beams. One of these is transmitted through a Fabry-Perot interferometer (FPI) and detected with the photodiode B. The second beam is only attenuated to an appropriate intensity level and then detected with the second photodiode A. The signal from the photodiode B is 'normalized' with that of photodiode A in order to become independent from laser intensity fluctuations. Frequency fluctuations of the laser lead to the change of the transmission signal through the FPI which gives rise to an error signal in the differential amplifier. The error signal is processed and separated into a high and a low frequency component. The high-frequency servo signal is sent to the so-called tweeter mirror mounted on a piezo-element and the low frequency component is sent as the servo signal to a galvo-drive which rotates the Brewster glass plate (woofer). While the tweeter mirror has a fast dynamic response up to ≈10 kHz but a small correction range of about 1 GHz, the woofers response is slower (≈400 Hz) but allows the corrections of more than 15 GHz. More details of the locking system are given in section 5.3.

The external FPI cavity is inappropriate for long-term frequency stabilization because the remaining drifts are specified to be on the order of 30 MHz/hour. As discussed, our applications require a frequency stability of better than 100 kHz over many hours or even days of operation. Hence, other frequency references were required to which the FPI length itself could be actively stabilized. We have used for the measurements presented here an additional stabilization to an iodine hyperfine transition and a frequency comb.

4.2   Frequency Comb

Absolute frequency measurement and stabilization in the optical region was until recently a complicated process and limited to only a few atomic transitions. On the other hand, measurements in the microwave region are established already for years due to the availability of high frequency counters and generators and the SI unit of time, the second, is based on a microwave transition between the hyperfine levels of ^{133}Cs. Bridging the gap between accurately known microwave frequencies (tens of gigahertz) and unknown optical frequencies (hundreds of terahertz) was only possible by building large and complex frequency chains. Frequencies from the microwave region were transfered to the optical region in multiple steps via harmonic and difference-frequency generation. However, this approach was realized only for a few optical frequencies.

In 1999, were introduced ultrafast Kerr-lens mode-locked Titanium:Sapphire (Ti:Sa) lasers into optical metrology [Cun01]. This was an important step toward a completely new approach for absolute frequency determination and stabilization of optical frequencies. Mode-locked lasers emit a periodic train of pulses of very short duration. The emission spectrum in the frequency domain corresponds to a comb of distinct lines (modes) with a well-defined spacing given by the repetition frequency f_{rep} [Cun01]. The mode spectrum should extend over a spectral width $\Delta\omega$ of a full optical octave, i.e., the highest frequencies are twice as large as the lowest frequencies. This optical octave condition is of utmost relevance for absolute frequency determination, as it will be discussed below. The ultrafast Ti:Sa laser, with pulse duration of 10 fs has a bandwidth $\Delta\omega$ of 100 THz (300 nm) and hence, covers about one third of an optical octave. Additional tools, namely microstructured nonlinear fibers, are now available which can sufficiently broaden the spectrum to reach a full optical octave. In the following sections, the foundations of the frequency comb technique are briefly summarized.

4.2.1   Mode-Locked Lasers

A laser can oscillate on many longitudinal modes of a resonator separated by $\Delta\nu = c/l$, where l is the length of a round-trip inside the resonator. The number of modes that can oscillate simultaneously is determined by the gain bandwidth $\Delta\omega$ of the active medium as shown in Fig. 4.2. For a HeNe laser $\Delta\nu$ is only about 1.5 GHz which corresponds typically to three longitudinal modes, whereas for a Ti:Sa laser $\Delta\omega$ is five orders of magnitude larger and the number of lasing modes reaches 250×10^3. Without special precautions, the individual longitudinal modes have random phases and thus, the modes interfere randomly. This causes intensity fluctuations but in the case that there are many
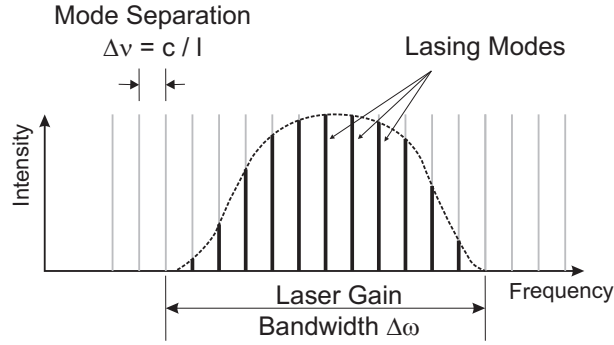
Figure 4.2. Resonator longitudinal modes with a separation $\Delta\nu$ and a laser gain bandwidth $\Delta\omega$.

modes in the resonator, the output averages to cw operation. By maintaining of a fixed relationship between the phases of the individual modes, the sum of all modes will form a giant and very short pulse [Sal07].

Such a phase relationship can be obtained by introducing an active or a passive mode-locking mechanism into the system. Active modulation is induced from an external signal, typically acousto-optic or electro-optic switches are used, which block the laser light path inside the resonator and opens only when the pulse approaches for the pulse duration [Sal07]. This must, of course, occur strongly synchonized with the pulse traveling time in the resonator. Intracavity light can also be actively modulated by varying the pump power, where the pump source goes synchronously on and off and acts as the mode-locked pump laser [Sal07]. Passive modulators, such as saturable absorbers, are placed directly in to the laser resonator and a self-modulation mechanism without any external signal takes place. The saturable absorber is a medium which acts differently for different laser intensities. Its absorption coefficient is large for low intensities and decreases for higher light intensities due to saturation. Oscillations can therefore only occur when the phases of the different modes are related and they form an intense pulse which will then be sustained in the resonator [Sal07]. Each time the pulse reaches the output coupler, light is emitted periodically, forming a train of short pulses with the pulse separation of twice the resonator length. Passive mode-locking can also be based on nonlinear Kerr-lens effect, where the high intensity light is focused differently than the low intensity light. A Kerr medium - it can be gain medium itself or another medium introduced in the resonator - acts as a lens, where the refractive index of the medium depends on the laser intensity,

$$n(I) = n + n_2 I, \tag{4.1}$$

$n(I)$ is the overall refractive index and n_2 is the nonlinear Kerr refractive index. If the highest intensity within the beam is at the center, the maximum change of the refractive

Nonlinear Kerr Medium
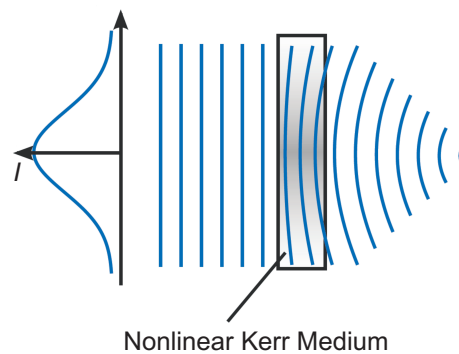
Figure 4.3. The third order nonlinear Kerr-lens effect for a Gaussian laser beam. If the highest intensity within the laser beam is at the center, the maximum change of the refractive index will be also at the center [Sal07]. The variable index of refraction acts as a focusing lens in the system.

index will be also at the center, see Fig. 4.3. By placing an aperture behind the Kerr lens, low intensities can be blocked, whereas high intensities pass through the aperture without attenuation.

Generally, the shortest pulses are achieved with the passive modulators, where the rapid recovery of the medium is advantageous compared to the active modulators [Sal07].

In practice, due to the dispersive media, different frequencies propagate through the medium with different velocities. The shortest possible pulses are reached either for zero or slight anomalous (negative) dispersion. To compensate a normal group velocity dispersion (GVD), bulk optical components such as prisms, diffraction gratings and dielectric mirrors [Okh04] or fibers with anomalous dispersion are used.

Femtosecond Ti:Sa lasers were mostly used for frequency comb generation until 2003. These lasers produce ultrashort optical pulses based on the Kerr-lens mode-lock mechanism. The Ti:Sa crystal is pumped by either an Ar^+ or a diode-pumped solid-state lasers. The crystal serves as the active medium and as the nonlinear mode-locked medium simultaneously. The positive GVD, generated by most of the bulk lasers can be effectively compensated with a pair of prisms or dielectric low-loss mirrors. A broad spectral width from 700 to 1000 nm can be extended to span an octave with a highly nonlinear microstructured fiber. Disadvantages of the Ti:Sa laser usage for frequency comb generation are continuously required alignments to start the mode-locking and to keep the laser in mode-locked operation. The accessible wavelength range of frequency combs based on Ti:Sa lasers extends from 400 to 1100 nm.

More recently, mode-locked doped fiber lasers (e.g. Erbium-doped, Ytterbium-doped) are in common use. The gain bandwidth of these rare-earth-doped fibers is sufficiently

large for ultra-short optical pulse generation, typically several tens of nanometers. The fiber lasers are pumped efficiently with low-cost diode lasers. Pulse repetition rates $f_{\rm rep}$ and the pulse duration is determined by the length of the fiber. For passive mode-locking Bragg mirrors and semiconductor saturable absorbers (SESAM) are used which have self-starting character and ensure short-pulse operation [Okh04]. They consist of intrinsic periodic structures which reflect optical frequencies selectively.

The fiber lasers are more compact and can be fabricated at lower cost compared to femtosecond Ti:Sa lasers. Moreover, the output is extending also into the near-infrared region from 1300 to 1700 nm which is of importance in telecommunications [Was03]. On the other hand, the performance of the fiber lasers is limited by strong nonlinearities in the fibers and relatively low pulse energy and peak power. These side effects have to be compensated by various methods, for example higher pulse energies can be obtained by subsequent amplification. Group velocity dispersion is much stronger compare to the Ti:Sa laser, due to the larger active medium and can be efficiently compensated by fiber Bragg grating or fused quartz fibers with anomalous dispersion [Dem03].

4.2.2   Frequency Comb Spacing and Position

An operating mode-locked laser emits a short pulse every time the circulating pulse inside the cavity reaches the output coupler. Due to the dispersion in the medium, the phase of the carrier wave and the phase of the pulse envelope are not synchronized. This results in a phase shift $\Delta\phi$ between them after each round trip inside the cavity, as shown in Fig. 4.4a as a time domain description of the output from the mode-locked laser. The separation time τ between the pulses depends on the cavity length l and the group velocity v_g, given by $\tau = l/v_g$.

Figure 4.4b shows the laser output in the frequency domain, which consists of a comb of equally spaced frequencies and the separation between the frequencies is given by the repetition rate $f_{\rm rep}$. Mathematically, the transfer from the time domain into the frequency domain is performed with a Fourier transformation, where a field of the single pulse is

$$E(t) = \tilde{E}(t)e^{i(w_c t + \phi_0)}. \tag{4.2}$$

The envelope function $\tilde{E}(t)$ after mode-locking should be strictly periodic with a period τ and the field of a periodic pulse train can be then written as

$$E(t) = \sum_n \tilde{E}(t - n\tau)e^{i[w_c t + \phi_0 + n(\Delta\phi - \omega_c \tau)]}, \tag{4.3}$$

where n is the integer number of pulses, ω_c is the carrier frequency and $\Delta\phi$ the puls-to-puls
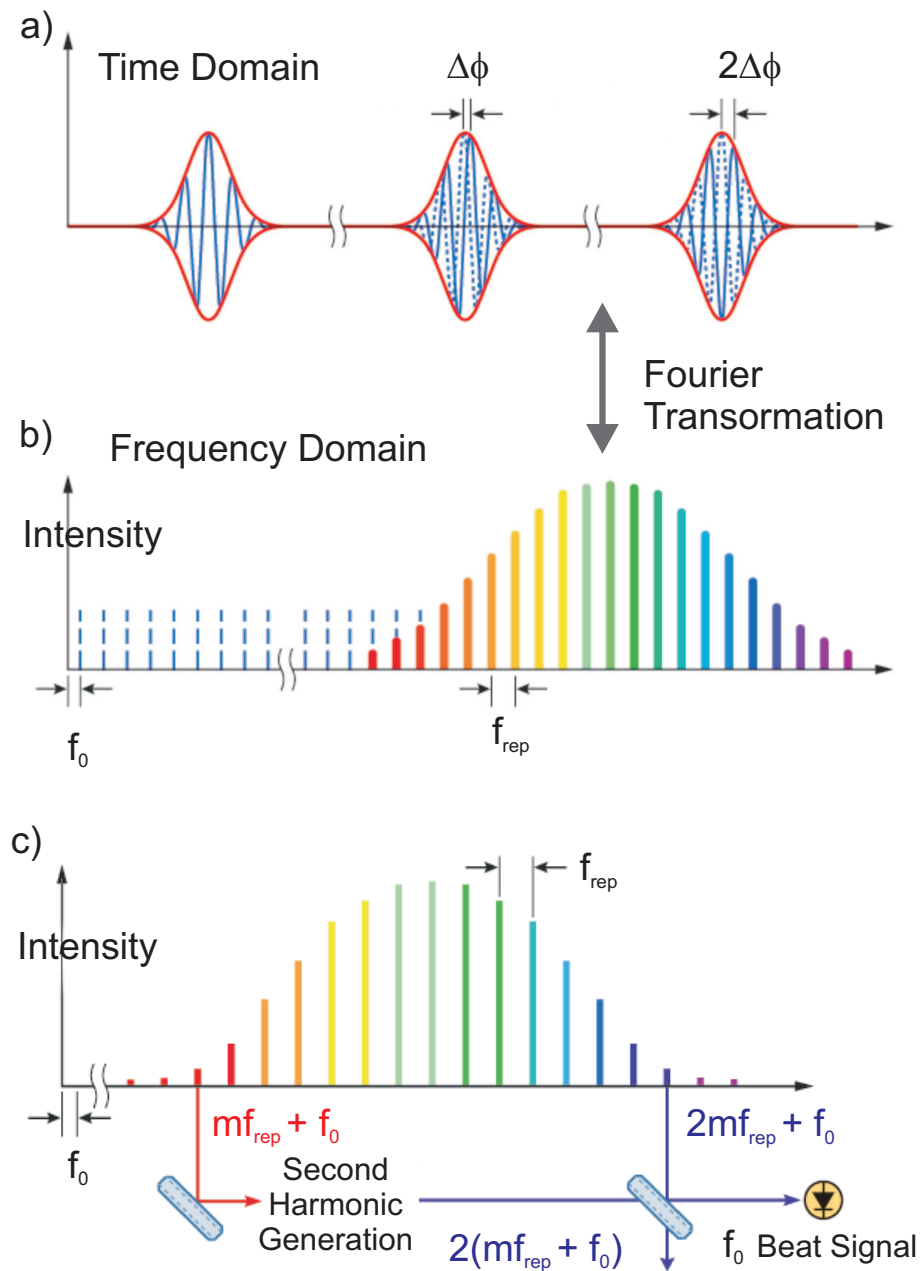
Figure 4.4. a) The periodic pulse train emitted from a mode-locked laser. After each round-trip is the phase of the carrier wave shifted compare to the phase of the pulse envelope by $\Delta\phi$. b) The frequency spectrum in a frequency domain (after the Fourier transformation) shows a comb of equidistant lines separated by a repetition rate f_{rep}. The phase shift is reflected in the so-called offset frequency f_0. c) With an octave spanning spectrum f_0 can be determined from a beat signal generated between the doubled frequency in the 'red' part of the spectrum with the frequency from the 'blue' part of the spectrum [Hech09].

phase shift between envelope and carrier. From the Fourier transformation

$$E(\omega) = \int\limits_{-\infty}^{\infty} \sum_n \tilde{E}(t - n\tau)e^{i[w_c t + \phi_0 + n(\Delta\phi - \omega_c\tau)]}e^{-iwt}dt, \tag{4.4}$$

we obtain

$$E(\omega) = e^{i\phi_0} \sum_n e^{in(\Delta\phi - \omega\tau)}\tilde{E}(\omega - \omega_c). \tag{4.5}$$

The spectral width, as given by $\tilde{E}(\omega)$ is inversely proportional to the pulse duration and centered at the carrier frequency ω_c. The important components are those for which the exponentials in the sum add up coherently because the phase shift between n and $n + 1$ is a multiple of 2π and $\Delta\phi - \omega\tau = 2m\pi$. The angular frequency of the m-th mode can be then written as

$$\omega_m = \frac{\Delta\phi}{\tau} - \frac{2m\pi}{\tau}, \tag{4.6}$$

or as $f_m = mf_{\text{rep}} + f_0$. Hence, the frequency spectrum of a mode-locked laser is a series of comb lines, separated by integer multiples of the repetition frequency f_{rep} plus the offset frequency f_0, with $f_{\text{rep}} = 1/\tau$ and $f_0 = \Delta\phi f_{\text{rep}}/2\pi$ [Cun01]. The offset frequency f_0 does not change the mode structure it just adds an offset from zero to the whole comb structure, i.e., it shifts the whole comb to the left or to the right depending on its sign.

The repetition rate can be simply detected with a fast photodiode and can be controlled by adjusting the resonator length. A servo loop can control the f_{rep} frequency of the laser by comparing this signal to a microwave clock. Until recently, the unsolved problem was the determination and control of f_0. This was first solved by fixing one comb mode to a separate optical reference frequency without direct detection of f_0 [Cor03]. Nowadays, the detection of f_0, can be achieved with an f-to-$2f$ self-referencing technique [Was03], where the octave spanning spectrum plays an important role. Such a spectrum provides two modes $f_m = 2(mf_{\text{rep}} + f_0)$ and $f_{2m} = 2mf_{\text{rep}} + f_0$ and the offset-frequency f_0 can be directly determined from a beat signal generated between the doubled frequency $2f_m$ obtained from the 'red part' of the spectrum and the f_{2m} frequency from the 'blue part' of the spectrum as it is shown in Fig. 4.4 c). Furthermore, it was found that f_0 can be controlled independently from f_{rep} by adjusting the pump power. Self-referenced detection of f_0 obviates the requirements of the optical reference [Was03]. For most of the applications both free parameters f_{rep} and f_0 which describe the frequency comb are stabilized to an external frequency reference and they are controlled separately. Since they are radio (rf) frequencies, a direct link to microwave standards is favorable [Kub05].
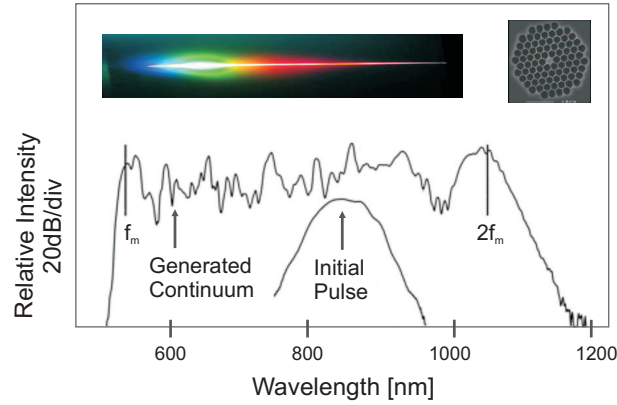
Figure 4.5. Continuum generation by an air-silica microsctructured fiber, (reproduced from Jones *et al.* 2000).

4.2.3   Spectral Broadening

Spectral broadening of the mode-locked lasers is desirable not only for measurements in the largest possible frequency interval but it is also required for the mentioned f-to-$2f$ self-referencing technique. The spectrum of short pulse lasers can be efficiently broadened in microstructured fibers which were developed recently [Jon00, Cun01]. They are based on strong contrast in refractive indexes. A core of the fiber produced from a fused silica is surrounded by air holes, as demonstrated in the inset of Fig. 4.5. When high intensity laser light is focused to the structured fiber many nonlinear processes like four-wave mixing, Raman scattering, Brillouin scattering, self-phase modulation, etc. will appear during the light propagation. These nonlinear processes produce new frequencies and broaden the input frequency spectrum considerably, see Fig. 4.5.

4.2.4   Optical Frequency Measurements

Optical frequency measurements are used for determinations of molecular, atomic or ionic transitions. As mentioned before, the frequency comb was used in the experiments described here for frequency stabilization and measurements of the single-mode ring lasers and determinations of transition frequencies in lithium atoms and beryllium ions. The frequency f of the laser can be determined with the frequency comb in the following way: The frequency of any comb mode can be written as a simple function of two rf frequencies, $f_{\mathrm{rep}}(\approx 100 \text{ MHz})$ and $f_0(\approx 40 \text{ MHz})$, $f_0 < f_r$. When the beat signal f_{beat} is produced between the external laser and the nearest comb mode, the frequency f of the external laser can be determined knowing f_r and f_0 according to

$$f = \pm f_0 + m f_{\text{rep}} \pm f_{\text{beat}}, \tag{4.7}$$

where m is the m-th mode of the comb (up to 10^6), which can be determined with modern wavemeters that have low uncertainties ($\approx$30 MHz). For measuring the laser frequency f, the beat signal is simply counted over an interval T. For stabilizing the laser frequency, f_{beat} is stabilized with the phase-lock-loop to a reference frequency. The sign in front of f_0 depends on the position of the frequency relative to zero point and the plus/minus sign in front of f_{beat} indicates if the f frequency is smaller or larger than the frequency of the nearest comb mode.

4.3   Frequency Standards

Frequency standards have been a highly active field over many centuries, mainly driven by the need of having clocks with improved accuracy.

Since 1967, the unit second is defined as the time of 9,192,631,770 cycles of the transition radiation in the ground state hyperfine splitting of the cesium (Cs) atom. An atomic Cs beam is probed by microwaves which are tuned across the two closely spaced hyperfine levels. When the microwave frequency is exactly adjusted to the Cs transition, the atoms absorb the microwaves and a signal generated by the absorption is fed back to the microwave source to stop the tuning at the specific frequency. The microwave Cs standard was improved after the development of the cooling and the trapping techniques for neutral atoms in a so called Cs fountain clock. Another frequency standard with superior short-term stability are hydrogen masers (often manufactured in Russia), however their long-term stability is lower. Rubidium standard clocks have lower accuracy compared to the previous ones but are in frequent use because of their low cost, small size, compatibility and good short-term stability [All97]. One of these RF standards is usually used as a frequency reference for a frequency comb. In lithium and beryllium experiments, described here, the commercial rubidium standard was used and the stability of the clock was transfered to the dye, respectively Ti:Sa lasers via the frequency comb.

Since the invention of the lasers optical frequency standards became important increasingly. Depending on the type, they provide very stable, reproducible and accurate frequencies which can serve as reliable frequency references. High accuracy indicates that the frequency, when averaged over a long time, accurately matches the specified frequency. High reproducibility (high precision) means that the repeated measurements give a small standard deviation and a high stability implies only small drifts of the measured frequencies.

Stability of the atomic clock is proportional to its operating frequency which is in optical region about 10^{15} Hz, 100 000 times larger as in the microwave regime. In optical standards is a stable reference frequency in a narrow optical absorption of atom or ion (few Hz or less) probed by a laser, the so called local oscillator with a narrow linewidth. Rapid laser oscillations are counted effectively with the frequency comb. Single ion candidates with very narrow forbidden transition stored in Paul or Penning traps are Hg^+, Sr^+, Yb^+ and In^+. Clouds of cold neutral atoms candidates like H, Ca, Rb, Sr, Yb are stored mainly in magneto-optical traps [Cun01].

Besides atoms and ions also molecule-based standards provide reliable frequency references. These are molecules like methane (CH_4), acetylene (HC_2H) or iodine (I_2) which also exhibit hyperfine structure that can be resolved with Doppler-free techniques like saturation spectroscopy. Especially the iodine molecules provide a multiple of rovibronical transitions over a spectral range of a few hundred nm in the whole visible region. Only a few of these lines were measured very accurately, but most of the lines can be calculated very reliably providing a large number of reference points. The laser stabilization to iodine lines was applied also in the beryllium experiment and the used iodine lines were accurately remeasured with the frequency comb.

Figure 4.6 shows an evolution and a comparison of the microwave and the optical standards in the last fifty years. The frequency standards can be found more often also in practice and daily use, e.g., in Global Positioning System (GPS) or in the synchronization support for a high-speed optical communication [Cun01].
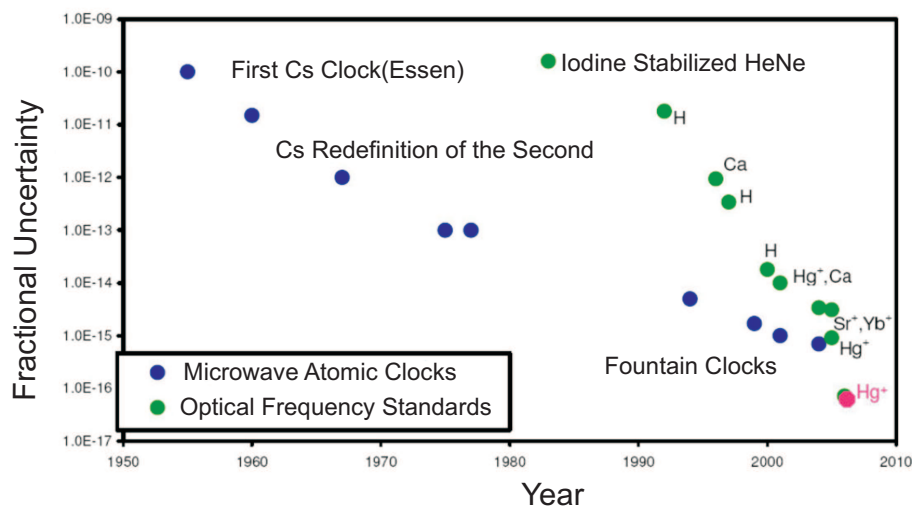
Figure 4.6. A comparison of frequency standards developed in the last fifty years [Pei09].

5 Frequency Comb Based Resonance Ion Spectroscopy on Lithium

In this chapter the latest absolute transition frequency measurements of stable lithium isotopes ^{6,7}Li in $2S \rightarrow 3S$ transition are described. Previously, precise measurements of the isotope shifts of lithium isotopes were performed during an online run at GSI in 2003 and two online runs in 2004 at the ISAC facility at TRIUMF in Canada [Ewa05, San05, San06]. The main goal was to obtain the nuclear charge radius of the most studied halo isotope ^{11}Li. In the experiment described here, a similar experimental set-up was used as in ISAC but the laser stabilization was based on a frequency comb. Absolute transition frequencies were measured with an accuracy improved by an order of magnitude compared to previous measurements. The first sections deals with the experimental set-up: lithium atomic beam production, the laser system and a laser stabilization to a frequency comb are described in detail. In the main part of this chapter the experimental results are discussed.

5.1 Atomic Beam Production

A simplified scheme of the experimental set-up is shown in Fig. 5.1. Lithium atoms were produced either by a heating graphite tube loaded with lithium metal shot as depicted in Fig. 5.1 or from a thin carbon foil doped with lithium nitrate as shown in Fig. 5.2. The sources did not differ much in the overall production of stable lithium isotopes, only in the emittance of the emerging beam. The graphite tube is 2 mm in inner diameter and has a length of 20 mm. The crucible was located at a distance of about 30 cm from the so-called ionization region of a quadrupole mass spectrometer (QMS), as depicted in Fig. 5.1 and was heated directly by a current of typically 40 A. The ionization region has a cylindrical shape with an entrance hole of 4.5 mm in diameter which collimates the atom beam entering from the graphite tube. The second source, a 300 nm thick carbon foil doped with about 5×10^{17} lithium atoms in the form of a lithium-nitrate solution, was located only a few millimeters from the entrance of the ionization region. The carbon foil was heated to typically $1800°$ with a few Watts of a beam from a CO_2 laser. Released lithium atoms were drifting into the ionization region with nearly no collimation. Ions that were produced by surface ionization on the hot graphite foil were repelled from the
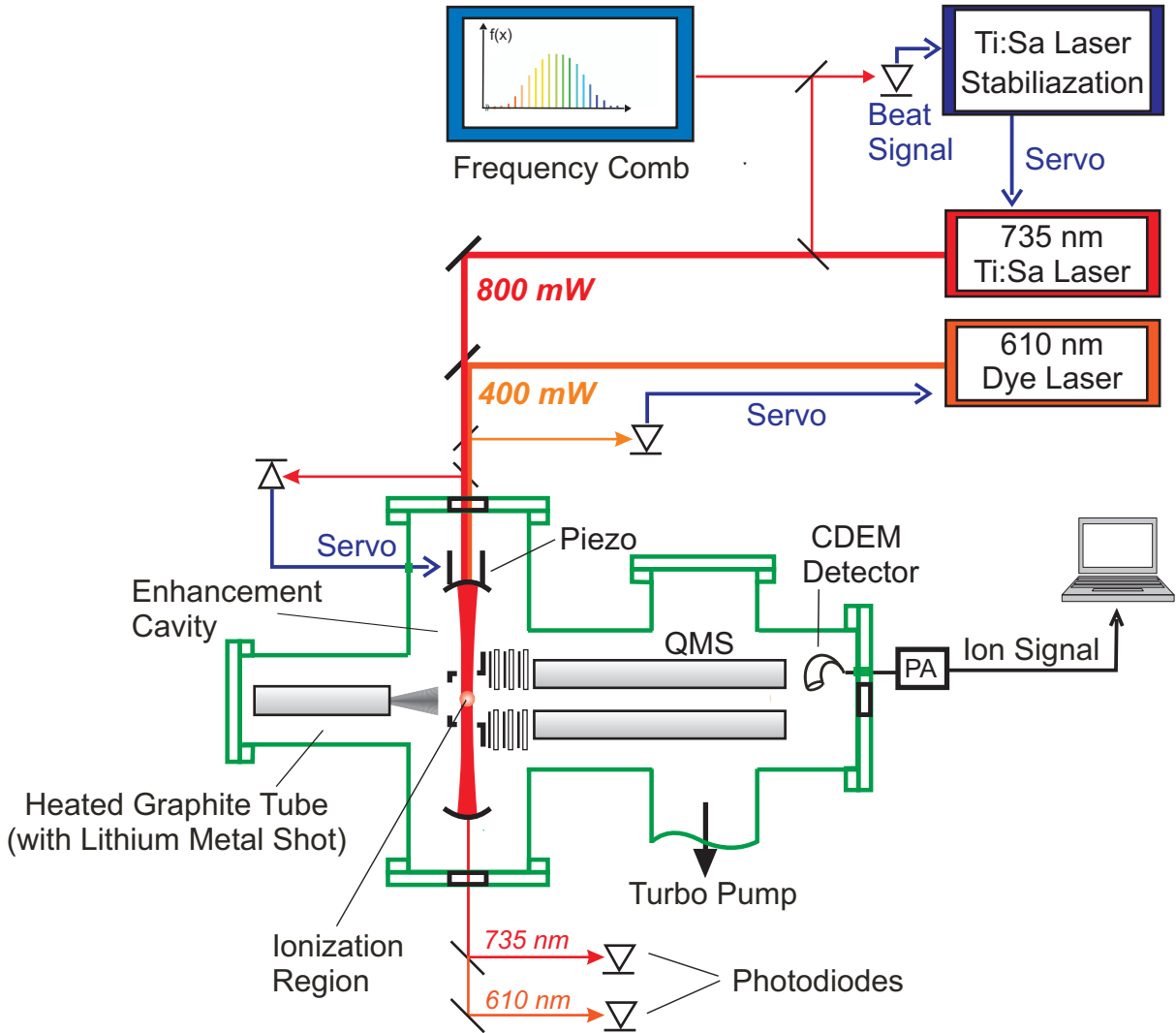
Figure 5.1. Experimental setup for frequency comb based absolute transition frequency measurements in the 2S - 3S transition of stable ^{6,7}Li.

ionization region by a slightly positive potential (4.9 V). The potential is chosen in such a way, that surface ions are sufficiently suppressed but electrons emitted from the hot surface and accelerated towards the ionization region do not gain sufficient energy to cause electron impact ionization of neutral lithium atoms, since the ionization potential is 5.391 eV. The geometry of the second source was analog to the set-up at TRIUMF for radioactive lithium isotopes in order to have similar conditions for the measurements.

5.2　The Laser System

The laser system for resonance ionization consists of a Ti:Sa laser running at 735 nm for the two-photon 2S → 3S transition and a dye laser at 610 nm for the resonance ionization along the 2P → 3D → Li$^+$ path after spontaneous decays from the 3S to the 3P level.
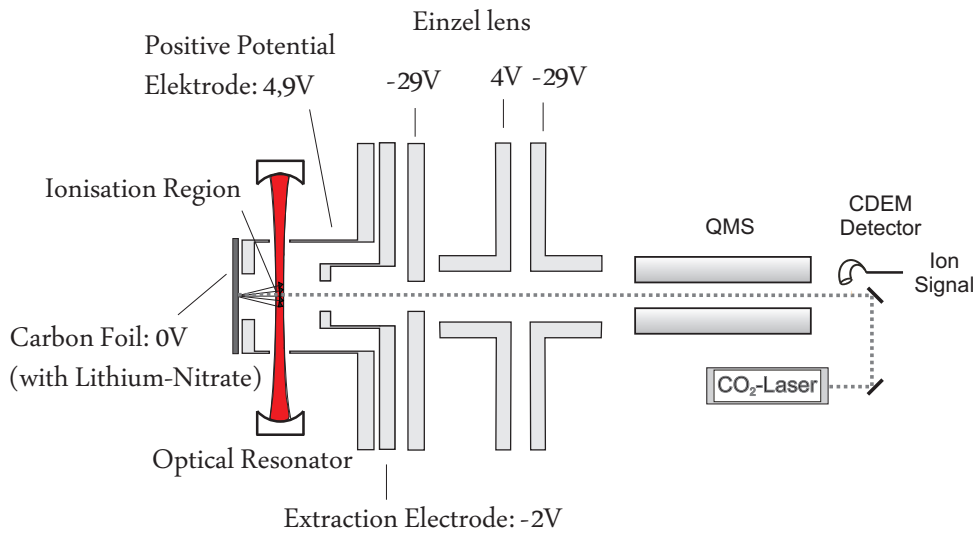
Figure 5.2. Lithium atomic and ionic beam production. The thin carbon foil is heated by the CO_2 laser and emitted atoms which drift toward the optical resonator are ionized in the optical resonator, mass separated in the quadrupole mass separator (QMS) and detected with a channeltron-type ion detector. Several electrodes are used to extract only the laser ions and to suppress the surface ions and electrons emitted from the hot surface of the foil.

The non-resonant ionization step can be induced either by 735 nm or 610 nm photons. Created ions were mass analyzed and then detected with the continuous dynode electron multiplier (CDEM). The extraction and detection efficiency of the QMS was well above 50%.

5.2.1   The Lasers

The tunable ring Ti:Sa laser (Coherent 899-21) was pumped with 10 W from a frequency-doubled Nd:YVO$_4$ laser (Coherent VERDI V18) and the tunable ring dye laser (Coherent 699-21) was operating with dye Rhodamin 6G solved in ethylenglycol (0.75 g/l) and was pumped with 8 W from a second VERDI laser (Coherent VERDI V8). The maximum output power of the Ti:Sa and the dye laser was 1200 mW and 400 mW, respectively. Both laser intensities were enhanced at the interaction point to achieve sufficient excitation efficiency in the non-linear two-photon process and the non-resonant ionization. Moreover, substantial power broadening is essential in the $2P \rightarrow 3D$ transition in order to excite all velocity classes and to become independent from the exact frequency of the dye laser as it is discussed below. This broadening is reached by resonance enhancement in a 'two-color' cavity. For referencing the Ti:Sa frequency to the frequency comb, a frequency offset locking between the comb-stabilized diode laser and the Ti:Sa laser was set-up. The stabilization chain and the feedback loop is discussed in more detail in the
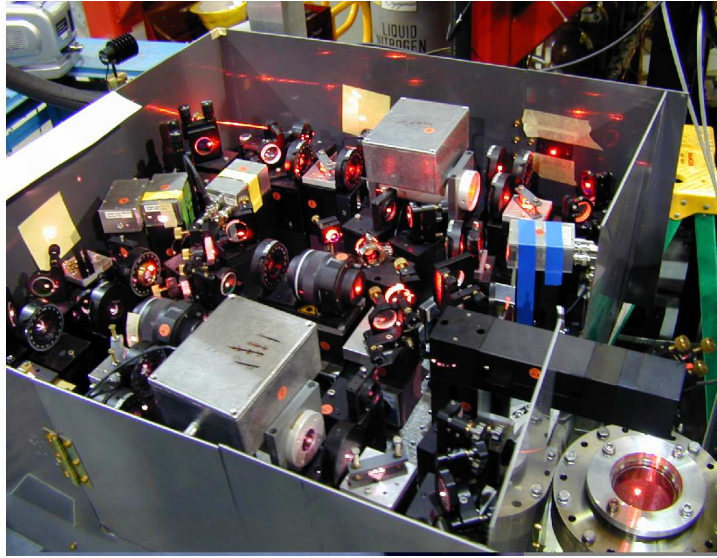
Figure 5.3. Photo of the optics that is being used for the enhancement cavity stabilization to the Ti:Sa laser and the dye laser stabilization to the cavity. The light from the Ti:Sa and the dye laser was coming from left, on the right-down corner is shown a part of the vacuum chamber, where the cavity was located. Stabilized light was entering the chamber through the viewport.

following section.

5.2.2   The 'Two-Color' Cavity

The enhancement cavity, a symmetrical optical resonator consisting of two spherical mirrors of 50 cm curvature radius separated by 30 cm was placed in a vacuum chamber. The laser spot size at the center of the cavity was calculated to be 0.46 mm. One of the resonator mirrors was mounted on a piezo-electric transducer in order to adjust the cavity length.

The light from the Ti:Sa laser and the dye laser was transported from the optical laser table to the vacuum chamber via single-mode (SM) fibers. The optics for cavity stabilization, that has been developed by Ewald [Ewa04], was located on top of the vacuum chamber, a photo is shown in Fig. 5.3 and a scheme of the set-up in Fig. 5.4. A detailed description of the optical scheme and the Pound-Drever-Hall locking scheme that was used can be found in [Ewa04] and [San05].

The laser intensity of the light after the SM fibers and the stabilization system was about 600 mW for the Ti:Sa and 150 mW for the dye laser. The light was vertically coupled to the cavity resonator via the viewport on one side of the vacuum chamber
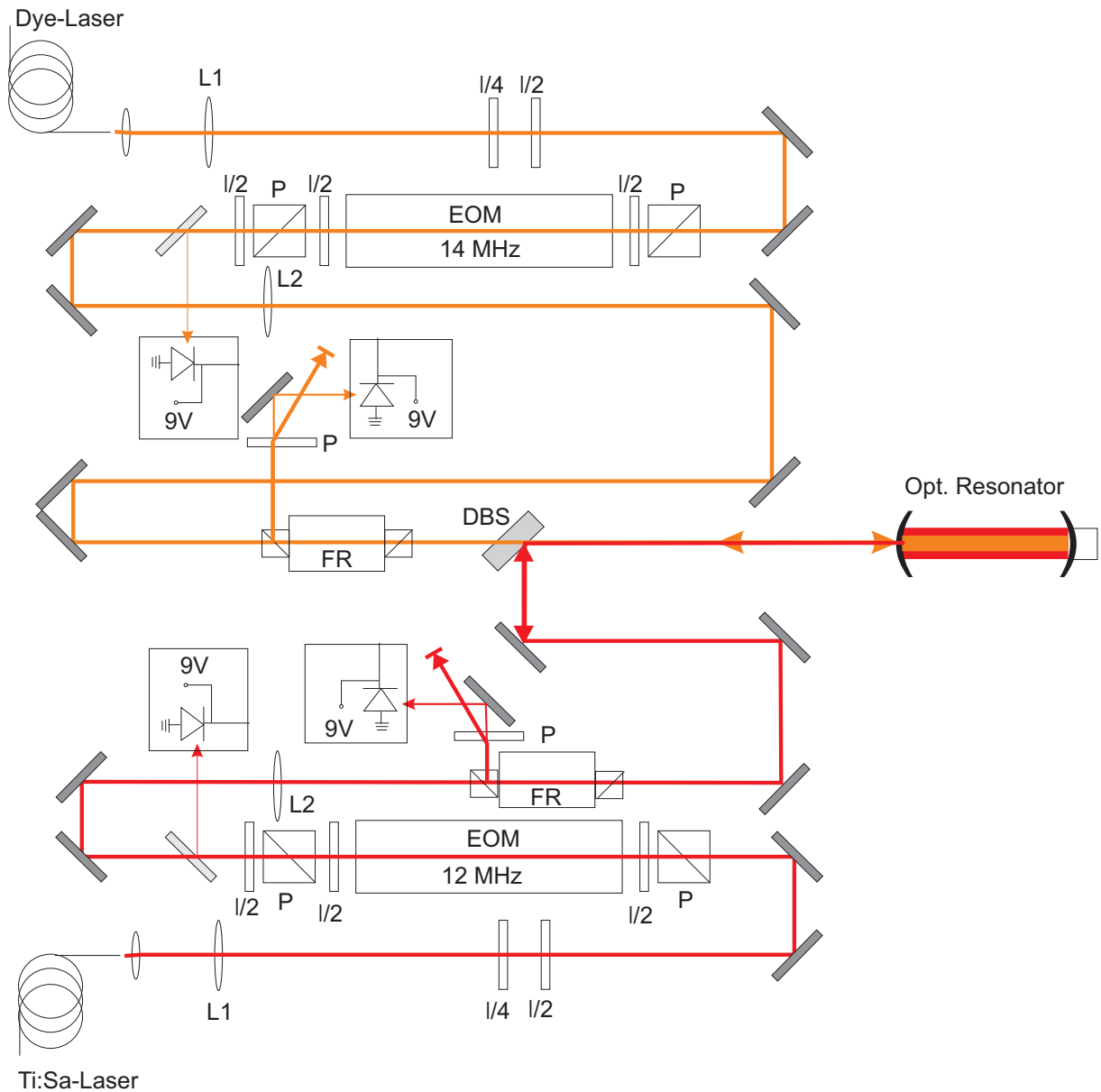
Figure 5.4. The schematic layout of the Pound-Drever-Hall cavity stabilization developed by [Ewa04]. L1 and L2 are lenses for beam collimation, $\lambda/2$ and $\lambda/4$ are waveplates to control the laser beam polarization, P is a polarization beam splitter, EOM is an electro-optical modulator to generate the sidebands, FR is a Faraday rotator to avoid back-reflections, DBS is a dichroic mirror which reflects the Ti:Sa wavelength (735 nm) and transmits the dye laser wavelength (610 nm) towards the optical resonator.

(lower right corner in Fig. 5.3). To enhance the light in the cavity, from both lasers at the same time, the following procedure was performed: The cavity was locked to the Ti:Sa laser by the Pound-Drever-Hall technique (PDH) [Dre83] to ensure resonance enhancement of the Ti:Sa frequency. The stabilization signal was obtained from the reflection of the carrier and two sidebands and the generated servo signal was applied to the piezoelectric transducer on which one of the cavity mirrors was mounted and that was used to adjust the cavity length. The dye laser was similarly locked to the cavity, again with PDH locking, but this time the servo signal was fed to the Coherent control box of the dye laser to adjust the dye frequency. This did not allow to lock the dye laser frequency independently from the Ti:Sa frequency. Feasible locking points for the dye laser were only the longitudinal modes of the cavity which has a free spectral range of about 500 MHz. Thus, the locking point of the dye laser might be as far as 250 MHz from the actual $2P \rightarrow 3D$ resonance frequency. Moreover, tuning the Ti:Sa laser induces a change in the cavity length and this will consequently cause a change in the dye laser frequency. Therefore, sufficient power broadening in the $2P \rightarrow 3D$ transition by the dye laser, as mentioned above, was essential. The resonance cavity had an enhancement factor of about 50-100 for the Ti:Sa laser and about 20 of the light from the dye laser. Part of the laser power stored in the cavity was passing through the high reflector of the cavity and left the vacuum chamber through a wedged viewport. This light was separated into the two wavelengths by a dichroic mirror and its power was measured with a set of photodiodes. The information about the (relative) laser power in the cavity was required for normalization as well as to correct for the occurrence of AC Stark shift in $2S \rightarrow 3S$ transition as will be discussed in the section 5.4.

5.3   Laser Frequency Stabilization

In the online lithium measurements a stabilized diode laser was used as a frequency reference for the Ti:Sa laser. The diode laser (DL 100), in Littrow configuration, was stabilized to a hyperfine component of an iodine line [Noe03]. In order to transfer the stability from the diode laser to the Ti:Sa laser, the technique of frequency-offset locking was used. Hence, all measurements of the different lithium isotopes were performed relative to this iodine line. A first attempt to determine the $2S \rightarrow 3S$ transition frequency in lithium was the measurement of the frequency of the iodine line with a frequency comb [Mis06, Rei07]. Due to inaccuracies of the locking points of the diode laser, the frequency uncertainty was on the order of 2 MHz and therefore a different approach was used for the measurements discussed in this thesis. A direct stabilization of the Ti:Sa

laser to a recently developed frequency comb was established.

A commercial frequency comb (Menlo Systems, FC 1500), based on an erbium-doped fiber laser pumped with a diode laser and operating at 1560 nm was used. A scheme of the frequency comb is shown in Fig. 5.5. The output from the fiber laser is in the first step amplified with an erbium doped fiber amplifier (EDFA) and divided into two parts. One part, broadened with a micro-structured fiber to span an optical octave, is used for carrier-envelope-offset (ν_{CE}) detection in the XPS 1500 section. The other part is amplified in the second EDFA and frequency doubled (SHG 780) to obtain light in the near-infrared region of 780 nm. The repetition rate (ν_{rep}), which is also the separation between the comb modes, is 100 MHz. Servo loops control both RF frequencies ν_{CE} and ν_{rep} of the laser by comparing their signals to a microwave Rubidium clock (Rb clock).

Although, the output from the frequency comb laser after SHG 780 is up to 100 mW, there are typically 10^6 comb modes in the output spectrum and so there is only a few tens of nanowatts of light per mode. Hence, another non-linear fiber after SHG 780 is used to control an intensity distribution and shift as much intensity as possible to the wavelength region, where the probing laser for stabilization is lasing. Sufficient laser power from the frequency comb and the Ti:Sa laser is required for proper beat signal production as shown later.

5.3.1   Beat Signal Generation

A small part of the Ti:Sa laser light was coupled to a standard single mode fiber (SM) and transferred to the frequency comb. The SM fiber was not polarization maintaining, hence, the Ti:Sa laser beam passed a $\lambda/4$ and $\lambda/2$ plate (300-1200 nm) at the entrance to the frequency comb, as shown in Fig. 5.5. The laser beam was combined with the frequency comb beam with a polarizing beam splitter cube (PBS, coating 400-1100 nm). The mixing ratio between the two beams could be adjusted with two $\lambda/2$ plates (600-1200 nm), placed in front of the PBS. Behind the PBS a second set of $\lambda/2$ plate and PBS was used to project both beams on the same polarization axis. Then the mixed beam was steered to a grating (1800 lines/mm) and directed through another mirror to the photodiode (PD). The beams, when impinging to the grating, must be properly overlapped since the angle of reflection from the grating depends on the incidence angle as well as on the wavelength. Already slight misalignments would results in the disappearance of the low-frequency beat signal. The grating was introduced to reduce the noise on the photodiode by rejecting unnecessary modes of the comb from the subsequent photodetector. All beat signals between the Ti:Sa laser and the different modes of the frequency comb were detected with the avalanche photodiode (APD 210, 400-1000 nm). However, only the
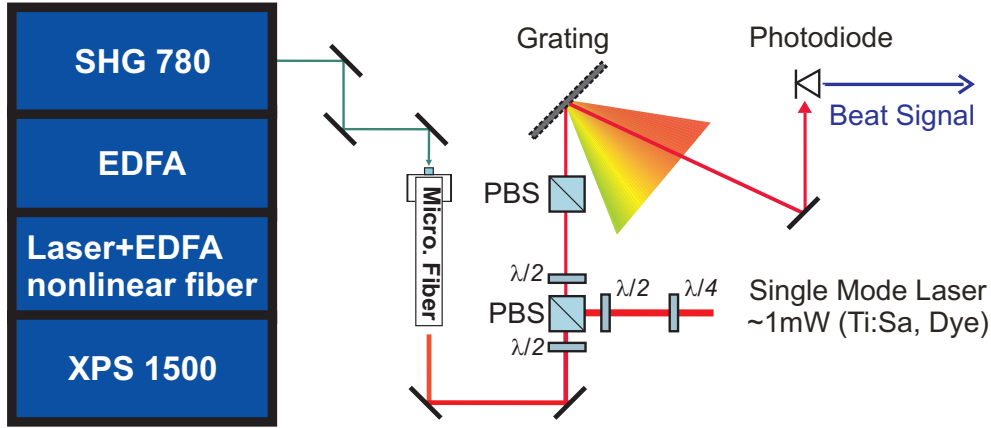
Figure 5.5. Scheme for a frequency comb laser beam generation and a coupling of one of a frequency comb mode and a single mode laser to the photodiode to generate a beat signal. Details are described in the text.

lowest beat frequency, i.e. with the nearest mode of the frequency comb spectrum would be transmitted through the RF filter already behind the APD since the electronics of the FC 1500 includes a bandpass filter at 30±5 MHz. Once the beat signal is observed on the spectrum analyzer, the intensity ratio between two beams is adjusted with the three $\lambda/2$ plates to obtain the maximum signal. To ensure good locking conditions, the beat signal for further signal processing must be at least 25 dB above the noise floor. Usually, the power level of the frequency comb was the most critical point. Each comb line had on average a power of only few tens of nanowatts, while the power of the Ti:Sa laser at the entrance of the PD was typically about 200 μW.

5.3.2   Beat Signal Processing

The beat signal from the PD passes first a 50 MHz low-pass filter, where all the beat components other than those with the nearest comb mode are rejected. After amplification, 1% of the signal was depicted on a spectrum analyzer, in order to optimize the beat signal. The main beat signal passes a band-pass filter of 30 MHz, thus, the beat frequency (f_{beat}) was stabilized at 30 MHz distance from the nearest comb mode. In principle, this beat frequency could be directly phase locked to a reference oscilator, however, in most cases the stabilization loop does not provide the required bandwidth. Therefore, the following scheme, shown in Fig. 5.6, was used. At first, the optical beat frequency was divided by factor of 2048 (2^{11}) or 4096 (2^{12}) in a frequency divider. The division factor depends on the bandwidth of the servo system. The frequency divider takes the sinusoidal signal as an input and generates a TTL signal, which was in our case divided by 2^x at the output (x depends on the application as discussed below). This output signal is compared to the
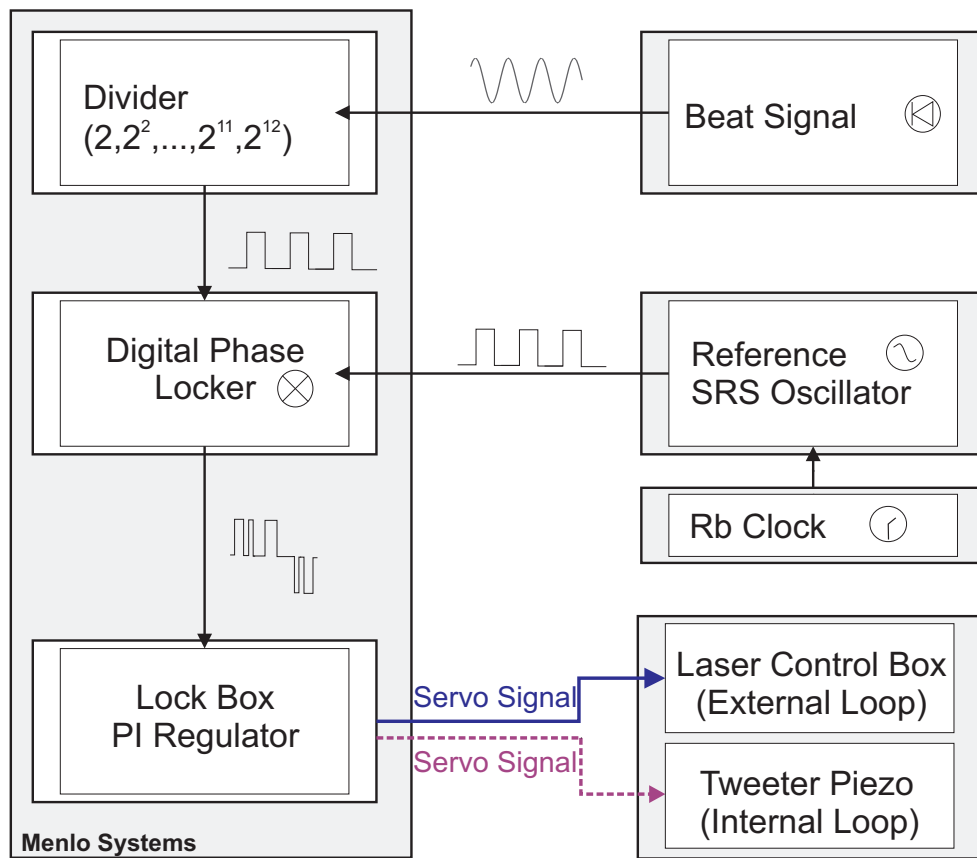
Figure 5.6. General stabilization loop for locking a single mode laser to the frequency comb.

TTL signals generated by a signal oscillator (Standford Research System SRS, locked to 10 MHz signal of a rubidium clock) in a digital phase-locked detector. The digital phase-locker permits a larger phase error than an analog detector and can therefore operate at a substantially lower locking bandwidth. Compact digital phase-locker (Menlo Systems) provided an analog output signal proportional to the phase difference between the oscillator (SRS) and the beat signal. Figure 5.6 illustrates a phase-locker output signal for two different input signals from the beat signal and the oscillator. The basic element of the phase-locker is a counter, where the beat signal counts up and the oscillator counts down. The output signal (error signal) is then processed in a proportional-integral (PI) controller and the output is amplified according to the servo-elements requirements (piezo, galvo) of the laser that is to be stabilized. The next section gives more details about the feedback loop realization for the Ti:Sa laser.

5.3.3 Feedback Control for the Laser Stabilization

Two possibilities were tested for a feedback loop of the Ti:Sa laser in order to control the laser frequency. In the first case the laser was locked to its external cavity (Fabry-Perot-Interferometer, external FPI) mounted on the Ti:Sa lasers side and the frequency comb was used to control the relatively slow thermal and pressure drifts of the cavity. This, the so called **external stabilization loop**, depicted as a solid blue line in Fig. 5.7, was finally used for the measurements of the lithium and beryllium isotopes. The second possibility, an **internal stabilization loop**, was realized by locking the laser directly to the frequency comb without using the external cavity. In this case, the servo signal was amplified by a high voltage amplifier and applied to the tweeter piezo of the Ti:Sa as depicted in Fig. 5.7 with dashed magenta lines.

When the external stabilization loop was used, the laser control box was operating in lock position and the laser was locked to the external cavity. As described shortly in section 4.1, the photodiode B, shown in Fig. 5.7, detects the laser light that is transmitted through the cavity (FPI interferometer). Using a differential amplifier, the signal is combined with the negative signal from the photodiode A, where the attenuated light intensity is monitored. Light intensities are adjusted in such a way that the signal from the photodiode A is half the peak voltage of the cavity transmission. When two signals are combined, a zero crossing at half the height of the cavity fringes occurs. This is largely independent of the output power of the laser. The generated correction signal is split into a high and low frequency part and applied to the tweeter piezo and the galvo-drive of the Brewster plate, respectively. The frequency response of the tweeter piezo is limited by the mass of the moving system consisting of the mirror and the piezo element and
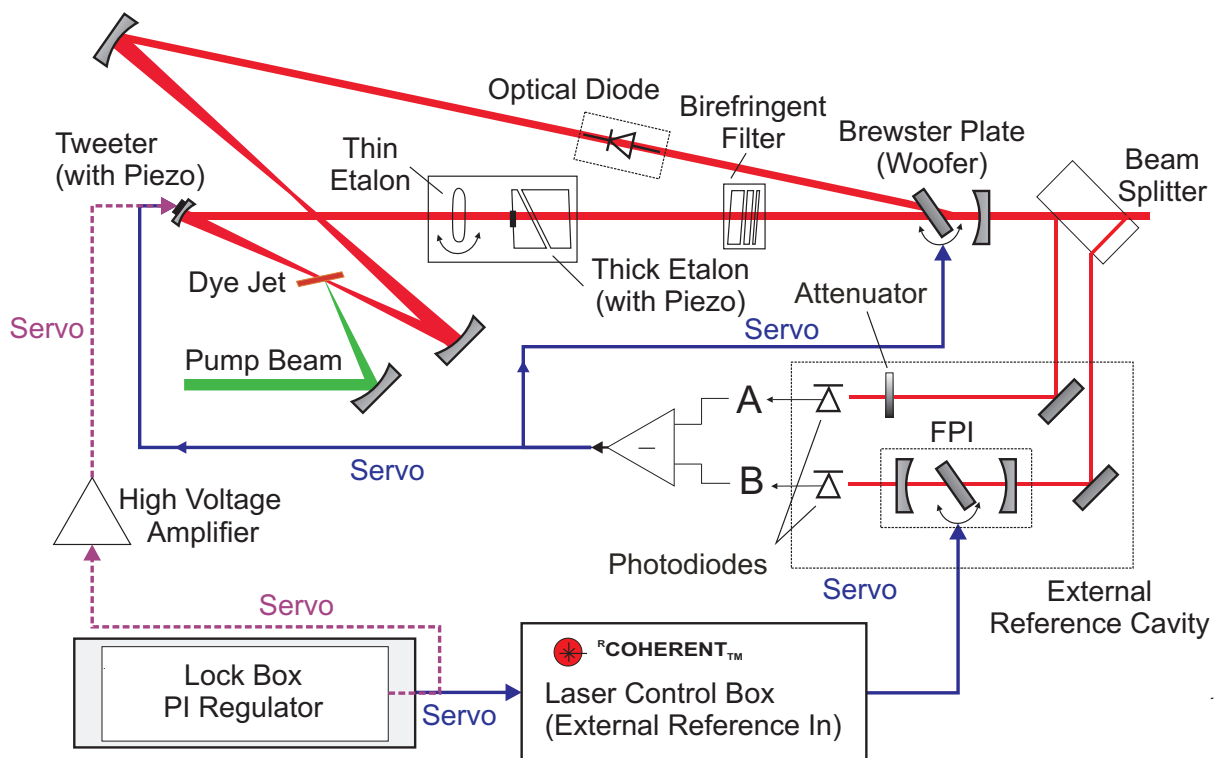
Figure 5.7. Two possibilities for stabilization of the Ti:Sa to the frequency comb: In the first one (**external stabilization loop**) the laser was stabilized to the external reference cavity and the correction signal from the comb lock served as a reference signal for the galvo drive in the FPI external cavity (depicted in solid blue lines). The second possibility for locking was the so-called **internal stabilization loop**, where the correction signal from PI regulator was applied directly to the piezo element on the tweeter mirror (depicted in dashed magenta lines).

the resonance frequencies of this system. The lowest resonance frequency of such piezo elements are typically on the order of 6 kHz and the dynamical range of the piezo has been measured to amount to about 1 GHz scanning range. A filter is installed in the feedback loop to suppress the eigefrequencies of the piezo-element and a to achieve a fast frequency response with sufficiently low phase shift. The angle of the Brewster plate (woofer) can be adjusted with the galvo-drive, where the applied signal changes the effective resonator length. The woofer has a frequency response of 400 Hz and a correction range in the order of 15 GHz. The combined operation of these two elements reduces the short-term laser linewidth down to about 1 MHz as desired for the application in this work.

External Stabilization Loop: In this case, the stabilization to the frequency comb was realized by applying the servo signal generated by the PI controller to the 'external scan' input of the laser control box. This signal is sent to the galvo-drive which rotates a Brewster plate inside the external cavity. Since the laser is locked to this cavity, the rotation of the Brewster plate causes a change of the effective length of the cavity and the laser frequency is changed accordingly until the right frequency is obtained. The amplification of the servo signal inside the control box as well as the dynamical range of the correction is set with the 'scan width' switch. This switch adjusts the slope in MHz/V and reacts on the 0-10 V input signal from the 'external scan'. We usually operated at the scan width of 800 MHz, at higher values the locking was not working anymore. The total gain in the feedback circuit was then probably too high and reduced the phase reserve below the critical value so that oscillation started. Since the bandwidth of the external scan loop is limited by the frequency response of the galvo-drive (woofer) up to 100 Hz, the frequency divider of the 30 MHz beat signal was set to 2048 or 4096. The SRS frequency was set to $30 \div 2048 = 14\,648.44$ Hz or $30 \div 4096 = 7\,324.22$ Hz, accordingly.

Internal Stabilization Loop: The second possibility for the Ti:Sa laser stabilization was also realized. Here, all corrections were applied internally, directly to the tweeter piezo and not to the control box as it was in the 'external stabilization' case. The laser was running without locking to the external FPI. However, the laser control box was still in use, since it keeps the length of a thick etalon optimized. The operational settings of the control box were 'free run' and 'manual scan'. The thick etalon, in the intracavity assembly (ICA) - two prisms mounted on the piezo-element - was steadily adjusted for maximum transmission. To keep the etalon in the maximum transmission, the distance of the two prisms was wiggled by a small amount with a 2 kHz sine wave applied to the piezo-element. These rapid changes cause amplitude fluctuations in the output light at

a frequency of 2 kHz, which are detected by the reference photodiode A in the reference cavity. Lock-in detection at 2 kHz is used to check whether the thick etalon is in the transmission maximum of the other intracavity elements and correct the length otherwise.

Stabilization to the frequency comb was realized by applying a high-voltage correction signal directly to the tweeter piezo of the Ti:Sa laser to change the resonator length and adjust the laser frequency. The stabilization loop, i.e. beat signal detection and servo signal generation, was almost identical with the one shown in Fig. 5.6 for the 'external' loop. But now all corrections were amplified to high voltage (0-500 V) and applied to the tweeter piezo with its frequency response up to 10 kHz and a correction range about 1 GHz. Due to the much faster response of the tweeter, compared to the galvo-drive in the 'external' case, the produced beat signal was divided only by a factor of 2 or 4 and the SRS frequency generator operated at 15 or 7.5 MHz, respectively. The servo signal generated by the PI controller was amplified by an high voltage amplifier (HV amplifier, 0-215 V) and applied to the tweeter piezo. Since the bandwidth of the feedback loop is much higher than in previous case, a better lock and a narrower linewidth are expected. Detailed test and results of the two locking schemes are presented in the next section.

5.3.4   Ti:Sa Laser Stability

After finding appropriate locking points, the locking parameters were optimized in order to observe reliable and stable locking conditions. For comparison, the produced beat signal and thus, the stability of the Ti:Sa laser, were analyzed in two different ways: The beat signal between the laser and a frequency comb mode was recorded for a few seconds with a fast spectrum analyzer (Hewlett Packard, Model HP 8592L, range 9 kHz-22 GHz) in order to determine the laser linewidth introduced by short-term frequency fluctuations. Furthermore, the long-term locking stability was measured and recorded with the frequency comb software for 10-30 minutes, where the beat signal was integrated for one second and the averaged beat frequency was plotted against time in one second steps. Comparison of the linewidths obtained from the spectrum analyzer and the evolutions of the beat frequency for 'external' and 'internal' stabilization is shown in Fig. 5.8. The spectra of the laser linewidths were averaged over 50 sweeps at the time base of 5 s and fitted with Lorentzian profiles. The evolutions of the beat frequency averaged over one second were recorded for about 10 minutes (600 s) and are fitted linearly. The FWHM of the Lorentzian fit is 500 kHz for the 'external' and 150 kHz for the 'internal' lock. The larger linewidth of the external lock was expected since the bandwidth of the feedback loop is considerably smaller and frequency fluctuations are therefore not corrected as quickly as it is in the case with the internal lock. The linewidth of 500 kHz is probably
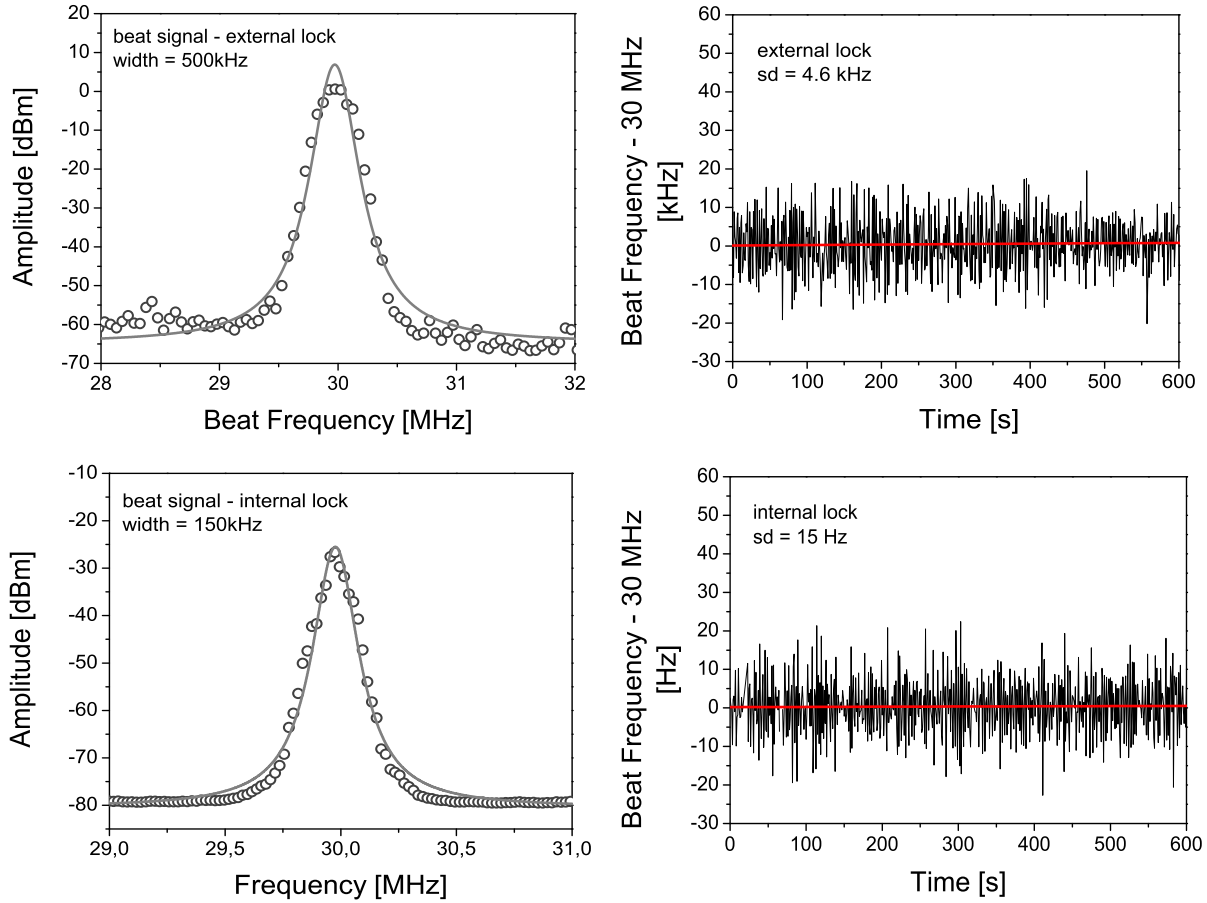
Figure 5.8. Comparison of the Ti:Sa laser stabilization for external (upper row) and internal locking (lower row). On the left side are shown the spectra of the beat signal of the Ti:Sa laser and the frequency comb mode, taken with a fast spectrum analyzer. Both are fitted with Lorentzian profile. In the right column the evolution of the beat signal with time is plotted for integration time of 1 second. Here, the solid line is a linear constant fit to the data.

limited by the locking of the Ti:Sa laser frequency to the external FPI. It compares well to the specification of 0.5-1 MHz short-term stability reported by the manufacturer for the Coherent 899. In comparison, the linewidth is reduced by about a factor of 3 when using the internal locking scheme and shows a more pronounced Lorentzian behavior. The evolutions of the beat frequency, depicted in the right column, exhibits for both cases an average frequency that is distributed around a nominal locking point of 30 MHz. Here, the superior behavior of the internal locking scheme is even more pronounced then in the linewidth. From a linear fit of the data a standard deviation of 4.6 kHz was observed for the external locking scheme, while for the internal lock it is reduced by almost three orders of magnitude to only 15 Hz.

A small deviation from the nominal locking point of 30 MHz was observed in some
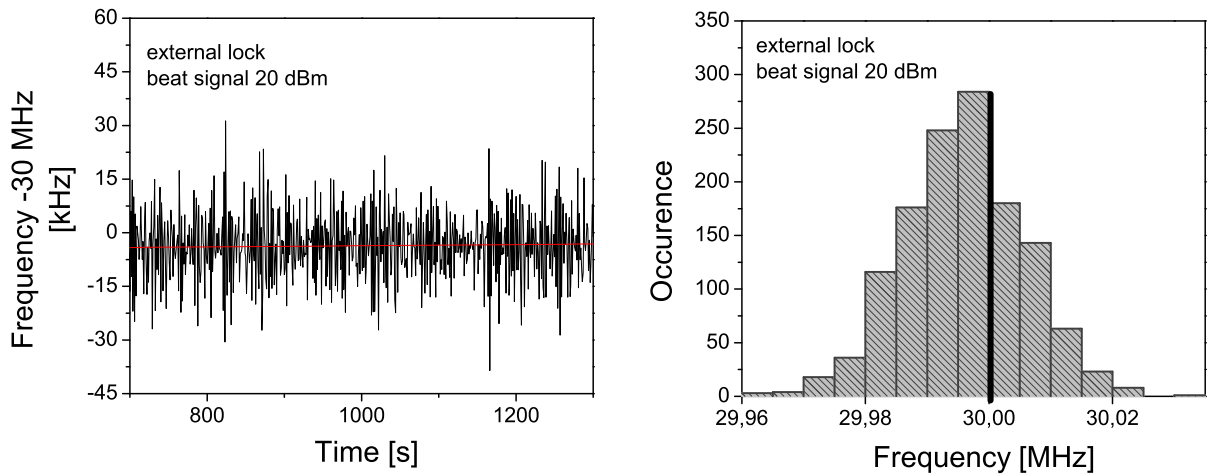
Figure 5.9. Evolution of the beat frequency (left) and beat frequency histogram (right) of the Ti:Sa while stabilized to the frequency comb when the S/N ratio of the beat was below 25 dB. The beat signal was averaged for 1 s. The beat frequencies are not symmetrically distributed around the locking point of 30 MHz.

measurements. According to Menlo Systems, this is an indication that the signal-to-noise (S/N) ratio of the generated beat signal is too small to be correctly processed electronically. In order to investigate this, the distribution of the measured beat frequencies for external locking was determined. Figure 5.9 shows the results: The measured beat frequencies are not symmetrically distributed around the locking point of 30 MHz. A histogram for the corresponding beat frequencies is shown in the right part of Fig. 5.9. The observed distribution exhibits a shift to lower frequencies, a larger number of occurrences is at lower frequencies. The hight of the beat signal in these measurements was about 20 dBm. When the beat height was even smaller or decreasing during the measurement, the beat frequencies tended to decrease with time and the linear fit acquired a slightly decreasing slope. A symmetric distribution of the beat frequencies around the locking point at 30 MHz was achieved with beat signal heights of 25 dBm and higher. Usually, the low laser power of the frequency comb mode and the alignment of the frequency comb output and the Ti:Sa laser were crucial to obtain a sufficiently large S/N ratio for the beat signal.

In spite of the narrower linewidth achievable with the 'internal' lock, for all measurements described in this thesis 'external' locking was used, because the galvo-drive can handle up to 15 times larger correction ranges compared to the tweeter piezo and was more reliable in long-term operation. This point is crucial, particular for online applications.

5.3.5   Scanning Procedure

To allow for the frequency tuning of the Ti:Sa laser in order to scan across the hyperfine structure of the different lithium isotopes, the SRS frequency generator for the frequency comb repetition rate was varied. Changing the SRS frequency between 19 and 21 MHz resulted in a repetition rate variation of 0.2 MHz (99.9 to 100.1 MHz). Consequently, the Ti:Sa laser frequency was tuned with the repetition rate. For ^{7}Li, for example, a change of the repetition rate of 0.1 Hz corresponded to a change of 410 kHz in the Ti:Sa laser frequency and 820 kHz in the $2S \rightarrow 3S$ two-photon transition frequency accordingly. Maximum required scanning range was less than 4 GHz at most. As the dye laser frequency was stabilized to the Ti:Sa laser frequency, the tuning of the Ti:Sa frequency changed simultaneously the dye laser frequency. Hence, the frequency of the dye laser was tuned away from the resonance frequency in the $2p_{3/2} - 3d_{5/2}$ transition. As mentioned before, due to the enhancement cavity this transition was considerably broadened to about 10 GHz with a flat top region of 2 GHz, and therefore the exact dye laser frequency was not critical for the lineshape.

5.4   Experimental Results

Offline measurements for stable lithium isotopes were accomplished at the GSI facility in Darmstadt in summer 2007. Two different atom sources were used for lithium production. In total about 150 scans were obtained in one week. The experimental results are described and discussed in the following sections.

5.4.1   Lithium Spectra in the $2S \rightarrow 3S$ Transition

Once the Ti:Sa laser was stabilized to one of the frequency comb modes at 30 MHz beat offset, the repetition rate ν_{rep} was changed in steps of 0.1 Hz, corresponding to a laser frequency of 410 kHz and the laser was slowly (1 step/second) scanned across the complete hyperfine structure.

A spectrum recorded for ^{7}Li in the $2S \rightarrow 3S$ transition over a frequency region of about 3 GHz is shown in Fig. 5.10. Here, the graphite crucible was used as atomic beam source. The hyperfine peaks, discussed in section 2.4, are labeled according to the inset. Selection rules in an $2s_{1/2} \rightarrow 3s_{1/2}$ two-photon transition allow only $\Delta F=0$ with a non-vanishing transition probability. Hence only two spatially well resolved spectral lines were observed. The overall fit that is shown as a solid line consists of a sum of a narrow Voigt profile for the dominant Doppler-free component and two Doppler-broadened Gaussian pedestals. The pedestals originate from Doppler broadened excitation with two photons from the
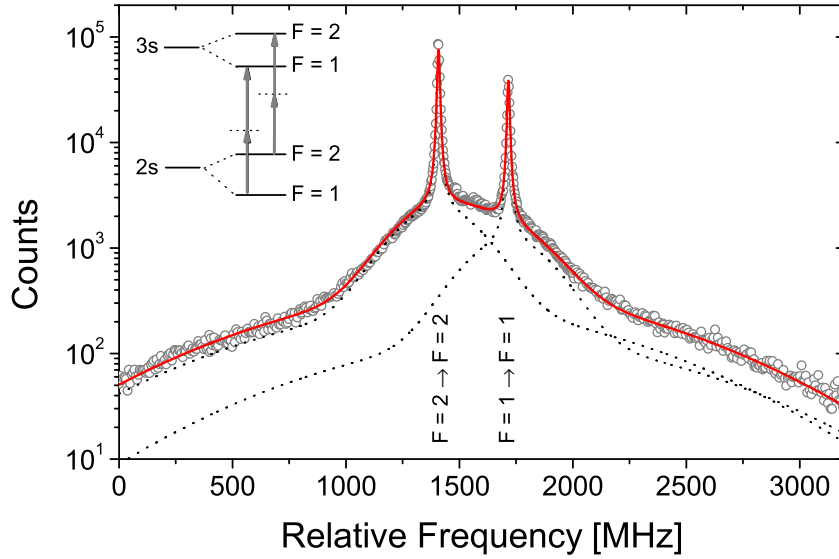
Figure 5.10. Spectrum for ^{7}Li in the $2S \rightarrow 3S$ transition. The start frequency corresponds to the frequency comb mode of 407 807 570 MHz. Light gray dots indicate the experimental data, the line is the overall fit to the experimental data. Dotted lines are the contributions from the individual peaks. Selection rules in s - s transitions allow only ΔF=0, hence only two lines were observed.

same direction in the atomic beam (FWHM = 800 MHz) and from the background gas (FWHM = 1.6 GHz). In previous offline experiments [Bus03], similar lineshapes were observed. Due to a better collimation, the width of the narrower Gaussian was by a factor of two smaller. In our setup, the atomic beam source was much closer to the entrance hole of the ionization region. Furthermore, the background pressure in the ionization region was larger since the oven was not in a separate and directly pumped chamber. This explains the stronger amplitude of the broad Gaussian. The model function fits the spectrum well, with a reduced χ^2 of 1.18. The narrow Doppler-free peaks are fitted with a Voigt profile with a Lorentzian width contribution of about 10.6 MHz and a Gaussian width of 4.3 MHz. The lifetime of the $3S$ level is 29.8 ns, corresponding to a natural linewidth of 5.3 MHz [God01, Fro98]. The increased Lorentzian width observed in our measurements is mainly attributed to the power broadening in agreement with the previous observation [Ewa04, San06]. The Gaussian component is about $2\times$ larger than expected from the linewidth of the Ti:Sa laser (1.2 MHz). This might be caused by problems of the fitting procedure to clearly separate the small Gaussian component. Skip-step scans, as shown in Fig. 5.11, were introduced to obtain better resolution for a center determination of two peaks. In the region of ±15 MHz around the center of each peak the scans were performed in smaller steps of 0.8 MHz. The region between the peaks was scanned much faster without data acquisition. Two spectra for ^{7}Li are recorded
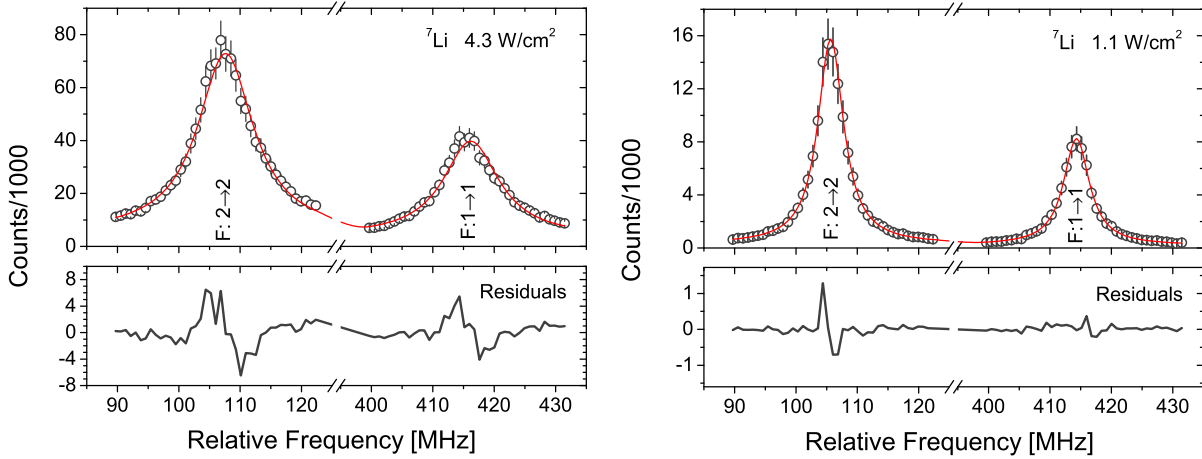
Figure 5.11. Skip-step scans for ^{7}Li recorded with two different Ti:Sa laser intensities. Fits (red solid line) consist of two Gaussian profiles for Doppler-broadened contribution and a Voigt profile for Doppler-free contribution as discussed in the text. Below the resonances corresponding residuals are shown, which indicate a slight asymmetry in the resonances. The frequency axis is given relative to the comb frequency of 407 808 870 MHz.

with two different laser intensities. The fit consists of two Gaussian backgrounds for the Doppler-broadened contributions and the Voigt profile for the Doppler-free contribution as discussed before. For the Gaussian parts, the widths and relative ratios were kept constant with the values obtained from the overall scan of the $2S \rightarrow 3S$ two-photon transition in Fig. 5.10. There is a slight asymmetry observed when the experimental data is fitted with the theoretical lineshape. Below the resonances in Fig. 5.11 the residuals between the fit and the experimental data points are shown, where the existing asymmetry is clearly visible. The occurrence of the asymmetry was studied in more detail, it was attributed to a spatially dependent ac-Stark shift and will be discussed in the following paragraph with line profile modeling.

Absolute Transition Frequency Determination The hyperfine peak centers ($\nu_{F=2\rightarrow F=2}$, $\nu_{F=1\rightarrow F=1}$) were set as free parameters in the peak fitting and the center of gravity (CG) of the transition was calculated from the peak positions according to

$$\nu_{CG} = \frac{5}{8}\nu_{F=2\rightarrow F=2} + \frac{3}{8}\nu_{F=1\rightarrow F=1}, \tag{5.1}$$

taking into account the line strengths in the transition.

The absolute frequency of the Ti:Sa laser at the CG was calculated according to 4.7 where m, the integer number of the closest comb mode, was obtained by determining the laser wavelength with a calibrated wavemeter (ATOS, Fitzeau Interferometer, $\Delta\nu_w$=100 MHz). The carrier envelope offset f_0 was stabilized to 20 MHz but since the fun-

damental light from the frequency comb at 1560 nm was subsequently frequency-doubled, $f_0 = \pm 40$ MHz has to be used in equation 4.7. The sign was determined depending on the lock point of the CEO offset. The beat signal frequency was stabilized at 30 MHz, when the Ti:Sa laser was locked to the frequency comb. The sign in front of f_{beat} was determined experimentally, when the laser was not stabilized to the frequency comb. By changing the repetition frequency to higher or to lower frequencies and watching a move of the beat signal on the spectrum analyzer one can determine whether the Ti:Sa laser frequency is above (+) or below (-) the comb mode frequency.

5.4.2   AC-Stark Shift

Skip-step spectra were recorded at different laser intensities and the transition frequencies are observed to be shifted in the presence of the strong laser fields. This is assigned to the so-called ac-Stark shift [Coh92]. Obtained transition frequencies at different laser intensities were plotted as a function of the Ti:Sa laser power measured behind the 'two-color' cavity, as shown in Fig. 5.12. The transition frequency shows a clear linear dependence on the Ti:Sa power and the final transition frequency is then taken as the extrapolated value of the linear fit to zero laser power. Along these measurements the dye laser intensity was kept constant. To determine the ac-Stark shift from both lasers, all measurements with
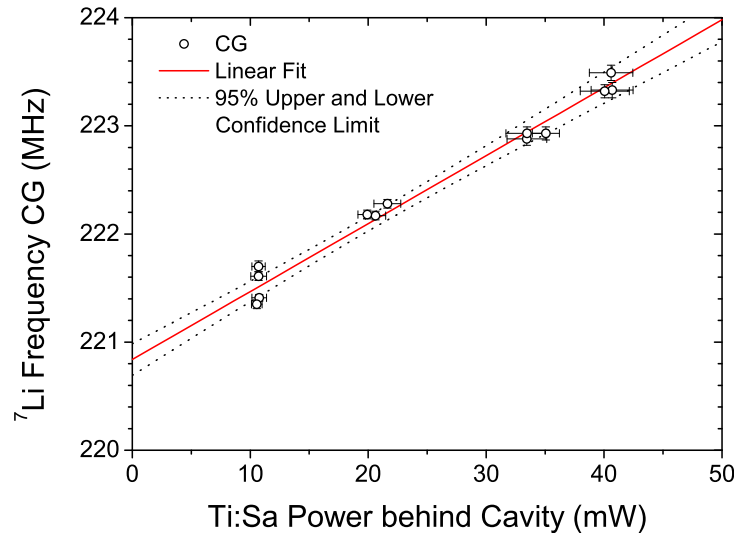
Figure 5.12. Ac-Stark shift of the ^{7}Li two-photon transition center of gravity as a function of the Ti:Sa laser power measured behind the 'two-color' cavity. The ^{7}Li frequency is relative to the comb frequency given in the caption of Fig.5.11. Experimental data points are fitted with a linear function. The value for the unperturbed transition frequency is extracted by the extrapolation of the linear fit to the zero laser power which is 220.84(7) MHz.
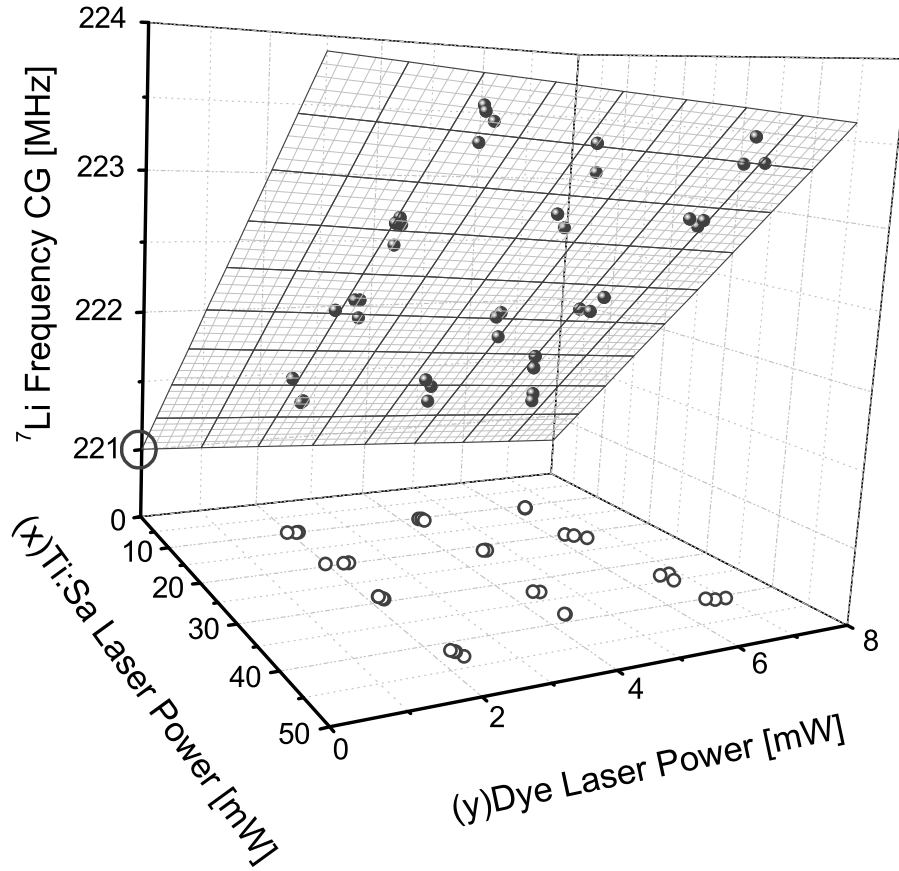
Figure 5.13. Three-dimensional view of the ac-Stark shift. Filled points are the experimental data and the open circles are the projection of these points to the x-y plane. The shaded plane is the two-dimensional fit of the experimental data. The small circle on the frequency axis indicates the frequency unperturbed by the laser fields which was obtained by extrapolation of the plane fit to zero laser powers which has a value of 220.93(5) MHz.

varying dye and Ti:Sa laser powers were plotted three-dimensionally, as depicted in Fig. 5.13.

The obtained experimental data points were fitted with a plane function. A value for the ^{7}Li CG which is unperturbed by the Ti:Sa laser and the dye laser field was obtained from an extrapolation of the plane to zero laser powers, i.e. it is the crossing point of the plane with the z-axis as shown in Fig. 5.13. Typically, 50 measurements were used for frequency extrapolation at the zero dye and Ti:Sa laser powers. Reduced χ^2 were ranging between 1 and 5 and the uncertainties were scaled with the square root of χ^2_{red}. About 150 spectra were recorded for ^{7}Li with two different atom sources as described in section 5.1. These spectra were combined into three groups and the extrapolated frequency values at zero laser powers did not show any systematic effects between both sources as can be seen in Fig. 5.14. The weighted average resulted in a transition frequency of
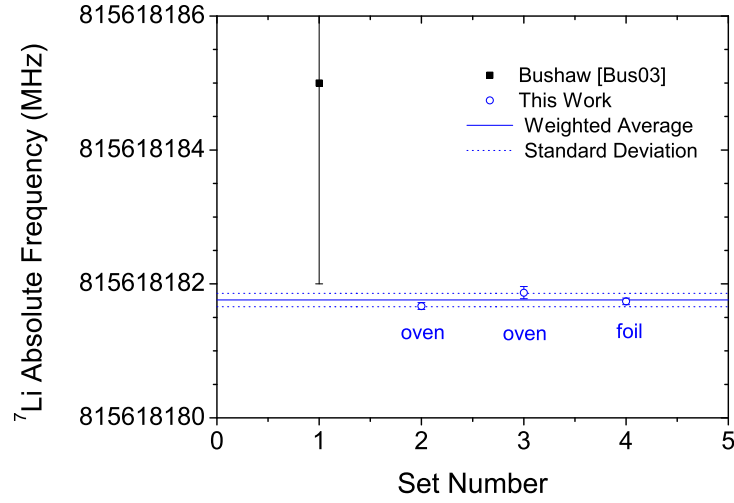
Figure 5.14. Absolute transition frequencies obtained for ^{7}Li. 150 spectra were combined into three groups and the resulting absolute transition frequency is the weighted average of those values.

815 618 181.735(71) MHz for ^{7}Li are shown in the same figure. Measurements on ^{6}Li were also performed with both atom sources. About 90 spectra were obtained and these were combined into two groups. Due to the low ^{6}Li abundance present in the samples, the fitting of the resonances was less precise and resulted in a ^{6}Li transition frequency of 815 606 727.882(180) MHz. The isotope shift between absolute frequencies of ^{6}Li and ^{7}Li is $\Delta\nu_{IS} = 11\ 453.85(19)$ MHz. The value is less precise but in very good agreement with the 11 453.984(20) MHz obtained from relative measurements [San06].

Line Profile Modeling As shown schematically in Fig. 5.15, the atomic beam was first collimated by a 4.5 mm aperture at the entrance of the ionization region. Afterwards it passed through the laser beam. The cavity was designed to have a soft focus in the center of the resonator. The laser beam cross section had a Gaussian distribution with a diameter of about 400 μm (FW 1/e). Under this geometry, atoms traversing through the center of the laser beam experience higher intensities as the ones flying through the wings, consequently the first ones will experience higher ionization efficiency and will have the largest ac-Stark shift. Atoms traversing through the wing of the laser beam experience smaller laser intensity but are in resonance at lower frequencies since the ac-Stark shift caused by the Ti:Sa laser light increases the resonance frequency. The effect is not symmetric since the signal of the atoms traversing through the wings of the laser beam appears in the lower frequency part of the resonance curve and the corresponding intensity in the higher frequency part is missing. To study the influence of
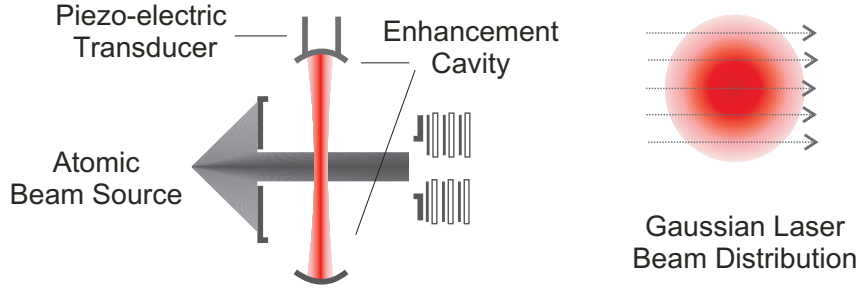
Figure 5.15. Draft shows schematically the ionization region of the quadrupole mass spectrometer. The atomic beam is first collimated by a 4.5 mm millimeter aperture. Afterwards it passes perpendicular through the laser beam which has a gaussian distribution as illustrated in the right sub figure.

the different ionization efficiency and the spatial ac-Stark on the line center frequencies a rate equation model was used. A scheme of the excitation is shown in Fig. 5.16.

Figure 5.16. Excitation ladder used in the model.

The two-photon transition rate as a function of laser intensity can be written as

$$W_{12} = \frac{I^2}{I_s^2} \frac{A_{23}^2}{4} \frac{A_{23}}{4\delta\omega^2 + A_{23}^2/4}, \qquad (5.2)$$

where $I_s = 167$ W/mm^{-2} is the saturation intensity that has been determined experimentally from the dependence of the linewidth on the laser intensity. $A_{23} = 1/\tau_{3s} = 33$ MHz and on-resonance transition rate $W_{12}(\delta\omega = 0) = (I^2/I_s^2)A_{23}$. The rate equation for excitation and ionization can be written as

$$\dot{N}_1 = W_{12}(N_2 - N_1) + A_{31}N_3, \qquad (5.3)$$
$$\dot{N}_2 = W_{12}(N_1 - N_2) - A_{23}N_2, \qquad (5.4)$$
$$\dot{N}_3 = A_{23}N_2 - A_{31}N_3 - \sigma_{Ion}\Phi N_3, \qquad (5.5)$$

with a transition rate $A_{31} = 1/\tau_{2p} = 37$ MHz and photon flux $\Phi = I_{Laser}/h\nu$. N_1, N_2 and N_3 are the populations of the 2S, 3S and 2P levels and σ_{Ion} is an ionization cross section. The impact of the laser ionization on the population can be expressed as

$$\dot{N}_{Ion} = -\dot{N}_{tot} = \sigma_{Ion}\Phi N_3, \qquad (5.6)$$

where N_{tot} is the total number of neutral atoms $(N_1 + N_2 + N_3)$. The numerical integration of these differential equations was performed using a Runge-Kutta algorithm. For more
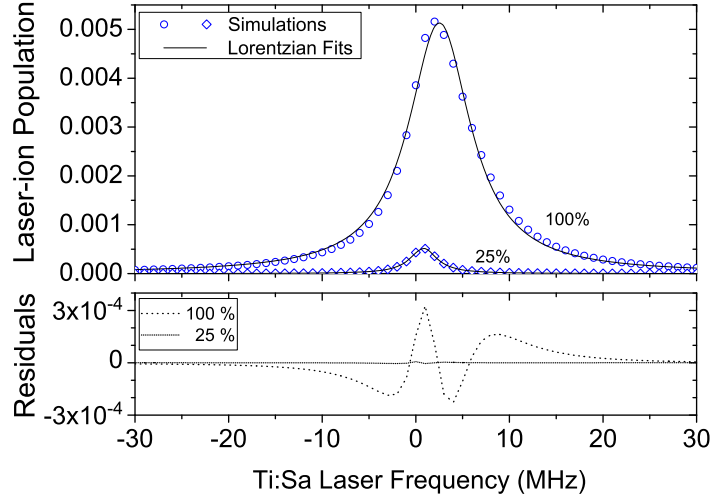
Figure 5.17. Line profile simulation for 'low-power' (25%, equivalent to 110 Wmm^{-2}) and high-power (100%, equivalent to 430Wmm^{-2}) [San09].

details about the laser- and ion-beam geometry and the parameters used in the model, it is referred to a recently published article [San09] about absolute transition measurements in ^{6,7}Li[1].

The ac-Stark shift was included artificially into the model, in this case the detuning of the laser frequency $\delta\omega = 2\pi\delta\nu$ given in equation 5.2 was replaced by

$$\delta\nu = \Delta\nu_{\text{Laser}} - a_{\text{ac-Stark}}I(x, y, t), \tag{5.7}$$

and the value of the linear $a_{\text{ac-Stark}}$ coefficient was adjusted to obtain the experimentally obtained ac-Stark shift from linear fit.

Fast intensity fluctuations on a timescale of few μs from the 'two-color' cavity length changes were also considered. The contribution to the line profile was studied by assuming a sinusoidal behavior for the intensity with the variation of 70% and a frequency of 30 kHz.

The residuals from line profile simulation for different laser powers (110 W/mm^2; 430 W/mm^2), shown in Fig. 5.17, demonstrate a similar behavior than the experimental data. Different laser field distributions - rectangular, Gaussian, Gaussian plus intensity fluctuations - were simulated at different laser intensities and the lineshapes were fitted with a Lorentzian function. The peak centers obtained from the fit were plotted as a function of the assumed laser power. The results for a Gaussian laser field distribution with intensity fluctuations is shown in Fig. 5.18. The four data points of highest power, which are in the region that was accessible for the experiment, were fitted linearly and extrapolated to the zero laser power. As can be also seen in Fig. 5.18 a systematic shift of

---

[1]The article is attached at the end of the thesis (section 5, pg. 11-15).
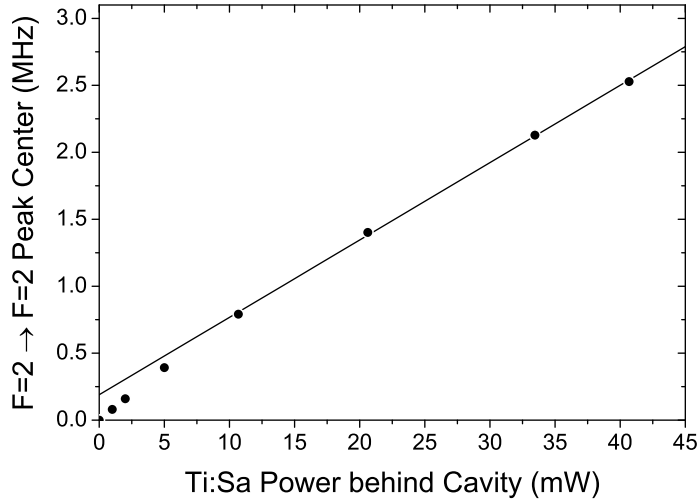
Figure 5.18. Simulated data obtained from a Gaussian laser field distribution involving the intensity fluctuations. The solid line is a linear fit ($y = 0.167 + 0.061x$) to the data between 10 mW$\leq P_{Ti:Sa} \leq$ 45 mW for the laser power [San09].

170 kHz appears. This additional shift was included in the determination of the absolute transition frequency. More details about the spatial ac-Stark shift behavior and obtained results are given in the attached article [San09].

5.4.3   Systematic Uncertainties

A summary of statistical and systematic uncertainties for the final absolute transition frequencies in the $2S \rightarrow 3S$ transition of ^{6,7}Li is given in table 5.1. The table includes also the correction from to the non-linear behavior of the ac-Stark shift asymmetry, as discussed above. The statistical uncertainty of 71 kHz is the standard deviation of all transition frequencies. On the experimental side there are three systematic contributions. The largest systematic uncertainty is due to the frequency comb reference and it is estimated to be 143 kHz. It was calculated based on the relative accuracy of the Rubidium clock (Rb clock, FS 725 Standford Research Systems) that is specified to be better than $\pm 5 \times 10^{-11}$ when calibrated with a possible drift of $\leq 5 \times 10^{-10}$ per year. The last calibration was 0.701 years before the measurements which corresponds to a relative drift of 3.5×10^{-10}. To obtain the uncertainty of the laser frequency, this relative uncertainty was multiplied by the comb mode number (4 078 088) times the repetition rate ν_{rep}=100 MHz and results in a frequency comb uncertainty of $\Delta\nu_{\mathrm{Comb}}$=163 kHz. The ac-Stark shift contribution was estimated as described before, to be 65 kHz. The last systematic error, unresolved Zeeman splitting caused by stray magnetic fields, is estimated to be less than 30 kHz, calculations are performed in [San05]. The magnetic field induced by the current

Table 5.1. Summary of statistical and systematic uncertainties of the absolute transition frequencies in ^{6,7}Li. All values are in kHz.

	^{7}Li	^{6}Li
Statistical	71	180
Systematic		
Frequency comb	143	143
Ac-Stark shift	65	65
Zeeman effect	30	30
Subtotal	160	160
Total	175	241

through the graphite tube in the crucible atom source could induce a Zeeman splitting, but as mentioned before no difference between the two atomic sources was observed. The total uncertainty of 175 kHz for the $2S \rightarrow 3S$ transition frequency is the square root of the quadratic sum of the statistical and the systematic uncertainties.

5.4.4   Discussion and Conclusion

The new value obtained in this thesis is compared to the calculated and measured $2S \rightarrow 3S$ transition frequencies in stable ^{6,7}Li obtained in the last two decades in Table 5.2 and Fig. 5.19. So far, theory calculations and experiments do agree within the relative large uncertainty of the theoretical values. Presently the calculations of the absolute transition frequencies on lithium and helium have been performed up to QED terms of order $\alpha^3 Ry$. Calculation for higher order terms of α up to $\alpha^5 Ry$ are partially available [Puch08] but they are still not complete and they are the main remaining source of uncertainty for the theoretical energy values given in Table 5.2. Presently, two groups are working on the theoretical evaluation of the absolute transition for lithium and helium and we hope that accuracy comparable to the experiment will be reached in the future. However, this is a demanding task and will probably take several years before completed.

To summarize: Accurate absolute transition frequencies of the $2S \rightarrow 3S$ two-photon transition of stable lithium isotopes ^{6,7}Li with an accuracy of 2×10^{-10} were achieved using frequency-comb-based laser spectroscopy. The combination of a Doppler-free two-photon transition and the resonance ionization technique allowed high-resolution measurements. The obtained values agree with previous values from online and offline measurements but accuracy was improved by an order of magnitude. In comparison with the latest

Table 5.2. Experimental (e) and theoretical (th) values on the $2s\,^2S_{1/2}\,-\,3s\,^2S_{1/2}$ transition frequencies of ^{7}Li and ^{6}Li. The values obtained from this work contain the correction of -170 kHz from ac-Stark shift discussed in section 5.4.3 and in [San09].

Reference	Year	Energy (cm^{-1})			Frequency (MHz)		
^{7}Li							
Radziemski [Rad95](e)	1995	27 206.0952	±	0.0010	815 618 215	±	30
Yan & Drake [Yan02](th)	2002	27 206.0924	±	0.0039	815 618 131	±	117
Bushaw [Bus03](e)	2003	27 206.0942	±	0.0001	815 618 185	±	3
Yan & Drake [Yan03](th)	2003	27 206.0926	±	0.0009	815 618 137	±	27
This, I$_2$-line[Rei07](e)	2004	27 206.09404	±	0.00009	815 618 180.5	±	2.7
Yan [Yan08](th)	2008	27 206.0936	±	0.0008	815 618 166	±	16
Puchalski & Pachucki[Puch08](th)	2008	27 206.0937	±	0.0006	815 618 170	±	19
This work(e)	2009	27 206.094082	±	0.000006	815 618 181.57	±	0.18
^{6}Li							
Radziemski [Rad95](e)	1995	27 205.7129	±	0.0010	815 606 754	±	30
Yan & Drake [Yan02](th)	2002	27 205.7104	±	0.0039	815 606 678	±	117
Bushaw [Bus03](e)	2003	27 205.71214	±	0.00010	815 606 731	±	3
Yan & Drake [Yan03](th)	2003	27 205.7105	±	0.0009	815 606 683	±	27
This, I$_2$-line[Rei07](e)	2004	27 205.71198	±	0.00009	815 606 726.6	±	2.7
Yan [Yan08](th)	2008	27 205.7115	±	0.0008	815 606 712	±	16
Puchalski & Pachucki[Puch08](th)	2008	27 205.7117	±	0.0006	815 606 717	±	19
This work(e)	2009	27 205.712014	±	0.000008	815 606 727.71	±	0.24
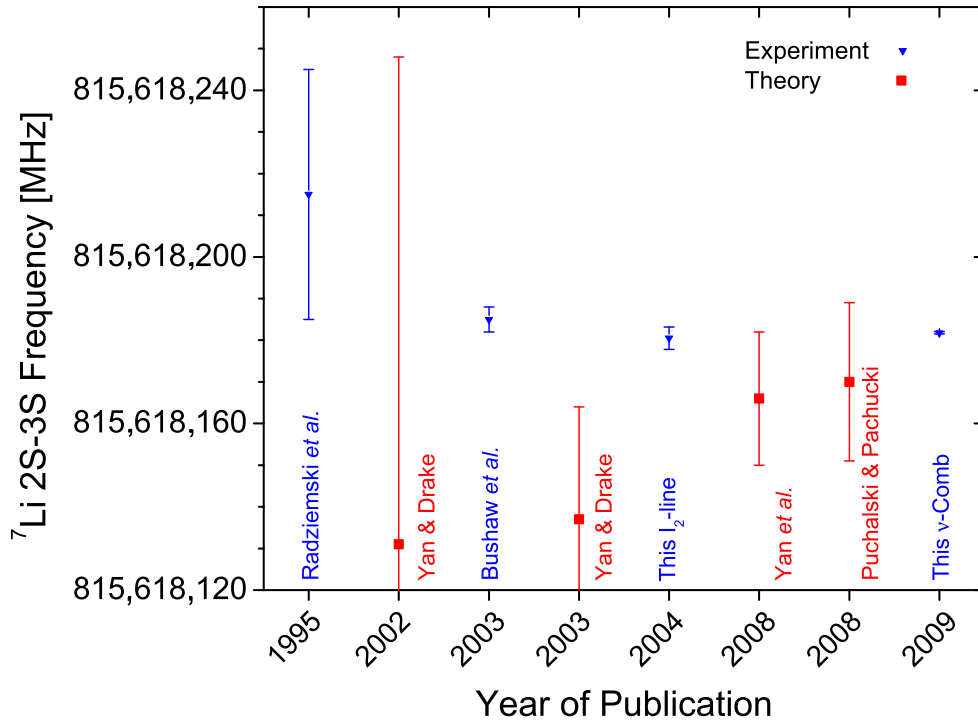
Figure 5.19. Theoretical and experimental transition frequency values of ^{7}Li in the $2s\,^2S_{1/2} - 3s\,^2S_{1/2}$ transition. References are listed in table 5.2.

theoretical values [Puch08] the difference between the theory and experiment is about 12 MHz but the values agree within their uncertainties since the calculations are about 100 times less accurate than the experiment. The determination of the nuclear charge radii for all lithium isotopes by purely optical means without dependence on a reference value from elastic electron scattering - as it was done for hydrogen [Ude97] - would be possible with theoretical calculations improved by two orders of magnitude.

Besides the transition reported here, further high accuracy measurements of the $2\,^3S_1 \rightarrow 2\,^3P_{0,1,2}$ transition in the two-electron system Li$^+$ as they have been already obtained at the test storage ring (TSR) at Heidelberg [Rei07b] and are under preparation at the MPQ in Garching in an ion trap would independently facilitate the absolute charge radius determination in a two-electron system, where the required accuracy might be reached easier than in the three-electron system of atomic lithium.

6 Frequency Comb Based Collinear Spectroscopy on Beryllium

6.1 Production and Preparation of Radioactive Beryllium Isotope Beams

The isotope shift measurements of beryllium isotopes were performed at the ISOLDE on-line isotope separator at CERN. A layout of the facility is depicted in Fig. 6.1. In total two beam-times were performed. The first one was during the off-line period, where the whole experimental set-up was tested with a beam of stable ^{9}Be and different settings were used to search for possible systematic errors. In the second beam-time the radioactive beryllium isotopes ^{7,10,11}Be were investigated. These radioactive species were produced
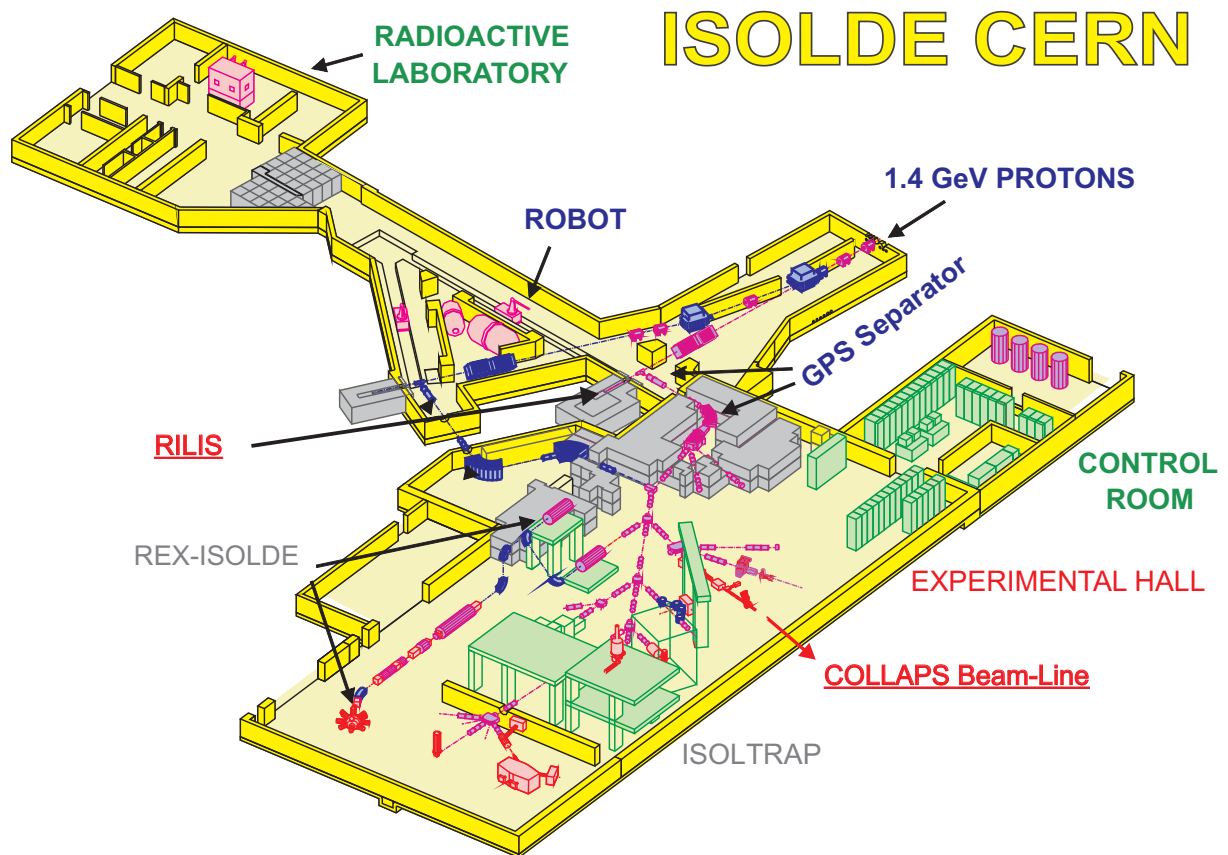
Figure 6.1. Layout of the ISOLDE facility at CERN.

Table 6.1. Production yields of beryllium isotopes at the ISOLDE facility provided by the resonance ionization laser ion source RILIS [Koe98]. The unit ions/μC can be roughly approximated to ions/s at these proton intensities.

RILIS	Half life	Yields, ions/μC
^{7}Be	53.12 d	1.4×10^{10}
^{10}Be	1.5×10^6 a	6×10^9
^{11}Be	13.8 s	7×10^6
^{12}Be	23.6 ms	1.5×10^3
^{14}Be	4.35 ms	4

by a fast proton beam coming from the proton synchrotron booster at 1.4 GeV impinging on a uranium-carbide target. The proton beam had a maximum intensity of 3×10^{13} protons per pulse. Impacting on a heavy target, different reactions like spallation, fission or fragmentation are induced. Produced atoms diffuse out of the target and effuse into the hot ionization tube where they were ionized, extracted and mass separated. The best option for ionization of beryllium isotopes is laser ionization, because the energy of 9.4 eV required for ionization is too high for surface ionization and plasma ionization is less efficient and delivers ions with a much larger uncertainty in the acceleration voltage. Moreover, the combination of laser ionization and mass separator is a very reliable way to obtain a beam of high chemical purity.

The resonance ionization laser ion source (RILIS) at ISOLDE employs for a selective excitation of atomic transitions a pulsed tunable laser radiation inside a hot cavity attached to the target [Fed08]. Beryllium atoms were ionized in a two-photon process as shown in Fig. 6.2. The first photon of 234.9 nm is used for resonant excitation to the $2s2p\,^1P_1$ state and the second photon of 297.3 nm for resonant photoionization through the $2p^2\,^1S_0$ autoionizing state. Two pulsed dye lasers, pumped with copper-vapor lasers, working at about 470 nm and 594 nm, were frequency-doubled to provide the resonant frequencies. Typical RILIS production rates of all beryllium isotopes are listed in table 6.1 [Koe98]. Mass separation was performed with the General Purpose Separator (GPS) with a mass resolution $m/\delta m = 2500$.

Efficient beam intensities required for collinear measurements
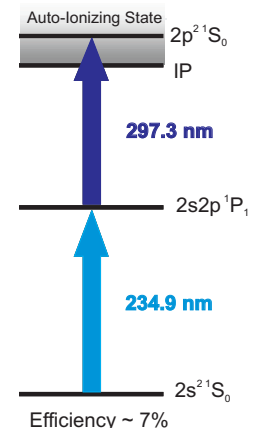
Figure 6.2. Scheme for laser ionization of beryllium atoms.
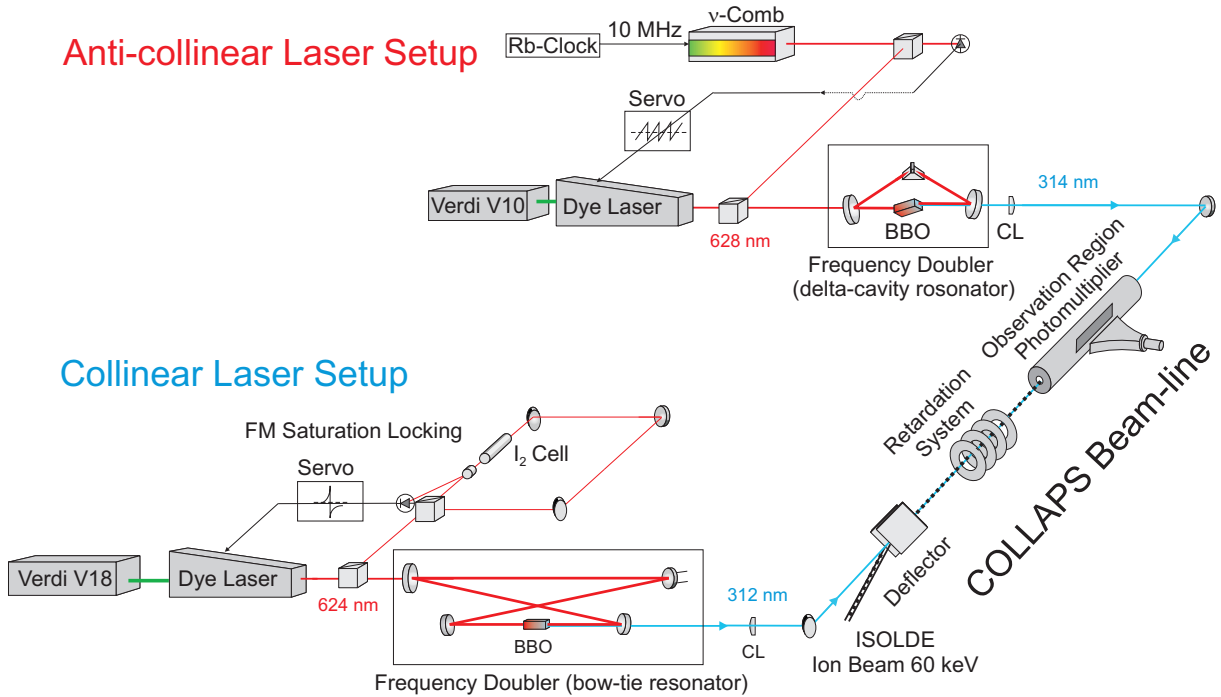
Figure 6.3. Experimental set-up for the beryllium measurements.

are about 10^5-10^7 ions/s, depending on the complexity of the
atomic spectrum and the background specifications. For systems with even numbers of
protons and neutrons, which do not exhibit hyperfine structure (e.g. ^{10}Be) lower beam
intensities of about 10^4 ions/s are sufficient, because the laser can interact with the same
ions in the interaction region several times.

6.2   Laser System

6.2.1   Overview

The whole laser set-up was built and tested in the department of Nuclear Chemistry,
University of Mainz and at GSI in Darmstadt, respectively. The schematic set-up of the
experiment is shown in Fig. 6.3. Two cw single-mode tunable ring dye lasers (Coher-
ent 699-21) were used to produce the fundamental frequency of 624 nm and 628 nm,
for collinear and anti-collinear laser beam, respectively. Both lasers were pumped with
frequency doubled Nd:YVO$_4$ lasers (VERDI V10, V18) with up to 10 W laser power at
532 nm. The dye solution was Sulfo-Rhodamin B disolved in ethylen-glycol (1.5 g/l)
running in the system at 7 bars. Maximum output power from the dye lasers was up to
600 mW. Two commercial frequency doublers were used for the second harmonic genera-
tion to produce 312 nm and 314 nm, respectively. The first one, a bow-type configuration

(Tekhnoscan FD-SF-07), was used to double the light from the collinear dye laser. The anti-collinear laser beam was doubled in a delta-cavity resonator (WaveTrain by Spectra Physics). All lasers and the complete stabilization system were operated in the laser laboratory located above the ISOLDE experimental hall. The light from the dye lasers was then transported from the laser laboratory to the ISOLDE hall via 20 meters long optical fibers and coupled to the frequency doublers. To avoid non-linear effects due to the relative high laser powers, like e.g. induced Brioullin scattering, a so-called photonic crystal fiber, which provides a large mode area (LMA) and hence lower intensities in the fiber, was used (LMA-20 by Crystal fibers). The fiber transmission was up to 60 percent. After the frequency doubling, we achieved up to 20 mW output of UV light (7% doubling efficiency), but for spectroscopy 5 mW were used at maximum in order to avoid saturation effects. The light after the frequency doublers was shaped with standard lenses and collimated beams with diameters of about 2-3 mm were obtained. Co- and counter propagating beams were carefully aligned and superimposed over a distance of about 5-6 m along the complete collinear beam-line. The angle between the two beams is thus expected to be smaller than 0.04 mrad. Galvo-driven mirrors are inserted in the laser beam path behind the frequency doubler which can be used to deflect the beam out of the beam-line. To achieve the sufficient frequency stability, the dye laser propagating in the collinear direction was stabilized to the iodine line with a saturation spectroscopy, while the anti-collinear laser was stabilized to the frequency comb (Menlo Systems FC1500). A photo which shows a part of the laser system is shown in Fig. 6.4.

6.2.2   Frequency Stabilization of the Anti-collinear Dye Laser

A detailed scheme of the laser set-up with the anti-collinear laser stabilized to the commercial frequency comb is shown in Fig. 6.5. The stabilization loop used to stabilize the dye laser was described in detail in section 5.3. To demonstrate the long-term dye laser stability reached with this locking scheme, the evolution of the laser frequency with and without external lock to the comb is shown in Fig. 6.6. One should note that the two curves are displayed with strongly different scaling factors in the y-axis. The beat signal was in both cases averaged over one second. The frequency stability with additional locking to the frequency comb is improved by three orders of magnitude.

6.2.3   Frequency Stabilization of the Collinear Dye Laser

A detailed experimental set-up of the collinear laser beam stabilized to an iodine line is shown schematically in Fig. 6.7. The Doppler-free frequency modulation saturation spectroscopy was used to stabilize the dye laser to the iodine line. The simplified setup of
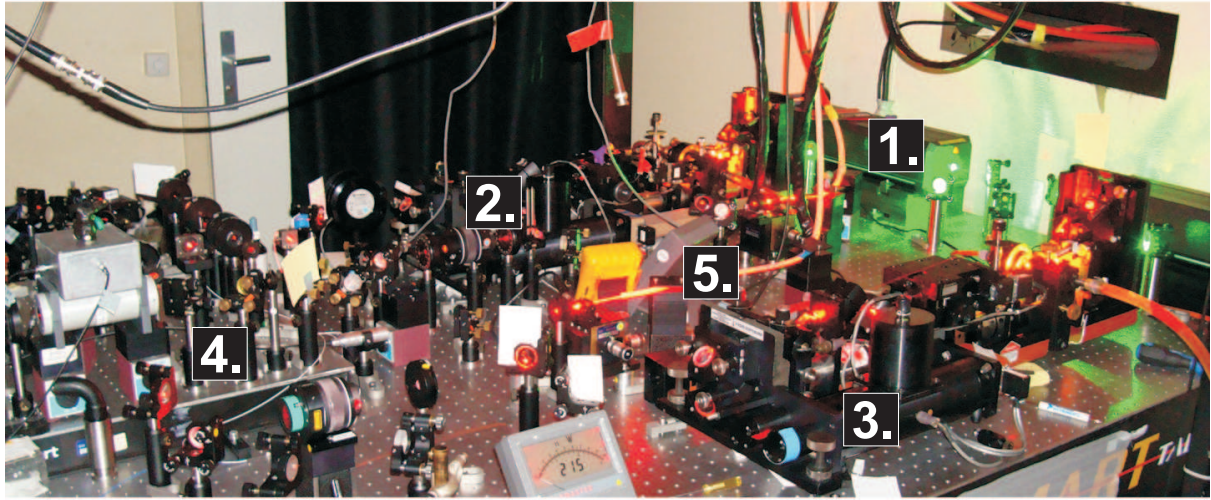
1. Pump laser Verdi V18
2. Ring dye laser (collinear)
3. Ring dye laser (anti-collinear)
4. Part of the FM saturation iodine lock
5. LMA photonic crystal fiber

Figure 6.4. Photo of the lasers and optics that was used in the beryllium experiment.

the stabilization is depicted in Fig. 6.8. The single-frequency dye laser beam is divided to the probe beam and more intensive pump beam (30/70) with orthogonal polarization axes. The pump beam passes the acousto-optic modulator (AOM), where its frequency is shifted and amplitude modulated. The less intensive probe beam propagating in the opposite direction is frequency modulated with an electro-optical modulator (EOM) and two side-bands with the same amplitudes but opposite phases are generated. Hence, the probe beam does not exhibit any amplitude modulation if detected on a photodiode. Pump and probe beams are superimposed in the iodine cell. The pump beam saturates the transition for the velocity class which is at resonance. If one of the side bands of the probe laser addresses the same velocity class it is less attenuated than the second side band since the atoms are already saturated by the pump beam. Thus, the beat signal between the second side band and the carrier is not compensated any more and an amplitude modulation signal is observed. The beat signals are demodulated and the correction signal is guided to the dye laser. This is only a simplified description and more details of the setup can be found in [Kri09].

During the measurements at ISOLDE, 12 suitable iodine lines were used to stabilize the collinear laser using this technique. The frequencies of the selected iodine lines were thoroughly measured with the frequency comb and are listed in table 6.2. Employed transitions are mainly R branch lines with an even angular momentum J in the ground-state because they have a hyperfine structure exhibiting 15 components with the a_1 compo-
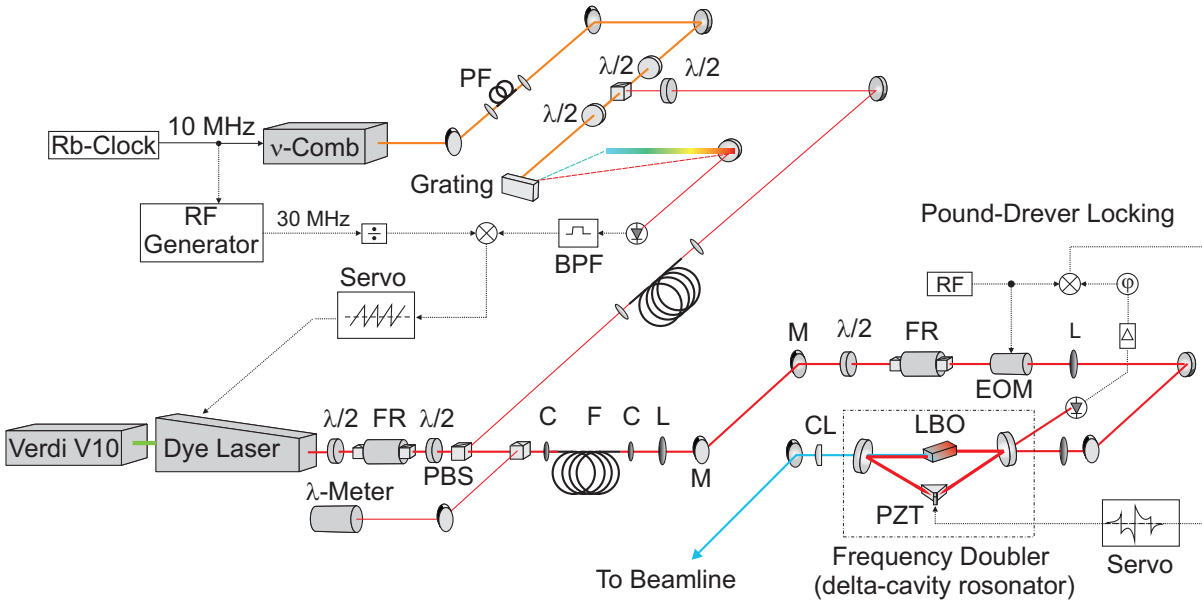
Figure 6.5. Detailed setup of the anti-collinear laser system: A beam from the dye laser at 628 nm is splitted with a polarization beam-splitter (PBS) and a small part ($\approx$2 mW) is coupled to an optical fiber and overlapped with the frequency comb laser for frequency stabilization. The use of the fiber was advantageous because when the dye laser was tuned and the beam path changed the alignment after the fiber was sustained. The frequency comb received the external stabilization signal from the Rb clock and the dye laser was stabilized to the comb with a frequency offset-locking described in detail in section 5.3. Part of the main beam is coupled to a wavemeter (λ-Meter) and the rest, typically 400 mW is coupled into an optical fiber (F) with 50% transmission. 20 meters long fiber transported the laser beam to the ISOLDE hall where a frequency doubler with delta-cavity resonator was placed. The resonator is locked to the dye laser frequency using the Pound-Drever-Hall locking scheme. FR stands for Faraday rotator to eliminate a back reflection and PF is a short fiber to control an intensity distribution.

nent being well separated at the beginning of the spectrum. This facilitates easy, reliable and reproducible locking during the beamtime. A short-term linewidth slightly below 1 MHz was typically obtained for both stabilized dye lasers. An evolution of the dye laser frequency while locking to the iodine transition is shown in Fig. 6.9

6.3   Set-up of the Beam-line

The experimental set-up of the collinear beam-line is shown schematically in Fig. 6.10.

After the laser ionization, extraction and mass separation, the ions are guided as a well collimated beam to the Collinear Laser Spectroscopy (COLLAPS) experiment. Here, the ions are first deflected into the beam-line with a 10° electrostatic deflector and superimposed with the laser beams. Alignment of the ion beam through the COLLAPS experimental beam-line was facilitated with two Faraday cups, one placed directly after
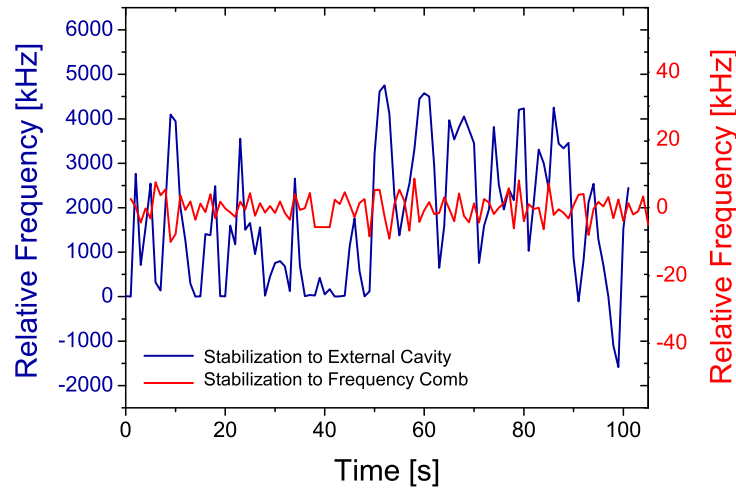
Figure 6.6. Evolution of the dye laser frequency with the laser stabilized to the external reference cavity (blue) and with an additional locking to the frequency comb (red). The frequency fluctuations are suppressed with the comb lock by three orders of magnitude.
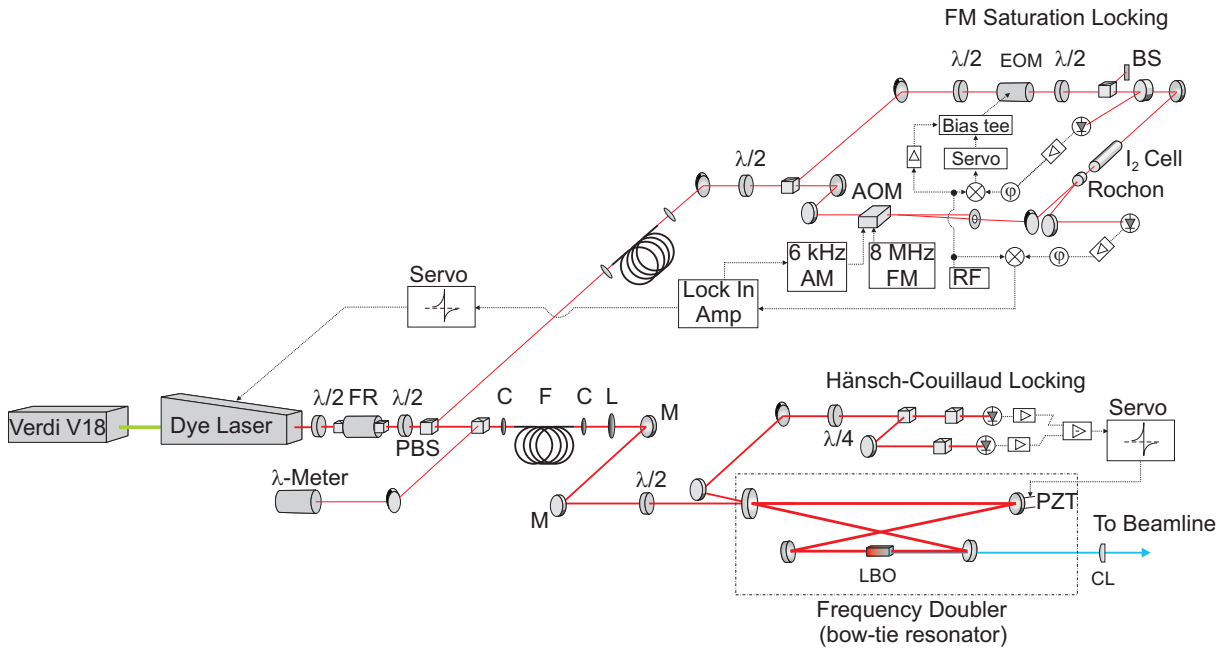
Figure 6.7. Detailed setup of the collinear laser system: A laser beam at 624 nm was divided with a polarization beam-splitter and small part ($\approx$15 mW) was coupled via an optical fiber to the FM saturation spectroscopy setup, described in the text. The part of the main beam was guided to a wavemeter (λ-Meter) and the rest coupled to a long optical fiber (20 m) and transported to the ISOLDE hall. The output from the fiber was frequency doubled in a bow-tie resonator with BBO crystal and guided to the beam-line. The resonator was locked to the dye laser frequency using the Hänsch-Couillaud locking scheme.
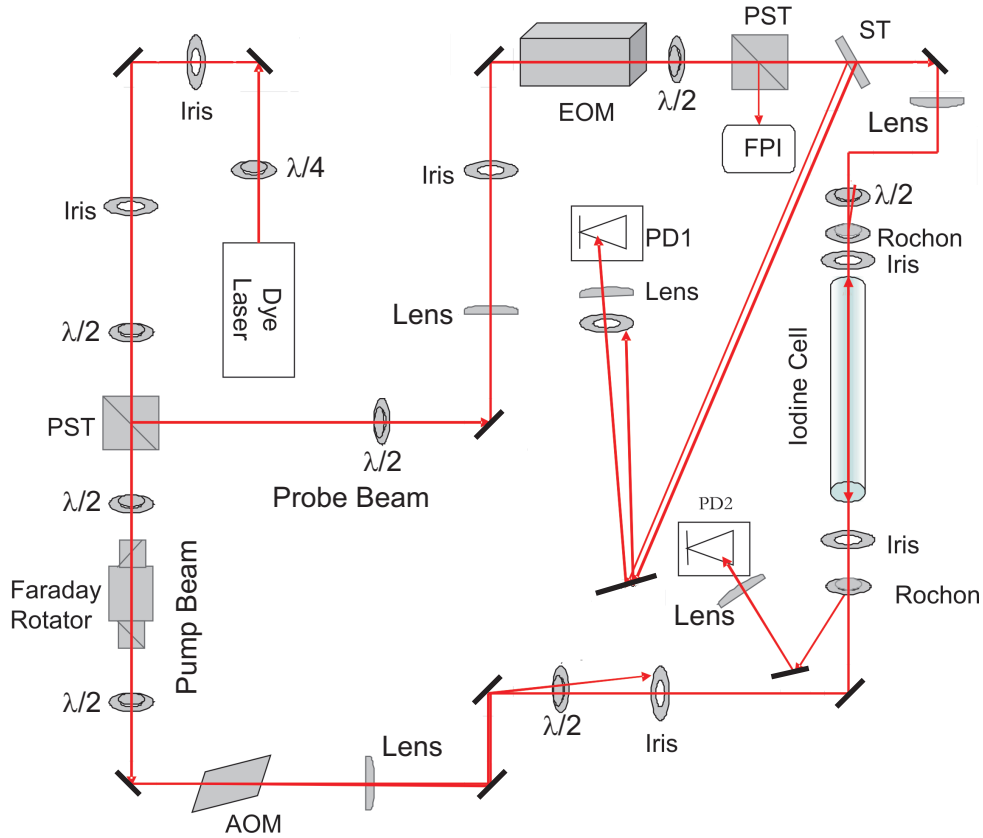
Figure 6.8. Simplified setup for Doppler-free frequency modulation saturation spectroscopy, where the collinear dye laser was stabilized to an iodine transition. The laser beam from the dye laser is divided to two parts with a polarization beam splitter (PST). A pump beam (70%) is passing through the acousto-optical modulator (AOM), where its frequency is shifted. A less intensive probe beam (30%) is frequency modulated in electro-optical modulator (EOM), where side-bands are generated. Both beams are superimposed in the iodine cell. More details about the modulation spectroscopy used in this experiment can be found in [Kri09].

the mass separator and the second one at the end of the beam-line. The transversal profile of the ion-beam could not be measured directly. Beam collimation was achieved by optimizing the transmittance through the beam-line with two electrostatic quadrupole lenses. The beam-line was kept in vacuum of about 10^{-6} mbar to avoid collisions of the ions with residual gas atoms. The linearly polarized laser beams were entering and leaving the beam-line through quartz windows cut at the Brewster angle to avoid reflections and scattering into the beam-line. Several adjustable irises and apertures with sizes down to 5 mm in diameter were mounted along the beam-line to have a control over the beam propagation direction and to ensure that the ion beam and the laser beams are properly aligned through the 5-6 meter long experimental beam-line. The power of both laser beams were measured before entering and after leaving the beam-line and the trans-

Table 6.2. List of the iodine lines used in the experiment. The frequencies of the iodine lines were determined with the frequency comb. The standard deviation of each iodine line, remeasured several times, is ≈ 550 kHz. The last column shows the observed deviations between the experimental values and literature values [Kri09], which are reported with an accuracy on the order of a few 10 MHz.

No.	HFS	Frequency, MHz	Deviation, MHz
1	R(62)(8-3)a_1	479 804 354.9	-0.27
2	R(70)(10-4)a_1	479 823 072.3	0.44
3	P(64)(10-4)a_1	479 835 708.7	0.66
4	R(60)(8-3)a_1	479 870 012.0	-0.08
5	R(58)(8-3)a_1	479 933 416.0	-0.01
6	R(54)(8-3)a_1	480 053 468.8	0.13
7	R(52)(8-3)a_1	480 110 119.4	0.60
8	R(50)(8-3)a_1	480 266 578.4	0.49
9	R(48)(8-3)a_1	480 314 236.6	0.60
10	R(42)(8-3)a_1	480 359 648.9	0.55
11	R(40)(8-3)a_1	480 402 815.6	0.68
12	R(36)(8-3)a_1	480 482 416.3	0.47
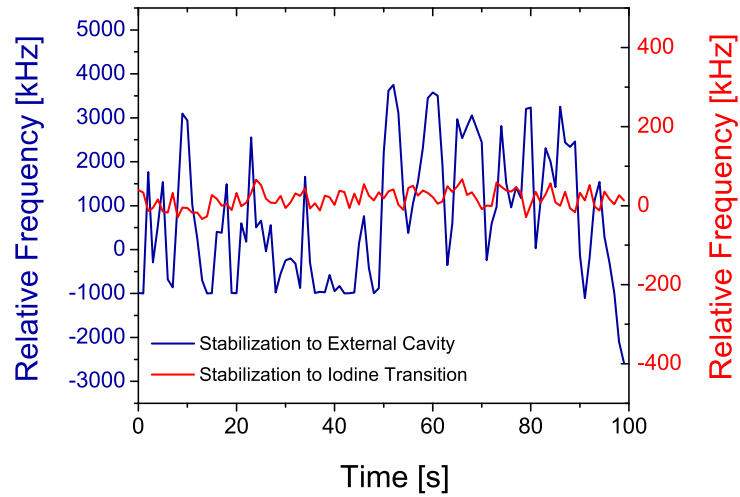
Figure 6.9. Evolution of the dye laser frequency with the laser stabilized to the external reference cavity (blue) and with an additional locking to the iodine transition (red). The frequency fluctuations are suppressed by almost two orders of magnitude when locking to the iodine line. It should be noted that the reference data for the simple external cavity lock is the same as that shown in Fig. 6.6.

mission was optimized while minimizing background on the photomultiplier tubes. Two photomultiplier tubes (CPMT, Hamamatsu) are mounted at the optical detection region. In order to increase the solid angle for fluorescence detection, a cylindrical, silver-coated surface (mirror) is located opposite to the PMT, and a 1:1 image of the beam is created by two 3-inch lenses, each in front of the uv sensitive PMT's. Lenses and photomultipliers are separated from the vacuum chamber by a quartz window. The detection region is 20 cm long and an external voltage can be applied to it to ensure that the ion beam interacts with the laser beam only in this region, where the resonance fluorescence is detected. Previous resonant interaction with the laser beam would lead to optical pumping into dark states for odd beryllium isotopes and repeatedly velocity-changing light scattering in case of even isotopes. Both would strongly affect sensitivity and accuracy of the collinear technique, respectively. Hence, Doppler-tuning is performed by changing the potential of the detection region. A voltage divider is used to apply fixed ratios of the detection-region potential to retardation lenses in front of the detection region. Doppler-tuning is facilitated by a constant high voltage supply (Fluke, 410 B, up to ± 10 kV) that can again be floated with a voltage provided by a Kepco amplifier (Model BOP 500M, ± 500 V) which is in turn controlled by a computer-based digital-to-analog converter (DAC, 18 bit, ± 10 V). The Kepco amplification factor is approximately 50 and is accurately measured repeatedly during the beamtime. The results of high voltage measurements are read out with a data acquisition system.
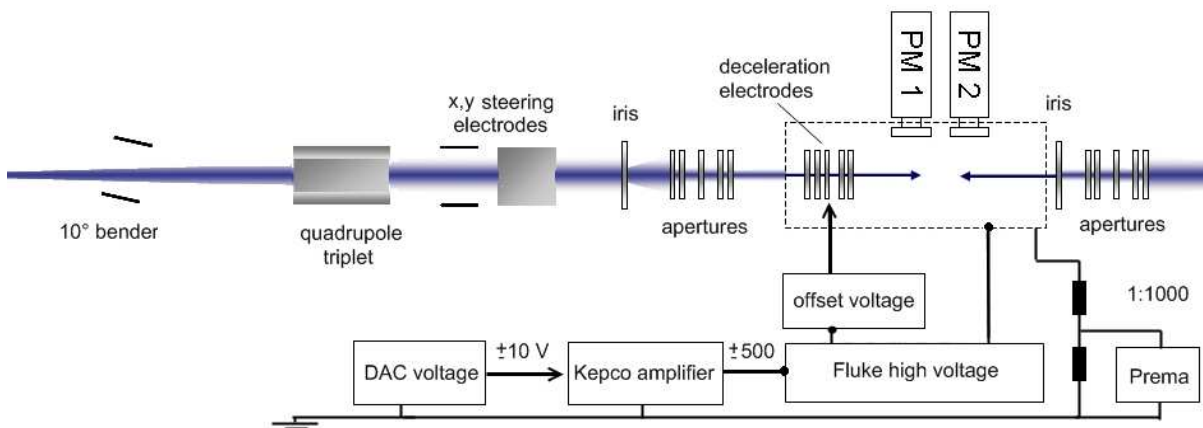
Figure 6.10. COLLAPS beam-line scheme taken from [Tie09]. The ion beam enters the beam-line via electrostatic deflector and passes the quadrupole triplet for beam focusing. Set of irises and apertures are mounted along the beam-line to ensure the proper overlap of the ion and laser beams. Behind the optical region, a Faraday cup can be inserted to detect the ion current with the sensitivity down to 10^{-12}A. A fluorescence signal is detected with two photomultipliers.
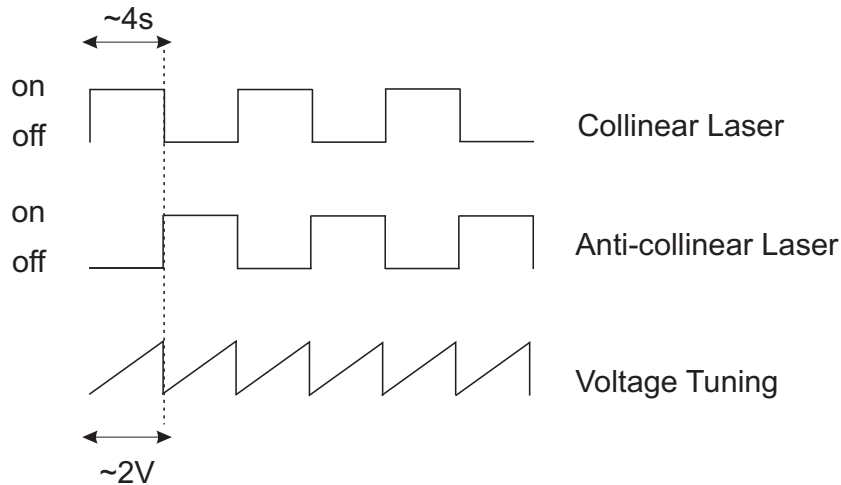
Figure 6.11. Sequence of scanning gates for collinear and anti-collinear laser. When the collinear scan was in progress the anti-collinear laser was blocked. After the scan was completed, the lasers were quickly switched and the anti-collinear scan within the same scanning range was accomplished.

6.4 Scanning Procedure

The measurements were performed as follows: The collinear laser was locked to a particular iodine line and superimposed with the ion beam. The Doppler tuning and the scanning range were adjusted in such a way, that the scan covers the complete hyperfine structure of the transition under investigation. Then, the frequency of the anti-collinear laser was locked to the frequency comb accordingly at such a frequency, that the hyperfine structure was covered for this laser as well in the same scanning region. Once the scan from the collinear laser was completed, the galvo-driven mirror was used to block the beam while the anti-collinear laser was opened. The sequence of the scanning gates and the scanning voltage is shown in Fig. 6.11. For the tuning voltage, dwell times of 20 ms per step were used with a scanning range of 400 to 800 channels depending on the isotope. A single spectrum was obtained by integrating over typically 50 scans (2-3 minutes) for ^{7,10}Be and 400 scans (20 minutes) for ^{11}Be. This quasi-simultaneous recording of collinear and anti-collinear spectra averages over short-term fluctuations of the acceleration voltage (ripple).

6.5 Experimental Results

We performed two beam-times for beryllium isotope shift measurements at ISOLDE. The first, an offline beam-time in May 2008, was as a trial run with the stable isotope ^{9}Be,
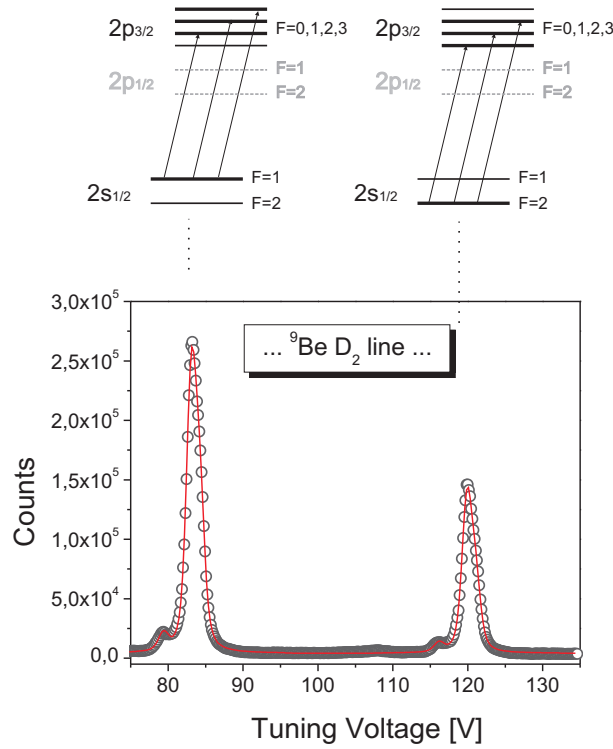
Figure 6.12. A typical spectrum of ^{9}Be obtained from the anti-collinear spectroscopy in the $2s_{1/2} \to 2p_{3/2}$ transition. Only two peaks from the $2s_{1/2}$ state are resolved. The red solid line is a theoretical Voigt fit with common linewidth for both peaks. The small side peaks are discussed in the text.

where several tests for systematic errors were performed. The later run was online (June 2008), with stable and radioactive beryllium isotopes up to one neutron halo isotope ^{11}Be.

6.5.1   Stable Beryllium Isotope ^{9}Be

During the offline measurements, stable beryllium atoms were evaporated directly from a heated tube loaded with beryllium. The tube was attached to the ion source and the beryllium atoms were resonantly ionized with the RILIS ion source as described in the section 6.1.

The complete experimental set-up was tested and different settings were applied in order to investigate possible systematics in the D_1 and D_2 line measurements. A typical spectrum obtained for ^{9}Be in the $2s_{1/2} \to 2p_{3/2}$ transition is shown in Fig. 6.12, where the fluorescence intensity is plotted against the Doppler-tuning voltage at the detection region. The DAC voltage used at the x-axis is afterwards about 50 times amplified by a Kepko calibration factor as discussed above. A fine and a hyperfine structure of the investigated beryllium isotopes are shown in section 2.4, the hyperfine splitting in the $2p_{3/2}$ level is not resolved.

Spectra of the D_1 line recorded for collinear and anti-collinear geometry at 60 kV acceleration voltage are shown in Fig. 6.13. The complete hyperfine structure in D_1 line is nicely resolved and collinear and anti-collinear spectra are 'mirror images' if plotted against the DAC voltage.

In all spectra, weak side peaks were observed on the left and right side of each peak. While those at the left (lower tuning voltage) are readily observed at 60 keV acceleration voltage, those appearing at the right side (higher tuning voltage) are more pronounced in spectra taken with 30 kV acceleration voltage as depicted in Fig. 6.14. Such spectra at 30 keV were analyzed only to determine the properties of these side-peaks, i.e., the distance from the main peak.

The side peaks at the left side are well understood and arise from inelastic collision of the beryllium ion with the residual gas. The ions are slowed down by energy of about 4 eV which corresponds to the energy required for excitation of the beryllium ion. The observed side peaks appear always at a fixed distance of 3.9 V from the main peak. The right peak is not completely understood yet. It is situated at the distance of about 2 eV from the main peak. Both peaks are included in the overall fit and the position and the intensity ratio between the main peak and the side peaks were kept equal for all peaks in a fit.

Systematic Uncertainties   At the offline test beam-time, 88 spectra of stable ^{9}Be in the D_1 line and a few also in D_2 line were collected and evaluated. Absolute transition frequency for ^{9}Be from all spectra was determined to be $\nu_0^9 = 957\,199\,552.3^{+1}_{-1.2}$ MHz for the D_1 line and $\nu_0^9 = 957\,396\,616.8^{+1.3}_{-1.5}$ MHz for the D_2 line, respectively. The asymmetric uncertainty is explained below. The transition frequencies from previous measurements $957\,199.65(11)$ GHz (D_1) and $957\,396.82(14)$ GHz (D_2) [Bol85] are less accurate by two orders of magnitude. The values from D_1 line differ by 100 MHz but agree within their uncertainties, whereas the difference of 185 MHz in the D_2 line is more significant.

In table 6.3 the contribution of statistical and systematic uncertainties to the absolute transition frequencies are listed. The statistical contribution is a standard deviation from all evaluated spectra. Several tests of the experimental set-up were performed in the offline run in order to study possible systematics.

During the measurements, 12 suitable iodine lines, listed in table 6.2, were used to stabilize the laser for collinear spectroscopy. All selected iodine lines were thoroughly measured with the frequency comb. For all lines we found excellent agreement with the frequencies predicted by the iodine program IodineSpec (Toptica Photonics). Differences of less than 1 MHz were observed in all but one case, which is well below the quoted
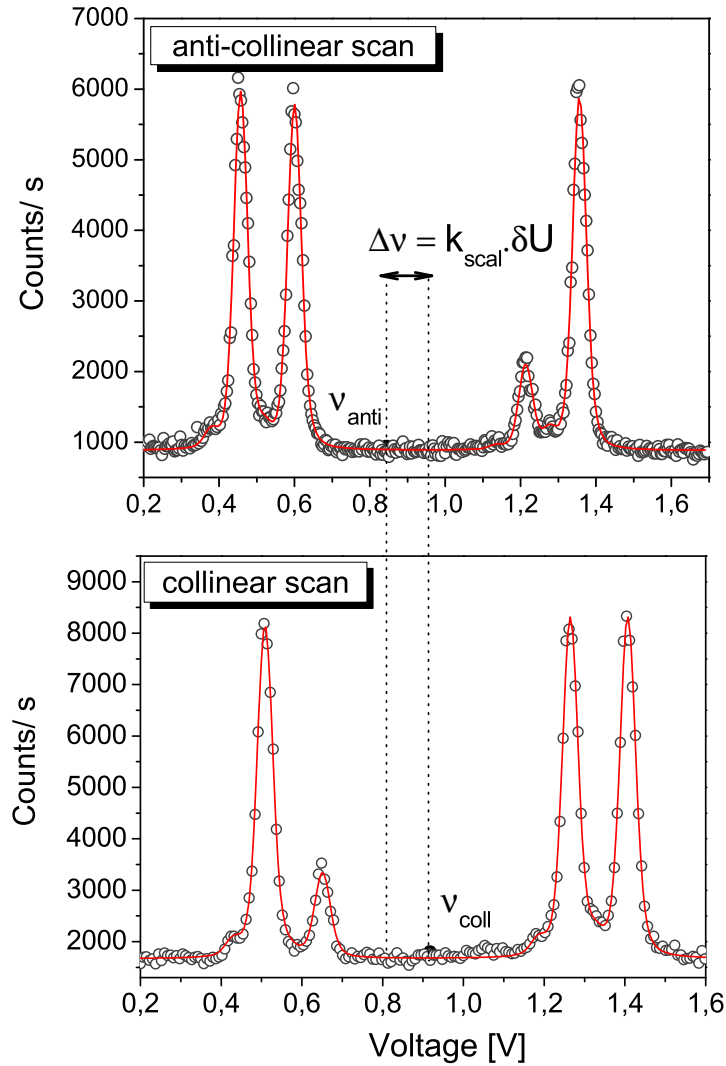
Figure 6.13. Spectra recorded for stable ^{9}Be in the $2s_{1/2} \rightarrow 2p_{1/2}$ transition. The upper spectrum is from the spectroscopy with the anti-collinear beam, where the laser beam travels opposite to the ion beam, the lower one is from the collinear spectroscopy, where the laser and ion beams travel in parallel. $\Delta\nu$ is the difference in center of gravity arising from different locking points of the collinear and anti-collinear lasers.
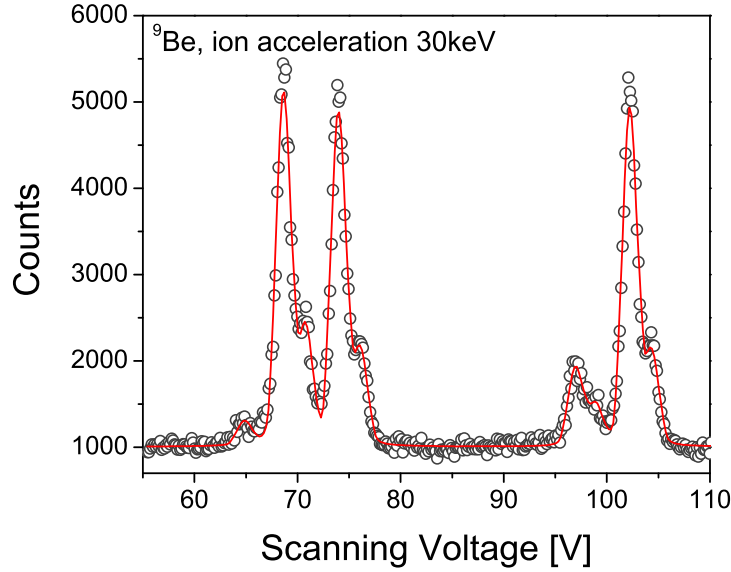
Figure 6.14. Spectrum recorded at 30 keV ISOLDE acceleration voltage to study closer the peak structure.

uncertainties the calculated transition frequencies which is typically a few MHz. The one exception, where a difference of 2 MHz was found was excluded from the measurements and is not reported here. Measurements of the Be resonances relative to the different iodine lines required different acceleration voltages, since the laser was stabilized at different frequencies. A voltage range of about ± 10 keV was covered. No systematic effects were observed in the obtained transition frequencies.

A misalignment between the laser and ion beams can introduce a large systematic shift in the transition frequencies. Two possible beam misalignments, which we tested during the measurements are shown in Fig. 6.15. The misalignment, where one of the laser beams was overlapped with the ion beam and centered through the beam-line and the second laser beam was slightly outstanding showed somewhat larger differences and a systematic uncertainty $\Delta\nu_a$ of approximately 500 kHz was estimated. On the other hand, the misalignment, where two laser beams were overlapped very well but they were commonly misaligned relative to the ion beam showed no systematic effect. The stronger effect is theoretically expected in laser-laser misalignment, since the Doppler shifts of the two laser beams do not cancel each other. Further tests were done with different laser powers starting at 0.5 mW up to 5 mW, where again no systematic shift was observed. Also different foci of the ion beam and the laser beams did not result in any systematic deviations.

Recoil shift, $\Delta\nu_{rs}$, appear due to the photon absorption, which slightly increase

Figure 6.15. An alignment of the laser and the ion beams. In the first case was one of the laser beams properly overlapped with the ion beam and the other laser beam was slightly misaligned. The second test was with two laser beams properly overlapped but they were slightly misaligned relative to the ion beam.

(collinear laser) or decrease (anti-collinear laser) the ion velocity. In both cases the resonance is shifted to higher frequencies and the uncertainty $\Delta\nu_{rs}$ contributes only to negative part of the total absolute transition uncertainty. Due to the dark states in the odd isotopes, ^{7,9,11}Be, ions in the interaction region do not absorb as many photons as ^{10}Be ions which are almost ideal two-level systems. Single photon absorption in ^{7,9,10,11}Be causes a change in the resonance frequency of 0.6, 0.47, 0.42 and 0.38 MHz, respectively. The averaged number of the absorbed photons is estimated to be 1.5 for odd isotopes and 3 for ^{10}Be [Tie09].

Concerning all studied systematic errors, the strongest contribution besides possible laser-beam misalignments stems from the uncertainty of the Rb-clock (FS 725 Standford Research Systems) $\Delta\nu_{fc}$, which was used as the reference for the frequency comb. The relative accuracy of the Rb-clock and the drift estimation are explained in section 5.4.3, where the same Rb clock was used for the lithium experiment. Here, the last calibration was performed by the manufacturer 1.5 years before the beryllium measurements and the drift corresponding to this period was calculated to be about 410 kHz at 626 nm.

The total uncertainty for the absolute transition frequency of the specific isotope was calculated according

$$\Delta\nu_0 = \sqrt{\Delta\nu_{st}^2 + \Delta\nu_a^2 + \Delta\nu_{rs}^2 + \Delta\nu_{fc}^2}, \tag{6.1}$$

since the individual uncertainties are not correlated. The absolute transition frequencies can be used to calculate the isotope shifts in the D_2 line of Be$^+$ ions. In this case the $\Delta\nu_{fc}$ are correlated. Here, the final uncertainty for the isotope shift between the reference isotope ^{9}Be and the studied isotope A' (^{7,10,11}Be) is given by

$$\Delta\nu_{IS}^{9A'} = \sqrt{(\Delta\nu_0^9)^2 + (\Delta\nu^{A'})^2 + (\Delta\nu_{rs}^9 - \Delta\nu_{rs}^{A'})^2}, \tag{6.2}$$

because the $\Delta\nu_{fc}$ error arising from the frequency comb is the same for all isotopes and largely cancels out when the isotope shift is determined.

An additional recoil correction, $\Delta\nu_{rc}$, has to be taken into account for the absolute transition frequency determination. The $\Delta\nu_{rc}$ correction is due to the momentum conservation, where the excitation energy of the atom has to be a bit higher as the expected

Table 6.3. Summary of statistical and systematic uncertainties of the absolute transition frequencies in ^{7,9,10,11}Be. Systematic errors arising from the laser beam misalignment $\Delta\nu_a$, recoil shift $\Delta\nu_{rs}$ and Rb-clock $\Delta\nu_{fc}$, the reference used for the frequency comb. All values are in MHz.

	^{7}**Be**	^{9}**Be**	^{10}**Be**	^{11}**Be**
Statistical	0.9	1.4	0.8	1.5
Systematic				
Frequency Comb $\Delta\nu_{fc}$	0.8	0.8	0.8	0.8
Misalignment $\Delta\nu_a$	0.5	0.5	0.5	0.5
Recoil Shift $\Delta\nu_{rs}$	0.9	0.8	1.3	0.6

energy depending on the mass and the transition frequency

$$\Delta\nu_{rc} = \frac{h\nu_0^2}{2Mc^2}. \tag{6.3}$$

The recoil correction was calculated to be about 0.2 MHz for all isotopes.

6.5.2   Radioactive Beryllium Isotopes ^{7,10,11}Be

The laser system described in the previous paragraphs was used for isotopes shift measurements in the D_1 line ($2s_{1/2} \rightarrow 2p_{1/2}$) as well as in the D_2 line ($2s_{1/2} \rightarrow 2p_{3/2}$). Results for the nuclear charge radii of radioactive beryllium isotopes in the D_1 line are presented in [Tie09] while this thesis focuses on the results obtained from the D_2 line.

Spectra for ^{7,9}Be have in the D_2 line six hyperfine components. However, the structure in the excited state is completely unresolved due to the natural linewidth which is 20 MHz while the splitting in the $2p_{3/2}$ state is only on the order of 10 MHz. Moreover, the observed linewidth in collinear spectroscopy is between 50 and 70 MHz. In the case of ^{11}Be, there are only three hyperfine components, but the hyperfine structure in the excited state is also not resolved. In Fig. 6.16 recorded spectra from collinear and anti-collinear spectroscopy on ^{7,10,11}Be are shown. In these spectra the tuning voltage was at the x-axis was converted into the frequency scale.

Different fitting functions were used to describe the experimental data. Graphs in Fig. 6.16 show fits with Voigt profiles to each component, but Lorentz and Gauss profiles were also used. In all cases common widths were used for all resolved peaks. Additionally, ^{9,11}Be were fitted with multi-line Minuit functions. This Minuit function was used for the data analysis of all isotopes in the D_1 line transition. It contains all allowed hyperfine transitions calculated from the nuclear spin and the angular momentum. Peaks were fitted with Voigt profiles of common linewidth. The Lorentzian linewidth of the Voigt
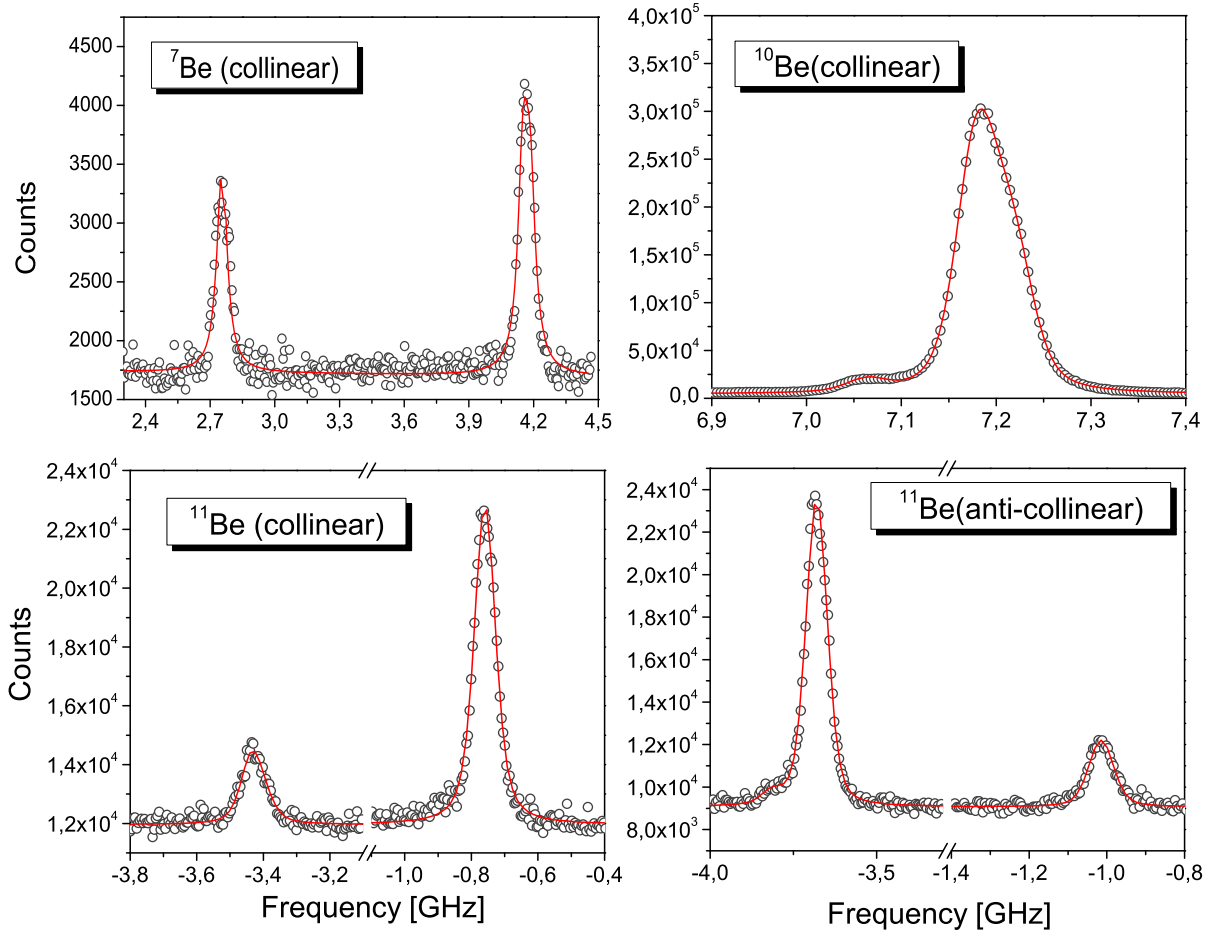
Figure 6.16. Spectra obtained in $2s_{1/2} \rightarrow 2p_{3/2}$ transition for ^{7,10,11}Be$^+$. Upper two spectra for ^{7}Be (left) and ^{10}Be (right) are obtained by collinear spectroscopy. Lower spectra are from collinear(left) and anti-collinear spectroscopy of the one-neutron halo isotope ^{11}Be. Experimental data are fitted with Voigt profiles as discussed in the text.
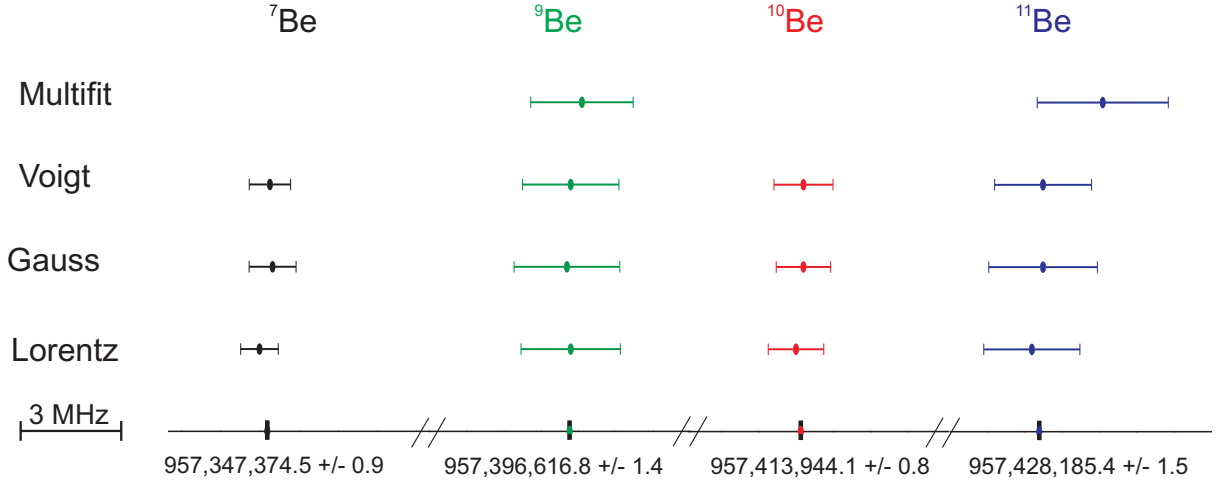
Figure 6.17. Absolute transition frequencies and corresponding standard deviation from the different fitting functions. Shown error bars are to scale, the scaling bar of 3 MHz is shown in the left-down corner of the figure.

profile was fixed to the natural linewidth while χ^2 minimalization was performed by freely varying the A_{2s} factor, peak amplitudes and peak centers. Interval factors A_{2p} and B_{2p} were introduced in the fitting routine but were as fixed parameters to speed up the fitting. The values for the interval factors A_{2p} and B_{2p} were taken from [Puch09]. Obtained values for the A_{2s} of -624.3(10) MHz for ^{9}Be and -2681(10) MHz for ^{11}Be agree very well with the values from the D_1 measurements [Tie09, Noe09] as well as with the theoretical values [Win83](^{9}Be), within the given uncertainties.

Amplitudes of the peaks with the lower intensities were in the fitting routine fixed at a value which is relative to the most intensive peak. This step was necessary to keep the number of free parameters on a reasonable level. The positions of the side peaks on the left and the right side were fixed relative to the main peaks at -4 and +2 V, respectively. The absolute transition frequencies and their corresponding standard deviations are compared in Fig. 6.17. The final absolute transition frequency was determined as the averaged value from all simple fits and the uncertainty was taken as the largest from all simple profiles, typically from the Gaussian fit. Although, the lowest reduced χ^2 was obtained with the Voigt fits, ranging between 5-8 for ^{7,9}Be and 4-6 for ^{11}Be, almost no deviations in the resulting absolute transition frequencies using different fitting were observed.

Absolute Transition Frequency Determination   The subsequent steps to extract the absolute transition frequency are summarized in table 6.4. The transition frequency ν_{coll} (ν_{anti}) from a collinear (anti-collinear) spectrum was determined as a CG of all resolved

peak centers and corresponding theoretical line strengths:

$$^{7}\text{Be}: \quad \nu_{\text{coll/anti}} \quad = \quad \frac{5}{8}\nu_{F=2 \,\rightarrow\, F'} + \frac{3}{8}\nu_{F=1 \,\rightarrow\, F'} \tag{6.4}$$

$$^{9}\text{Be}: \quad \nu_{\text{coll/anti}} \quad = \quad \frac{5}{8}\nu_{F=2 \,\rightarrow\, F'} + \frac{3}{8}\nu_{F=1 \,\rightarrow\, F'} \tag{6.5}$$

$$^{10}\text{Be}: \quad \nu_{\text{coll/anti}} \quad \rightarrow \quad \text{peak center} \tag{6.6}$$

$$^{11}\text{Be}: \quad \nu_{\text{coll/anti}} \quad = \quad \frac{3}{4}\nu_{F=2 \,\rightarrow\, F'} + \frac{1}{4}\nu_{F=1 \,\rightarrow\, F'}, \tag{6.7}$$

where $F = 1, 2$ are hyperfine components in the ground state from which the transition starts and F' is unresolved hyperfine level in the $2p_{3/2}$ state.

As shown in Fig. 6.13, ν_{coll} and ν_{anti} differ by a value $\Delta\nu$, which must be corrected to have both CG at the same acceleration voltage and hence at the same ion velocity. Then the general formula

$$(\nu_{\text{coll}} - \Delta\nu) \cdot \nu_{\text{anti}} = \nu_0^2 \tag{6.8}$$

can be applied. The absolute transition frequencies from the online beam-time in D_2 line are listed in the table 6.5.

Since the spectra were recorded in a voltage range, the conversion scaling-factor of 30-40 MHz per Volt was calculated depending on the total applied voltage and the specific isotope. Due to the mass difference, the isotope with the higher mass is accelerated less compared to the lighter ones. In the case of ^{9}Be at 50 keV acceleration voltage, the conversion factor around the center-of-gravity was about 35 MHz/ Volt.

For ^{10}Be, which has the simple structure with no hyperfine splitting, we obtained higher statistics. When fitted with a single peak, the experimental data shows a clear asymmetry, as can be seen in the upper row of Fig. 6.18.

When the additional peak on the left side, caused by inelastic collisions, was included, the χ^2 was reduced but the asymmetry remained. Only with an additional third peak on the right side of the main peak a good description of the experimental data was obtained. The origin of the asymmetry (the third peak) could arise from the laser ion source RILIS but so far it is not completely understood. However, the asymmetry did not show a big impact on the obtained absolute transition frequencies. Slight differences in the CG frequency appear in collinear and anti-collinear spectrum with opposite sign and cancel out when the absolute transition frequency is determined. In table 6.6 the absolute transition frequencies obtained with the three different number of Voigt peaks of the common linewidth are listed.

To check if the position of the unknown right peak is reproducible for all the data in ^{10}Be, the position of the right peak was left as a free parameter. However, to decrease the number of free parameters, the position of the known left peak was fixed at the distance

Table 6.4. Determination of the absolute transition frequency from the obtained spectra for collinear and anti-collinear spectroscopy. The total acceleration voltage which was applied to the ions includes the ISOLDE voltage (up to 60 keV), Fluke voltage ($\pm$ 10 keV) and the Kepko offset voltage at which the center-of-gravity (CG) was deduced from all hyperfine components. The difference between the total voltages in collinear and the anti-collinear geometry arises from not perfectly chosen frequency locking points of the two dye lasers. This difference in a voltage scale δU can be converted to a frequency scale $\Delta \nu$ with a scaling factor k_{scal} ($\nu_0(\text{lit}) =$ 957 396.82(14) GHz [Bol85]). For beryllium, a conversion scaling-factor of 30-40 MHz per Volt was calculated depending on the total applied voltage and the specific isotope. In order to obtain the absolute transition frequency, both laser frequencies have to be measured at the same acceleration voltage, i.e., at the same ion velocity. Therefore, one of the frequencies is artificially shifted by this frequency difference $\Delta \nu$. The absolute transition frequency of the beryllium ion at rest ν_0 is then determined according to equation 6.8 as listed in the last row of the table.

Total Voltage (coll.) U_{coll} (V)	$U_{\text{coll}} = (\text{ISOLDE} + \text{Fluke} + \text{CG}_{\text{coll}})$
Total Voltage (anti-coll.) U_{anti} (V)	$U_{\text{anti}} = (\text{ISOLDE} + \text{Fluke} + \text{CG}_{\text{anti}})$
Total Voltage Difference δU (V)	$\delta U = U_{\text{coll}} - U_{\text{anti}}$
Scaling Factor (coll.) k_{coll} (MHz/V)	$k_{\text{coll}} = \gamma \cdot \nu_0(\text{lit}) \cdot \beta \cdot (1 - \sqrt{1 - 1/U_{\text{coll}}})$
Scaling Factor (anti-coll.) k_{anti} (MHz/V)	$k_{\text{anti}} = \gamma \cdot \nu_0(\text{lit}) \cdot \beta \cdot (1 - \sqrt{1 - 1/U_{\text{anti}}})$
Scaling Factor Mean Value k_{scal} (MHz/V)	$k_{\text{scal}} = (k_{\text{coll}} + k_{\text{anti}})/2$
δU Converted into Frequency $\Delta \nu$ (MHz)	$\Delta \nu = \delta U \cdot k_{\text{scal}}$
Collinear Laser Frequency ν_{coll} (MHz)	
Anti-collinear Laser Frequency ν_{anti} (MHz)	
ν_{coll} Corrected (MHz)	$\nu_{\text{coll}} \text{ (corrected)} = (\nu_{\text{coll}} - \Delta \nu)$
Absolute Transition Freq. ν_0 (MHz)	$\boldsymbol{\nu_0 = \sqrt{(\nu_{\text{coll}} - \Delta \nu) \cdot \nu_{\text{anti}}}}$

Table 6.5. The absolute transition frequencies ν_0 including the recoil corrections $\Delta\nu_{\text{rc}}$ in the $2s_{1/2} \rightarrow 2p_{3/2}$ transition from online measurements. $\Delta\nu_0$ is the total uncertainty and contains quadratically added statistical error and systematic errors. In the last column are listed the recoil shifts $\Delta\nu_{\text{rs}}$ for each transition which contribute to negative part of the total uncertainty. All values are in MHz.

Isotope	ν_0	$\Delta\nu_0$	$\Delta\nu_{\text{rs}}$
^{7}Be	957 347 374.5	+1.3/-1.6	-0.9
^{9}Be	957 396 616.6	+1.7/-1.9	-0.8
^{10}Be	957 413 943.9	+1.2/-1.8	-1.3
^{11}Be	957 428 185.2	+1.7/-1.8	-0.6
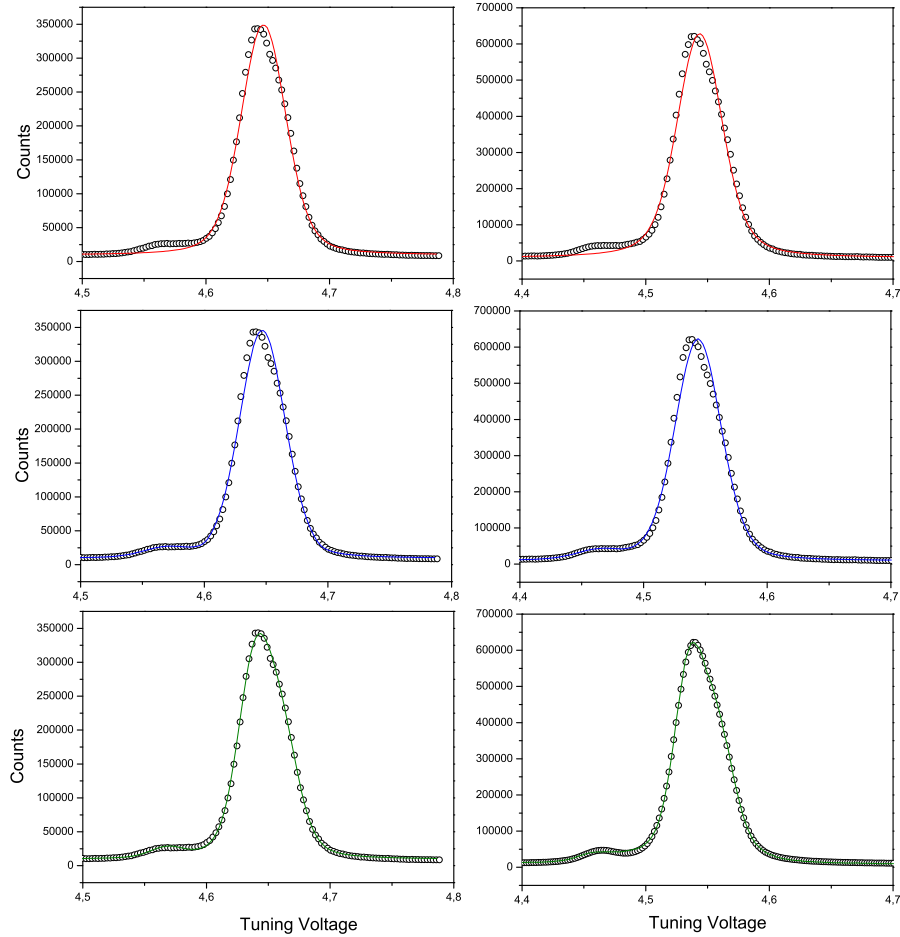
Figure 6.18. Scans from collinear (left) and anticollinear spectroscopy (right) of ^{10}Be$^+$, where in top row only one (fit in red), in the second two of them (fit in blue) and in the third three (green) Voigt peaks were used for fitting.

Table 6.6. Center of gravities (CG_{coll}, CG_{anti}) and the final absolute transition frequencies (ν_0) of $^{10}Be^+$ for the same experimental data fitted with one, two and three peaks, as depicted in Fig. 6.18. All frequencies are given in MHz. In the last two columns the corresponding reduced χ^2 obtained from the different fit is listed.

	CG_{coll}	CG_{anti}	ν_0	χ^2 (coll)	χ^2 (anti)
1 peak	8,212.8	8,030.9	957,413,944.6	611	1,424
2 peaks	8,213.5	8,031.6	957,413,944.6	212	570
3 peaks	8,199.4	8,017.7	957,413,944.5	111	247

of 3.99 V from the main peak and the amplitude ratio between the right peak and the main peak was fixed at 0.5, where it showed the best fit. The position of the right peak was varying in different spectra and was not reproducible, however this had no important impact on the results, since the shift of the CG frequency was in the collinear and the anti-collinear again about the same and canceled when the absolute transition frequency was determined.

6.5.3 Isotope Shifts and Nuclear Charge Radii

From the absolute transition frequencies discussed in the previous section, the isotope shifts in the D_2 line were extracted. According to the theory chapter, those are related to the change in the nuclear charge radii by

$$\delta \left\langle r_c^2 \right\rangle^{9,A'} = \frac{\delta\nu_{IS}^{9,A'} - \delta\nu_{MS}^{9,A'}}{C} \tag{6.9}$$

with the field shift coefficient C as listed in table 2.2. Using the absolute charge radius of ^9Be from elastic electron scattering, the absolute root-mean-square charge radius of the unknown isotope $\sqrt{\langle r_c^2 \rangle^{A'}}$ can be obtained according to equation 2.22. The results listed in table 6.7 are plotted and compared with the D_1 line results in Fig. 6.19. The radius is decreasing from ^7Be to ^{10}Be and then again substantially increasing for ^{11}Be. Excellent agreement between the two measurements is observed, but the charge radii from the D_2 line measurements have considerably larger uncertainty, which seems to be overestimated. In the following discussion of the charge radii, are therefore compared recent theoretical predictions with the radii extracted from the D_1 measurements.

Table 6.7. Extracted nuclear charge radii r_c from the D_2 line measurements. Differences in nuclear charge radii $\delta \langle r_c^2 \rangle$ are calculated from isotope shifts $\delta\nu_{\mathrm{IS}}^{9,A}$, field shifts $\delta\nu_{\mathrm{FS}}^{9,A}$ (reference isotope is ^{9}Be), the theoretical mass shifts $\delta\nu_{\mathrm{MS}}^{9,A}$ and field shift constants that are taken from [Yan08] (first row for each isotope) and [Puch09b] (second row). The calculated field shift constant C is -16.912 MHz/fm^2 [Yan08]. Uncertainties of the absolute charge radii r_c include the uncertainty of the reference radius $r_c(^9\mathrm{Be}) = 2.519(12)$ fm [Jan72].

Isotope	$\delta\nu_{\mathrm{IS}}^{9,A}$, MHz	$\delta\nu_{\mathrm{MS}}^{9,A}$, MHz	$\delta\nu_{\mathrm{FS}}^{9,A}$, MHz	$\delta \langle r_c^2 \rangle$, fm^2	$r_c(\mathrm{D}_2)$, fm
^{7}Be	-49 242(2.0)	-49 231.827(39)	-10(2)	0.61(12)	2.637(55)
		-49 231.779(35)			
^{9}Be	-	-	-	-	-
^{10}Be	17 327(2.0)	17 312.569(13)	15(2)	-0.87(12)	2.339(53)
		17 312.553(13)			
^{11}Be	31 569(2.3)	31 564.168(24)	5(2)	-0.28(14)	2.463(62)
		31 564.207(31)			
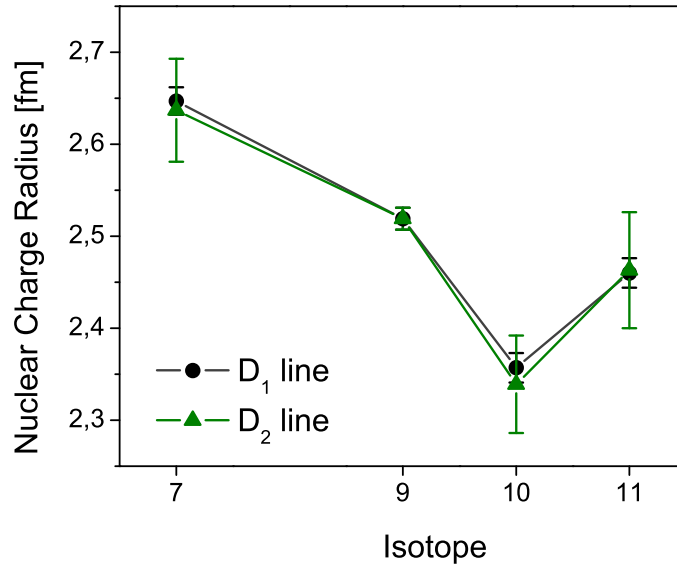
Figure 6.19. The nuclear charge radii obtained from collinear laser spectroscopy on beryllium isotopes in the D_1 and D_2 line.

6.6 Discussion and Conclusion

The nuclear charge radii of ^{7,10}Be and of the one neutron halo ^{11}Be have been extracted for the first time in a model-independent way by measuring the atomic isotope shift and using the recent atomic structure calculation of the atomic structure [Noe09, Tie09]. The comparison of the experimental values and the existing values from theoretical predictions is shown in Fig. 6.20. For those nuclear models, where the neutrons and the protons were reported as point-like particles, the point-proton root-mean-square radii were converted to root-mean-square charge radii by folding in the proton mean-square charge radius $\langle R_{\mathrm{p}}^2 \rangle = 0.895(18)$ fm^2 [Sic03] and the neutron mean-square charge radius $\langle R_{\mathrm{n}}^2 \rangle = -0.113(7)$ fm^2 [Kop95]. The nuclear charge radius can be then written as

$$\langle r_{\mathrm{c}}^2 \rangle = \langle r_{\mathrm{pp}}^2 \rangle + \langle R_{\mathrm{p}}^2 \rangle + \langle R_{\mathrm{n}}^2 \rangle + \frac{3\hbar^2}{4m_{\mathrm{p}}^2 c^2} \ , \tag{6.10}$$

where m_{p} is the mass of the proton and the last term $3\hbar^2/4m_{\mathrm{p}}^2 c^2 \approx 0.033$ fm^2 is the Darwin-Foldy term [Fri97].

As shown, all theoretical model predictions are in a good agreement with the charge radius evolution, specific features are especially well reproduced depending on the model. In the case of Greens function Monte-Carlo (GFMC) calculations [Pie01, Pie02], the agreement for the isotope pair ^{9,10}Be is striking, whereas the decrease between ^{7}Be and ^{9}Be is slightly underestimated and a charge radius calculation for ^{11}Be has not been obtained to date. Improved No-core Shell model (NCSM) calculations [For09] include the halo nucleus and show the best agreement with the experimental data for the ^{10}Be isotope. Fermionic molecular dynamic (FMD) calculations [Nef09] are especially developed for the description of nuclei with clustering and halos. The obtained values are slightly larger than the experimental values but the systematic trend is very well reproduced. Compared to the preliminary results plotted in [Noe09], more recent calculations which are discussed in [Zak10] resulted in an increased radius for ^{7}Be due to a very weak energy dependence on the separation of the α and the triton cluster in this nucleus. In summary, a relatively good agreement between the predictions of nuclear models and the experimental results is observed, contrary to the case of the lithium isotopes where much larger deviations are observed, as discussed in section 5.4.4.

^{7}Be composed of an α particle and a triton cluster has a bigger spatial distribution than the heavier isotopes which are composed of two α particles and additional neutrons. ^{8}Be would be composed of two α particles and is unbound while the additional neutron in ^{9}Be holds the α particles together. Two neutrons in ^{10}Be obviously tight the two α particles even more and the third additional neutron in ^{11}Be leads to the halo phenomenon. This
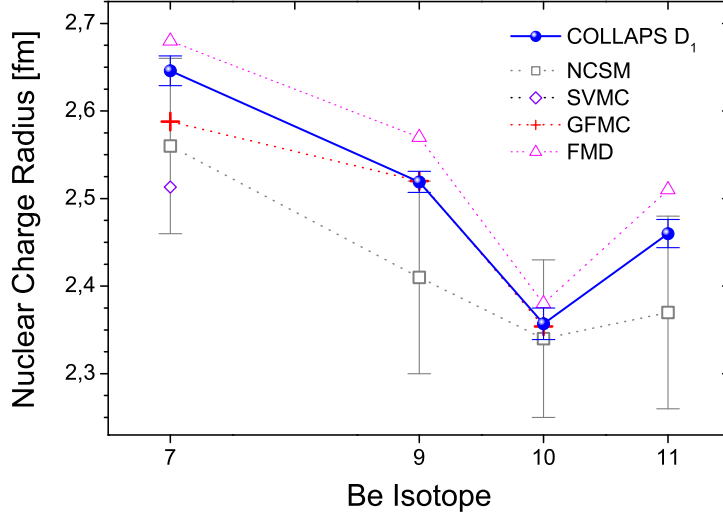
Figure 6.20. Experimental (D_1 line) and theoretical nuclear charge radii. All theoretical predictions follow the trend of the experimental charge radii well. Recently published values from No Core Shell Model (NCSM) [For09] show a good agreement within the uncertainties. In the case of Greens Function Monte Carlo calculations (GFMC) the agreement for the isotope pair ^{9,10}Be is striking [Pie01, Pie02]. The value for ^{11}Be have not been obtained up to date. Values from Fermionic Molecular Dynamic (FMD) calculations [Nef09] are slightly too large compared to the experimental results but nicely reproduce the systematic trend. SVMC nuclear charge radius for ^{7}Be is from Stochastic Variational Multicluster method [Suz98].

trend, the clustering and FMD calculations are in detail analyzed in [Zak10], attached to this thesis.

The halo-neutron extends the nuclear matter distribution but can also cause an increase in the charge distribution: The inner core of the ^{11}Be nucleus is ^{10}Be which moves around the center of mass (CM) as depicted in Fig. 6.21. In this interpretation, the 0.11 fm increase in the mean square charge radius between ^{10}Be and ^{11}Be would correspond to a squared distance between the center of the ^{10}Be core and the CM[1]:

$$r_{\text{Core}-\text{CM}}^2 = r_c^2(^{11}\text{Be}) - r_c^2(^{10}\text{Be}) = \delta \left\langle r_c^2 \right\rangle^{10,11}, \tag{6.11}$$

which is 0.7 fm. Hence, the halo neutron would be at the distance of 7 fm from the CM according to

$$r_{\text{halo}-\text{CM}} = r_{\text{Core}-\text{CM}} \ \frac{m(^{10}\text{Be})}{m(\text{neutron})}, \tag{6.12}$$

where the mass ratio of the ^{10}Be and the halo-neutron is about 10. The distance of 7 fm is in very good quantitative agreement with the model suggested already in

---

[1]Here, the small contribution from the mean-square neutron charge radius was neglected.
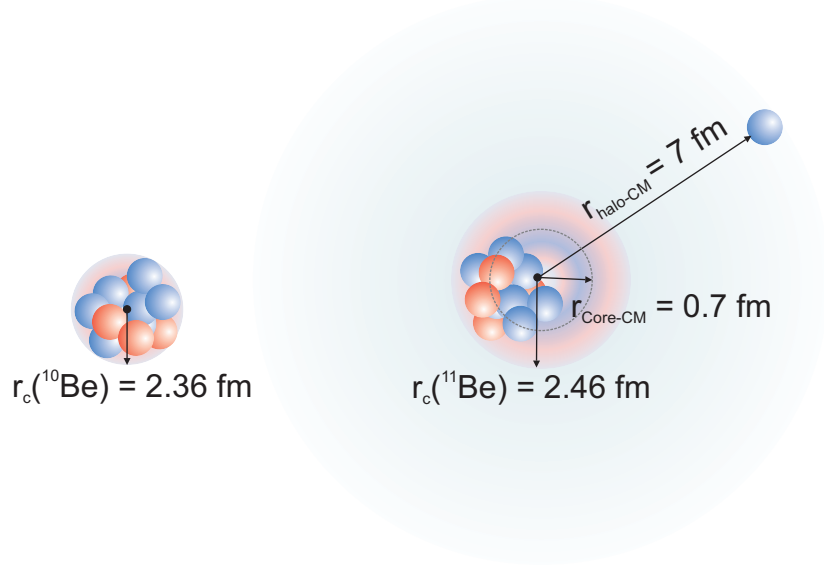
Figure 6.21. An illustrated matter distributions and measured charge radii in ^{10}Be and ^{11}Be. When the change of the charge radius in these isotopes is assigned to the halo neutron which moves an inert ^{10}Be core around center of mass(CM) then the distance between CM of ^{11}Be and center-of-gravity of ^{10}Be is calculated to be 0.7 fm. From the CM and a mass ratio the halo neutron is calculated to be at a distance of 7 fm.

1987 [Han87], where an exponentially decreasing probability for halo neutrons was suggested with a decay length of $\rho = \hbar/\sqrt{2\mu E_B}$. Using the one neutron separation energy $S_N =$ 501.25(58) keV and the reduced mass for ^{11}Be [Rin09], this results in $\rho =$ 6.6 fm. The simple explanation of the center of mass motion to determine the distance between loosely bound halo nucleons and the inner core was also used in the helium case, where ^{6}He and ^{8}He are two- and four-neutron halos, respectively. In these isotopes, the inner core is a compact and strongly bound α particle and therefore this approach is appropriate. However, the change in the charge radius can also be partially caused by different intrinsic nucleon distribution in the ^{10}Be core of ^{11}Be, which means that the core has the same number of the nucleons but a different distribution of them compared to the free ^{10}Be nucleus. Examples of intrinsic proton and neutron density distributions in ^{10}Be and ^{11}Be obtained from FMD calculations are shown in Fig. 6.22. These distributions show a clear cluster structure of two α particles and surrounding neutrons. The change in the charge radius can therefore also be explained by pulling the two α particles in ^{11}Be further apart. If this effect would have to explain the total change in the charge radius, the distance between the α clusters in ^{10}Be and ^{11}Be can be extracted according to

$$r_{\alpha-\alpha}^2 = r_c^2(^{10}\text{Be}/^{11}\text{Be}) - r_\alpha^2, \tag{6.13}$$
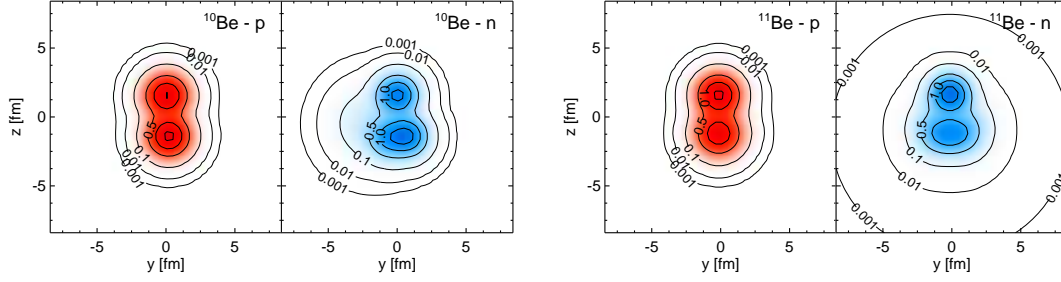
Figure 6.22. Examples for intrinsic proton and neutron density distributions from Fermionic Molecular Dynamics calculations. The cluster structure with two α clusters and surrounding neutrons is clearly visible.

with an α rms radius of 1.681(4) fm [Sic08]. The distance in ^{10}Be is calculated to be 3.30(5) fm and in ^{10}Be 3.60(5) fm, which corresponds to an increase of 10%. These arguments and estimations are put on a firmer ground in the attached publication [Zak10].

A better estimation is possible if measurements of the one-neutron removal channel in electromagnetic and nuclear inelastic scattering of the halo nucleus are taken into account [Pal03]. From those measurements, a rms radius of the $2s_{1/2}$ neutron wave function of 5.7(4) fm for ^{11}Be was deduced. The combination of this value with the measured charge radius of ^{11}Be results in a size of 2.40(2) fm for the ^{10}Be core in ^{11}Be, which is about 1.6(1.1)% larger than the free ^{10}Be nucleus.

The measured charge radii can also be combined with the measurements of the matter distribution and the B(E1) transition strength, suggested recently by I. Tanihata. This could lead to a precise determination of two contributions (CM core motion due to the halo neutron and the distance between two α clusters in the nucleus) and draw a very detailed picture of the ^{11}Be structure.

Apart from the nuclear structure investigation, the comparison between the D$_1$ and D$_2$ line measurements allows a consistency test of the measurements and the mass shift calculations. Therefore, the splitting isotope shift (SIS), which is the difference in the isotope shifts between the two fine structure transitions is extracted. This difference arises from the spin-orbit coupling and can be used to test the theoretical mass shift calculations. Beryllium is a good candidate, since the value is expected to be in the MHz region. For lithium, the predicted value is an order of magnitude smaller, between ^{6}Li and ^{7}Li it was calculated to be 0.396 MHz [Yan08]. The most recent experimental values of -0.863(70) MHz [Das07] and 0.155(77) MHz [Nob06] do neither agree with each other nor with the predicted value. The value obtained for beryllium can be compared to the theoretical value, which is nearly independent of both, QED and nuclear volume effects,

Table 6.8. Isotope shifts $\delta\nu_{\mathrm{IS}}^{9,A}$ in the $2s_{1/2} \rightarrow 2p_{1/2}$ (D$_1$) and $2s_{1/2} \rightarrow 2p_{3/2}$ (D$_2$) transitions and extracted splitting isotope shifts $\delta\nu_{\mathrm{SIS}}$. In the last two columns the values for $\delta\nu_{\mathrm{SIS}}$ from two independent theoretical calculations are listed. All values are given in MHz.

Isotope	$\delta\nu_{\mathrm{IS}}$ D$_1$	$\delta\nu_{\mathrm{IS}}$ D$_2$	$\delta\nu_{\mathrm{SIS}}$	$\delta\nu_{\mathrm{SIS}}$ [Puch09]	$\delta\nu_{\mathrm{SIS}}$ [Yan08]
^{7}Be	-49 236.94(80)	-49 242(2.0)	-5.2(2.2)	-6.037(1)	-6.049
^{10}Be	17 323.82(82)	17 327(2.0)	3.0(2.4)	2.097(1)	2.13
^{11}Be	31 565.04(86)	31 569(2.3)	3.7(2.5)	3.965(1)	3.878

and gives a good opportunity to compare directly theory and experiment. Isotope shifts in D$_1$ and D$_2$ line and SIS values from this experiment and two independent theoretical predictions are listed in the table 6.8. The values are in a good agreement, although the SIS uncertainties from the experiment are still relatively large. Improved measurements of the isotope shift in D$_2$ line, planned at RIKEN [Nak06], with ions stored and cooled in RF trap have a potential to improve these values.

7 Summary and Outlook

In this work the measurements of the absolute transition frequencies of lithium and beryllium isotopes with specialized high precision laser spectroscopy techniques are reported. The obtained experimental results in combination with accurate theoretical calculations of three-electron systems allowed us to extract the root-mean-square nuclear charge radii of these light isotopes. It is demonstrated that the frequency comb technology has a strong impact also in the field of nuclear structure investigations.

Lithium The high-resolution Doppler-free two-photon spectroscopy and the resonance ionization technique were applied to the stable lithium atoms in order to measure the absolute transition frequencies in the the $2S \rightarrow 3S$ two-photon transition in ^{6,7}Li. Therefore, the experimental setup developed previously for online measurements of short-lived lithium isotopes [Ewa04, San05] was operated online with stable lithium isotopes. In this work a new scheme for the stabilization of the single mode lasers was developed. The new stabilization scheme using a frequency comb allows the stabilization of lasers to arbitrary and accurately known frequencies. The frequency comb itself is stabilized to a rubidium clock ($\delta\nu/\nu = 5 \times 10^{-11}$) and this stability is transfered directly into the optical regime of the comb.

Applying the direct stabilization to the frequency comb, absolute transition frequencies of the $2S \rightarrow 3S$ transition were measured with an accuracy of 2×10^{-10}. The obtained values agree with previous values from online and offline measurements but accuracy was improved by an order of magnitude. In comparison with the latest theoretical values [Puch08] the difference between theory and experiment is about 12 MHz but the values agree within their uncertainties since the calculations are about 100 times less accurate than the experiment. The determination of the nuclear charge radii for all lithium isotopes by purely optical means without dependence on a reference value from elastic electron scattering - as it was done for hydrogen [Ude97] and deuterium [Hub98] - would be possible with theoretical calculations improved by two orders of magnitude.

Besides the transition reported here, further high accuracy measurements of the $2\,^3S_1 \rightarrow 2\,^3P_{0,1,2}$ transition in the two-electron system Li$^+$ as they have been already obtained at the test storage ring (TSR) at Heidelberg [Rei07b] and are under preparation at the MPQ in Garching in an ion trap would independently facilitate the absolute

charge radius determination in a two-electron system, where the required accuracy might be reached easier than in the three-electron system of atomic lithium.

Beryllium An advanced collinear laser spectroscopy technique with two counter-propagating laser beams allowed for the first time the measurements of optical isotope shifts for short-lived beryllium isotopes. Absolute transition frequencies with a relative accuracy of $\delta\nu/\nu = 2 \times 10^{-9}$ and isotope shifts were determined in the $2s_{1/2} \rightarrow 2p_{3/2}$ transition of Be$^+$ and the root-mean-square nuclear charge radii of the isotopes ^{7,10,11}Be were extracted with 2% uncertainty. Results confirmed the previous measurements in the $2s_{1/2} \rightarrow 2p_{1/2}$ transition presented in [Tie09] and [Noe09]. However, the uncertainty of the results presented here is larger due to the unresolved hyperfine structure in the $2p_{3/2}$ level.

The general trend of the charge radii decreasing from ^{7}Be to ^{10}Be is well understood taking the cluster nature of these nuclei into account. Theoretical predictions are in a good agreement with the experimental values. The increase in the charge radius between ^{10}Be and ^{11}Be can be presented as a combination of two effects. One is the interaction between the core and the halo neutron and the other is the intrinsic structure of the core, where the two α particles in the ^{10}Be core are pulled away and in consequence extend the charge radius.

From the D$_1$ and D$_2$ line measurements we have extracted also the splitting isotope shift. This is consistent with the theoretical calculations and provides a valuable check of the beryllium experiment.

With an improved signal detection, the current setup can be used in the near future to perform measurements also for the isotope ^{12}Be with 24 ms half-life, which has three orders of magnitude lower production rates compared to ^{11}Be. The isotope ^{12}Be is of interest from several points: Recently it was reported that the nucleus has a two-neutron halo formation in spite of a relatively large separation energy of $S_{2n} = 3.76$ MeV [Ili08]. Moreover, the structure of the ^{12}Be ground state is not completely understood up to date and the size of the charge radius would give valuable hints of admixtures from other shell model states. The beamtime for ^{12}Be is planned at the ISOLDE facility in spring 2010 with the GPS satellite receiver as frequency reference for the frequency comb and an ion-photon coincidence signal detection [Gep09]. Even more ambitious are measurements on the isotope ^{14}Be with 4 ms half-life and production rates of a few ions/s at current ISOL (Isotope Separation On Line) facilities. Such measurements might become possible at future in-flight facilities like FAIR in Darmstadt or FRIB[1] in East Lansing.

---

[1]FRIB - Facility for Rare Isotope Beams planned at MSU

Bibliography

[Alk96] J. S. Al-Khalili and J. A. Tostevin: *Matter Radii of Light Halo Nuclei*, Physical Review Letters, **76**, 3903-3906, (1996).

[Alk06] G. D. Alkhazov, A. V. Dobrovolsky and A. A. Lobodenko: *Experimental studies of the nuclear spatial structure of neutron-rich He and Li isotopes*, Physics of Atomic Nuclei, **69**, 1124-1131, (2006).

[Alk04] J. S. Al-Khalili: *An Introduction to Halo Nuclei*, The Euroschool Lectures on Physics with Exotic Beams, Vol. I, **651**, (2004).

[All97] D. W. Allan, *The Science of Timekeeping*, Hewlet Packard Application Note, (1997).

[Ara01] K. Arai, Y. Ogawa, Y. Suzuki and K. Varga: *Microscopic Multicluster Description of Light Exotic Nuclei with Stochastic Variational Method on Correlated Gaussians*, Progress of Theoretical Physics Supplement, **142**, 97-156, (2001).

[Arn87] E. Arnold, J. Bonn, R. Gegenwart, W. Neu, R. Neugart, E. W. Otten, G. Ulm, K. Wendt and the ISOLDE Collaboration: *Nuclear Spin and Magnetic Moment of ^{11}Li*, Physics Letters B, **197**, 311-314, (1987).

[Arn92] E. Arnold, J. Bonn, A. Klein, R. Neugart, M. Neuroth, E. W. Otten, P. Lievens, H. Reich, W. Widdra and the ISOLDE Collaboration: *Quadrupole moment of ^{11}Li*, Physics Letters B, **281**, 16-19, (1992).

[Arn94] E. Arnold, J. Bonn, A. Klein, P. Lievens, R. Neugart, M. Neuroth, E. W. Otten, H. Reich, and W. Widdra: *The quadrupole moment of the neutron-halo nucleus ^{11}Li*, Zeitschrift für Physik A, **349**, 337-338, (1994).

[Aud97] G. Audi, O. Bersillon, J. Blachot and A. H. Wapstra: *The NUBASE evaluation of nuclear and decay properties*, Nuclear Physics A, **624**, 1-124, (1997).

[Bla92] B. Blank, J.-J. Gaimard, H. Geissel, K.-H. Schmidt, K. Stelzer, K. Smmerer, D. Bazin, R. Del Moral, J. P. Dufour, A. Fleury, F. Hubert, H.-G. Clerc and M. Steiner: *Charge-changing cross sections of the neutron-rich isotopes $^{8,9,11}Li$*, Zeitschrift fr Physik A, **343**, 375-379, (1992).

[Bol85]   J. J. Bollinger, J. S. Wells, D. J. Wineland and W. M. Itano: *Hyperfine structure of the 2p 2P$_1$/2 state in $^9Be^+$*, Physical Review A, **31**, 2711-2714, (1985).

[Bor05]   D. Borremans, D. L. Balabanski, K. Blaum, W. Geithner, S. Gheysen, P. Himpe, M. Kowalska, J. Lassen, P. Lievens, S. Mallion, R. Neugart, G. Neyens, N. Vermeulen and D. Yordanov: *New measurement and reevaluation of the nuclear magnetic and quadrupole moments of ^8Li and ^9Li*, Physical Review C, **72**, 044309, (2005).

[Bum72]   F. A. Bumiller, F. R. Buskirk, J. N. Dyer and W. A. Monson: *Elastic Electron Scattering from ^6Li and ^7Li at Low Momentum Transfer*, Physical Review C, **5**, 391-395, (1972).

[Bus03]   B. A. Bushaw, W. Nörtershäuser, G. Ewald, A. Dax and G. W. F. Drake: *Hyperfine splitting, isotope shift, and level energy of the 3S states of $^{6,7}Li$*, Physical Review Letters, **91**, 043004, (2003).

[Car76]   G. Carboni, G. Gorini, G. Torelli, L. Palffy, F. Palmonari, E. Zavattini: *Precise measurements of the $2s_{1/2} - 2p_{1/2}$ splitting in the $\mu^{(-4)}He^+$ muonic atom*, Nuclear Physics A **278**, 381-386 (1977).

[Coh92]   C. Cohen-Tannoudji, J. Dupont-Roc, G. Grynberg: *Atom-Photon Interactions: Basic Processes and Applications*, John Wiley & Sons, New York (1992).

[Cor03]   K. L. Corwin, I. Thomann, T. Dennis, R. W. Fox, W. Swann, E. A. Curtis, C. W. Oates, G. Wilpers, A. Bartels, S. L. Gilbert, L. Hollberg, N. R. Newbury, S. A. Diddams, J. W. Nicholson, M. F. Yan: *Absolute-frequency measurements with a stabilized near-infrared optical frequency comb from a Cr:forsterite laser*, Optics Letters, **29**, 4, (2004).

[Cun01]   Steven T. Cundiff, Jun Ye, and John L. Hall: *Optical frequency synthesis based on mode-locked lasers*, Review of Scientific Instruments **72**,10 (2001).

[Das07]   D. Das and V. Natarajan: *Absolute frequency measurement of the lithium D lines: Precise determination of isotope shifts and fine-structure intervals*, Physical Review A, **75**, 052508-9, (2007).

[Dem03]   W. Demtröder: Laser Spectroscopy, *Basic Concepts and Instrumentation*, Springer, (2003).

[Dob06] A. V. Dobrovolsky, G. D. Alkhazov, M. N. Andronenko, A. Bauchet, P. Egelhof, S. Fritz, H. Geissel, C. Gross, A. V. Khanzadeev and G. A. Korolev: *Study of the nuclear matter distribution in neutron-rich Li isotopes*, Nuclear Physics A, **766**, 1-24, (2006).

[Dra02] G. W. F. Drake: *Progress in helium fine-structure calculations and the fine-structure constant*, Canadian Journal of Physics, **80**, 1195-1212, (2002).

[Dra05] G. W. F. Drake, W. Nörtershäuser and Z.-C. Yan: *Isotope shifts and nuclear radius measurements for helium and lithium*, Canadian Journal of Physics, **83**, 311-325, (2005).

[Dra06] G. Drake and Z. C. Yan: *Studies of light halo nuclei by the isotope shift method*, Hyperfine Interactions, **172**, 141-147, (2006).

[Dre83] R. W. P. Drever, J. L. Hall, F. V. Kowalski, J. Hough, G. M. Ford, A. J. Munley and H. Ward: *Laser Phase and Frequency Stabilisation Using an Optical Resonator*, Applied Physics B, **31**, 97-105, (1983).

[Ege02] P. Egelhof, G. D. Alkhazov, M. N. Andronenko, A. Bauchet, A. V. Dobrovolsky, S. Fritz, G. E. Gavrilov, H. Geissel, C. Gross, A. V. Khanzadeev, G. A. Korolev, G. Kraus, A. A. Lobodenko, G. Mnzenberg, M. Mutterer, S. R. Neumaier, T. Schfer, C. Scheidenberger, D. M. Seliverstov, N. A. Timofeev, A. A. Vorobyov and V. I. Yatsoura: *Nuclear-matter distributions of halo nuclei from elastic proton scattering in inverse kinematics*, European Physical Journal A, **15**, 27-33, (2002).

[Elze]   R. Elze: *Kernphysik* Vorlesung für Studenten den Physik und anderer Naturwissenschaften, http://www.uni-frankfurt.de/fb/fb13/ikf/Lehrende/Elze/index.html

[Ewa04] G. Ewald, W. Nörtershäuser, A. Dax, S. Götte, R. Kirchner, H.-J. Kluge, T. Kühl, R. Sánchez, A. Wojtaszek, B. A. Bushaw, G. W. F. Drake, Z.-C. Yan and C. Zimmermann: *Nuclear Charge Radii of ^{8,9}Li Determined by Laser Spectroscopy*, Physical Review Letters, **93**, 113002, (2004).

[Ewa05] G. Ewald: *Messung der Ladungsradien der radioaktiven Lithium-Isotope ^{8}Li und ^{9}Li*, Dissertation zur Erlangung der Doktorwürde, Naturwissenschaftlich-Mathematischen Gesamtfakultät, Ruprecht-Karls-Universität Heidelberg, (2005).

[Fed08]   V. N. Fedosseev, L. E. Berg, N. Lebas, O. J. Launila, M. Lindroos, R. Losito, B. A. Marsh, F. K. Osterdahl, T. Pauchard, G. Transtromer and J. Vannesjo: *ISOLDE RILIS: New beams, new facilities*, Nuclear Instruments & Methods in Physics Research Section B-Beam Interactions with Materials and Atoms, **266**, 4378-4382, (2008).

[For05]   C. Forssen, P. Navratil, W. E. Ormand and E. Caurier: *Large basis ab initio shell model investigation of Be-9 and Be-11*, Physical Review C, **71**, 044312, (2005).

[For09]   C. Forssen, E. Caurier, P. Navratil: *Charge radii and electromagnetic moments of Li and Be isotopes from the ab initio no-core shell model*, Physical Review C, **79**, 021303(R), (2009).

[Fri97]   J. L. Friar, J. Martorell and D. W. L. Sprung: *Nuclear sizes and the isotope shift*, Physical Review A, **56**, 4579-4586, (1997).

[Fro98]   C. Froese Fischer, M. Saparov, G. Gaigalas and M. Godefroid: *Breit-Pauli Energies, Transition Probabilities, and Lifetimes for* $2s, 2p, 3s, 3p, 3d, 4s_2$ *Levels of the Lithium Sequence Z=3-8*, Atomic Data and Nuclear Data Tables, **70**, 119-134, (1998).

[Gei99]   W. Geithner, S. Kappertz, M. Keim, P. Lievens, R. Neugart, L. Vermeeren, S. Wilbert, V. N. Fedoseyev, U. Köster, V. I. Mishin, V. Sebastian and the ISOLDE Collaboration: *Measurement of the Magnetic Moment of the One-Neutron Halo Nucleus* ^{11}Be, Physical Review Letters, **83**, 3792, (1999).

[Gei00]   W. Geithner, K. M. Hilligsoe, S. Kappertz, G. Katko, M. Keim, S. Kloos, G. Kotrotsios, P. Lievens, K. Marinova, R. Neugart, L. Vermeeren and S. Wilbert: *Accurate isotope shift measurements on short-lived neon isotopes*, Hyperfine Interactions, **127**, 117-120, (2000).

[Gei02]   R. W. Geithner: *Nuclear Moments and Differences in Mean Square Charge Radii of Short-Lived Neon Isotopes by Collinear Laser Spectroscopy*, Fachbereich Physik, Johannes Gutenberg-Universität Mainz, (2002).

[Gep09]   Ch. Geppert, A. Krieger, R. Sánchez, M.L. Bissell, K. Blaum, M. Hammen, M. Kowalska, J. Krämer, K. Kreim, R. Neugart, B. Sieber, D.T. Yordanov, C. Zimmermann and W. Nörtershäuser: *High Precision Laser Spectroscopy on* ^{12}Be, CERN INTC-P-214-ADD-2, (2009).

[God01]   M. Godefroid, C. F. Fischer and P. Jnsson: *Non-relativistic variational calcu-*
          lations of atomic properties in Li-like ions: LiI to OVI, Journal of Physics B,
          34, 1079-1104, (2001).

[Hae80]   T. Hänsch and B. Couillaud: *Laser frequency stabilization by polarisation spec-*
          troscopy of a reflecting reference cavity, Optics Communications, **35**, 441-444,
          (1980).

[Han87]   P. G. Hansen, and B. Jonson: *The Neutron Halo of Extremely Neutron-Rich*
          Nuclei, Europhysics Letters, **4**, 409-414, (1987).

[Hech09] J. Hecht, *FREQUENCY COMBS - Frequency combs achieve extreme precision*,
          Laser Focus World, **45**, 6, (2009).

[Hub98]   A. Huber, T. Udem, B. Gross, J. Reichert, M. Kourogi, K. Pachucki, M. Weitz
          and T. W. Hänsch: *Hydrogen-Deuterium 1S-2S Isotope Shift and the Structure*
          of the Deuteron, Physical Review Letters, **80**, 468-471, (1998).

[Hur79]   G. S. Hurst, M. G. Payne, S. D. Kramer and J. P. Young: *Resonance Ionization*
          Spectroscopy and One-Atom Detection, Reviews of Modern Physics, **51**, 767-
          819, (1979).

[Hyl28]   E. A. Hylleraas: *Über den Grundzustand des Heliumatoms*, (1928).

[Ili08]   S. Ilieva: *Investigation of the nuclear matter density distributions of the exotic*
          ^{12}Be, ^{14}Be *and* ^{8}B *nuclei by elastic proton scattering in inverse kinematics.*
          Fachbereich Physik, Johannes Gutenberg Universität Mainz, (2008).

[Ita83]   W. M. Itano: *Chemical-Shift Correction to the Knight-Shift in Beryllium*, Phys-
          ical Review B, **27**, 1906-1907, (1983).

[Jag74]   C. W. de Jager, H. de Vries and C. de Vries: *Nuclear Charge- and*
          Magnetization-Density Distribution Parameters from Elastic Electron Scatter-
          ing, Atomic Data and Nuclear Data Tables, **14**, 479-508, (1974).

[Jan72]   J. A. Jansen, R. T. Peerdeman and C. De Vries: *Nuclear charge radii of* ^{12}C
          and ^{9}Be, Nuclear Physics A, **188**, 337-352, (1972).

[Jon00]   D. J. Jones, S. A. Diddams, J. K. Ranka, A. Stentz, R. S. Windeler, J. L. Hall,
          S. T. Cundiff: *Carrier-Envelope Phase Control of Femtosecond Mode-Locked*
          Lasers and Direct Optical Frequency Synthesis, Science **288**, 634, (2000).

[Jon04]   B. Jonson: *Light dripline nuclei*, Physics Reports **389**, 1-59, (2004).

[Kau76]   S. L. Kaufman: *High-resolution laser spectroscopy in fast beams*, Optics Communications, **17**, 309-312, (1976).

[Kap98]   S. Kappertz: *Exotic Nuclei and Atomic Masses*, B. M. Sherrill *et al.* (Eds.), AIP 110 (1999).

[Kna00]   K. M. Knaak: *Konzeption und Aufbau eines Experiments zur Spectroskopischen Messung von Hochspannung* , Ruprecht Karls Universität, Heidelberg, (2000).

[Koe98]   U. Koester, J. Barker, R. Catherall, V.N. Fedoseyev, U. Georg, G. Huber, Y. Jading, O. Jonsson, M. Koizumi, K.-L. Kratz, E. Kugler, J. Lettry, V.I. Mishin, H.L. Ravn, V. Sebastian, C. Tamburella, A. Wöhr, and the ISOLDE Collaboration: *On-line separation of short-lived beryllium isotopes*, ENAM98 AIP Conf. Proc. **455**, 989, (1998).

[Kop95]   S. Kopecky, P. Riehs, J. A. Harvey and N. W. Hill: *New Measurement of the Charge Radius of the Neutron*, Physical Review Letters, **74**, 2427-2430, (1995).

[Kop97]   S. Kopecky, J. A. Harvey, N. W. Hill, M. Krenn, M. Pernicka, P. Riehs, and S. Steiner: *Neutron charge radius determined from the energy dependence of the neutron transmission of liquid ^{208}Pb and ^{209}Bi*, Physical Review C, **56**, 2229-2237, (1997).

[Kri09]   A. Krieger: *Aufbau eines jodstabilisierten Farbstofflasers zur kollinearen Spektroskopie und sein Einsatz zur Hochspannungsmessung an ISOLDE*, Master Thesis, Johannes Gutenberg-Universitt Mainz, (2008).

[Kub05]   P. Kubina, F. Adler, G. Grosche, T. Hnsch, R. Holzwarth, A. Leitenstorfer, B. Lipphardt, H. Schnatz, *Long term comparison of two fiber based frequency comb systems*, Optics Express, **13**, 3, (2005).

[Li71]   C. C. Li, I. Sick, R. R. Whitney and M. R. Yearian: *High-energy electron scattering from ^6Li*, Nuclear Physics A, **162**, 593-592, (1971).

[Mis06]   N. Miski-Oglu: *Bestimmung der absoluten Frequenz der a1 HFS-Komponente des $X^1\sum_{0g}^+ \rightarrow B^3\prod_{0u}^+$ R(114)11-2 Übergangs des Jod-Moleküls*, First Year Report, Universität Mainz, (2006).

[Mue07]   P. Müller, I. A. Sulai, A. C. C. Villari, J. A. Alcantara-Nunez, R. Alves-Conde, K. Bailey, G. W. F. Drake, M. Dubois, C. Eleon, G. Gaubert, R. J. Holt, R. V. F. Janssens, N. Lecesne, Z. T. Lu, T. P. O'Connor, M. G. Saint-Laurent, J. C. Thomas and L. B. Wang: *Nuclear Charge Radius of ^{8}He*, Physical Review Letters, **99**, 252501-4, (2007).

[Nak06]   T. Nakamura, M. Wada, K. Okada, A. Takamine, Y. Ishida, Y. Yamazaki, T. Kambara, Y. Kanai, T. M. Kojima, Y. Nakai, N. Oshima, A. Yoshida, T. Kubo, S. Ohtani, K. Noda, I. Katayama, V. Lioubimov, H. Wollnik, V. Varentsov and H. A. Schuessler: *Laser spectroscopy of $^{7,10}Be^{+}$ in an online ion trap*, Physical Review A, **74**, 052503-5, (2006).

[Nef09]   T. Neff, , priv. comm. (2009).

[Neu81]   R. Neugart: *Laser Spectroscopy on Mass-separated Radioactive Beams*, Nuclear Instruments and Methods, **186**, 165-175, (1981).

[Neu08]   R. Neugart, D. L. Balabanski, K. Blaum, D. Borremans, P. Himpe, M. Kowalska, P. Lievens, S. Mallion, G. Neyens, N. Vermeulen and D. T. Yordanov: *Precision Measurement of ^{11}Li Moments: Influence of Halo Neutrons on the ^{9}Li Core*, Physical Review Letters, **101**, 132502, (2008).

[Nob06]   G. A. Noble, B. E. Schultz, H. Ming and W. A. van Wijngaarden: *Isotope shifts and fine structures of Li-6,Li-7 D lines and determination of the relative nuclear charge radius*, Physical Review A, **74**,(2006).

[Noe03]   W. Nörtershäuser, A. Dax, G. Ewald, I. Katayama, R. Kirchner, H.-J. Kluge, T. Kühl, R. Sánchez, I. Tanihata, M. Tomaselli, H. Wang and C. Zimmermann: *A setup for high-resolution isotope shift measurements on unstable lithium isotopes*, Nuclear Instruments and Methods in Physics Research B, **204**, 644-648, (2003).

[Noe09]   W. Nörtershäuser, D. Tiedemann, M. Žáková, Z. Andjelkovic, K. Blaum, M. L. Bissell, R. Cazan, G. W. F. Drake, C. Geppert, M. Kowalska, J. Krämer, A. Krieger, R. Neugart, R. Sánchez, F. Schmidt-Kaler, Z. C. Yan, D. T. Yordanov and C. Zimmermann: *Nuclear Charge Radii of Be-7,Be-9,Be-10 and the One-Neutron Halo Nucleus Be-11*, Physical Review Letters, **102**, 062503, (2009).

[Noe09b]   W. Nörtershäuser, article in progress (2009).

[Nov09]   C. Novotny, G. Huber, S. Karpuk, S. Reinhardt, D. Bing, D. Schwalm, A. Wolf, B. Bernhardt, T. W. Hänsch, R. Holzwarth, G. Saathoff, Th. Udem, W. Nörtershäuser, G. Ewald, C. Geppert, T. Kühl, T. Stöhlker, G. Gwinner: *Sub-Doppler laser spectroscopy on relativistic beams and tests of Lorentz invariance*, Physical Review A **80**, 022107, (2009).

[Oka08]   K. Okada, M. Wada, T. Nakamura, A. Takamine, V. Lioubimov, P. Schury, Y. Ishida, T. Sonoda, M. Ogawa, Y. Yamazaki, Y. Kanai, T. M. Kojima, A. Yoshida, T. Kubo, I. Katayama, S. Ohtani, H. Wollnik and H. A. Schuessler: *Precision Measurement of the Hyperfine Structure of Laser-Cooled Radioactive $^7Be^+$ Ions Produced by Projectile Fragmentation*, Physical Review Letters, **101**, 212502, (2008).

[Okh04]   Oleg Okhotnikov, A. Grudinin, M. Pessa1 *Ultra-fast fibre laser systems based on SESAM technology: new horizons and applications*, New Journal of Physics (bf6) 177 (2004).

[Ott89]   E. W. Otten: *Nuclear Radii and Moments of unstable Isotopes*, Treatise on heavy ion science, Plenum Publishing Corp. (Springer), **8**, (1989).

[Pal03]   R. Palit, P. Adrich, T. Aumann, K. Boretzky, B. V. Carlson, D. Cortina, U. D. Pramanik, T. W. Elze, H. Emling, H. Geissel, M. Hellström, K. L. Jones, J. V. Kratz, R. Kulessa, Y. Leifels, A. Leistenschneider, G. Münzenberg, C. Nociforo, P. Reiter, H. Simon, K. Sümmerer and W. Walus: *Exclusive measurement of breakup reactions with the one-neutron halo nucleus ^{11}Be*, Physical Review C, **68**, 034318, (2003).

[Pie01]   S. C. Pieper and R. B. Wiringa: *Quantum Monte Carlo Simulations of Light Nuclei*, Annual Review of Nuclear and Particle Science, **51**, 53-90, (2001).

[Pie02]   S. C. Pieper, K. Varga, and R. B. Wiringa: *Quantum Monte Carlo calculations of A = 9,10 nuclei*, Physical Review C, **66**, 044310, (2002).

[Pei09]   E. Peik, PTB Braunschweig, private comm. (2009).

[Puch06]   M. Puchalski, A. M. Moro and K. Pachucki: *Isotope Shift of the $3^2S_{1/2} - 2^2S_{1/2}$ Transition in Lithium and the Nuclear Polarizability*, Physical Review Letters, **97**, 133001-4, (2006).

[Puch06]   M. Puchalski and K. Pachucki: *Ground-state wave function and energy of the lithium atom*, Physical Review A, **73**, 022503, (2006).

[Puch08] M. Puchalski and K. Pachucki: *Relativistic, QED, and finite nuclear mass corrections for low-lying states of Li and Be$^+$*, Physical Review A, **78**, 052511, (2008).

[Puch09] M. Puchalski and K. Pachucki: *Fine and hyperfine splitting of the 2P state in Li and Be$^+$*, Physical Review A, **79**, 032510, (2009).

[Puch09b] M. Puchalski, private comm., (2009).

[Rad95] L. J. Radziemski, J. R. Engleman and J. W. Brault: *Fourier-transform-spectroscopy measurements in the spectra of neutral lithium, ^{6}Li I and ^{7}Li I (LI I)*, Physical Review A, **52**, 4462-4470, (1995).

[Rei07] S. Reinhardt, B. Bernhardt, C. Geppert, R. Holzwarth, G. Huber, S. Karpuk, N. Miski-Oglu, W. Nrtershuser, C. Novotny and T. Udem: *Absolute frequency measurements and comparisons in iodine at 735 nm and 772 nm*, Optics Communications, **274**, 354-360, (2007).

[Rei07b] S. Reinhardt, G. Saathoff, H. Buhr, L. Carlson, A. Wolf, D. Schwalm, S. Karpuk, C. Novotny, G. Huber, M. Zimmermann, R. Holzwarth, T. Udem, T. Hänsch and G. Gwinner: *Test of relativistic time dilation with fast optical atomic clocks at different velocities*, Nature Physics, **3**, 1-4, (2007).

[Rei07c] S. Reinhardt, G. Saathoff, H. Buhr, L. A. Carlson, A. Wolf, D. Schwalm, S. Karpuk, Ch. Novotny, G. Huber, M. Zimmermann, R. Holzwarth, T. Udem, T. W. Hänsch, G. Gwinner: *Test of relativistic time dilation with fast optical atomic clocks at different velocities*, Nature Physics **3**, 861-864, (2007).

[Rii06] K. Riisager:*Nuclear Halos and Experiments to Probe Them*, The Euroschool Lectures on Physics with Exotic Beams, Vol. II, **651**, (2004).

[Rin09] R. Ringle, M. Brodeur, T. Brunner, S. Ettenauer, M. Smith, A. Lapierre, V. L. Ryjkov, P. Delheij, G. W. F. Drake, J. Lassen, D. Lunney and J. Dilling: *High-precision Penning trap mass measurements of Be-9,Be-10 and the one-neutron halo nuclide Be-11*, Physics Letters B, **675**, 170-174, (2009).

[Sal07] B. E. A Saleh, M. C. Teich: *Fundamentals of Photonics*, Wiley & Sons, (2007).

[San05] R. Sánchez: *Nuclear Charge Radius of the Halo Nucleus Lithium-11*, Fachbereich Physik, Johannes Gutenberg-Universität Mainz, (2005).

[San06]   R. Sánchez, W. Nörtershäuser, G. Ewald, D. Albers, J. Behr, P. Bricault, B.
           A. Bushaw, A. Dax, J. Dilling, M. Dombsky, G. W. F. Drake, S. Götte, R.
           Kirchner, H.-J. Kluge, T. Kühl, J. Lassen, C. D. P. Levy, M. R. Pearson, E.
           J. Prime, V. Ryjkov, A. Wojtaszek, Z.-C. Yan and C. Zimmermann: *Nuclear
           Charge Radius of ^{11}Li: the Influence of Halo Neutrons*, Physical Review Let-
           ters, **96**, 033002, (2006).

[San09]   R. Sánchez, M. Žáková, Z. Andjelkovic, B. Bushaw, K. Dasgupta, G. Ewald,
           C. Geppert, H.-J. Kluge, J. Krämer, M. Nothhelfer, D. Tiedemann, D. Win-
           ters and W. Nörtershäuser: *Absolute frequency measurements on the $2S - 3S$
           transition of lithium-6,7*, New Journal of Physics, **11**, 073016, (2009).

[Scha80]   L. A. Schaller, L. Schellenberg, A. Ruetschi and H. Schneuwly: *Nuclear charge
           radii from muonic X-ray transitions in beryllium, boron, carbon and nitrogen*,
           Nuclear Physics A, **343**, 333-346, (1980).

[Sic75]   I. Sick,B. Bellicard, M. Bernheim, B. Frois, M. Huet, Ph. Leconte, J. Mougey,
           Phan Xuan-Ho, D. Royer, and S. Turck *Shell Structure of the ^{58}Ni Charge
           Density*, Physical Review Letters, **35**, 910, (1975).

[Sic03]   I. Sick: *On the rms-radius of the proton*, Physics Letters B, **576**, 62-67, (2003).

[Sic08]   I. Sick: *Precise root-mean-square radius of He-4*, Physical Review C, **77**,
           041302(R), (2008).

[Sic09]   I. Sick, private communication, 2009

[Sim05]   H. Simon: *Technical Proposal for the Design, Construction, Commissioning,
           and Operation of the ELISe setup*, GSI, (2005).

[Sto05]   N. J. Stone: *Table of nuclear magnetic dipole and electric quadrupole moments*,
           Atomic Data and Nuclear Data Tables, **90**, 75-176, (2005).

[Sue67]   L. R. Suelzle, M. R. Yearian and H. Crannell: *Elastic Electron Scattering from
           ^6Li and ^7Li*, Physical Review, **132**, 9921004, (1967).

[Sun91]   D. Sundholm and J. Olsen: *Large MCHF calculations on the hyperfine structure
           of Be(^3P_O): the nuclear quadrupole moment of ^9Be*, Chemical Physics Letters,
           177, 1, 91-97, (1991).

[Suz98]   Y. Suzuki, N. Tanaka and K. Varga: *Stochastic variational method for light
           unstable nuclei*, Journal of Physics G, **24**, 1491-1497, (1998).

[Tan85]   I. Tanihata, H. Hamagaki, O. Hashimoto, Y. Shida, N. Yoshikawa, K. Sugi-moto, O. Yamakawa, T. Kobayashi and N. Takahashi: *Measurements of interaction cross sections and nuclear radii in the light p-shell region*, Physical Review Letters, **55**, 2676-2679, (1985).

[Tan88]   I. Tanihata, T. Kobayashi, O. Yamakawa, S. Shimoura, K. Ekuni, K. Sugimoto, N. Takahashi, T. Shimoda and H. Sato: *Measurement of Interaction Cross-Sections Using Isotope Beams of Beryllium and B and Isospin Dependence of the Nuclear Radii*, Physics Letters B, **206**, 592-596, (1988).

[Tan96]   I. Tanihata: *Neutron halo nuclei*, Journal of Physics G, **22**, 157-198, (1996).

[Tie09]   D. Tiedemann: *Nuclear charge radius determination of $^{7,10}Be$ and the one-neutron halo nucleus ^{11}Be*. Institut für Kernchemie, Johannes Gutenberg-Universität Mainz, (2009).

[Tor08]   R. Torabi, GSI, priv. comm. (2008).

[Ude97]   T. Udem, A. Huber, B. Gross, J. Reichert, M. Prevedelli, M. Weitz and T. W. Hänsch: *Phase-Coherent Measurement of the Hydrogen $1S-2S$ Transition Frequency with an Optical Frequency Interval Divider Chain*, Physical Review Letters, **79**, 2646-2649, (1997).

[Wan04]   L.-B. Wang, P. Mueller, K. Bailey, G. W. F. Drake, J. P. Greene, D. Henderson, R. J. Holt, R. V. F. Janssens, C. L. Jiang, Z.-T. Lu, T. P. O'Connor, R. C. Pardo, K. E. Rehm, J. P. Schiffer, and X. D. Tang: *Laser Spectroscopic Determination of the ^6He Nuclear Charge Radius*, Physical Review Letters, **93**, 142501, (2004).

[Wan04b] L.-B. Wang: *Determination of the helium-6 nuclear charge radius using high-resolution laser spectroscopy*, University of Illinois at Urbana-Champaign, (2004).

[Was03]   B. R. Washburn, S. Diddams, N. R. Newbury, J. W. Nicholson, M. F. Yan, C. G. Jrgensen, *Phase-locked, erbium-fiber-laser-based frequency comb in the near infrared*, Optics Letters, **29**, 3 (2004).

[Win83]   D. J. Wineland, J. J. Bollinger and W. M. Itano: *Laser-Fluorescence Mass Spectroscopy*, Physical Review Letters, **50**, 628-631, (1983).

[Yan96]   F. Yang, H. J. Hamilton: *Modern Atomic and Nuclear Physics*, The McGraw-Hill Companies, (1996).

[Yan00]   Z.-C. Yan and G. W. F. Drake: *Lithium isotope shifts as a measure of nuclear size*, Physical Review A, **61**, 022504, (2000).

[Yan02]   Z.-C. Yan and G. W. F. Drake: *Lithium transition energies and isotope shifts: QED recoil corrections*, Physical Review A, **66**, 042504-1 - 8, (2002).

[Yan03]   Z.-C. Yan and G. W. F. Drake: *Bethe Logarithm and QED Shift for Lithium*, Physical Review Letters, **91**, 113004, (2003).

[Yan08]   Z. C. Yan, W. Nörtershäuser and G. W. F. Drake: *High precision atomic theory for Li and Be$^+$: QED shifts and isotope shifts*, Physical Review Letters, **100**, 243002, (2008).

[Yan08b] Z. C. Yan, W. Nörtershäuser and G. W. F. Drake: *Erratum: High Precision Atomic Theory for Li and Be$^+$: QED Shifts and Isotope Shifts*, Physical Review Letters, **102**, 249903(E), (2009).

[Zak10]   M. Žáková, Z. Andjelkovic, M. L. Bissell, K. Blaum, G.W.F. Drake, Ch. Geppert, M. Kowalska, J. Krämer, A. Krieger, T. Neff, R. Neugart, M. Lochmann, R. Sánchez, F. Schmidt-Kaler, D. Tiedemann, Z.-C. Yan, D. T. Yordanov, C. Zimmermann, W. Nörtershäuser: *Isotope shift measurements in the $2s_{1/2} - 2p_{3/2}$ transition of Be$^+$ and extraction of the nuclear charge radii for ^{7,10,11}Be*, to be submitted, (2010).

New Journal of Physics

Absolute frequency measurements on the 2S → 3S transition of lithium-6,7

Rodolfo Sánchez[1,5]**, Monika Žáková**[2]**, Zoran Andjelkovic**[2]**,
Bruce A Bushaw**[3]**, Kamalesh Dasgupta**[4]**, Guido Ewald**[1]**,
Christopher Geppert**[1,2]**, H-Jürgen Kluge**[1]**, Jörg Krämer**[2]**,
Matthias Nothhelfer**[2]**, Dirk Tiedemann**[2]**, Danyal F A Winters**[1]
and Wilfried Nörtershäuser[1,2]

[1] GSI Helmholtzzentrum für Schwerionenforschung GmbH, Planckstrasse 1,
D-64291 Darmstadt, Germany
[2] Institut für Kernchemie, Johannes Gutenberg-Universität Mainz,
Fritz-Straßman-Weg 2, D-55128 Mainz, Germany
[3] Chemical Sciences Division, Pacific Northwest National Laboratory,
Richland, WA 99352, USA
[4] Bhabha Atomic Research Center, Mumbai 400085, India
E-mail: R.Sanchez@gsi.de

Abstract. The frequencies of the 2S–3S two-photon transition for the stable lithium isotopes were measured by cavity-enhanced Doppler-free laser excitation that was controlled by a femtosecond frequency comb. The resulting values of 815 618 181.57(18) and 815 606 727.59(18) MHz, respectively, for ^{7}Li and ^{6}Li are in agreement with previous measurements but are more accurate by an order of magnitude. There is still a discrepancy of about 11.6 and 10.6 MHz from the latest theoretical values. This is comparable to the uncertainty in the theoretical calculations, while uncertainty in our experimental values is more than a hundred-fold smaller. More accurate theoretical calculation of the transition frequencies would allow extraction of the absolute charge radii for these stable isotopes, which in turn could improve nuclear charge radii values for the unstable lithium isotopes.

[5] Author to whom any correspondence should be addressed.

IOP Institute of Physics ⏀ DEUTSCHE PHYSIKALISCHE GESELLSCHAFT

Contents

1. Introduction

The binding energy of an atomic state is one of the most fundamental quantities in quantum mechanics. Experiments can nowadays reach accuracy levels sufficient to extract improved values of fundamental constants like the fine structure constant α or to probe the structure of the nucleus. Even though the nucleus is five orders of magnitude smaller than the atom, its finite size significantly alters atomic energy levels. A second effect that can alter the energy level is the electric polarizability of the nucleus. This contribution is usually on the kHz scale but for exotic nuclei with large $B(E1)$ linestrength this effect can be larger. The contribution has been recently calculated for the first time for a halo nucleus and was found to contribute with 39 kHz to the isotope shift between ^{9}Li and ^{11}Li [1]. Calculations for ^{11}Be, the nucleus with the largest known $B(E1)$ strength, give a contribution of 208(21) kHz [2].

A complete treatment of level energies and isotope shifts requires the consideration of non-relativistic, relativistic, quantum electrodynamical (QED) and nuclear structure contributions. The non-relativistic energies and lowest-order relativistic corrections can now be calculated to spectroscopic accuracy [2]–[7], but the QED corrections still limit the overall accuracy. One of the main difficulties and long-standing problems was the calculation of the so-called Bethe logarithm, which is the dominant part of the electron self-energy. Its calculation for hydrogen-like [8] and helium-like systems [9] was recently followed by the report of the complete calculation of QED terms up to the order of α^3 Ry [2, 7, 10] for lithium atoms. In [10] Yan and Drake calculated the Bethe logarithm $\ln k_0$ to a relative accuracy of 10^{-6}, and in [11] Pachucki reports on the Bethe logarithm of the four-electron system beryllium with a relative accuracy of 10^{-5}.

The main motivation of these theoretical works was the accurate determination of the mass-dependent terms in the transition energies that lead to the so-called mass shift in the transition frequencies between different isotopes of the same element. Accurately calculated mass shifts play a key role in several experiments that determine the charge radius of halo isotopes, which have been carried out recently [12]–[17] or are planned for the near future [18, 19]. In these experiments, the change in the transition frequency between the isotopes A

Table 1. Contributions of the various expansive terms to the absolute 2S–3S transition energy in ^{7}Li. All values are in given MHz. Values from [2] are based on table III in this reference.

Term	Yan et al [7] [a]	Puchalski and Pachucki [2]
E_{NR}	$815\,561\,313.44 \pm 0.03$	$815\,561\,313.5 \pm 0.1$
E_{Rel}	$62\,629.4 \pm 0.6$	$62\,628.0 \pm 0.7$
E_{QED}	-5768 ± 30	-5763 ± 19
E_{FS}	-8.95 ± 0.24	-8.9 ± 0.2
Total	$815\,618\,166 \pm 30$	$815\,618\,170 \pm 19$

[a] Erratum submitted to *Phys. Rev. Lett.*

and A' (the isotope shift $\delta\nu^{A,A'}$) was accurately measured. After subtracting the calculated mass-dependent shift, the so-called field shift is obtained, which is due to the change in the nuclear charge distribution between the isotopes A and A'. This field shift is sensitive to $\delta\langle r^2\rangle^{A,A'}$, i.e. the change in the mean-square nuclear charge radius. To determine the charge radii in a series of isotopes, a reference charge radius has to be measured using a different method, e.g. electron scattering. Unfortunately, these scattering experiments are usually much less accurate than optical measurements and the uncertainty of the reference radius often dominates the final uncertainty of the nuclear charge radii. Thus, it would be very advantageous if the total charge radius of an isotope could be extracted directly from optical measurements. In principle, this should be possible because the transition frequency carries information about the total nuclear charge radius. The total energy of an atomic state is usually expanded in the form

$$E = E_{\mathrm{NR}} + E_{\mathrm{Rel}} + E_{\mathrm{QED}} + E_{\mathrm{FS}}, \tag{1}$$

where E_{NR} is the non-relativistic energy, E_{Rel} is the relativistic correction, E_{QED} is the QED shift and E_{FS} is the finite nuclear size correction. The most accurate treatments available solve the non-relativistic Schrödinger equation variationally in multiple-basis sets in Hylleraas coordinates [10, 11] and use the resulting wave functions to calculate relativistic and QED corrections perturbatively. Table 1, summarized from [2, 7, 20], lists the different contributions to the $1\mathrm{s}^2\,2\mathrm{s}\,^2\mathrm{S}_{1/2} - 1\mathrm{s}^2\,3\mathrm{s}\,^2\mathrm{S}_{1/2}$ transitions in ^{7}Li. The non-relativistic contributions include the first- and second-order mass polarization term. E_{Rel} are the lowest-order α^2 Ry relativistic corrections from the Breit–Pauli interaction, including the first-order mass polarization term, and E_{QED} include the lowest-order α^3 Ry electron–nucleus and electron–electron terms, and higher-order terms of $O(\alpha^4\,\mathrm{Ry})$ and higher. The total transition energy deviates from the value reported in [7] because instead of using the Bethe logarithm reported in table I in [7] for calculating the transition frequency, an obsolete value from [10] has been used erroneously.

The nuclear size contribution E_{FS} has been calculated using a ^{7}Li charge radius of 2.39(3) fm [21, 22] determined by elastic electron-scattering. According to [10], the field shift can be calculated from

$$E_{\mathrm{FS}} = \left(C_{r_{\mathrm{rms}}^2}^{(0)} + C_{r_{\mathrm{rms}}^2}^{(1)} \frac{\mu}{M} \right) r_{\mathrm{rms}}^2, \tag{2}$$

with $C_{r_{\mathrm{rms}}^2}^{(0)} = 1.5664\,\mathrm{MHz\,fm^{-1}}$ and $C_{r_{\mathrm{rms}}^2}^{(1)} = 4.652\,\mathrm{MHz\,fm^{-2}}$, μ is the electron reduced mass and M is the nuclear mass. Elastic electron scattering provides reliable nuclear charge radii for

stable isotopes. The uncertainty of the results, however, limits the accuracy with which the radii for heavier lithium isotopes can be determined using isotope shift measurements by optical spectroscopy. Presently, the uncertainty in the transition frequency calculation is twice as large as the total nuclear size contribution. The calculated frequency can be compared with the so-far most accurate 2S–3S transition frequency determination of $\nu_0 = 815\,618\,185(3)$ MHz [23]. The theoretical values [2, 7] agree within the estimated theoretical uncertainties, which are about ten times larger than the experimental uncertainty. If the calculated accuracy can be improved by about two orders of magnitude, a direct determination of the nuclear charge radius from the optical measurements comes into reach. According to (1) and (2), the charge radius can be then calculated from

$$r_{\text{rms}}^2 = \frac{\nu_0 - (E_{\text{NR}} + E_{\text{Rel}} + E_{\text{QED}})}{C_{r_{\text{rms}}^2}^{(0)} + C_{r_{\text{rms}}^2}^{(1)} \frac{\mu}{M}} \; . \tag{3}$$

A total accuracy of $\delta \nu_0 \approx 200$ kHz in the transition frequency measurement and a comparably small uncertainty in the theoretical part $\delta \nu_{\text{Theory}}$ will allow for a determination of the charge radius with an accuracy of

$$\delta r_{\text{rms}} = \frac{1}{2 r_{\text{rms}}} \frac{1}{C_{r_{\text{rms}}^2}^{(0)} + C_{r_{\text{rms}}^2}^{(1)} \frac{\mu}{M}} \sqrt{\left(\delta \nu_0\right)^2 + \left(\delta \nu_{\text{Theory}}\right)^2} \approx 0.038 \, \text{fm}, \tag{4}$$

which is comparable to the current uncertainty from electron scattering but relies purely on optical measurements and model-independent atomic theory. A similar approach has been used for hydrogen [24] for which QED calculations and transition frequency measurements have already reached a much higher accuracy.

Here, we report the measurement of a lithium transition frequency with a femtosecond laser frequency comb that could lead to a direct charge radius determination, once theory has reached comparable precision. The accuracy in the 2S–3S transition frequency is improved by one order of magnitude compared to the previous measurement [23].
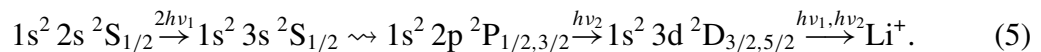
2. Experimental set-up

The 2S–3S two-photon transition was induced in a thermal atomic beam of lithium atoms and the excitation was monitored by resonance ionization spectroscopy followed by single ion detection with a quadrupole mass spectrometer (QMS). For the measurements presented here, two atom sources were used. The first, which is schematically shown in figure 1, was a resistively heated graphite tube loaded with lithium metal. The graphite tube has a diameter of 2 mm, an inner length of 20 mm and it was heated by a current of typically 40 A. The furnace exit was located approximately 30 cm away from the ionization region of a commercial QMS. This ionization region has a cylindrical shape with a 4.5 mm diameter entrance aperture, hence, the atom beam entering the interaction region with the laser beam was collimated to approximately 1°. In a second set of experiments, a dilute solution of lithium nitrate was deposited onto a thin carbon foil located a few millimeters away from the first electrostatic lens. The graphite foil was then heated with a few watts from a CO_2 laser focused onto the foil, which raised the foil temperature above 1800 °C. The lithium nitrate was reduced and lithium atoms were released from the foil. The atoms left the surface with a $\cos^2$ distribution and entered the interaction region with practically no collimation. This geometry was chosen to have the same conditions as in the isotope shift measurements of radioactive isotopes [12, 15].
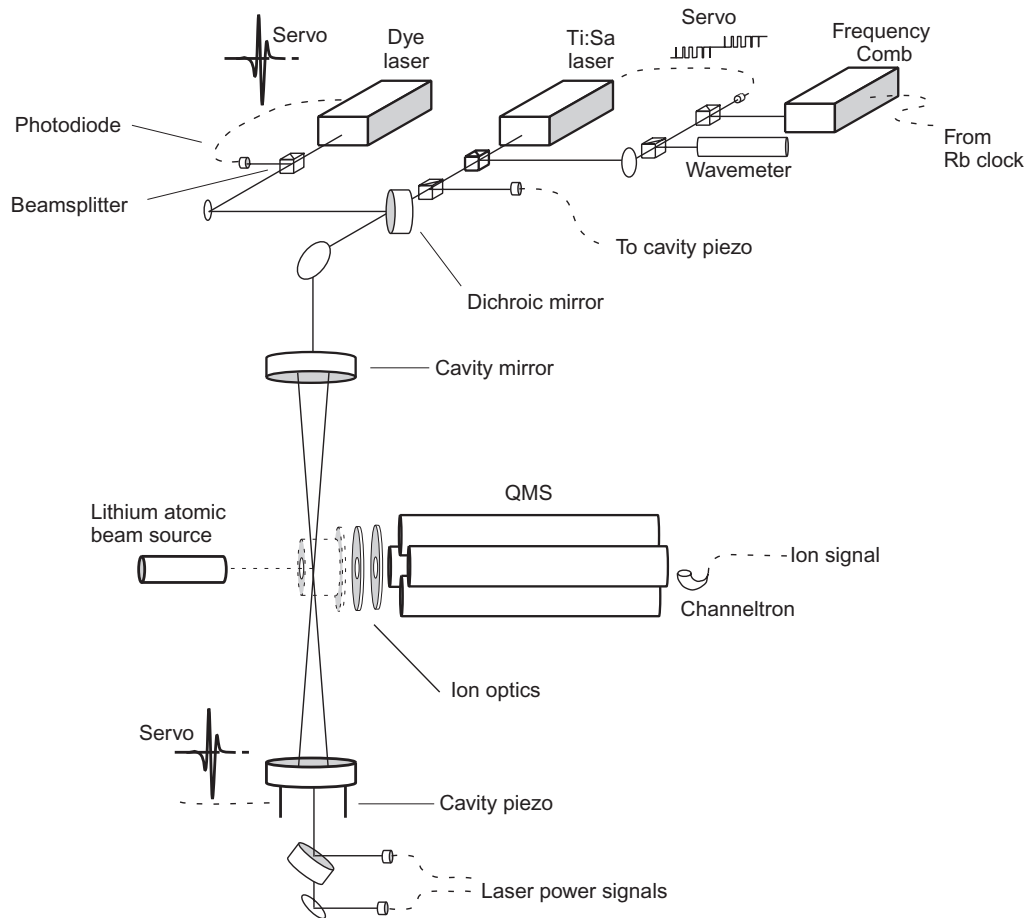
Figure 1. Experimental set-up.

The ionization region consists of a small cylinder with two holes on the barrel with about 4 mm in diameter through which the laser beams entered. Atoms crossing this region were excited and ionized by laser light from two lasers with wavelengths $\lambda_1 = 735.1$ nm and $\lambda_2 = 610.5$ nm along the excitation path

$$1s^2\,2s\,^2S_{1/2} \overset{2h\nu_1}{\to} 1s^2\,3s\,^2S_{1/2} \rightsquigarrow 1s^2\,2p\,^2P_{1/2,3/2} \overset{h\nu_2}{\to} 1s^2\,3d\,^2D_{3/2,5/2} \overset{h\nu_1,h\nu_2}{\longrightarrow} Li^+. \qquad (5)$$

The first step is a two-photon excitation followed by spontaneous decay to the 2P level out of which the electron is further promoted via the 3D level into the continuum. Resulting ions were extracted out of the interaction region into the QMS, mass separated and detected with a continuous dynode electron multiplier (CDEM) [25]. The extraction and detection efficiency for the ions was above 50%. Laser light for the two resonant transitions was produced with an argon-ion laser pumped titanium:sapphire (Ti:Sa) laser (Model Coherent 899-21, 735 nm) and a Rhodamine-6G ring dye laser (Coherent 699-21, 610 nm) that was pumped by a frequency-doubled Nd:YVO$_4$ laser (Coherent Verdi-V8). The laser light was transported to the experimental set-up with two single-mode fibers. To produce counter-propagating beams for the two-photon excitation and to obtain the high intensities that are required to drive the two-photon transition, the laser light from the Ti:Sa laser was coupled into a symmetric spherical-mirror optical resonator mounted inside the vacuum chamber. One of the resonator

mirrors was positioned with a piezoelectric transducer and the cavity length was locked to the Ti:Sa laser by the Pound–Drever–Hall (PDH) locking technique [26] to ensure continuous resonance enhancement for all frequencies. Simultaneous enhancement for both laser beams inside the optical resonator was achieved by combining the beams with a dichroic beamsplitter and locking the dye laser to the optical resonator by controlling its frequency, again using the PDH locking. A small amount of laser light, proportional to the light power circulating within the resonance cavity, exited the cavity through the high-reflector, and left the vacuum chamber through a wedged viewport (to avoid interference effects in measurements of the transmitted laser intensities). It was separated again into the two wavelength components with another dichroic beamsplitter. Each beam was directed onto a photodiode and the photocurrent was recorded to track the laser powers inside the cavity.

The maximum output power of the Ti:Sa (dye) laser was 1200 mW (400 mW) of which up to 900 mW (250 mW) was transported through the fiber. After the optics for phase modulation used for PHD locking, beam shaping for mode matching and dye-Ti:Sa beam overlap, about 600 mW (150 mW) was left at the viewport into the vacuum chamber. With this input power, a power of approximately 40 mW (7 mW) was observed at the photodiode behind the cavity. Spherical cavity mirrors, with 500 mm radius of curvature and spaced by 300 mm, yielded a cavity g-parameter of 0.16. The calculated focal spot size at the center of the cavity was 0.46 mm. Combined with the 98% reflectivity of the input mirror and a finesse of 110, the calculated intensity of the Ti:Sa laser beam in the interaction region was roughly 400 W mm^{-2}, which is larger than the estimated saturation intensity of $\approx$170 W mm^{-2}. For the dye laser a maximum intensity of 74 W mm^{-2} was expected, a value that surpasses the theoretical saturation intensity of $I_{\text{Sat}} = \pi h c A_{\text{3D–2P}}/\lambda^3 = 0.18$ mW mm^{-2} (where $A_{\text{3D–2P}} = 8.653 \times 10^7$ [27] has been used) by orders of magnitude. This leads to strong saturation broadening of the 2P–3D dipole transition such that the fine structure of both levels was covered within the linewidth and an almost constant excitation efficiency was observed over a range of 2 GHz. The ionization step was non-resonant and it was not sensitive to the exact frequencies of the laser.

The Ti:Sa laser was phase-locked to one of the modes of a commercial fiber-laser-based femtosecond frequency comb (Menlo Systems, Model FC 1500). The erbium-doped fiber laser was operated at a wavelength of approximately 1560 nm and a frequency comb in the red and near infrared region was produced by frequency doubling and subsequent spectral broadening in a nonlinear fiber. The laser repetition rate, ν_{rep}, of approximately 100 MHz was stabilized by comparing the output of a radio frequency (RF) generator (Stanford Research Systems, Model SRS 543) with the difference between the 98th harmonic of the 10 MHz output of a rubidium clock (Stanford Research Systems, Model FS 725) and the 10th harmonic of the repetition rate that was recorded with a fast photodiode. By varying the SRS frequency between 19 and 21 MHz the repetition rate of the laser was chosen between 99.9 and 100.1 MHz. The beat signal, ν_{Beat}, between the Ti:Sa laser and the nearest comb mode was detected with a fast photodiode and stabilized to an offset frequency of 30 MHz with a digital phase-lock system (Menlo Systems, FCX 200). The servo signal for the stabilization of the Ti:Sa-laser was applied to the external-scan input of the Coherent 899-21 controller. This limited the servo bandwidth to approximately 100 Hz but the fast internal stabilization of the Ti:Sa laser to its reference cavity reduced the laser linewidth to about 1 MHz. Once the Ti:Sa laser frequency was locked to the nth comb mode it was calculated according to

$$\nu_{\text{Ti:Sa}} = n \times \nu_{\text{rep}} \pm 2 \times \nu_{\text{CEO}} \pm \nu_{\text{Beat}}, \tag{6}$$
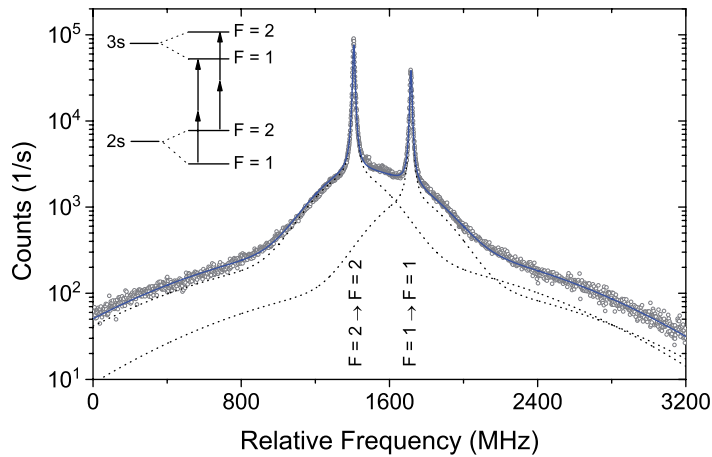
Figure 2. Overall lineshape for the 2S–3S two-photon transition in ^{7}Li. The Ti:Sa laser frequency is given relative to the frequency comb mode of 407 807 570 MHz. The line is the overall fit to the experimental points (○). The dotted lines are the contributions of the individual peaks.

where n is the number of the comb mode to which the laser was locked. The carrier envelope offset ν_{CEO} of the femtosecond laser was stabilized to 20 MHz and it was doubled to account for the laser frequency doubling. The Ti:Sa-comb beat frequency $\nu_{Beat} = 30$ MHz was stabilized as described above. The sign of the CEO and beat frequencies were determined experimentally and they were then fixed during the measurements. The mode number n can either be determined from a set of measurements at different repetition rates or by using a lambdameter with a resolution of better than 100 MHz. We have used a Fizeau–Interferometer (ATOS). The Ti:Sa laser frequency can then be tuned in a controlled and precise manner by changing the repetition frequency of the femtosecond fiber laser. Therefore, the frequency of the SRS RF generator was computer controlled via a GPIB interface. Scans of the hyperfine structure of the lithium transitions were recorded by changing the repetition rate in steps of 0.1 Hz. This corresponded to a step width of approximately 410 kHz ($n \approx 4\,100\,000$) in the Ti:Sa laser frequency and, thus, about 820 kHz in the two-photon transition frequency.

The dye laser frequency was tuned close to the resonance of the 2p ^{2}P$_{3/2}$ → 3d ^{2}D$_{5/2}$ transition and then locked to the nearest longitudinal mode of the enhancement cavity. Hence, the frequency was not fixed exactly on the resonance transition. However, due to the enhanced power inside the cavity, the transition was broadened to about 10 GHz (full-width at half-maximum (FWHM)) with a flat-top region of 2 GHz. Therefore the exact frequency position as well as the small frequency shift that appears during a scan of the Ti:Sa laser frequency did not have a detectable influence on the transition probability and, hence, on the lineshape of the resonance line.

3. Overall spectrum

Figure 2 shows a spectrum recorded for ^{7}Li. At the start of the scan, the Ti:Sa was locked to comb mode number 4 078 075 at 100 MHz repetition frequency and both beat note and carrier offset frequency were locked with positive sign, resulting in a total Ti:Sa frequency of 407 807 570 MHz. The scan was performed by increasing the repetition rate in steps of 0.5 Hz

(2.04 MHz of the Ti:Sa frequency) and integrating the ion counts for 1 s at each point. The transition is splitted into two hyperfine components ($I = 3/2$ for ^{7}Li) as shown schematically in the inset of figure 2. The selection rules for a $^2S_{1/2} \rightarrow ^2S_{1/2}$ transition require $\Delta F = 0$, hence, only two lines were observed.

The centers of the two lines were found by fitting theoretical line profiles to the signal. The fit function was a sum of two Gaussian pedestals, corresponding to Doppler-broadened excitation in the atomic beam (FWHM = 800 MHz) and in the background gas (FWHM = 1.6 GHz), and a Voigt profile for the Doppler-free two photon excitation. The fitting function includes nine free parameters: these are the positions of the two peaks that are also identical with the background Gaussian centers, the Gaussian and Lorentzian widths of the Voigt profiles, the widths of the two background Gaussians, the amplitude of the Voigt profile and the amplitude of the two background Gaussians relative to the Voigt profile intensity. Besides the absolute amplitude of the Voigts and their positions, all parameters were constrained to be identical for both hyperfine components. No additional baseline offsets were used in the fit. The Gaussian backgrounds were both produced by the simultaneous absorption of two co-propagating photons whereas the Doppler-free component arose from the absorption of counter-propagating photons. In previous atomic beam measurements [23], we observed similar spectra but with a much smaller width of only 30 MHz for the stronger Gaussian component. This was attributed to Doppler-broadened excitation of lithium atoms in the well collimated atomic beam. The much larger width observed here was probably due to lower atomic beam collimation and scattering due to the higher background gas pressure. In the present experiment, the atomic beam oven was not operated in a separate chamber with a differential pumping as it was done in [23]. Nonetheless the model function fitted the observed spectrum very well with a reduced $\chi^2 = 1.18$. The Doppler-free peak had a 10.6 MHz (FWHM) Lorentzian component. This was about twice the 5.3 MHz expected from the 29.8 ns lifetime of the 3S level [27, 28], mainly caused by power broadening. The Gaussian component of the Voigt had a width of 4.3 MHz, which was about 3–4 times the laser jitter width of the Ti:Sa laser of about 1.2 MHz.

Once the center of the two hyperfine transitions was obtained, the center of gravity (cg) of the hyperfine structure was calculated according to

$$\nu_{cg} = \tfrac{5}{8}\nu_{F=2 \rightarrow F=2} + \tfrac{3}{8}\nu_{F=1 \rightarrow F=1} \tag{7}$$

for ^{7}Li and

$$\nu_{cg} = \tfrac{2}{3}\nu_{F=3/2 \rightarrow F=3/2} + \tfrac{1}{3}\nu_{F=1/2 \rightarrow F=1/2} \tag{8}$$

for ^{6}Li, respectively.

4. Skip-step scans

To obtain better statistics for the determination of peak positions, skip-step scans were used as shown in figure 3. High-resolution scans were recorded in a 30 MHz frequency window around each resonance with steps of 0.8 MHz while inter-peak regions were scanned quickly without data acquisition (skipped steps). Figure 3 shows spectra for two different Ti:Sa laser powers: (a) 100% and (b) 25% of the maximum power available. The solid line represents the overall fitting function that includes the Gaussian backgrounds with linewidth parameters fixed at values obtained from the overall spectrum in figure 2. The intensity of the Doppler-free components, their Gaussian and Lorentzian Voigt component widths and their amplitudes relative to the Doppler-broadened Gaussian background were used as fitting parameters.
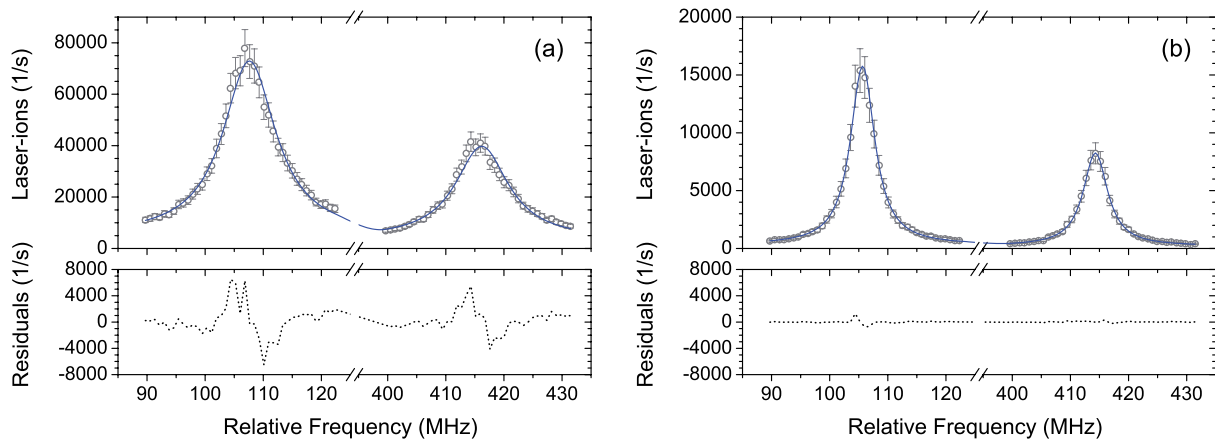
Figure 3. Skip-step scans of ^{7}Li for Ti:Sa laser intensity of (a) $430\,W\,mm^{-2}$ and (b) $110\,W\,mm^{-2}$. The black lines are the fits while the dotted lines show the behavior of the residuals. The frequency axes are relative to the start frequency of the scan of $407\,808\,870\,MHz$.

Below each resonance, the residual between the experimental data and the fitted function are shown. An asymmetry of the recorded spectrum, that is not reproduced by the fitting function, can be clearly observed, particularly at high laser power (a). We tested whether this effect could be caused by an asymmetry of the Gaussian pedestal which could arise from a misalignment of the atomic beam, but we found that the asymmetry was too strong to arise from the weak background. Moreover, the strong power dependence would not be expected in this case. We assume that the asymmetry is caused by a spatially dependent ac-Stark shift as will be discussed below.

Skip-step spectra like those shown in figure 3 were recorded for varying intensities of the Ti:Sa and of the dye lasers. The observed resonances were fitted and the center of gravity of the hyperfine structure was calculated. Figure 4 shows the measured centers of gravity as a function of the Ti:Sa laser power measured behind the cavity. During these measurements the dye laser power was kept constant. The data points are well described by a linear function, as expected for an ac-Stark shift with the lasers far-off resonance for all dipole transition involving the 2S or 3S levels. The extrapolated frequency at zero laser power is the resonance frequency unperturbed by the Ti:Sa laser field. To eliminate similar ac-Stark shifts from the dye laser, we plotted all measurements with varying dye and Ti:Sa laser powers three-dimensionally and fitted a plane to the data points. In this way the actual laser power in each measurement can be directly plotted and small drifts of the dye laser power during an ac-Stark shift measurement with the Ti:Sa laser do not influence the result. The data points and the fitted plane are shown in figure 5.

Typically we used about 50 measurements for a single extrapolation to the intercept frequency at the point of zero dye and Ti:Sa intensities. Reduced χ^2 of these fits were between 1 and 5 and the uncertainties obtained from the fitting routine were scaled with the square root of χ^2_{red}. We have recorded about 150 spectra for ^{7}Li over three days with both types of atom sources (see section 2). Those were combined to three data sets for extrapolation of the resonance frequency. No systematic offset between the oven and foil measurements was observed and all values agreed well within their uncertainties. The weighted average of the results is $815\,618\,181.735\,(71)\,MHz$. For ^{6}Li, measurements were also carried out with both
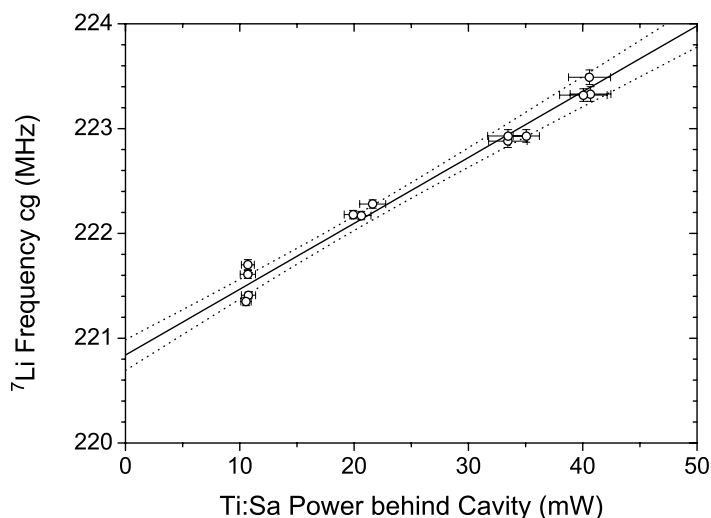
Figure 4. Ac-Stark shift for ^{7}Li two-photon transition as a function of the power of the Ti:Sa laser. The frequency axis is relative to the start frequency as given for figure 3. The centers of gravity of the hyperfine structure splitting ($\circ$) are fitted with a linear function (solid line) $\nu_{cg} = b_0 + b_1\,P_{Ti:Sa}$, where $b_0 = 220.84(7)$ MHz and $b_1 = 0.062(3)$ MHz mW^{-1}. If the intensity inside the cavity is used, b_1 changes to b_1(intracavity) $= 0.0058(3)$ MHz W^{-1} mm^2. The upper and lower 95% confidence levels are represented by the dotted lines.
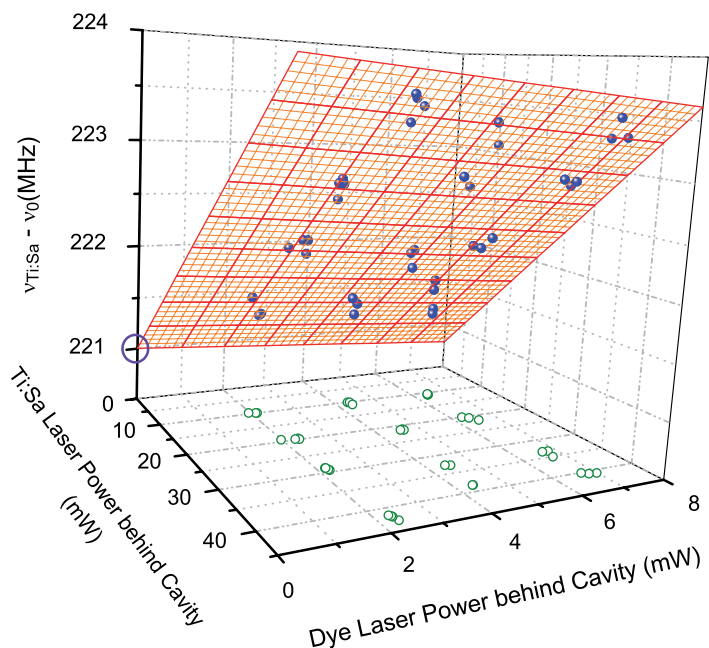
Figure 5. Two-dimensional plot of the ac-Stark shift. The filled points are the experimental data and the open circles are the projection of these points on the x–y plane. The shaded plane is the two-dimensional fit: $\nu_{cg} = B_0 + B_1\,P_{Ti:Sa} + B_2\,P_{Dye}$. $B_0 = 220.93(5)$ MHz, $B_1 = 0.065(1)$ MHz mW^{-1}, and $B_2 = -0.024(8)$ MHz mW^{-1} (in terms of the laser intensity inside the cavity $B_1 = 0.0061(1)$ MHz W^{-1} mm^2, and $B_2 = -0.0022(8)$ MHz W^{-1} mm^2).

atom sources and about 90 spectra were taken and separated into two sets. Statistical precision of fitting the resonance signal was worse due to the $\approx 7\%$ abundance of ^{6}Li in the natural abundance samples used for the measurements. In combination this led to a larger overall uncertainty and a value of $815\,606\,727.882\,(180)$ MHz was obtained. The isotope shift taken as a difference between these two absolute frequencies is $\Delta \nu_{\mathrm{IS}} = 11\,453.85\,(19)$ MHz, which is in good agreement with the more accurate value of $11\,453.984\,(20)$ MHz obtained from relative measurements [15].

5. Line profile modeling

To estimate the influence of the residual asymmetry (figure 3) on the line center frequencies we had first to understand its origin. Atoms that are not passing through the center of the laser beam experience lower intensities and, thus, smaller ac-Stark shifts. The effect is not symmetric since all atoms passing through the wings are shifted to one side of the resonance. The center region has the highest intensity and therefore the highest ionization efficiency but also the largest ac-Stark shift. Atoms traversing the wings of the laser beam have a smaller ionization efficiency but they are in resonance at lower frequencies since the ac-Stark shift (due to the Ti:Sa laser) increases the resonance frequency. Thus, they appear on the lower frequency side of the resonance curve and the corresponding intensity above the resonance is missing. A similar effect is caused by laser intensity fluctuations that occur due to changes in the length of the enhancement cavity that are too fast to be completely compensated by the locking servo loops. Again, the signal is shifted into the frequency range below the resonance frequency observed at highest cavity power. To quantitatively understand whether these effects distort the line profile in the observed way, we performed simulations of the ionization process in the laser fields.

5.1. The model

To understand the line profile we have used a rate equation model to calculate the time-varying ionization efficiency of atoms passing the laser beam at different positions. A scheme of the simplified excitation ladder that has been used is shown in figure 6(a). The two-photon transition rate as a function of laser intensity is given by

$$W_{12} = \frac{I^2}{I_S^2} \frac{A_{23}^2}{4} \frac{A_{23}}{4\delta\omega^2 + A_{23}^2/4}, \tag{9}$$

with the on-resonance transition rate $W_{12}(\delta\omega = 0) = (I^2/I_S^2)A_{23}$, $A_{23} = 1/\tau_{3s} = 33$ MHz and $I_S = 167$ W mm^{-2} being the total Einstein A coefficient between the 3S and 2P levels and the saturation intensity for the two-photon transition, respectively. I_S has been experimentally determined from the dependence of the linewidth on the laser intensity. This simplified transition rate for the two-photon transition fulfills the following conditions for the lineshape: (a) at low laser intensity we observe a Lorentzian with a width of A_{23}, (b) with increasing intensity the transition rate increases proportional to the square of the intensity, (c) at the saturation intensity $I = I_S$ the pump rate at resonance is as large as the relaxation rate and (d) the linewidth increases with intensity according to $(1 + (I/I_S)^2)^{1/2}$. It may be noted that it is not necessary to distinguish between the decay into the two fine structure levels 2P$_{1/2}$ and 2P$_{3/2}$ since both have the same probability of being ionized as well as for decay back into the 2S$_{1/2}$ ground state. The latter has
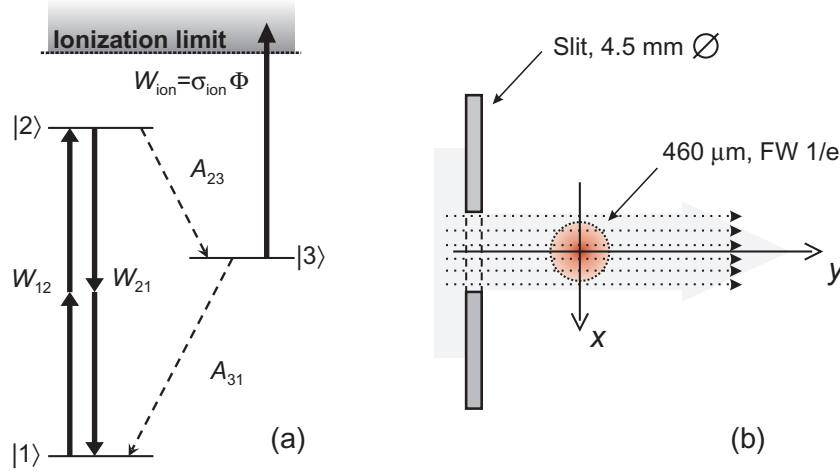
Figure 6. Schematic representation of (a) the excitation ladder used in the model, and (b) a collimated atomic lithium beam passing through a Gaussian laser field distribution.

a transition rate of $A_{31} = 1/\tau_{2p} = 37\,\text{MHz}$ (see table 2). The rate equations for excitation and ionization are then given by

$$\dot{N}_1 = W_{12}(N_2 - N_1) + A_{31}N_3,$$
$$\dot{N}_2 = W_{12}(N_1 - N_2) - A_{23}N_2, \qquad (10)$$
$$\dot{N}_3 = A_{23}N_2 - A_{31}N_3 - \sigma_{\text{Ion}}\Phi N_3,$$

with the photon flux $\Phi = I_{\text{Laser}}/h\nu$ of the ionization laser and the ionization cross section σ_{Ion}. N_1, N_2 and N_3 are the populations of the 2S, 3S and 2P levels, respectively, and $N_{\text{tot}} = N_1 + N_2 + N_3$ is the total number of neutral atoms. Now we add the effect of the laser ionization onto the population

$$\dot{N}_{\text{Ion}} = -\dot{N}_{\text{tot}} = \sigma_{\text{Ion}}\Phi N_3. \qquad (11)$$

The numerical integration of these coupled differential equations was performed using an adaptive-step-size 4th order Runga–Kutta algorithm taken from [29]. We have taken into account the laser intensity profile, the displacement along x from the center of the laser beam, and the velocity distribution within the atomic beam. The assumed geometry is shown in figure 6(b): a 4.5 mm diameter hole is used to collimate the atomic beam from the graphite oven; 6 mm behind the aperture the atoms cross the laser beam in the relatively soft focus of the enhancement cavity with a full width 1/e diameter of 460 μm.

The Gaussian intensity distribution of the laser beams has two effects on the interaction: (i) regarding the reference frame of the atomic beam in the longitudinal direction, the atom experiences a continually changing intensity, hence varying W_{12} values and ionization rates as it passes through the laser beams; (ii) in the transverse dimension, some atoms pass through a region off-center of the laser beams and encounter overall reduced intensities. The longitudinal distribution is easily accounted for by using an appropriate time-space transformation for the given atomic velocity. In this way, the W_{12} value and the photon flux Φ responsible for the two-photon excitation and ionization rates during the numerical integration are continuously adjusted. In contrast, the transverse dimension requires adding another dimension to the overall

Table 2. Typical parameters used in the simulations.

Parameter	Symbol	Value	Unit	Reference
Full decay rates	A_{23}	33.0	MHz	[28]
	A_{31}	7.0	MHz	[28]
Laser wavelength	λ	735.0	nm	
Two-photon saturation intensity	I_S	167	W mm^{-2}	[31]
Ionization cross section	σ_{ion}	2×10^{-15}	cm^2	This work
Ac-Stark shift coefficient	$a_{ac-Stark}$	Variable	MHz mW^{-1}	This work
Laser beam waist (1/e)	w_{laser}	460	μm	[31]
Temperature	T	2000	K	This work

integration procedure. Integration over the spatial displacement in the x-direction and the velocity distribution was performed as a discrete summation, typically over 19 and 40 segments, respectively. The atomic beam intensity distribution along x was assumed to have a rectangular profile limited by sharp mechanical apertures. The velocity distribution was assumed to be Maxwell–Boltzmann for the thermal source. When expressed as the flux distribution in an atomic beam, it is given by [30]

$$\Phi_{\text{Atoms}}(\upsilon) = 2\alpha^{-4}\upsilon^3 \exp\left(-\upsilon^2/\alpha^2\right) \, d\upsilon, \tag{12}$$

where $\alpha = \sqrt{2kT/m}$ is the most probable velocity. The integration was carried out up to 4α where the relative flux dropped to 2×10^{-5} of the maximum. To avoid artificial intensity oscillations that can occur when discrete velocity segments are taken in regular increments, a quasi Monte-Carlo approach was used. At each position-velocity step the particular values were randomized within the range of $\pm dx/2$ and $\pm d\upsilon/2$, where dx and $d\upsilon$ are the summation step sizes. For the laser's Gaussian intensity profiles, integration was carried out over four times the FWHM of the beam diameter corresponding to points where the intensity has dropped off to 10^{-4} of the maximum value.

In equation (9), the effect of power broadening for the transition line profile is included. However, the ac-Stark effect is not taken into account. This effect is caused by non-resonant interaction of the S levels with all available P levels in the atom in the presence of strong laser fields. To artificially include the effect in the model, we consider in $\delta\omega = 2\pi\delta\nu$ not only the usual detuning of the laser frequency $\Delta\nu_{\text{Laser}}$ but also the additional linear ac-Stark shift

$$\delta\nu = \Delta\nu_{\text{Laser}} - a_{ac-Stark}I(x, y, t) \tag{13}$$

and replace the term $\delta\omega$ in (9) with this position-dependent function. The value of the linear ac-Stark shift coefficient $a_{ac-Stark}$ was adjusted to obtain the experimentally observed ac-Stark shift depicted in figure 4. Fast intensity fluctuations on a timescale of a few μs due to cavity length fluctuations were observed with intensity droppings down to 30% of maximum. To estimate the influence on the line profile, we assumed a sinusoidal behavior for the intensity with a variation of 70% and a frequency of $\sim$30 kHz. To average over different phases at the time when the atom enters the laser beam, another discrete summation with a step size of 4° was carried out, covering the full possible range of 360°.
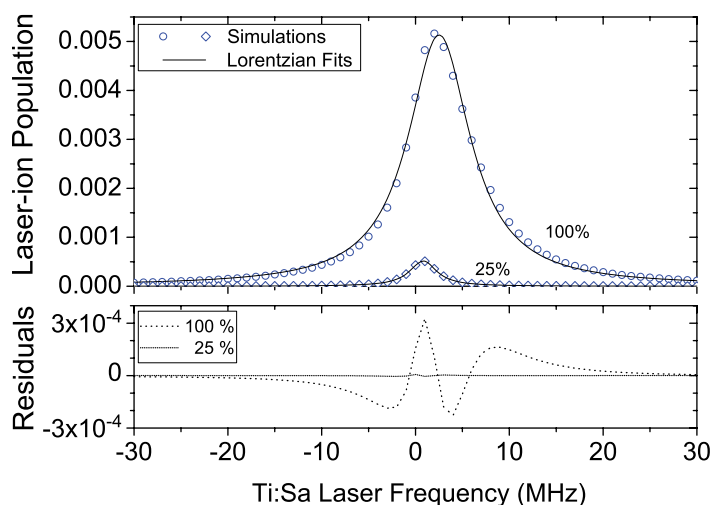
Figure 7. Line profile simulation for 'low-power' (25%, equivalent to 110 W mm^{-2}) and 'high-power' (100%, equivalent to 430 W mm^{-2}).

5.2. Results

We will now discuss the results of lineshape calculations. First, the lineshape and the shifts of resonance centers are discussed before we turn to the relevance of these calculations for the determination of the transition frequency.

5.2.1. Lineshapes. Figure 7 shows the results of lineshape calculations at typical laser powers used in 'high-power' and 'low-power' measurements. Lorentzian line profiles have been fitted to the simulated data and the residuals between the fit and the simulated data are plotted in the lower part of the figure. The residuals show a similar behavior as in the case of the experimental data (figure 3).

Figure 8 shows the calculated lineshape for different distributions of the laser field: a rectangular profile that has a homogeneous laser intensity distributed all over the area of the laser beam (R), a Gaussian profile with stationary laser power (G) and a Gaussian profile that takes into account the intensity fluctuations of the laser beam (GF). The simulations were performed at the highest laser intensity used experimentally. The most striking difference between the rectangular and Gaussian profiles is the reduction in ionization efficiency and a shift of the resonance center of 1.7 MHz in the case of the Gaussian profile. Both effects are caused by the reduction of laser intensity in the non-central region of the laser beam and, hence, the lower excitation efficiencies and ac-Stark shifts. The Gaussian with intensity fluctuations only introduces small differences when compared to the same Gaussian distribution without fluctuations.

5.2.2. Ac-Stark shift. Line profiles of the hyperfine transition of ^{7}Li were simulated at different laser intensities of the laser field for a Gaussian distribution with intensity fluctuations. From these profiles the peak centers were extracted and the results are plotted in figure 9 as a function of the laser power measured behind the cavity. A linear fit was performed on the region where the experimental data have been obtained (10 mW $\leqslant P_{\text{Ti:Sa}} \leqslant$ 45 mW). At lower laser
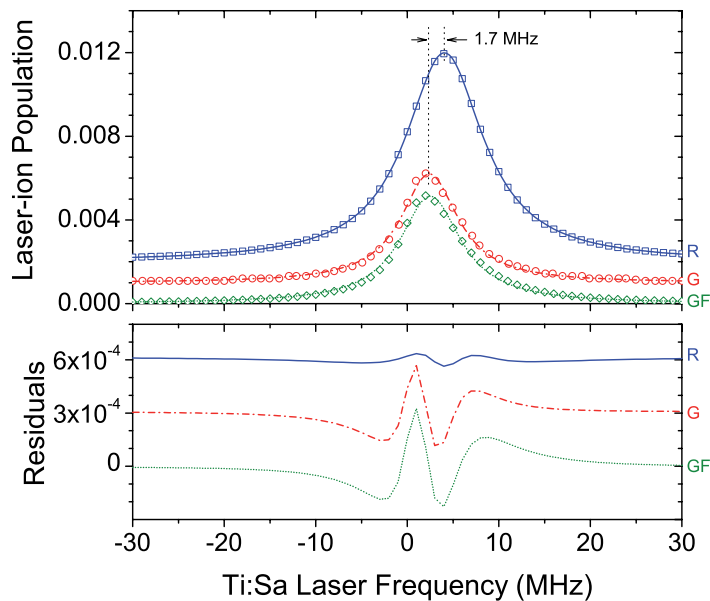
Figure 8. Simulation of the line profile for different laser field distributions, R: rectangular, G: Gaussian and GF: Gaussian plus intensity fluctuations. These lineshapes have also been fitted with Lorenztian line profiles and the corresponding residuals are plotted in the lower part of the graph. Line profiles R and G and their residuals have been artificially shifted vertically (offsets of 10^{-3} and 3×10^{-4}, respectively) in order to be distinguished from each other.

intensities, the simulated data smoothly move away from the linear behavior approaching zero. By considering only a linear ac-Stark shift, a systematic shift of 170 kHz is introduced in the determination of the peak center. Such a deviation is not observed if we assume a rectangular laser beam profile. In this case the linear behavior continues and by extrapolation the correct frequency is obtained. Thus, we believe that the additional shift is real and is introduced by the increasing distortion of the peak profile. To estimate the uncertainty of this correction, we have performed similar calculations as shown in figure 9 for various amounts of laser intensity fluctuations (20–80%) since this is the least known parameter in the model. The results span a range of 65 kHz, which has fully been taken as an additional systematic uncertainty.

In the simulation, we have only considered the intensity distribution and fluctuations of the Ti:Sa-laser field: it has considerably higher intensity, is completely responsible for the resonance transition, and represents the dominant source for non-resonant ionization. Moreover, the ac-Stark shift coefficient for the dye laser light extracted from figure 5 is $-0.0022(8)\,\mathrm{MHz\,W^{-1}\,mm^2}$, whereas it is 2.7 times larger for the Ti:Sa laser light ($0.0061(1)\,\mathrm{MHz\,W^{-1}\,mm^2}$).

6. Summary of systematic uncertainties

Table 3 shows statistical and systematic errors that contributed to the overall uncertainty of the 2S–3S transition frequency of ^{7}Li. The statistical uncertainty is given as the standard deviation of the individual results. A systematic error that has to be taken into account is the uncertainty

IOP Institute of Physics 🔶 DEUTSCHE PHYSIKALISCHE GESELLSCHAFT
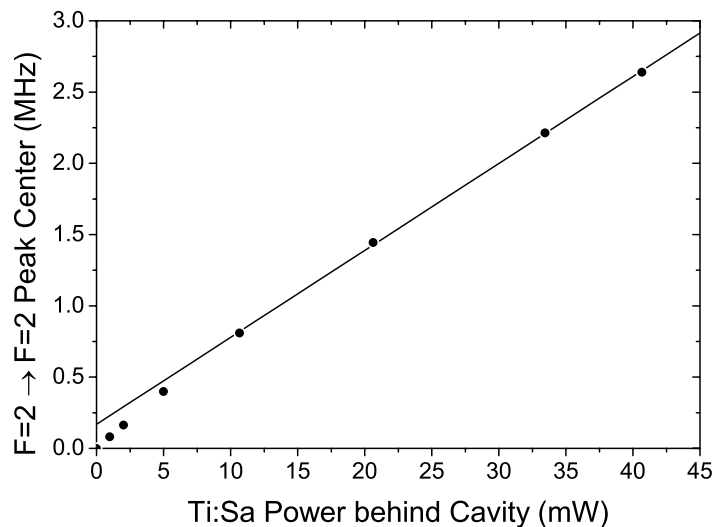
Figure 9. Simulation of a one-dimensional ac-Stark shift (full dots). The solid line ($y = 0.167 + 0.061x$) is a linear fit to the data between $10\,\text{mW} \leqslant P_{\text{Ti:Sa}} \leqslant 45\,\text{mW}$.

Table 3. Summary of statistical and systematic uncertainties of the absolute transition frequencies in ^{6,7}Li. All values are in kHz.

	^{7}Li	^{6}Li
Statistical	71	180
Systematic		
Frequency comb	143	143
Ac-Stark shift	65	65
Zeeman effect	30	30
Subtotal	160	160
Total	175	241

of the rubidium clock (FS725 from Stanford Research Systems) that was used as a reference frequency for the comb. It was calibrated by the manufacturer 256 days ($= 0.701$ years) before and the data were taken during one week. The Rb standard is specified to provide a relative accuracy of better than $\pm 5 \times 10^{-11}$ at the date of calibration and a drift of $< 5 \times 10^{-10}\,\text{year}^{-1}$. The relative uncertainty of the Rb frequency standard at the time of the measurement, and therefore of the frequency comb, was taken as the time since calibration multiplied by the yearly drift which amounts to 3.5×10^{-10}. To obtain the uncertainty of the laser frequency, this relative uncertainty was multiplied by the comb mode number that we have been using. This is 4 078 088 times the repetition rate $\nu_{\text{rep}} = 100\,\text{MHz}$, and therefore $\Delta\nu_{\text{Comb}} = 143\,\text{kHz}$. As discussed in section 5.2 the only other significant systematic uncertainty is that caused by the asymmetric line profile.

The effect of unresolved Zeeman splitting caused by stray magnetic fields was estimated to be less than 30 kHz for both isotopes. The strongest effect would be expected from the magnetic field induced by the current through the graphite crucible. However, a systematic offset between measurements with the oven and foil was not observed.

IOP Institute of Physics **Φ** DEUTSCHE PHYSIKALISCHE GESELLSCHAFT

Table 4. Experimental (e) and theoretical (th) values on the $2s\,^2S_{1/2} - 3s\,^2S_{1/2}$ transition frequencies of ^{7}Li and ^{6}Li. The values of this work contain a $-170\,$kHz correction to account for the ac-Stark shift effect, which is discussed in section 5.2.2. The value of ^{6}Li given in the last row was obtained by combining the ^{7}Li value of this work and the measured isotope shift given in table I of [15].

		Reference	Year	Energy (cm^{-1})	Frequency (MHz)
^{7}Li	e	Radziemski *et al* [32]	1995	$27\,206.0952 \pm 0.0010$	$815\,618\,215 \pm 30$
	th	Yan and Drake [6]	2002	$27\,206.0924 \pm 0.0039$	$815\,618\,131 \pm 117$
	e	Bushaw *et al* [23]	2003	$27\,206.0942 \pm 0.0001$	$815\,618\,185 \pm 3$
	th	Yan and Drake [10]	2003	$27\,206.0926 \pm 0.0009$	$815\,618\,137 \pm 27$
	e	This, I$_2$-line [33]	2004	$27\,206.094\,04 \pm 0.000\,09$	$815\,618\,180.5 \pm 2.7$
	th	Yan *et al* [7]	2008	$27\,206.0936 \pm 0.0010$	$815\,618\,166 \pm 30$
	th	Puchalski and Pachucki [2]	2008	$27\,206.0937 \pm 0.0006$	$815\,618\,170 \pm 19$
	e	This work	2009	$27\,206.094\,082 \pm 0.000\,006$	$815\,618\,181.57 \pm 0.18$
^{6}Li	e	Radziemski *et al* [32]	1995	$27\,205.7129 \pm 0.0010$	$815\,606\,754 \pm 30$
	th	Yan and Drake [6]	2002	$27\,205.7104 \pm 0.0039$	$815\,606\,678 \pm 117$
	e	Bushaw *et al* [23]	2003	$27\,205.712\,14 \pm 0.000\,10$	$815\,606\,731 \pm 3$
	th	Yan and Drake [10]	2003	$27\,205.7105 \pm 0.0009$	$815\,606\,683 \pm 27$
	e	This, I$_2$-line [33]	2004	$27\,205.711\,98 \pm 0.000\,09$	$815\,606\,726.6 \pm 2.7$
	th	Yan *et al* [7]	2008	$27\,205.7115 \pm 0.0010$	$815\,606\,712 \pm 30$
	th	Puchalski and Pachucki [2]	2008	$27\,205.7117 \pm 0.0006$	$815\,606\,717 \pm 19$
	e	This work	2009	$27\,205.712\,014 \pm 0.000\,008$	$815\,606\,727.71 \pm 0.24$
	e	Direct meas. ^{7}Li + IS [15]	2009	$27\,205.712\,013 \pm 0.000\,006$	$815\,606\,727.59 \pm 0.18$

7. Results and discussion

Table 4 and figure 10 show those experimental and theoretical frequency values of the 2S–3S transition, which have been obtained within the last two decades. The 175 kHz total uncertainty value of our measurement is the quadratic sum of the statistical and systematic uncertainties.

Our experimental value given for the year 2004 was not published independently. We previously reported isotope shift measurements that were referenced to a diode laser locked to a saturated absorption signal of the hyperfine component of the molecular iodine spectrum [12]–[14]. Since then, the absolute frequency of the I$_2$-stabilized diode laser has been measured with the frequency comb [33]. These were then combined to calculate the absolute transition frequency of the 2S–3S transition of the stable lithium isotopes. The uncertainty was in this case dominated by the fact that we used a different laser and stabilization system for the iodine measurements and an additional but stable offset frequency was found. Therefore, a systematic uncertainty of about 3 MHz for the exact locking point of the diode laser system had to be added.

There is still a discrepancy between theory and experiment. Presently the calculations of the absolute transition frequencies on lithium and helium have been performed up to QED terms of order α^3 Ry. Calculation for higher order terms of α up to α^5 Ry are partially available [2] but they are still not complete and they are the main remaining source of uncertainty for
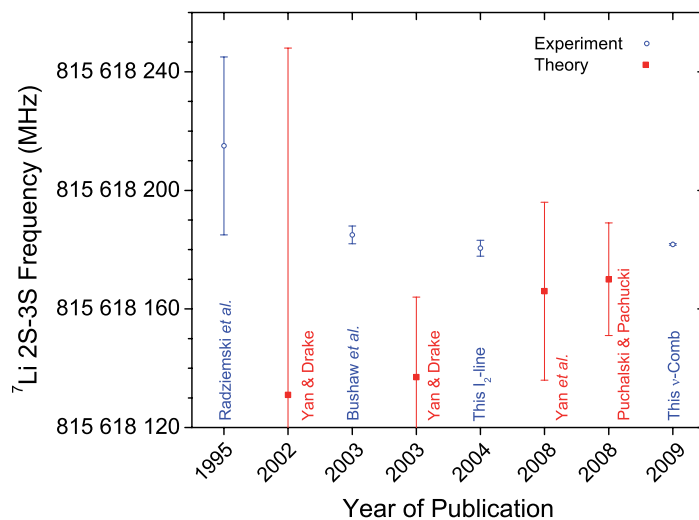
Figure 10. Theoretical and experimental transition frequency values of ^{7}Li in the $2s\,^2S_{1/2}$–$3s\,^2S_{1/2}$ transition.

the theoretical energy values given in Table 4. Presently, two groups are working on the theoretical evaluation of the absolute transition for lithium and helium and we hope that accuracy comparable to the experiment will be reached in the future.

8. Conclusions

Two-photon laser spectroscopy and resonance ionization together with accurate frequency determination via the frequency comb have allowed us to measure the absolute transition frequencies of the 2S–3S transition of the stable lithium isotopes ^{7}Li and ^{6}Li with an accuracy of 2×10^{-10}. The values obtained for ^{7}Li and ^{6}Li are in agreement with previous results [23] but one order of magnitude more accurate. The new results still disagree by about 12 MHz with the latest theoretical values obtained in [2] which are about 100 times less accurate than the experimental values obtained here. Once the theoretical calculation of the 2S–3S transition energies can be improved by these two orders of magnitude, the extraction of the nuclear charge radii of the lithium isotopes will be possible. Besides the transition reported here, further high accuracy measurements of the $2\,^3S_1 \rightarrow 2\,^3P_{0,1,2}$ transition in the two-electron system Li$^+$, as have already been obtained at the test storage ring (TSR) at Heidelberg [34] and are under preparation at the MPQ in Garching, would independently facilitate the absolute charge radius determination.

Acknowledgments

IOP Institute of Physics ⏀ DEUTSCHE PHYSIKALISCHE GESELLSCHAFT

References

[1] Puchalski M, Moro A M and Pachucki K 2006 *Phys. Rev. Lett.* **97** 133001
[2] Puchalski M and Pachucki K 2008 *Phys. Rev.* A **78** 052511
[3] Drake G W F and Yan Z-C 1992 *Phys. Rev.* A **46** 2378
[4] Yan Z-C and Drake G W F 1995 *Phys. Rev.* A **52** 3711
[5] Yan Z-C and Drake G W F 2000 *Phys. Rev.* A **61** 022504
[6] Yan Z-C and Drake G W F 2002 *Phys. Rev.* A **66** 042504
[7] Yan Z-C, Nörtershäuser W and Drake G W F 2008 *Phys. Rev. Lett.* **100** 243002
[8] Drake G W F and Swainson R A 1990 *Phys. Rev.* A **41** 1243
[9] Drake G W F and Goldman S P 1999 *Can. J. Phys.* **77** 835
[10] Yan Z-C and Drake G W F 2003 *Phys. Rev. Lett.* **91** 113004
[11] Pachucki K and Komasa J 2004 *Phys. Rev. Lett.* **92** 213001
[12] Ewald G *et al* 2004 *Phys. Rev. Lett.* **93** 113002
[13] Ewald G *et al* 2005 *Phys. Rev. Lett.* **94** 039901
[14] Wang L-B *et al* 2004 *Phys. Rev. Lett.* **93** 142501
[15] Sánchez R *et al* 2006 *Phys. Rev. Lett.* **96** 033002
[16] Müller P *et al* 2007 *Phys. Rev. Lett.* **99** 252501
[17] Nörtershäuser W *et al* 2009 *Phys. Rev. Lett.* **102** 062503
[18] Žáková M, Geppert C, Herlert A, Kluge H-J, Sánchez R, Schmidt-Kaler F, Tiedemann D, Zimmermann C
    and Nörtershäuser W 2006 *Hyperfine Interact.* **171** 189
[19] Nakamura T *et al* 2006 *Phys. Rev.* A **74** 052503
[20] Drake G W F 2009 private communication
[21] de Jager C W, de Vries H and de Vries C 1974 *At. Data Nucl. Data Tables* **14** 479
[22] Suelzle L R, Yearian M R and Crannell H 1967 *Phys. Rev.* **132** 992
[23] Bushaw B A, Nörtershäuser W, Ewald G, Dax A and Drake G W F 2003 *Phys. Rev. Lett.* **91** 043004
[24] Udem T, Huber A, Gross B, Reichert J, Prevedelli M, Weitz M and Hänsch T W 1997 *Phys. Rev. Lett.*
    79 2646
[25] Nörtershäuser W *et al* 2003 *Nucl. Instrum. Methods Phys. Res.* B **204** 644
[26] Drever R W P, Hall J L, Kowalski F V, Hough J, Ford G M, Munley A J and Ward H 1983 *Appl. Phys.*
    B **31** 97
[27] Godefroid M, Fischer C F and Jönsson P 2001 *J. Phys. B: At. Mol. Opt. Phys.* **34** 1079
[28] Froese Fischer C, Saparov M, Gaigalas G and Godefroid M 1998 *At. Data Nucl. Data Tables* **70** 119
[29] Press W H, Teukolsky S A, Vetterling W T and Flannery B P 1996 *Numerical Recipes in C* (Cambridge:
    Cambridge University Press)
[30] Kusch P and Hughes V W 1959 *Atomic and Molecular Beam Spectroscopy, Handbuch der Physik* Part 1
    (Berlin: Springer)
[31] Ewald G 2005 *Messung der Ladungsradien der radioaktiven Lithium-Isotope Li-8 und Li-9* (Heidelberg:
    Ruprecht-Karls-Universität Heidelberg) pp 52, 73
[32] Radziemski L J, Engleman R Jr and Brault J W 1995 *Phys. Rev.* A **52** 4462
[33] Reinhardt S *et al* 2007 *Opt. Commun.* **274** 354
[34] Reinhardt S *et al* 2007 *Nat. Phys.* **3** 861

Isotope shift measurements in the $2s_{1/2} \to 2p_{3/2}$ transition of Be$^+$ and extraction of the nuclear charge radii for ^{7,10,11}Be

M. Žáková[1], **Z. Andjelkovic**[1], **M. L. Bissell**[2], **K. Blaum**[3], **G.W.F. Drake**[4], **Ch. Geppert**[5,6], **M. Kowalska**[7], **J. Krämer**[1], **A. Krieger**[1], **M. Lochmann**[1], **T. Neff**[5], **R. Neugart**[8], **W. Nörtershäuser**[1,5], **R. Sánchez**[5,1], **F. Schmidt-Kaler**[9], **D. Tiedemann**[1], **Z.-C. Yan**[10], **D. T. Yordanov**[7], **C. Zimmermann**[6]

[1]Institut für Kernchemie, Universität Mainz, D-55128 Mainz, Germany; [2]Instituut voor Kern- en Stralingsfysica, Katholieke Universiteit Leuven, B-3001 Leuven, Belgium; [3]Max-Planck Institut für Kernphysik, D-69117 Heidelberg, Germany; [4]Department of Physics, University of Windsor, Windsor, Ontario, Canada, N9B 3P4; [5]GSI Helmholtzzentrum für Schwerionenforschung GmbH, D-64291 Darmstadt, Germany; [6]Physikalisches Institut, Universität Tübingen, D-72076 Tübingen, Germany; [7]CERN, Physics Department, CH-1211 Geneva 23, Switzerland; [8]Institut für Physik, Universität Mainz, D-55099 Mainz, Germany; [9]Quanteninformationsverarbeitung, Universität Ulm, D-89069 Ulm, Germany; [10]Department of Physics, University of New Brunswick, Fredericton, New Brunswick, Canada E3B 5A3

E-mail: `w.noertershaeuser@uni-mainz.de`

Abstract. We have performed isotope shift measurements in the $2s_{1/2} \to 2p_{3/2}$ transition of Be$^+$ ions using advanced collinear laser spectroscopy with two counter-propagating laser beams. Measurements involving a frequency comb for laser stabilization and absolute frequency determination allowed us to determine the isotope shifts with an accuracy of 2 MHz. From the isotope shifts between ^{9}Be and ^{7,10,11}Be, high-accuracy mass shift calculations and the charge radius of the reference isotope ^{9}Be we determined nuclear charge radii for the isotopes ^{7,10}Be and the one-neutron halo nucleus ^{11}Be. The results are compared to nuclear structure calculations using the Fermionic Molecular Dynamics model which reproduce well the general trend of the radii. Decreasing charge radii from ^{7}Be to ^{10}Be are explained by the cluster structure of the nuclei. The increase from ^{10}Be to ^{11}Be is mainly caused by the halo neutron by which the ^{10}Be core moves relative to the center of mass. Polarization of the ^{10}Be core has only a small influence on the charge radius.

1. Introduction

Charge radii are among the basic properties of nuclei being used to test the predictions of nuclear structure models. In general, electron scattering experiments can to some degree provide the radial charge distribution and the nuclear charge radius, but they are not applicable for short-lived isotopes so far. For those, mainly two experimental approaches exist: nuclear reaction processes and optical precision spectroscopy. The matter radius can be extracted from nuclear interaction cross sections [1] and it was shown that the charge-changing cross sections show a Z dependency that is very similar to nuclear radii measured by electron scattering [2]. While charge-changing cross sections were investigated for nuclei close to the valley of stability [3] mainly for astrophysical applications, only few attempts were made to extract charge distribution information for very exotic isotopes [4, 5, 6]. Isotope shift measurements using optical spectroscopy can provide nuclear-model independent information on the nuclear charge radius and, thus, on the proton distribution in the nucleus. The comparison of charge and matter radii is particularly interesting on systems which show a strongly different distribution of protons and neutrons inside the nucleus. These are namely nuclei with a neutron or proton skin or a so-called halo. Halo nuclei were discovered by Tanihata *et al.* in 1985 [1]. They performed nuclear reaction experiments with nuclei of light elements and observed significant changes in the interaction cross section between neighboring isotopes close to the neutron dripline. A notable increase for dripline nuclei was explained by a significantly extended matter distribution. It was proposed that this extension arises from weakly bound neutrons which form a region of diluted nuclear matter around a compact core with 'normal' nuclear density [7]. Since then, many experiments were carried out to understand these extraordinary systems. The most intensely studied halo nuclei are ^{6,8}He, ^{11}Li, ^{11}Be and ^{14}Be [8].

High-resolution optical spectroscopy [9] has considerably contributed to our understanding of halo nuclei. Collinear laser spectroscopy in combination with the β-NMR technique allowed the determination of the spin and the magnetic dipole moment of ^{11}Li [10] and ^{11}Be [11] as well as the determination of the electric quadrupole moment of ^{11}Li [12]. The results could be used to exclude a possible deformation of ^{11}Li because the spin 3/2 belongs to a spherical state, the magnetic moment lies close to the Schmidt value, and the quadrupole moment is similar to that of ^{9}Li. Both these values, which were improved recently [13, 14], again indicate that the nucleus is nearly spherical.

Soon, the question about the nuclear charge radii of these exotic nuclei was raised and their importance for a better understanding of the interaction between halo and core was pointed out. Until now only two groups succeeded in measuring nuclear charge radii of the light halo systems in helium [15] and lithium [16] by high-precision laser spectroscopy. The extraction of nuclear charge radii from these isotope shift measurements had become only possible because the mass-dependent part of the isotope shift could be calculated with sufficiently high accuracy, which is currently possible for atomic systems with up to three electrons. Yan and Drake published their first results

with spectroscopic accuracy for transitions in lithium in 2000 [17] and the calculations have been continuously improved since then [18, 19, 20, 21].

Standard collinear laser spectroscopy is not directly suitable for isotope shift measurements on the lightest elements. Until recently, ^{17}Ne was the lightest short-lived isotope for which so far charge radius information has been obtained using this technique [22]. The reason for that is an insufficient accuracy in the acceleration voltage measurements. Consequently, the uncertainty of the Doppler shift of the fast ion beam by far exceeds the finite-size contribution to the isotope shift. This extremely small contribution of about 10^{-8} of the total transition frequency contains the essential information on the nuclear charge radius.

Recently, we described an advanced technique for spectroscopy on fast atoms and ions [23]. This approach combines collinear and anti-collinear laser spectroscopy and the absolute laser frequencies are determined with an accuracy better than 1 MHz employing a frequency comb. The technique was successfully applied for the measurements of the absolute transition frequencies in the $2s_{1/2} \rightarrow 2p_{1/2}$ transition of ^{7,9,10,11}Be$^+$ ions [24]. In combination with accurate calculations of the mass-dependent isotope shift [20, 21] these transition frequencies were used to determine the changes in the mean-square nuclear charge radii along this chain of isotopes [23].

In the measurement presented here, we determine the isotope shifts in the $2s_{1/2} \rightarrow 2p_{3/2}$ transition with an accuracy of approximately 2 MHz, which is more than one order of magnitude higher than that in [25]. This allows the extraction of the nuclear charge radii with an accuracy that is comparable to that in the D$_1$ line [23] and our results confirm the charge radii extracted from those. Additionally, the splitting isotope shift, i.e., the difference in the isotope shift between the two fine structure levels, was obtained and is compared to theoretical predictions which are nearly independent of both QED and nuclear volume effects. This provides a consistency check of the calculations as well as of the measurements.

Unlike binding energies, charge radii provide a direct test of the wave functions obtained from nuclear structure calculations. As charge radii are sensitive to the asymptotic behavior of the wave function, they can be related to the evolution of clustering or the development of halos. In this paper the measured charge radii are compared to recent No-Core Shell Model (NCSM) results [26] and new calculations in the Fermionic Molecular Dynamics (FMD) approach are presented.

2. Experimental

The experimental setup used for the isotope shift measurements on beryllium isotopes has been described in previous publications [23, 27] and will be summarized here only briefly. The measurements were performed at the on-line isotope separator (ISOLDE) at CERN. Radioactive beryllium atoms, produced by 1.4 GeV proton-induced fragmentation reactions in a uranium carbide target, were ionized by resonance laser
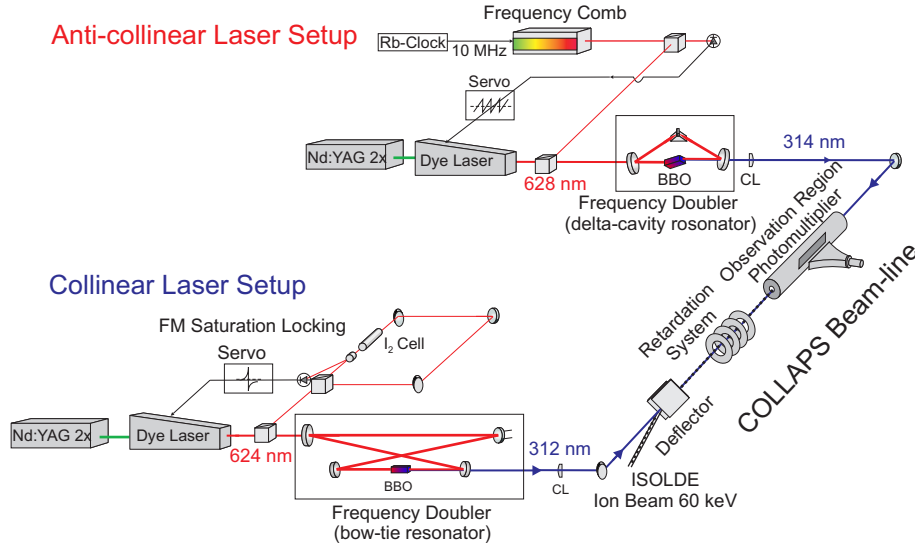
Figure 1. Simplified scheme of the experimental setup. The frequencies of the dye lasers for collinear and anti-collinear excitation were stabilized to a hyperfine transition of molecular iodine and to a frequency comb, respectively. The light from both lasers was frequency doubled and overlapped with the ion beam.

ionization (RILIS) and mass separated after acceleration to an energy of about 50 keV. A Be$^+$ ion beam was then delivered to the beamline for collinear laser spectroscopy (COLLAPS) where it was superimposed with two laser beams - one in collinear and one in anti-collinear direction. Both lasers were locked at fixed frequencies, while the ion beam was accelerated or decelerated into the detection region by applying an additional high voltage between +10 kV and -10 kV. Resonance fluorescence was observed with photomultiplier tubes mounted at the beamline. The high voltage of ISOLDE and the voltage applied at the optical detection region were measured by utilising high-voltage dividers which were calibrated with a 1 ppm high-voltage divider developed and built at the University of Münster [28].

The final velocity of the ions shifts the rest-frame resonance frequency ν_0 to

$$\nu_c = \nu_0 \cdot \gamma \cdot (1 + \beta) \tag{1}$$

$$\nu_a = \nu_0 \cdot \gamma \cdot (1 - \beta) \tag{2}$$

in collinear and anti-collinear direction, respectively. Changing the post-acceleration voltage at the detection region thus allows Doppler-tuning of the effective frequencies ν_c and ν_a across the fixed laser frequency. The laser frequencies for collinear and anti-collinear excitation are chosen such that the hyperfine structure patterns are covered for both directions within a small voltage range and that the centers of gravity (cg) almost coincide. With the cg coinciding for both laser beam directions the rest-frame transition frequency ν_0 can be determined solely from the laser frequencies according to

$$\nu_0^2 = \nu_c \cdot \nu_a. \tag{3}$$

A simplified scheme of the laser setup is shown in figure 1. Two cw-single-mode ring dye lasers (Coherent 699-21) with a linewidth of about 1 MHz were used to produce the fundamental wavelengths of 628 nm and 624 nm for anti-collinear and collinear excitation, respectively. The laser for collinear excitation was stabilized to a suitable iodine hyperfine transition while the other was directly locked to a fiber-laser-based frequency comb (Menlo Systems, FC1500). Therewith it was possible to determine the absolute laser frequencies with a relative accuracy of 10^{-9}. In total 12 iodine lines were chosen for the measurements. All lines are R branch lines with an even angular momentum J in the ground state. This is favourable, because they have a hyperfine structure exhibiting 15 components with the a_1 component well separated at the lower frequency side of the spectrum. This facilitates easy, reliable and reproducible locking during the beam time. The absolute locking frequencies for all selected iodine transitions were measured several times before, during and after the beam time with the frequency comb, to obtain accurate frequency information. For all lines very good agreement was found with the predicted frequencies from the iodine program IodineSpec (Toptica Photonics). In all cases deviations of less than 1 MHz were observed which is well below the quoted uncertainties of the calculated transition frequencies of a few MHz. The laser light was transported to the COLLAPS beamline by micro-structured fibers (LMA-20, Crystal Fibers). Two frequency doublers (SpectraPhysics Wavetrain and Tekhnoscan FD-SF-07) were used for the generation of ultraviolet light which is required for the $2s_{1/2} \rightarrow 2p_{3/2}$ transition in Be$^+$ (312 nm and 314 nm in collinear and anti-collinear direction, respectively). A power of up to 15 mW was achieved in the ultraviolet, but for spectroscopy this was attenuated to values below 5 mW to avoid saturation effects.

The laser - laser and laser - ion beam overlap was optimized using two irises and a combination of small apertures with diameters down to 5 mm along the beamline. The irises could be closed during the alignment procedure to a diameter of 1 mm but were opened during measurements to avoid scattered light causing additional background. Systematic uncertainties due to, *e.g.*, the ion - laser and laser - laser beam misalignment, the ion and laser beam divergence, or the momentum transfer to the ions by repetitive absorption of photons, were investigated in an off-line test run on the stable ^{9}Be. The main source of systematic uncertainty of about 500 kHz was found to be a possible misalignment between the two laser beams. Concerning absolute transition frequencies, an additional uncertainty of about 800 kHz arises from the uncertainty of the Rb-clock that is used as a reference for the frequency comb. However, the latter can be neglected in isotope shift measurements. It contributes to all isotopes with the same sign and similar size and largely cancels when the difference of the transition frequencies between two isotopes is calculated. All measurements were consecutively repeated several times. Collinear and anti-collinear spectra were recorded quasi-simultaneously by alternately blocking one of the laser beams in a fast sequence and scanning the Doppler-tuning voltage across the resonances in typically 400 steps for the odd and 100 steps for the even isotopes. For one spectrum, 50-400 such scans, each taking about 4-8 s, were integrated depending on the production rate of the respective isotope. In total, 10-20
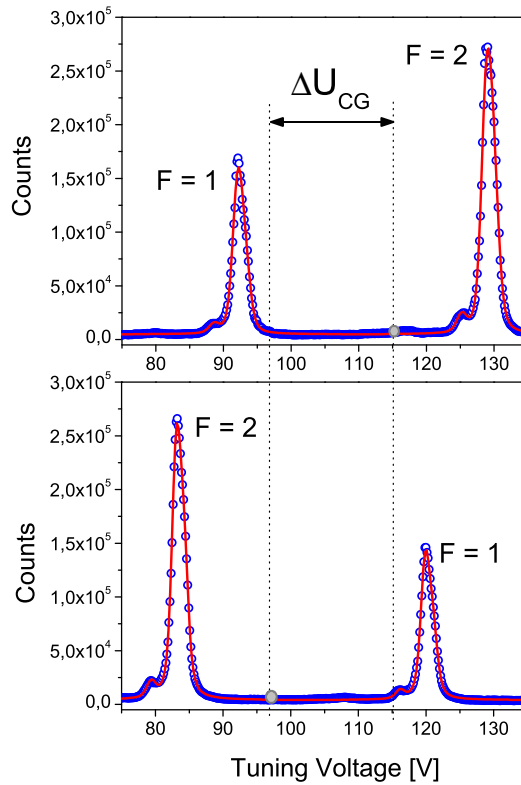
Figure 2. Collinear (top) and anti-collinear (bottom) spectrum recorded for the stable isotope ^{9}Be in the $2s_{1/2} \rightarrow 2s_{3/2}$ transition as a function of the Doppler tuning voltage applied to the detection region. The solid line is the overall fitting function with a Voigt profile for each peak.

spectra with sufficient statistics were recorded for each isotope.

3. Experimental Results

Figure 2 shows the collinear and anti-collinear spectra for ^{9}Be in the $2s_{1/2} \rightarrow 2p_{3/2}$ transition as a function of the applied tuning voltage. The observed peaks are labeled according to the respective $2s_{1/2}$ ground state hyperfine level F. The hyperfine structure in the upper $2p_{3/2}$ level is not resolved, because the splitting is less than 10 MHz while the natural linewidth of the transition is 20 MHz. Furthermore, the observed linewidth in collinear spectroscopy is broadened to 50-70 MHz and, hence, only the ground state splitting is resolved, which ranges from 0.5-3.6 GHz for the different isotopes. The solid line represents a fit with a Voigt lineshape function and is discussed below. The dashed vertical lines mark the center of gravity voltages (U_{cg}) of both scans, which do not exactly coincide but are separated by ΔU_{cg} which amounts to a few Volts.

The cg frequencies from the collinear and anti-collinear direction have to be combined to extract the rest-frame transition frequency. Since they do not appear at exactly the same acceleration voltage, the small correction ΔU_{cg} must be introduced for

either one of the two spectra. First, the scaling factor k between voltage and frequency is determined for the acceleration voltage around the center of gravity. Depending on the isotope, this factor is between 30 and 40 MHz/V. Using this scaling factor k, the frequency detuning $\Delta\nu_{\rm cg} = k \times \Delta U_{\rm cg}$ can be calculated‡. It is required to artificially shift one of the laser frequencies to observe both centers of gravity at the same acceleration voltage. With the shift applied to the anti-collinear laser frequency, the rest-frame transition frequency can be calculated by

$$\nu_0^2 = \nu_c \times (\nu_a + \Delta\nu_{\rm cg}), \tag{4}$$

where ν_a and ν_c are the doubled frequencies of the two locked dye lasers.

The spectra of $^9\mathrm{Be}^+$ were fitted with a multiple peak function containing all hyperfine transitions calculated from the nuclear spin and the atomic angular momentum. Each transition was fitted with a Voigt profile and common linewidth for all transitions. The small magnetic dipole and electric quadrupole interval factors $A_{2p_{3/2}}$ and $B_{2p_{3/2}}$, were taken from theoretical calculations [29]. They were introduced in the fitting routine as fixed parameters. The transition amplitudes were calculated relative to the strongest line according to the corresponding Racah intensity distributions. This procedure was necessary to ensure fitting results within physically meaningful constraints. In figure 2, a small peak on the left side of each hyperfine transition is visible. This peak arises from inelastic collisions of ions in the beam with residual gas atoms along the beamline. In such collisions Be^+ ions can be excited into the $2p$ states. The energy for this process is taken from the ions kinetic energy and is emitted in form of a photon. Hence, those ions have resonance positions 3.97 eV below the main peak. This effect was included in the fitting function and was treated as an additional Voigt peak at a fixed distance from the main peak with identical relative intensities compared to the main peak of the respective hyperfine component.

In order to test the sensitivity of the resulting transition frequency to the unresolved hyperfine splitting and the particular lineshape model, $^9\mathrm{Be}$ spectra obtained in collinear and anti-collinear excitation were also fitted independently with different lineshape functions. Besides the fit with fixed $2p_{3/2}$ hyperfine parameters described above, fits with single Voigtian, Gaussian and Lorentzian profiles for each of the two hyperfine peaks, constrained to have common line widths parameters, were performed. For each lineshape function, the cg frequencies were then combined to calculate the rest-frame frequency. The standard deviation of all measurements for one isotope and lineshape model was used as the statistical uncertainty of this value. The results for ν_0 obtained for the different lineshapes, scattered only by a fraction of this statistical uncertainty, indicating a negligible dependence on the chosen lineshape. Hence, the mean value of ν_0 obtained for the different lineshape functions was taken as the experimental transition frequency whereas the largest statistical uncertainty observed in the different fittings was kept as the final uncertainty.

‡ The small error introduced by this linearization is insubstantial compared to the statistical and other sources of uncertainty and can be neglected.
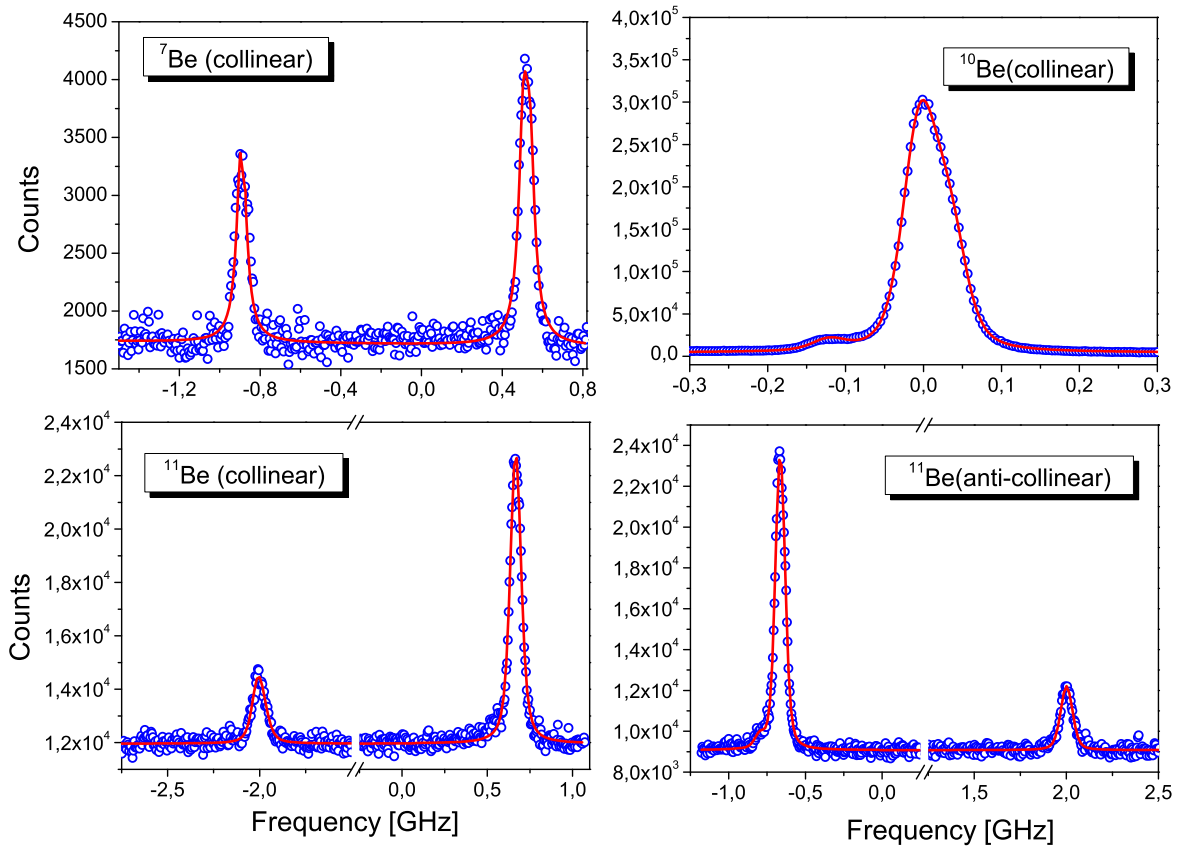
Figure 3. Spectra recorded for radioactive ^{7,10,11}Be isotopes in $2s_{1/2} \rightarrow 2p_{3/2}$ transition. Solid lines are Voigt fit functions. Frequencies are relative to the center of gravity of the respective isotope.

For the radioactive isotopes a similar procedure was used. Spectra for ^{7,10,11}Be are shown in figure 3. Here the voltage axis is converted to a frequency scale. Solid lines show the fitting results with a Voigtian line profile where the hyperfine splitting in the upper state was disregarded. A multi-line fit with individual hyperfine transitions as it was performed for ^{9}Be was only possible for ^{11}Be, since there is no information on the spectroscopic quadrupole moment of ^{7}Be and ^{10}Be does not exhibit any hyperfine structure $(I = 0)$.

A special case is ^{10}Be, where the best counting statistics was obtained. For this isotope an additional asymmetry was observed in the line shapes. Such asymmetries shift the cg frequency in collinear and anti-collinear direction by approximately the same amount but with opposite sign in the frequency domain. Consequently, this contribution largely cancels when the rest-frame frequency ν_0 is calculated. Nevertheless, for comparison a third peak component beside the small inelastic collision contribution, residing on the higher frequency side of the resonance, was added to the fitting function, which resulted in a much better description of the profile as it is shown in the spectrum of ^{10}Be in figure 3. The possible origin of this structure is not fully understood yet. While the individual peak position in collinear and anti-collinear spectra obtained from

Table 1. Extracted rms nuclear charge radii R_{c} from the $2s_{1/2} \to 2p_{3/2}$ (D_2) line compared to those obtained from the $2s_{1/2} \to 2p_{1/2}$ (D_1) transition [23]. Differences in the mean-square nuclear charge radii $\delta \langle r_c^2 \rangle$ are calculated from isotope shifts $\delta\nu_{\mathrm{IS}}^{9,A}$. The field shifts $\delta\nu_{\mathrm{FS}}^{9,A}$ (reference isotope is ^{9}Be) are calculated using the theoretical mass shifts $\delta\nu_{\mathrm{MS}}^{9,A}$ taken from literature. Uncertainties of the absolute charge radii R_{c} from the D_2 and D_1 line include the uncertainty of the reference radius $R_{\mathrm{c}}(^9\mathrm{Be}) = 2.519(12)$ fm [31].

| Isotope	$\delta\nu_{\mathrm{IS}}^{9,A}$, MHz	$\delta\nu_{\mathrm{MS}}^{9,A}$, MHz	$\delta\nu_{\mathrm{FS}}^{9,A}$, MHz	$\delta \langle r_c^2 \rangle$, fm^2	$R_{\mathrm{c}}(D_2)$, fm	$R_{\mathrm{c}}(D_1)$, fm
^{7}Be	-49 242.1(2.0)	-49 231.827(39)*	-10.3(2.0)	0.61(12)	2.637(55)	2.647(17)
		-49 231.779(35)$^\diamond$				
^{10}Be	17 326.8(2.0)	17 312.569(13)*	14.2(2.0)	-0.87(12)	2.339(53)	2.357(18)
		17 312.553(13)$^\diamond$				
^{11}Be	31 568.8(2.3)	31 564.168(24)*	4.9(2.3)	-0.28(14)	2.463(62)	2.463(16)
		31 564.207(31)$^\diamond$				

* Ref [20]
$\diamond$ Ref [30]

the fits of ^{10}Be$^+$ with one, two and three Voigt peaks differ by as much as 15 MHz, the rest-frame frequencies calculated by combining the collinear and anti-collinear results agree within 500 kHz. This clearly demonstrates the robustness of the collinear - anti-collinear approach with respect to the details of the lineshape function.

The isotope shifts relative to ^{9}Be were calculated from the fitting results and are listed in table 1. Using the precise mass shift calculations from [20, 30] the field shift, which is proportional to the change in the mean-square nuclear charge radius, can be calculated by

$$\delta \langle r_c^2 \rangle^{9,A'} = \frac{\delta\nu_{\mathrm{IS}}^{9,A'} - \delta\nu_{\mathrm{MS}}^{9,A'}}{C} \tag{5}$$

with the field shift constant $C \approx 17$ MHz/fm^2. For the data analysis more precise values for C taken from [21] were used, which show small isotopic variations. The rms nuclear charge radii were calculated based on the charge radius $R_c(^9\mathrm{Be}) = 2.519(12)$ fm that was determined by elastic electron scattering [31]. A change of this reference charge radius would lead to a constant shift for all isotopes, not influencing the variations along the isotopic chain. The obtained rms charge radii as listed in table 1 are plotted in figure 4 and compared to the results from the $2s_{1/2} \to 2p_{1/2}$ transition. Both data sets agree very well within their uncertainties, but due to the resolved hyperfine structure in the D_1 line these previous values are slightly more precise.

Before we discuss the evaluated charge radii, a comparison between the isotope shifts in the D_1 and the D_2 transition should be made. These values are listed in table 2 and the difference between them is the so-called splitting isotope shift (SIS). The measured SIS are in a good agreement with the theoretical predictions but the uncertainties are still relatively large. An improved measurement of the isotope shift in
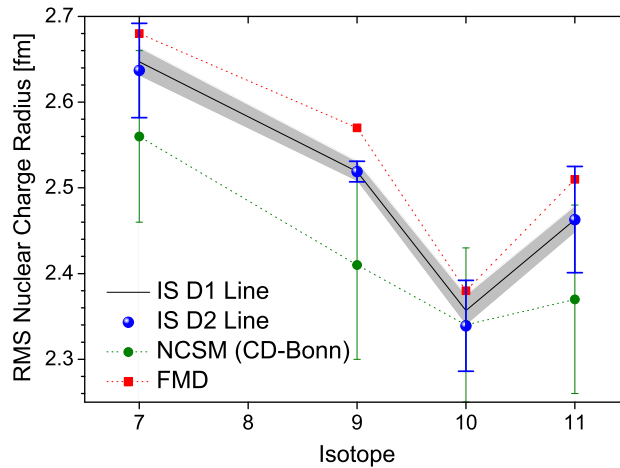
Figure 4. Nuclear charge radii of ^{7,9,10,11}Be obtained from isotope shift measurements, FMD multiconfiguration mixing calculations (FMD) and calculations in the No-Core Shell Model (NCSM) with the CD-Bonn potential [26]. Radii extracted from the isotope shift in the D_1 line are represented by the black solid line and the grey area indicates the corresponding uncertainty. Radii extracted from the D_2 transition are shown as individual symbols with error bars.

Table 2. Experimental isotope shifts $\delta\nu_{\mathrm{IS}}^{9,A}$(exp) in the $2s_{1/2} \rightarrow 2p_{1/2}$ (D_1) and $2s_{1/2} \rightarrow 2p_{3/2}$ (D_2) transitions and extracted splitting isotope shifts $\delta\nu_{\mathrm{SIS}}$(exp). In the last two columns the values for $\delta\nu_{\mathrm{SIS}}$ from two independent theoretical calculations are listed. All values are given in MHz.

Isotope	$\delta\nu_{\mathrm{IS}}$ D_1(exp)	$\delta\nu_{\mathrm{IS}}$ D_2(exp)	$\delta\nu_{\mathrm{SIS}}$(exp)	$\delta\nu_{\mathrm{SIS}}$ [29]	$\delta\nu_{\mathrm{SIS}}$ [20]
^{7}Be	-49 236.94(80)	-49 242.1(2.0)	-5.1(2.2)	-6.037(1)	-6.049
^{10}Be	17 323.82(82)	17 327.3(2.0)	3.5(2.4)	2.097(1)	2.13
^{11}Be	31 565.04(86)	31 569.6(2.3)	3.6(2.5)	3.965(1)	3.878

the $2s_{1/2} \rightarrow 2p_{3/2}$ line, as it is planned at RIKEN [25, 32] with stored and laser cooled ions in an RF ion trap, could clearly improve this comparison.

The best studied example for the SIS in a three-electron system is the lithium atom. Here, the value predicted from theory for the SIS between ^{6}Li and ^{7}Li is 0.396 MHz [20]. The most recent experimental values of -0.863(70) MHz [33] and 0.155(77) MHz [34] neither agree with each other nor with the predicted theoretical value. Therefore, the measured SIS for the $2p$ states in Be$^+$ is an important consistency check for theory and experiment.

4. Discussion

The charge radii presented here agree well with those reported earlier from our measurements in the D_1 transition [23]. There, we explained the general trend of the charge radii from ^{7}Be to ^{10}Be by the underlying cluster nature of these nuclei: The large nuclear charge radius of ^{7}Be $(= \alpha + t)$ arises from the low cluster-threshold of only 1.586 MeV, which implies an extended wave function for the relative motion of the clusters. While ^{8}Be $(= \alpha + \alpha)$ is unbound, the additional neutron in ^{9}Be glues together the two α particles with a relatively small binding energy of only 1.573 MeV, which is reflected again in a correspondingly large charge radius. ^{10}Be, on the other hand, is well bound and the nucleus is stiff against a variation in the distance of the α clusters. The additional neutron in ^{11}Be can either occupy a $1p_{1/2}$ orbit (in the excited $1/2^-$ state at 320 keV) or an orbit in the $2s_{1/2}$ shell for the $1/2^+$ ground state. The experimental binding energy is only 504 keV and an extended halo is expected. Even if the core is not polarized the charge radius will change, as the ^{10}Be core will move with respect to the center of mass of the nucleus, according to

$$R_c^2(^{11}\text{Be}) = R_c^2(\text{core}) + \frac{1}{11^2}R_{\text{core}-n}^2 + \frac{1}{4}R_n^2, \tag{6}$$

with the core-neutron distance $R_{\text{core}-n}$ and the mean-square charge radius of the neutron $R_n^2 = -0.117(4)$ fm^2 [35]. In the following, we will discuss conclusions to be drawn from the combination of our results with other experiments and present details of fermionic molecular dynamics calculations on the beryllium isotopes.

Using the charge radii extracted from the D_1 transition, listed in table 1, and assuming that there is no polarization of the ^{10}Be core we obtain $R_{\text{core}-n} = 8.09(1.22)$ fm. To get an idea how far the assumption of the absence of core polarization is valid, this number can be compared with data from electromagnetic and nuclear inelastic scattering on ^{11}Be: by measuring the one-neutron removal channel a radius for the valence neutron of 5.7(4) fm was deduced [36]. With this value, the center-of-mass motion of ^{10}Be would result in a ^{11}Be charge radius slightly smaller than observed in our measurements and an additional increase of the core charge radius to 2.41(2) fm is required to explain the experimental ^{11}Be charge radius. Hence, the charge radius of the core is expected to be about 2.2(1.8) % larger than that of the free ^{10}Be nucleus.

Recently it has been pointed out by Tanihata that the measured charge radii can also be combined with measurements of the matter distribution and the B(E1) transition strength [37]. This will allow to disentangle core excitation and center of mass motion much more precisely and will draw a very detailed picture of the ^{11}Be structure.

In our previous publication [23], we compared the experimental data to theoretical predictions from *ab initio* calculations in the Green's Function Monte Carlo (GFMC) approach [38, 39](no result for ^{11}Be is so far available), No-Core Shell Model (NCSM) calculations and the Fermionic Molecular Dynamics (FMD) approach. Here, we compare them with updated NCSM results [26] using the CD-Bonn interaction and present new FMD calculations. Nuclear charge radii obtained from these theoretical models are

Table 3. Root-mean-square nuclear charge radii R_c for beryllium isotopes obtained from different theoretical calculations (th) and isotope shift measurements IS (exp). Experimental charge radii are the weighted averages of the values attained from the D_1 [23] and D_2 transitions (this work). All values are given in fm.

Isotope	FMD (th)	NCSM (th)	GFMC (th)	IS (exp)
^{7}Be	2.68	2.56(10)	2.588	2.646(16)
^{9}Be	2.57	2.41(11)	2.520	2.519(12)
^{10}Be	2.38	2.34(9)	2.354	2.355(17)
^{11}Be	2.51	2.37(11)	-	2.463(15)

FMD - Fermionic Molecular Dynamics (this work)

NCSM - No Core Shell Model with CD-Bonn potential [26]

GFMC - Green's Function Monte-Carlo calculations [38, 39]

shown in figure 4. Error bars for the NCSM radii were estimated based on model space size and oscillator frequency dependence [26]. Charge radii obtained with the INOY interaction, which provides binding energies closer to experiment than the CD-Bonn interaction, are significantly smaller and outside the CD-Bonn error bars. Although the charge radii are in general too small, the NCSM calculations are able to describe the decrease from ^{7}Be to ^{10}Be but they show only a small increase for the ^{11}Be charge radius. This is a deficiency of the NCSM model space which has difficulties to properly desribe the neutron halo in ^{11}Be. This problem is now being attacked by coupling the NCSM with the cluster model [40]. Root mean square nuclear charge radii obtained from theoretical calculations and isotope shift measurements are listed in table 3.

5. Fermionic Molecular Dynamics

Fermionic Molecular Dynamics (FMD) [41] is a many-body approach especially suited for the description of nuclei with cluster or halo structure. It has been used successfully to describe form factors and charge radii of light nuclei in the p shell and sd shell [22, 42]. In the present calculation the intrinsic many-body basis states are given by Slater determinants $|Q\rangle$ using a superposition of two Gaussian wave packets for each single-particle state. The parameters of the wave packets are mean position, mean momentum, width and orientation of the spin. The basis is very flexible, it contains the harmonic oscillator shell model states as well as Brink-type cluster model states as limiting cases. The variable width parameter allows an efficient description of spatially extended nucleon wave functions as appearing in halo nuclei. To restore the symmetries of the Hamiltonian, the Slater determinant is projected on parity, angular momentum and total linear momentum $|Q; J^\pi MK, \vec{P} = 0\rangle$. Diagonalizing the Hamiltonian in the basis spanned by different K quantum numbers provides the states $|Q; J^\pi M\kappa, \vec{P} = 0\rangle$ which are used as many-body basis states.
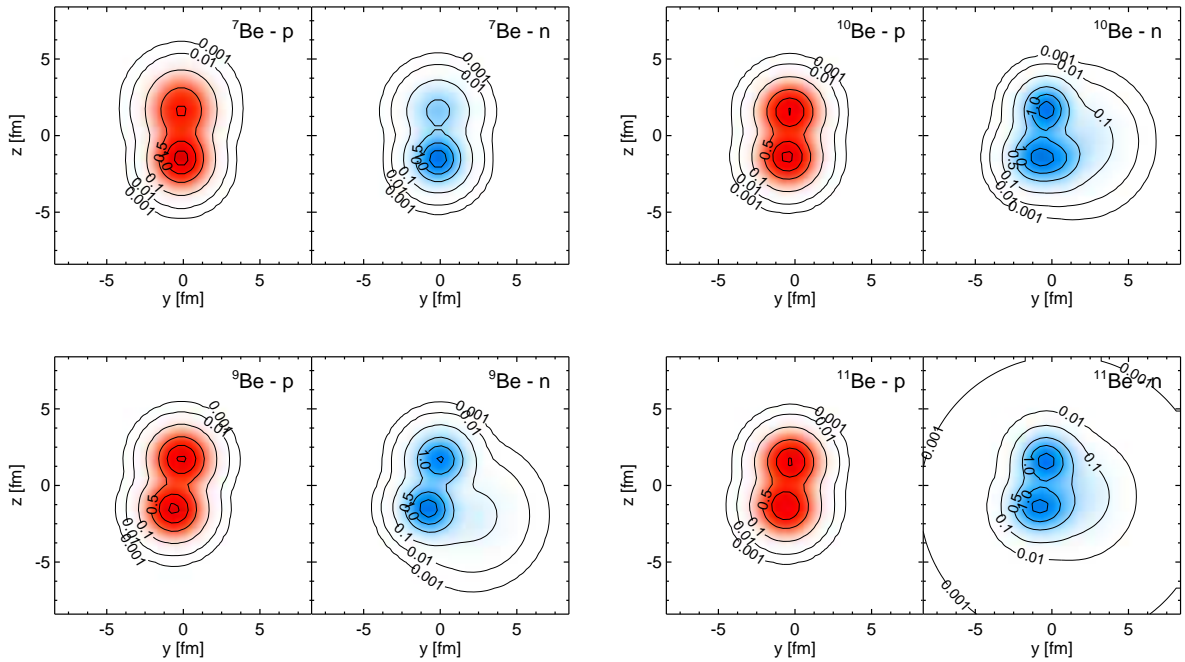
Figure 5. Cuts through the proton and neutron densities of the intrinsic states obtained in FMD VAP calculations. Contour lines are in units of half nuclear matter density.

The effective interaction is based on V_{UCOM} derived from the realistic Argonne V18 interaction by explicit treatment of short-range central and tensor correlations in the unitary correlation operator method [43]. It also includes a phenomenological two-body correction term that has been fitted to the binding energies and radii of doubly-magic nuclei up to ^{48}Ca. No parameters have been adjusted for the beryllium isotopes.

The parameters of the wave function were obtained by variation of the energy after projection (VAP) on parity and angular momentum. In figure 5 cuts through the proton and neutron densities of the intrinsic states are shown. In contrast to mean field calculations the intrinsic states obtained in VAP calculations show a pronounced α-clustering (α particle-^{3}He in the case of ^{7}Be). As the cluster thresholds, especially in ^{7}Be and ^{9}Be, are low, we expect an extended wave function for the relative motion of the clusters. Already in a single Slater determinant the relative distance of the clusters has a Gaussian distribution, but for a realistic description a superposition of several many-body states is needed. We generated such many-body states by imposing constraints on the distance between the clusters. A good measure for the distance of the clusters (assuming no significant polarization of the clusters) is the rms radius of the proton distribution with respect to the center of charge (R_{pp}). This is different from the charge radius which measures the proton radius with respect to the center of mass and which is therefore sensitive not only to the distance of the clusters but also to the motion of the clusters relative to the center of mass.

For each nucleus we performed VAP calculations with a constraint on the radius
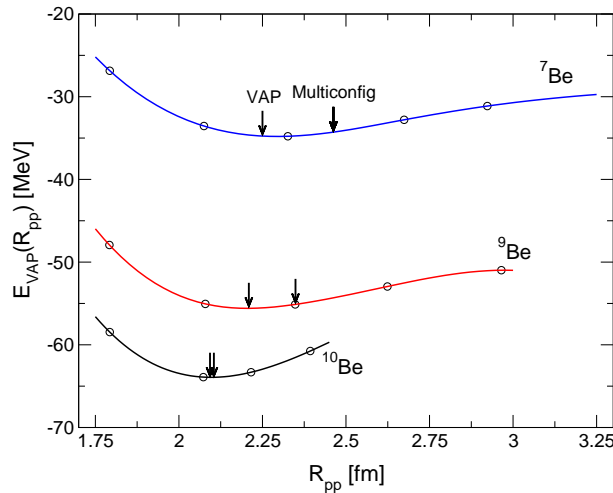
Figure 6. Energies of FMD configurations for ^{7,9,10}Be obtained in variation after projection (VAP) calculations. The proton radius with respect to the center of charge R_{pp} is used as a constraint for the intrinsic state. Arrows indicate the R_{pp} expectation values obtained in the VAP minimum and from multiconfiguration mixing calculations.

R_{pp} of the intrinsic states. In figure 6 the energies are shown as a function of R_{pp}. The energy surfaces are very flat for ^{7}Be and ^{9}Be. Therefore configurations with large R_{pp} will contribute to the ground state and will increase also the charge radius significantly compared to the VAP calculation using a single configuration. In ^{10}Be, on the other hand, the energy surface is rather steep and extended configurations will not significantly contribute to the ground state. Assuming no polarization of the clusters the R_{pp} values can be translated into rms cluster distances of 4.23 fm (^{7}Be), 4.08 fm (^{9}Be) and 3.51 fm (^{10}Be).

For ^{11}Be the situation is different. The neutron separation energy is very small and it is therefore not surprising that the FMD configuration obtained in the unconstrained VAP calculation essentially corresponds to the ^{10}Be VAP state plus an additional neutron in an extended s-orbit. Whereas R_{pp} is almost identical in the ^{10}Be and ^{11}Be VAP states, the charge radius increases significantly. This is due to the motion of the ^{10}Be core with respect to the total center of mass. For an improved description of ^{11}Be we did not only use the R_{pp} constraint which affects mainly the ^{10}Be core but also varied a second many-body state in a multiconfiguration calculation for each R_{pp}. By this procedure configurations with a ^{10}Be core in the 2^+ state and the valence neutron occupying a d-orbit are included. This admixture of core polarized configurations improves the ^{11}Be binding energy by about 1 MeV and is necessary to get ^{11}Be bound with respect to ^{10}Be. It leads to a slight increase of R_{pp} from 2.10 fm in ^{10}Be to 2.19 fm in ^{11}Be. However the effect on the charge radius of the ^{10}Be core is very small, it changes from 2.52 fm to 2.51 fm.

In summary, all FMD charge radii are slightly too large compared to the experimental results (see figure 4) but nicely reproduce the systematic trend. The FMD calculations presented in [23] did not include configurations with large cluster

distances and therefore smaller radii, especially for ^{7}Be and ^{9}Be, were obtained. When comparing the absolute charge radii, one should keep in mind that the absolute charge radii deduced from $\delta \langle r_c^2 \rangle$ depend on the reliability of $R_c(^9\text{Be})$ from electron scattering data.

To summarize, we have measured the isotope shifts in the $2s_{1/2} \rightarrow 2p_{3/2}$ transition of Be$^+$ and extracted the nuclear charge radii for ^{7,10,11}Be. The radii were compared to results of our previous measurement in the $2s_{1/2} \rightarrow 2p_{1/2}$ transition and good agreement was found. When combined with results from electromagnetic and nuclear inelastic scattering of ^{11}Be a small 2.2(1.8)% charge-radius increase of the core in ^{11}Be compared to the free ^{10}Be nucleus can be deduced. Results are also compared to calculations in the Fermionic Molecular Dynamics approach which were able to explain their systematic behavior. Thus, it can be concluded from theory and experiment that the dominant contribution to the change in the charge radius between ^{10}Be and ^{11}Be is the center-of-mass motion of the ^{10}Be core caused by the halo neutron, whereas the contribution of core polarization is rather small. Additionally, the splitting isotope shift in the $2p$ states was evaluated, showing good consistency with theoretical predictions. This provides an important consistency check of the charge radius measurements on beryllium isotopes.

References

[1] Tanihata I *et al* 1985 *Physics Letters B* **160** 380
[2] Brohm, T. *et al* 1991 *GSI Scientific Report 1990* **91-1** 12
[3] Webber W R *et al* 1990 *Physical Review C* **41** 520
[4] Blank B *et al* 1992 *Zeitschrift fuer Physik A* **343** 375-379
[5] Chulkov L *et al* 1996 *Nuclear Physics A* **603** 219-237
[6] Chulkov L *et al* 2000 *Nuclear Physics A* **674** 330-342
[7] Hansen P G and Jonson B 1987 *Europhysics Letters* **4** 409
[8] Jonson B 2003 *Physics Report* **389** 1-59
[9] Otten E W 1989 *Treatise Heavy Ion Science* **8** 515
[10] Arnold E *et al* 1987 *Physics Letters B* **197** 311
[11] Geithner W *et al* 1999 *Physical Review Letters* **83** 3792
[12] Arnold E *et al* 1992 *Physics Letters B* **281** 16
[13] Borremans D *et al* 2005 *Physical Review C* **72** 044309
[14] Neugart R *et al* 2008 Physical Review Letters **101** 132502
[15] Mueller P *et al* 2007 *Physical Review Letters* **99** 252501
[16] Sánchez R *et al* 2006 *Physical Review Letters* **96** 033002
[17] Yan Z-C and Drake G W F 2000 *Physical Review A* **61** 022504
[18] Yan Z-C and Drake G W F 2003 *Physical Review Letters* **91** 113004
[19] Puchalski M, Moro A M and Pachucki K 2006 *Physical Review Letters* **97** 133001
[20] Yan Z C, Noertershaeuser W and Drake G W F 2008 *Physical Review Letters* **100** 243002
[21] Puchalski M and Pachucki K 2008 *Physical Review A* **78** 052511

[22] Geithner W *et al* 2008 *Physical Review Letters* **101** 252502
[23] Noertershaeuser W *et al* 2009 *Physical Review Letters* **102** 062503
[24] Geppert C *et al* 2010 *to be published*
[25] Nakamura T *et al* 2006 *Physical Review Letters* **96** 252502
[26] Forssén C, Caurier E, Navrátil P 2009 *Physical Review C* **79** 021303(R)
[27] Sánchez R *et al* 2009 *Canadian Journal of Physics* **87** 825
[28] Thuemmler T, Marx R and Weinheimer Ch 2009 in *New Journal of Physics* **11** 103007
[29] Puchalski M and Pachucki K 2009 *Physical Review A* **79** 032510
[30] Puchalski M 2009 private communication
[31] Jansen J A, Peerdeman R T and De Vries C 1972 *Nuclear Physics A* **188** 337
[32] Takamine A *et al* 2009 *European Physical Journal A* **42** 369
[33] Das D and Natarajan V 2007 *Physical Review A* **75** 052508
[34] Noble G A, Schultz B E, Ming H and van Wijngaarden W A 2006 *Physical Review A* **74**
[35] Kopecky S *et al* 1997 *Physical Review C* **56** 2229
[36] Palit R *et al* 2003 *Physical Review C* **68** 034318
[37] Tanihata I 2009 private communication
[38] Pieper S C and Wiringa R B 2001 *Annual Review of Nuclear and Particle Science* **51**, 53-90
[39] Pieper S C, Varga K and Wiringa R B 2002 *Physical Review C* **66** 044310
[40] Quaglioni S and Navrátil P 2009 *Physical Review C* **79** 044606
[41] Neff T, Feldmeier H 2008 *The European Physical Journal Special Topics* **156** 69
[42] Chernykh M *et al* 2007 *Physical Review Letters* **98** 032501
[43] Neff T, Feldmeier H 2003 *Nuclear Physics* **A713** 311

Nuclear Charge Radii of ^{7,9,10}Be and the One-Neutron Halo Nucleus ^{11}Be

W. Nörtershäuser,[1,2] D. Tiedemann,[2] M. Žáková,[2] Z. Andjelkovic,[2] K. Blaum,[3] M. L. Bissell,[4] R. Cazan,[2] G. W. F. Drake,[5] Ch. Geppert,[1,6] M. Kowalska,[7] J. Krämer,[2] A. Krieger,[2] R. Neugart,[2] R. Sánchez,[1] F. Schmidt-Kaler,[8] Z.-C. Yan,[9] D. T. Yordanov,[3] and C. Zimmermann[6]

[1]*GSI Helmholtzzentrum für Schwerionenforschung GmbH, D-64291 Darmstadt, Germany*
[2]*Institut für Kernchemie, Universität Mainz, D-55128 Mainz, Germany*
[3]*Max-Planck-Institut für Kernphysik, D-69117 Heidelberg, Germany*
[4]*Instituut voor Kern- en Stralingsfysica, Katholieke Universiteit Leuven, B-3001 Leuven, Belgium*
[5]*Department of Physics, University of Windsor, Windsor, Ontario, Canada, N9B 3P4*
[6]*Physikalisches Institut, Universität Tübingen, D-72076 Tübingen, Germany*
[7]*CERN, Physics Department, CH-1211 Geneva 23, Switzerland*
[8]*Quanteninformationsverarbeitung, Universität Ulm, D-89069 Ulm, Germany*
[9]*Department of Physics, University of New Brunswick, Fredericton, New Brunswick, Canada E3B 5A3*
(Received 6 September 2008; published 13 February 2009)

Nuclear charge radii of ^{7,9,10,11}Be have been determined by high-precision laser spectroscopy. On-line measurements were performed with collinear laser spectroscopy in the $2s_{1/2} \rightarrow 2p_{1/2}$ transition on a beam of Be$^+$ ions. Collinear and anticollinear laser beams were used simultaneously, and the absolute frequency determination using a frequency comb yielded an accuracy in the isotope-shift measurements of about 1 MHz. Combining this with accurate calculations of the mass-dependent isotope shifts yields nuclear charge radii. The charge radius decreases from ^{7}Be to ^{10}Be and then increases for the halo nucleus ^{11}Be. When comparing our results with predictions of *ab initio* nuclear-structure calculations we find good agreement. Additionally, the nuclear magnetic moment of ^{7}Be was determined to be $-1.3995(5)\mu_N$ and that of ^{11}Be was confirmed with an accuracy similar to previous β-NMR measurements.

PACS numbers: 21.10.Ft, 27.20.+n, 32.10.Fn, 42.62.Fi

The discovery of halo nuclei in 1985 [1] triggered a large number of experiments in order to understand the properties and behavior of these extraordinary systems. In a halo nucleus, individual nucleons, in most cases neutrons, can reside far away from the nuclear core. The best established and investigated neutron-halo nuclei are ^{6,8}He, ^{11}Li, and ^{11}Be. In a neutron-halo nucleus, the change of the nuclear charge distribution provides information on the interactions between the different subsystems of the strongly clustered nucleus. Such changes may originate from two effects: first, the motion of the nuclear core relative to the center of mass, and second, core polarization induced by the interaction between the halo neutrons and the core. In the case of helium the nuclear core is tightly bound and only a 4% contribution of core excitation is expected [2]. The dominant part of the change is induced by the center-of-mass motion. Conversely, the ^{9}Li core in ^{11}Li is rather soft and core polarization can play a much more important role [3]. Separation between these effects is not trivial since the correlation between the halo neutrons needs to be considered. Thus, to develop a consistent picture of neutron-rich light nuclei, more data are necessary for different systems, which is a motivation to determine accurately the charge radii of ^{7,9,10,11}Be. ^{11}Be is the first one-neutron halo nucleus for which the charge radius is reported.

The only known model-independent way to determine charge radii of unstable isotopes is the laser spectroscopic

measurement of the nuclear-volume dependent isotope shift. Nuclear-volume shifts for isotopes of the light elements are very small, and short-lived isotopes can be produced only in marginal quantities. Therefore, high-precision measurements are extremely difficult. Moreover, it is a major challenge to separate these small effects from the mass shifts which dominate by 3 orders of magnitude. A breakthrough on the theoretical side was the sufficiently accurate calculation of mass shifts for systems with up to three electrons [4–8]. The first application of these results was to determine the charge radii of ^{6,7,8,9}Li [9] and ^{6}He [10]. Later, the charge radius of the two-neutron halo nucleus ^{11}Li [11] and recently that of the four-neutron halo nucleus ^{8}He [12] were determined based on these calculations. The results are now benchmark tests for nuclear-structure theory.

Ab initio descriptions of the structure of light nuclei based on realistic two- and three-nucleon interactions have been developed during the past years. In particular, Greens function Monte Carlo (GFMC) calculations, fermionic molecular dynamics (FMD), and large basis no-core shell model (NCSM) calculations, have predicted nuclear charge radii of beryllium isotopes. Moreover, the charge radius of ^{7}Be gives constraints for the determination of the ^{7}Be$(p, \gamma)^8$B S factor that is crucial for solar neutrino experiments [13,14]. For these reasons, the isotope shift of beryllium isotopes has recently attracted considerable interest. Measurements on

trapped and cooled ions in a Paul trap have been proposed for the $D1$ line [15] and first results in the $D2$ line were reported [16]. However, these measurements have not yet reached the accuracy required to extract the field shift.

We have developed a technique to determine the optical transition frequencies in collinear laser spectroscopy and used it for on-line measurements on ^{7,9,10,11}Be. The radioactive isotopes were produced at ISOLDE (CERN) with a 1.4 GeV proton beam impinging on a uranium carbide target. Beryllium atoms were ionized with the laser ion source (RILIS). After extraction, acceleration to 50 kV and mass separation, the ions were delivered to the collinear laser spectroscopy setup [17]. This has been used for isotope-shift measurements on many elements down to neon ($Z = 10$) [18]. However, for very light elements the systematic uncertainties caused by the measurement of the acceleration voltage exceed the nuclear-volume effect. Now, we can overcome these limitations employing a frequency comb and measuring the absolute transition frequencies ν_p for parallel and ν_a for antiparallel geometry of ion and laser beams. This yields the rest frame frequency ν_0 independently of the acceleration voltage via the relativistic formula $\nu_0^2 = \nu_p \nu_a$.

A schematic layout of the setup and the laser system is shown in Fig. 1. The ion beam is superimposed with the co- and counterpropagating laser beams by an electrostatic $10°$ deflector. The laser beams enter and leave the beam line through a pair of Brewster windows. Two adjustable irises and additional fixed-size apertures with diameters down to 5 mm are used along the beam line to ensure good overlap and to avoid stray light in the optical detection region. Doppler tuning is performed by changing the potential of the detection region in the range of ± 10 kV. Two photomultipliers are used for resonance fluorescence detection.

The output of two dye lasers was frequency doubled to produce ultraviolet light at 313 nm and the UV beams were well collimated over a distance of about 8 m with a beam diameter of about 3–4 mm, well adapted to the ion beam
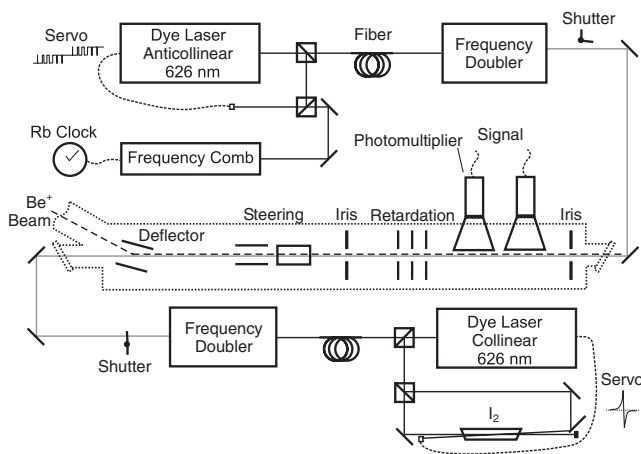
size. To avoid strong optical pumping and saturation broadening of the induced transitions, the UV light was attenuated to less than 5 mW. The fundamental light at 626 nm for collinear and anticollinear excitation was frequency stabilized in different ways. One of the dye lasers was locked to an iodine line using frequency modulation saturation spectroscopy, while the second one was locked to a frequency comb (Menlo Systems FC1500). During the beam time, the frequency of the iodine-locked laser was repeatedly measured with the frequency comb. In total, 12 different iodine lines were used and their frequencies measured with standard deviations on the order of 20 kHz. The Rb clock that was used as a reference oscillator for the frequency comb introduces an additional systematic uncertainty of about 350 kHz. However, this contribution cancels out for the isotope shifts in which frequency differences are evaluated.

Measurements were performed with the frequency of the collinear laser locked to a suitable iodine line. The voltage of the detection region was tuned to record the hyperfine-structure pattern of the collinear excitation. Then, the frequency of the anticollinear dye laser was locked to the frequency comb and its frequency chosen such that the resonance pattern was covered by the same voltage range. Repetitive scanning was performed by tuning the voltage
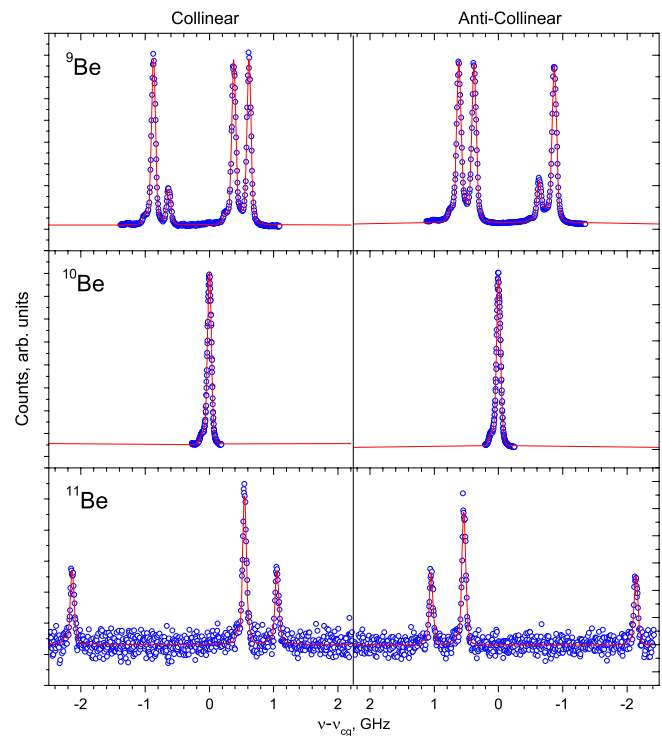

FIG. 2 (color online).   Fluorescence spectra for ^{9,10,11}Be$^+$ in the $2s_{1/2} \rightarrow 2p_{1/2}$ transition as a function of the Doppler-tuned frequency in collinear (left) and anticollinear (right) excitation. Frequencies are given relative to the respective hyperfine-structure center of gravity for the odd isotopes and the resonance frequency for ^{10}Be. Solid lines are fitting results for Voigt profiles as discussed in the text.

FIG. 1.   Setup for collinear laser spectroscopy with parallel and antiparallel excitation and a frequency comb for reference.

across this range. Dwell times of 20 ms per step were used, resulting in about 4 s per scan. Two remote-controlled mirrors were used to block alternately one of the two laser beams during each scan. Typically 2×50 scans were accumulated for isotopes with high yields, whereas up to 2×400 scans were taken for a spectrum of ^{11}Be (see Fig. 2).

The spectra were fitted with Voigt profiles of common widths for all hyperfine-structure components. The hyperfine pattern was reproduced by direct calculation of the $F \to F'$ resonance position from

$$\nu_{FF'} = \nu_{\mathrm{cg}} + \frac{1}{2}[A_{2p}C(F, I, J) - A_{2s}C(F', I, J)] \quad (1)$$

with the center-of-gravity frequency ν_{cg}, the A factors of the ground (A_{2s}) and excited states (A_{2p}), respectively, and $C(F, I, J) = F(F + 1) - I(I + 1) - J(J + 1)$. Chi-square minimization was done by varying A and ν_{cg} amongst other parameters. Weak satellite peaks arising at higher acceleration voltages due to inelastic collisions with residual gases were also included in the fitting function. The achievable accuracy was tested in an off-line beam time and systematic shifts of the transition frequency were evaluated. Only a small effect caused by beam misalignments could be observed.

The obtained isotope shifts $\delta\nu_{\mathrm{IS}}^{9,A} = \nu_0(^A\mathrm{Be}) - \nu_0(^9\mathrm{Be})$ are listed in Table I. The quoted uncertainty represents the standard error of the mean of individual results from all measurements on a particular isotope. An uncertainty of 0.5 MHz accounting for possible misalignments of the laser and ion beam overlap was added quadratically. Recoil corrections in the isotope shift are only at the 10% level of the final uncertainty. Charge radii are deduced by subtracting the mass-dependent isotope shift of the respective isotope pair as calculated in Ref. [7]. The remaining nuclear-volume shift provides the change in the mean-square nuclear charge radius $\delta\langle r_c^2\rangle$ between two isotopes. Absolute charge radii r_c must be related to at least one isotope for which the absolute radius is known and can then be deduced according to

$$r_c^2(^A\mathrm{Be}) = r_c^2(^9\mathrm{Be}) + \frac{\delta\nu_{\mathrm{IS}}^{9,A} - \delta\nu_{\mathrm{MS}}^{9,A}}{C} \quad (2)$$

with the theoretically calculated electronic factor $C = -16.912$ MHz/fm^2 [7].

TABLE I. Isotope shifts $\delta\nu_{\mathrm{IS}}^{9,A}$ in the $D1$ line and theoretical mass shifts $\delta\nu_{\mathrm{MS}}^{9,A}$ [7,8] for ^{A}Be-^{9}Be. Uncertainties for the absolute charge radius r_c include the uncertainty in the reference radius $r_c(^9\mathrm{Be}) = 2.519(12)$ fm [18].

	$\delta\nu_{\mathrm{IS}}^{9,A}$, MHz	$\delta\nu_{\mathrm{MS}}^{9,A}$, MHz	$\delta\langle r_c^2\rangle^{9,A}$, fm^2	r_c, fm
^{7}Be	$-49\,236.9(9)$	$-49\,225.75(4)$	$0.66(5)$	$2.647(17)$
^{9}Be	0	0		$2.519(12)$
^{10}Be	$17\,323.8(13)$	$17\,310.44(1)$	$-0.79(8)$	$2.357(18)$
^{11}Be	$31\,565.0(9)$	$31\,560.31(6)$	$-0.28(5)$	$2.463(16)$

For stable ^{9}Be, r_c was determined by elastic electron scattering [19], and by muonic atom spectroscopy [20]. Reported charge radii of 2.519(12) fm [19] and 2.39(17) fm differ by 0.13 fm but agree within the rather large uncertainty of the muonic atom result. We have used the electron scattering result, but we note that this was not obtained in a completely nuclear-model independent way. Hence, reanalysis of the Be scattering data, as performed for the proton [21], would be useful to determine whether the small uncertainty of 0.012 fm is reliable. However, a small change in the reference radius causes primarily only a parallel shift of all charge radii.

Results for $\delta\langle r_c^2\rangle$ and r_c are listed in Table I. Isotope shifts in the $D2$ line have also been measured and are still under evaluation. The extracted charge radii agree with the values reported here, but are less accurate due to unresolved hyperfine structures.

The derived nuclear charge radii are shown in Fig. 3: r_c decreases from ^{7}Be to ^{10}Be, but then increases for ^{11}Be. The decrease is probably caused by the clusterization of ^{7}Be into an α cluster and a triton cluster, whereas ^{9,10}Be are considered to be $\alpha + \alpha + n$ and $\alpha + \alpha + n + n$ systems, respectively, and are more compact. According to a simple frozen core two-body model the increase from ^{10}Be to ^{11}Be can be attributed to the motion of the ^{10}Be core relative to the center of mass. Using $r_c^2(^{11}\mathrm{Be}) = R_{\mathrm{cm}}^2 + r_c^2(^{10}\mathrm{Be})$ a rms distance of 7.0 fm between the neutron and the center of mass of ^{11}Be can be extracted directly from $\delta\langle r_c^2\rangle$.

To test nuclear-structure theories, predictions from different models are included in Fig. 3. Reported point-proton radii r_{pp} were converted to nuclear charge radii r_c by folding in proton R_p [21] and neutron R_n [22] rms charge radii and adding the Darwin-Foldy term [23]:
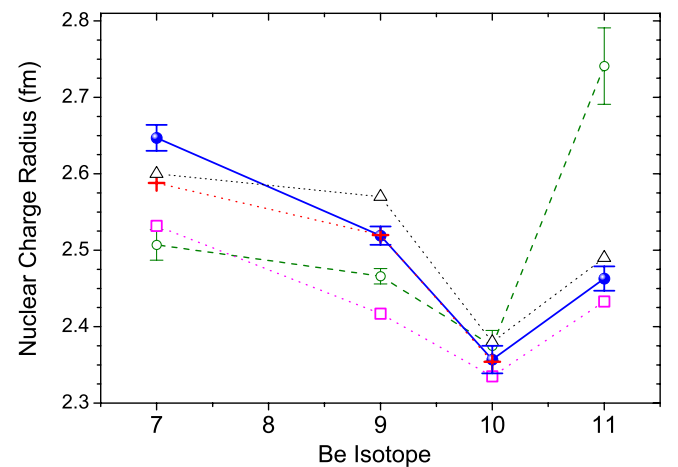

FIG. 3 (color online). Experimental charge radii of beryllium isotopes from isotope-shift measurements (●) compared with values from interaction cross-section measurements (○) and theoretical predictions: Greens-function Monte Carlo calculations (+) [2,24], fermionic molecular dynamics (△) [25], ab $initio$ no-core shell model (□) [13,26,27].

TABLE II. Magnetic dipole coupling constants A of the $2s_{1/2}$ and the $2p_{1/2}$ states and the magnetic moments of the odd isotopes.

Isotope	A_{2s} (MHz)	A_{2p} (MHz)	$\mu(\mu_N)$	Ref.
^{7}Be	$-742.90(25)$	$-140.17(18)$	$-1.3995(5)$	this work
			$-1.398(15)$	[28]
^{9}Be	$-624.97(4)$	$-118.00(4)$		this work
	$-625.008837048(10)$	$-118.6(36)$	$-1.177432(3)$	[29,30]
^{11}Be	$-2677.4(8)$	$-505.4(5)$	$-1.6813(5)$	this work
			$-1.6816(8)$	[31]

$$\langle r_c^2 \rangle = \langle r_{\rm pp}^2 \rangle + \langle R_p^2 \rangle + \frac{N}{Z}\langle R_n^2 \rangle + \frac{3\hbar^2}{4m_p^2 c^2}. \qquad (3)$$

Nuclear-model dependent charge radii extracted from interaction cross-section measurements [24] show a similar trend as our data but changes are smaller for the isotopes below ^{10}Be and overestimated for ^{11}Be. All theoretical model predictions show good agreement with our results. Depending on the model, specific features are especially well reproduced. In the case of GFMC calculations [2,25] the agreement for ^{9,10}Be is striking whereas the decrease between ^{7}Be and ^{9}Be is slightly underestimated. Unfortunately, a charge radius calculation for ^{11}Be has not been obtained to date. FMD [26] and improved NCSM [14,27,28] calculations include the halo nucleus and the change between ^{10}Be and ^{11}Be is very well predicted. Concerning the other isotopes FMD does a better job for the isotope pair ^{9,10}Be, whereas the change in the pair ^{7,9}Be is best described by the NCSM results (note that the absolute charge radius depends on the reference radius).

From fitting the observed hyperfine structures we obtain the magnetic dipole constant A for the $2s$ and the $2p_{1/2}$ states as listed in Table II. Based on the precision measurement of A_{2s} in ^{9}Be [30] and the corresponding nuclear magnetic moment $\mu = -1.177432(3)\mu_N$ [31], we determine the magnetic moments of ^{7}Be and ^{11}Be. For ^{11}Be we confirm the previously measured value from an optical pumping β-NMR experiment [32]. For ^{7}Be, an earlier value from optical hyperfine measurements [29] is improved by more than an order of magnitude.

To summarize, we have measured the charge radii of ^{7,9,10,11}Be with on-line frequency-comb based collinear laser spectroscopy. From a simple frozen-core two-body model we obtain a rms distance of about 7 fm between the halo neutron and the center of mass in ^{11}Be. Comparison with elaborate nuclear-structure calculations (GFMC, FMD, and LBSM) shows in all cases good agreement with our measurement. The magnetic moment of ^{11}Be has been confirmed and the accuracy for ^{7}Be considerably improved. The developed experimental technique has the potential to be applied to the very short-lived nuclei ^{12,14}Be and can generally improve the accuracy of collinear laser spectroscopy where this is required.

[1] I. Tanihata *et al.*, Phys. Rev. Lett. **55**, 2676 (1985).
[2] S. C. Pieper and R. B. Wiringa, Annu. Rev. Nucl. Part. Sci. **51**, 53 (2001).
[3] R. Neugart *et al.*, Phys. Rev. Lett. **101**, 132502 (2008).
[4] Z.-C. Yan and G. W. F. Drake, Phys. Rev. A **61**, 022504 (2000).
[5] Z.-C. Yan and G. W. F. Drake, Phys. Rev. Lett. **91**, 113004 (2003).
[6] M. Puchalski, A. M. Moro, and K. Pachucki, Phys. Rev. Lett. **97**, 133001 (2006).
[7] Z. C. Yan, W. Nörtershäuser, and G. W. F. Drake, Phys. Rev. Lett. **100**, 243002 (2008).
[8] M. Puchalski and K. Pachucki, Phys. Rev. A **78**, 052511 (2008).
[9] G. Ewald *et al.*, Phys. Rev. Lett. **93**, 113002 (2004).
[10] L.-B. Wang *et al.*, Phys. Rev. Lett. **93**, 142501 (2004).
[11] R. Sánchez *et al.*, Phys. Rev. Lett. **96**, 033002 (2006).
[12] P. Mueller *et al.*, Phys. Rev. Lett. **99**, 252501 (2007).
[13] A. Csoto and K. Langanke, Nucl. Phys. A **636**, 240 (1998).
[14] P. Navrátil, C. A. Bertulani, and E. Caurier, Phys. Rev. C **73**, 065801 (2006).
[15] M. Záková *et al.*, Hyperfine Interact. **171**, 189 (2006).
[16] T. Nakamura *et al.*, Phys. Rev. A **74**, 052503 (2006).
[17] R. Neugart, Nucl. Instrum. Methods Phys. Res. **186**, 165 (1981).
[18] W. Geithner *et al.*, Hyperfine Interact. **129**, 271 (2000).
[19] J. A. Jansen, R. Th. Peerdeman, and C. de Vries, Nucl. Phys. A **188**, 337 (1972).
[20] L. A. Schaller *et al.*, Nucl. Phys. A **343**, 333 (1980).
[21] I. Sick, Phys. Lett. B **576**, 62 (2003).
[22] S. Kopecky *et al.*, Phys. Rev. C **56**, 2229 (1997).
[23] J. L. Friar, J. Martorell, and D. W. L. Sprung, Phys. Rev. A **56**, 4579 (1997).
[24] I. Tanihata *et al.*, Phys. Lett. B **206**, 592 (1988).
[25] S. C. Pieper, K. Varga, and R. B. Wiringa, Phys. Rev. C **66**, 044310 (2002).
[26] R. Torabi, GSI Darmstadt (private communication).
[27] C. Forssén, P. Navratil, W. E. Ormand, and E. Caurier, Phys. Rev. C **71**, 044312 (2005).
[28] P. Navrátil (private communication).
[29] S. Kappertz *et al.*, in *ENAM98: Exotic Nuclei and Atomic Masses*, edited by B. M. Sherrill *et al.* (AIP, Woodbury, NY, 1999), p. 110.
[30] D. J. Wineland, J. J. Bollinger, and W. M. Itano, Phys. Rev. Lett. **50**, 628 (1983).
[31] W. M. Itano, Phys. Rev. B **27**, 1906 (1983).
[32] W. Geithner *et al.*, Phys. Rev. Lett. **83**, 3792 (1999).

Towards a nuclear charge radius determination for beryllium isotopes

**M. Žáková · Ch. Geppert · A. Herlert · H.-J. Kluge ·
R. Sánchez · F. Schmidt-Kaler · D. Tiedemann ·
C. Zimmermann · W. Nörtershäuser**

Abstract We propose determination of isotope shifts for radioactive beryllium isotopes using laser cooled ions in a linear radio frequency (RF) trap. Based on these measurements, combined with precise mass shift calculations, it will be possible to extract model-independent nuclear charge radii of ^{7,9,10}Be and the one-neutron halo ^{11}Be with precision better than 3%. Radioactive beryllium isotopes produced at ISOLDE and ionized with a laser ion source will be cooled and bunched in the radio frequency quadrupole buncher of ISOLTRAP. Ion temperatures will be reduced to the mK range by sympathetic cooling with co-trapped laser cooled ions in a specially designed two-stage linear RF trap. Resonances will be detected via fluorescence and frequencies measured with a femtosecond frequency comb.

Key words laser spectroscopy · isotope shift · nuclear charge radius ·
linear radio frequency trap · halo nuclei

M. Žáková (✉) · R. Sánchez · D. Tiedemann · W. Nörtershäuser
Johannes Gutenberg-Universität Mainz, Mainz, Germany
e-mail: m.zakova@gsi.de

Ch. Geppert · H.-J. Kluge · W. Nörtershäuser
GSI, Darmstadt, Germany

A. Herlert
CERN, CH-1211 Genéve 23, Genéve, Switzerland

H.-J. Kluge
Universität Heidelberg, Heidelberg, Germany

F. Schmidt-Kaler
Universität Ulm, Ulm, Germany

C. Zimmermann
Eberhard-Karls-Universität Tübingen, Tübingen, Germany

1 Introduction

More than 20 years ago Tanihata [1] discovered that some isotopes of light elements close to the neutron drip line have nuclear matter radii much larger than their neighbors. These nuclear matter radii were extracted from breakup cross-section measurements. It was soon proposed that the observed large radii are caused by weakly bound nucleons that form a so-called halo around a compact nuclear core. This discovery inspired a large variety of experiments in which properties of these halo nuclei were studied [2].

One of the early arising questions was to which extent the structure of the nuclear core is modified by the orbiting halo nucleon(s). Laser spectroscopy provides a model-independent way to access nuclear ground state properties, like spins, electromagnetic moments and nuclear charge radii. ^{11}Li was the first halo nucleus that was studied in this way. In a series of measurements the COLLAPS collaboration at ISOLDE determined the nuclear magnetic dipole moment and the electric quadrupole moment using the β-NMR technique [3–5]. Concerning the halo structure of ^{11}Li, the most remarkable result is the small difference in the moments in ^{9}Li and ^{11}Li. The magnetic moments are close to the Schmidt value and are less than 10% different, while the nuclear quadrupole moments agreed within their uncertainties. More recently, the magnetic dipole moment of ^{11}Be has been measured [6] by the same technique and the measurements of ^{9,11}Li were improved [7, 8].

The halo-core interaction can also be probed by measuring the change in the nuclear charge radius and therefore a determination of this quantity is of great interest for halo isotopes. However, it was only recently that such measurements became possible for the radioactive isotopes of the lightest nuclei [3–6]. Based on new and very specialized techniques, two groups have succeeded in measuring, for the first time, optical isotope shifts of very light radioactive nuclei ($Z<10$) with a precision that is sufficient to extract nuclear charge radii. At the Argonne National Laboratory the charge radius of ^{6}He was obtained from laser spectroscopy on helium atoms confined in a magneto-optical trap [9], while an international collaboration, lead by GSI Darmstadt and the University of Tübingen, developed a method for high-resolution resonance ionization spectroscopy and measured the charge radii of ^{8,9}Li at GSI [10, 11] and of ^{11}Li [12] at the ISAC mass separator at TRIUMF. Both ^{6}He and ^{11}Li are two-neutron halo nuclei and a charge radius measurement of the one-neutron halo ^{11}Be will provide important complementary information. In this contribution we describe the proposed *Be*ryllium *T*rap for *I*nvestigation of *N*uclear charge r*a*dii (BeTINa).

2 Experimental method

2.1 Optical isotope shift

The isotope shift (IS) in an electronic transition, i.e. the difference in transition frequencies between two isotopes, has two origins: The difference in nuclear mass affects exact electron energies due to the nuclear motion around the center of mass (mass shift, MS), while the spatial extent of the nuclear charge leads to a difference in the binding energy (volume or field shift, FS) for electrons which have non-zero probability of being inside the nucleus. While the MS between two isotopes with mass numbers A and A' is proportional to

$$\delta\nu_{\mathrm{MS}}^{AA'} \propto \frac{M_A - M_{A'}}{M_A \cdot M_{A'}},$$

and thus becomes smaller for heavier elements, the nuclear volume effect increases with Z. For example, in helium, lithium and beryllium transitions, the field shift contributes approximately only 1 MHz, while the mass shift is on the order of several 10 GHz. Separation of the two effects can only be achieved if the mass shift in the electronic transition can be reliably calculated with an accuracy of 10^{-5} or better. To reach this accuracy, relativistic and quantum electro-dynamical corrections have to be taken into account. Such calculations were demonstrated for the three-electron system lithium a few years ago [13–15] and since have been considerably improved [16].

The Be^+ ion is also a three-electron system and can be calculated with the techniques already developed for the case of lithium. The nuclear volume shifts can be determined according to

$$\delta\nu_{FS} = \delta\nu_{IS}^{Exp} - \delta\nu_{MS}^{Theorie}.$$

Using the well-known nuclear charge radius dependence of the field shift

$$\delta\nu_{FS} = \frac{2\pi}{3}\Delta|\psi(0)|^2 \cdot \delta\langle r_c^2\rangle,$$

where $\Delta|\Psi(0)|^2$ is the change of the electron probability at the nucleus in the transition (deducible from atomic theory). From these, one obtains an expression for change in the root-mean-square nuclear charge radius of the isotope A'

$$\langle r_c\rangle^{A'} = \langle r_c\rangle^A + \frac{\delta\nu_{IS}^{Exp} - \delta\nu_{MS}^{Theorie}}{\frac{2\pi}{3}\Delta|\Psi(0)|^2},$$

provided that the nuclear charge radius of a reference isotope A is known. The charge radius of stable ^9Be, which has been determined with sufficient precision by both electron scattering [17, 18] and spectroscopy on muonic atoms [19], will be used as the reference.

2.2 Laser excitation scheme

Almost all transitions from the Be^+ ground state are in the vacuum-ultraviolet range; the only one that is relatively accessible with available commercial laser systems is the $2s\rightarrow 2p$ transition at 313 nm. Stable $^9Be^+$ ions stored and cooled in RF traps are one of the workhorses of quantum computing experiments, and thus provides a well-established starting point for the currently proposed experiments. All odd beryllium isotopes exhibit hyperfine structure due to non-vanishing nuclear spins and are, thus, not two-level systems. To avoid optical pumping into the dark states, and to allow many absorption-emission cycles, an RF frequency electric field will be applied to couple the $2s_{1/2}$ ground state hyperfine levels to mix their populations. The fine structure splitting allows two possible transitions, $2s_{1/2}\rightarrow 2p_{1/2}$ and $2s_{1/2}\rightarrow 2p_{3/2}$, but hyperfine structure splitting can be resolved only in the $2s_{1/2}\rightarrow 2p_{1/2}$ transition. The 8.1(4) ns lifetime of the $2p$ level [20] corresponds to a natural linewidth ($\Gamma = 1/2\pi\tau$) of 20 MHz (FWHM). Thus, line centers must be determined to an accuracy of better than 1% (200 kHz) to extract meaningful values for nuclear charge radii.

2.3 Production and transfer of radioactive berillium ions

All radioactive beryllium isotopes can be produced at the ISOLDE facility at CERN. The laser ion source has demonstrated yields $>10^6$ ions/s for the halo isotope ^{11}Be, and these
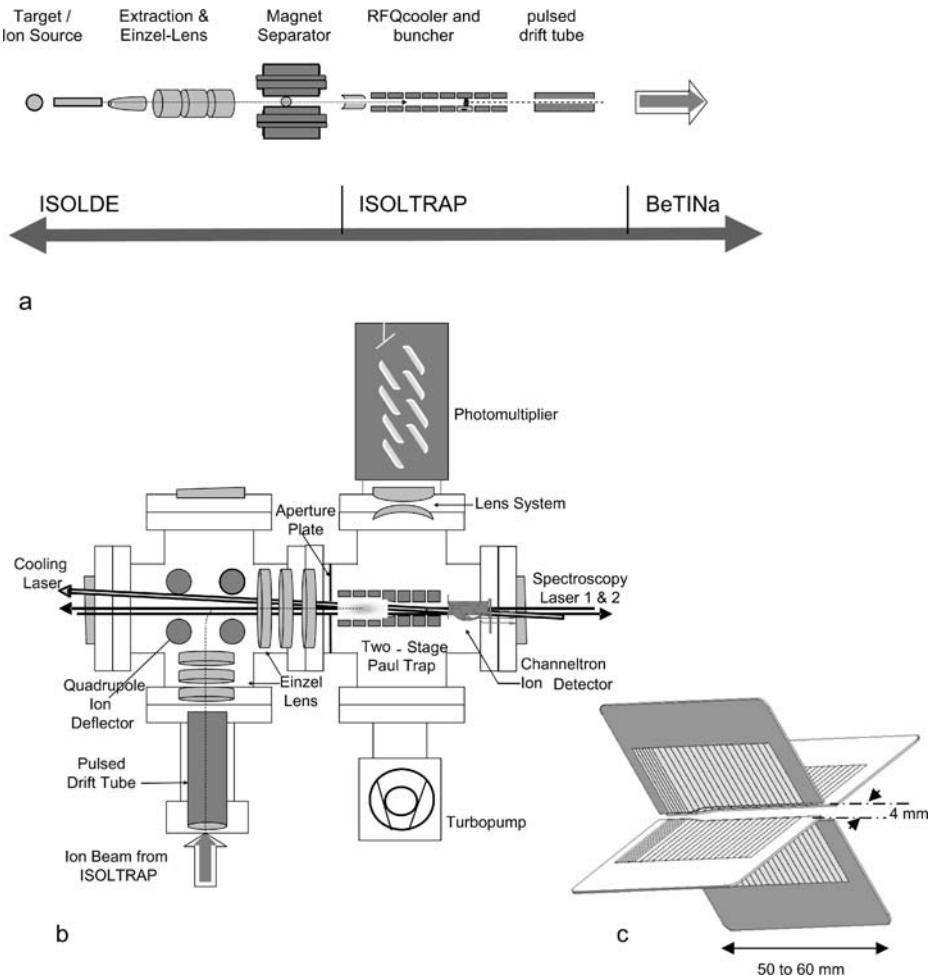
Fig. 1 ISOLDE ion source and radio frequency quadrupole cooler and buncher of ISOLTRAP (**a**); Schematic experimental set-up (**b**) and especially designed RF trap for BeTINa (**c**). Details are described in the text

have been delivered to other laser spectroscopy experiments [6]. Even higher yields have been produced for the lighter radioactive isotopes ^{7,10}Be. The ISOLTRAP collaboration operates a gas-filled radio frequency quadrupole (RFQ) cooler and buncher as illustrated in Fig. 1a [21]. Ions produced by ISOLDE can be accumulated and converted into low-energy, low-emittance ion pulses. Ions captured inside the RFQ lose transverse and longitudinal energy due to collisions with buffer gas. They then accumulate in the potential minimum in front of the trap exit, and are released as a pre-cooled ion bunch with a well defined time structure. A pulsed drift tube is finally used to reduce the bunch energy to approximately 3 keV, a value optimal for transport through the stray fields of the ISOLTRAP magnet to the BeTINa experiment.
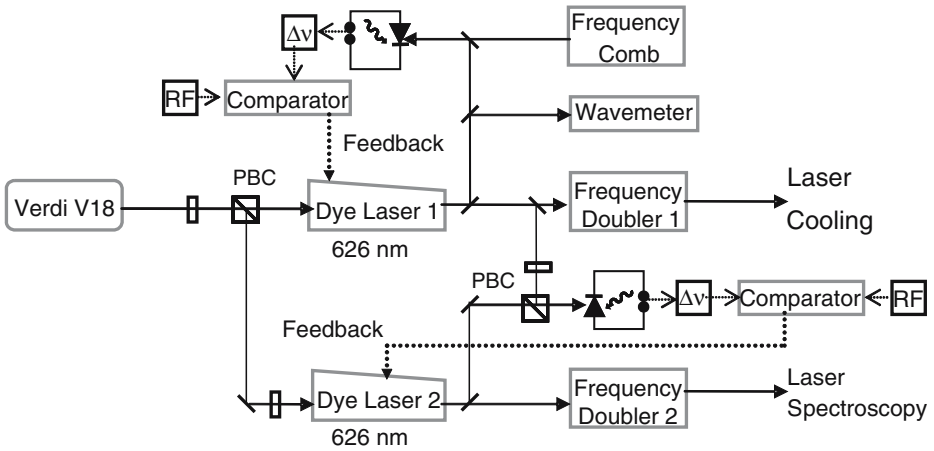
Fig. 2 Scheme of the laser system and the stabilization chain, *RF*: radio frequency generator, $\Delta\nu$: beat frequency signal, *PB*: polarizing beam splitter cube

2.4 Experimental procedure

2.4.1 Linear RF-trap

A sketch of the BeTINa experimental set-up is shown in Fig. 1b. An ion bunch from the ISOLTRAP RFQ system will be delivered through a second pulsed drift tube, where the beam energy is further reduced from 3 keV down to a few 10 eV to facilitate ion capture in the subsequent trap. Two Einzel lenses and a quadrupole ion deflector are used to inject these low-energy ions into a specially designed two-stage linear RF trap, shown in Fig. 1c. A combination of two linear RF traps with different free field radii is driven by the same RF frequency. The first trap (cooler trap) with the larger radius will be used to catch the radioactive Be^+ ions and to cool them sympathetically with simultaneously stored and laser-cooled Ca^+ or Mg^+ ions. Sympathetic cooling is similar to buffer gas cooling, but it reaches lower temperatures by dissipating Be^+ ion energy into an ensemble of laser cooled Ca^+ ions. The light pressure of the laser beam will be used to partially separate the Be^+ ions from the cooling species, and a voltage sequence applied to the multiply segmented DC electrode structure will transfer the Be^+ ions into the narrower spectroscopy trap for additional laser cooling and fluorescence spectroscopy.

2.4.2 Laser set-up

The scheme of the laser system for spectroscopy and laser cooling is shown in Fig. 2. It uses two cw tunable single-mode ring dye lasers operated at 626 nm, which will be frequency doubled to reach the $2s_{1/2} \rightarrow 2p_{1/2}$ transition wavelength at 313 nm. As shown in the figure, the first dye laser, for laser cooling, will be stabilized via frequency offset locking to a femtosecond frequency comb generated with a mode-locked Er-doped fiber laser. The second dye laser, for spectroscopy, will be locked via beat-frequency comparison with the comb-stabilized dye laser. A similar stabilization technique was used in an experimental test of special relativity at GSI Darmstadt [17], where a cw tunable single-

mode titanium:sapphire ring laser was stabilized to the frequency comb. A laser linewidth of 100 kHz was reached with this combination. Acousto-optic modulators (not shown) will be used for fast switching between the spectroscopy and cooling lasers. Spectroscopy will be done with the cooling laser off, and exposure time will be short enough to prevent significant ion heating. Once the spectroscopy laser is turned off, the cooling laser is turned on again to remove any excess energy gained by the ions. Resonance frequencies from the spectroscopy will be determined via fluorescence detection with a photomultiplier and/or a CCD camera. With this set-up we should be able to observe a transition linewidth close to the natural linewidth. To determine the center of a 20 MHz wide line to an accuracy of approximately 1% of the linewidth should be reachable considering the rather high yields and relatively long half-lives of the beryllium isotopes up to the one neutron halo [11]Be. However, systematic studies of the exact lineshape and carefully avoiding or correcting all frequency shift effects will be necessary to reach the required precision.

3 Conclusions and outlook

Measurements of isotope shifts by precision laser spectroscopy of trapped and cooled ions will provide valuable information for the determination of the nuclear charge radii of the Be isotopes. We plan to investigate the isotopes [7,9,10]Be and the one-neutron halo system [11]Be. Assembling of the experimental set-up and off-line test experiments are taking place at the Nuclear Chemistry Department at the University of Mainz, Germany. We plan to move the whole equipment and to install it for on-line measurements at the ISOLDE facility at CERN, Switzerland in 2008.

References

1. Tanihata, I., Hamagaki, H., Hashimoto, O., Shida, Y., Yoshikawa, N., Sugimoto, K., Yamakawa, O., Kobayashi, T., Takahashi, N.: Phys. Rev. Lett. **55**, 2676–2679 (1985)
2. Tanihata, I.: J. Phys., G **22**, 157–198 (1996)
3. Arnold, E., Bonn, J., Gegenwart, R., Neu, W., Neugart, R., Otten, E.W., Ulm, G., Wendt, K., ISOLDE Collaboration: Phys. Lett., B **197**, 311–314 (1987)
4. Arnold, E., Bonn, J., Klein, A., Neugart, R., Neuroth, M., Otten, E.W., Lievens, P., Reich, H., Widdra, W., ISOLDE Collaboration: Phys. Lett., B **281**, 16–19 (1992)
5. Arnold, E., Bonn, J., Klein, A., Lievens, P., Neugart, R., Neuroth, M., Otten, E.W., Reich, H., Widdra, W.: Z. Physik, A **349**, 337–338 (1994)
6. Geithner, W., Kappertz, S., Keim, M., Lievens, P., Neugart, R., Vermeeren, L., Wilbert, S., Fedoseyev, V.N., Köster, U., Mishin, V.I., Sebastian, V.: Phys. Rev. Lett. **83**, 3792–3795 (1999)
7. Borremans, D., Balabanski, D.L., Blaum, K., Geithner, W., Gheysen, S., Himpe, P., Kowalska, M., Lassen, J., Lievens, P., Mallion, S., Neugart, R., Neyens, G., Vermeulen, N., Yordanov, D.: Phys. Rev., C **72**(4), 044309 (2005)
8. Neugart, R.: Phys. Rev. Lett. (in preparation) (2006)
9. Wang, L.-B., Mueller, P., Bailey, K., Drake, G.W.F., Greene, J.P., Henderson, D., Holt, R.J., Janssens, R.V.F., Jiang, C.L., Lu, Z.-T., O'Connor, T.P., Pardo, R.C., Rehm, K.E., Schiffer, J.P., Tang, X.D.: Phys. Rev. Lett. **93**, 142501 (2004)

10. Ewald, G., Nörtershäuser, W., Dax, A., Götte, S., Kirchner, R., Kluge, H.-J., Kühl, T., Sanchez, R., Wojtaszek, A., Bushaw, B.A., Drake, G.W.F., Yan, Z.-C., Zimmermann, C.: Phys. Rev. Lett. **93**, 113002 (2004)

11. Ewald, G., Nörtershäuser, W., Dax, A., Götte, S., Kirchner, R., Kluge, H.-J., Kühl, T., Sanchez, R., Wojtaszek, A., Bushaw, B.A., Drake, G.W.F., Yan, Z.-C., Zimmermann, C.: Phys. Rev. Lett. **94**, 039901 (2005)

12. Sánchez, R., Nörtershäuser, W., Ewald, G., Albers, D., Behr, J., Bricault, P., Bushaw, B.A., Dax, A., Dilling, J., Dombsky, M., Drake, G.W.F., Götte, S., Kirchner, R., Kluge, H.-J., Kühl, T., Lassen, J., Levy, C.D.P., Pearson, M.R., Prime, E.J., Ryjkov, V., Wojtaszek, A., Yan, Z.-C., Zimmermann, C.: Phys. Rev. Lett. **96**, 033002 (2006)

13. Yan, Z.-C., Drake, G.W.F.: Phys. Rev., A **61**, 022504 (2000)

14. Yan, Z.-C., Drake, G.W.F.: Phys. Rev., A **66**, 042504 (2002)

15. Yan, Z.-C., Drake, G.W.F.: Phys. Rev. Lett. **91**, 113004 (2003)

16. Puchalski, M., Komasa, J., Moro, A.M., Pachucki, K.: Phys. Rev. Lett. in preparation (2006)

17. de Jager, C.W., de Vries, H., de Vries, C.: Atom. Data Nucl. Data Tables **14**, 479–508 (1974)

18. Jansen, J.A., Peerdeman, R.T., De Vries, C.: Nucl. Phys., A **188**(2), 337–352 (1972)

19. Schaller, L.A., Schellenberg, L., Ruetschi, A., Schneuwly, H.: Nucl. Phys., A. **343**, 333–346 (1980)

20. Andersen, T., Jessen, K.A., Sørensen, G.: Phys. Rev. **188**, 76–81 (1969)

21. Herfurth, F., Dilling, J., Kellerbauer, A., Bollen, G., Henry, S., Kluge, H.-J., Lamour, E., Lunney, D., Moore, R.B., Scheidenberger, C., Schwarz, S., Sikler, G., Szerypo, J.: Nucl. Instr. Meth. Phys. Res., A. **469**, 254–275 (2001)